Nanostructured Graphene Electrodes for Energy Applications

Thomas O. M. Samuels

Supervised by Jamie H. Warner

Linacre College

Department of Materials

University of Oxford

A Thesis Submitted for the Degree of

Doctor of Philosophy

October 2017

Declaration

The material contained within this thesis has not previously been submitted for a degree at the University of Oxford or any other university. The research reported within this thesis has been conducted by the author unless indicated otherwise.

Copyright

The copyright of this thesis rests with the author. No quotation from it should be published without the prior written consent of the author, and any information derived from it should be acknowledged.

Abstract

Polymer electrolyte (or proton exchange) membrane fuel cells (PEMFCs) are promising for green energy applications, particularly for automobiles. However, the cost and durability issues surrounding the platinum/carbon (Pt/C) electrode materials are barriers to their widespread use. The development of electrodes which have better utilisation of Pt crystals, and which retain their activity for longer periods of time, are of great interest to the fuel cell community. Graphene is a promising candidate for catalyst support applications because of its advantageous properties. For this reason the production of graphene and graphene hybrid catalyst supports, and their interactions with Pt particles, are active areas of research. This project involved the synthesis of 3D graphene and graphene hybrid materials, their integration with Pt nanocrystals, and investigations of their electrochemical stability.

Firstly, 3D multilayer graphene foam was synthesised using a chemical vapour deposition (CVD) method. This was then used as a substrate in order to investigate the role of oxygen-plasma induced defects on the graphene surface on the synthesis of Pt nanocrystals formed through thermal annealing. It was found that the induction of defects could increase the nucleation density, and decrease and narrow the size distribution of Pt nanocrystals. In addition, results suggest that Pt can prevent certain types of defects from healing during heat treatment.

A novel method was then explored to produce 3D graphene and 3D graphene/carbon nanotube (CNT) powders using the thermal annealing of nickel acetate. The synthesis can be varied to produce a variety of materials with different crystallinities, and it was found that rapid heating was a key factor for the formation of the CNTs. These materials were

explored as supports for thermally produced Pt nanocrystals and compared to commercially available carbon black, and it was found that good dispersion could not be achieved on the supports with the poorest crystallinity. Some of the materials produced performed similarly to HiSPEC 3000, a commercially available catalyst, in cyclic voltammetry (CV) experiments.

Within the past few years, a popular strategy to increase the durability of Pt/C catalysts has been to cover the Pt crystals with a protective layer. A CVD approach was used to modify a commercially available Pt/C catalyst with graphene layers. These were studied using HRTEM, and their electrochemically active surface areas (ECSAs) and durabilities were examined using CV experiments. Only a detrimental effect of the graphene layers was found in this case, and the reasons for why this might be the case are discussed.

Publications

(1) **Samuels, T. O. M.**; Robertson, A. R.; Kim, H.; Pasta, M.; Warner, J. H. Three Dimensional Multi-layered Graphene and Multi-layer Graphene-CNT Hybrid Materials via Rapid Thermal Annealing of Nickel Acetate as a Pt Nanoparticle Support. *J. Mater. Chem. A.*, **2017**, *5*, 10457-10469.

(2) **Samuels, T. O. M.**; Robertson, A. R; Pasta, M.; Warner, J. H. Influence of CVD Grown Graphene Shells on the Stability of Pt Catalysts on Carbon Supports. *In Preparation*

(3) Wang, X.; Hooper, T. N.; Kumar, A.; Priest, I. K.; Sheng, Y.; **Samuels, T. O. M.**; Wang, S.; Robertson, A. W.; Pacios, M.; Bhaskaran, H.; Weller, A. S.; Warner, J. H. Oligomeric Aminoborane Precursors for the Chemical Vapour Deposition Growth of Few-Layer Hexagonal Boron Nitride. *CrystEngComm*, **2016**, *19*, 285–294.

(4) Li, H.; Wang, S.; Sawada, H.; Han, G. G. D.; **Samuels, T.**; Allen, C. S.; Kirkland, A. I.; Grossman, J. C.; Warner, J. H. Atomic Structure and Dynamics of Single Platinum Atom Interactions with Monolayer MoS_2. *ACS Nano*, **2017**, *11*, 3392-3403

(5) Siritanaratkul, B.; Megarity, C. F.; Roberts, T.; **Samuels, T. O. M.**; Winkler, M.; Warner, J. H.; Happe, T.; Armstrong, F. A. Transfer of Photosynthetic $NADP^+$/NADPH Recycling Activity to a Porous Metal Oxide for Highly Specific, Electrochemically-driven Organic Synthesis. *Chem. Sci.*, **2017**, *8*, 4579-4586.

Work from Chapter 5 has been published in Ref [1].

Work from Chapter 6 has been submitted in Ref [2].

Acknowledgements

The production of this thesis would not have been possible without the input and support of several people. Primarily I would like to thank my supervisor, Professor Jamie Warner. In addition to providing me with advice, supervision, encouragement, and training, he also enabled me to develop my own ideas and pursue them. He also provided me with the opportunity to visit Korea for experiments and enabled me to attend a conference in Singapore, both these experiences were invaluable.

In addition, I would like to give thanks to Prof. Mauro Pasta, whose electrochemical equipment and knowledge supported me significantly in the third year of my DPhil, and whose comments and contribution to my paper drafts were extremely helpful.

During my DPhil, I was privileged enough to be able to visit collaborators in the Korea Institute for Energy Research (KIER) for a three-week research trip. I would like to extend my thanks to Heeyeon Kim for her kindness and for hosting me during this period, and to her students Kun-Hyun Kwon and Dong-Sung Choi for teaching me electrochemical techniques and making me feel so welcome.

I would also like to thank Dr. Alex Robertson for always being able to find the time to look at my samples using the AC-TEM. Some conclusions in this thesis would not be possible without the insight gained from this technique.

I must also extend my gratitude to various members of support staff who trained me during my project. I would like to thank Paul Pattinson for his help with SEM. I would also like to thank Susan Warren and Colin Johnston, for training me on several pieces of OMCS equipment.

There were times during my DPhil where I thought I might not make it through, and I will never forget the emotional support and kindness shown to me by the many friends I was fortunate enough to have at Oxford. Several of them are particularly important to the completion of this thesis. Firstly, I would like to thank my lab mates for their company and companionship in the lab. My DPhil would not have been possible without the emotional and occasional (probably not occasional enough for their liking) financial support of my mum, dad and sister. I didn't visit them anywhere near enough over the course of my DPhil.

Finally, I'd like to thank Sam, who helped me when no one else could have done. I'm extremely privileged to have his friendship.

Contents

Chapter 1

Introduction

1.1 Project Aims

The aims of this project were to investigate the use of graphene in Pt/C composite materials that could act as fuel cell electrode materials. This involved trying to understand how the nature of the graphene support affects the Pt crystals formed on its surface via a thermal annealing approach. Another aim of this project was to explore novel methods which could be used to produce 3D structured graphene electrodes. Lastly, commercially Pt/C catalysts were modified with graphene to understand the role that carbon layers covering the crystals has on the electrochemical activity and durability. The overall aim was to contribute knowledge which can be used to improve the design of fuel cell electrodes to produce electrode materials with desirable properties.

1.2 Scope of this Thesis

Firstly, a brief explanation of the scientific background of the project is presented in a literature review. This aims to explain fuel cells, different support materials including graphene, the synthesis of Pt/graphene composites, interactions between Pt and graphene, and finally information about the performance of graphene in fuel cell testing and some strategies to increase the durability of these materials.

Chapter 3 presents the methodology used to carry out experiments in the thesis. The principles underpinning the techniques are briefly introduced. The experimental procedures are explained, though some more detailed experimental protocols are included in subsequent chapters.

Three chapters of original research are then presented. Chapter 4 involves the synthesis of 3D graphene foam using a CVD process adapted from the literature. The chapter details the synthesis and structural characteristics of this material. The effects of oxygen plasma treatments on the structure of the graphene foam are then presented, followed by an investigation into how the plasma treatment affects the thermal growth of Pt nanoparticles. In addition, an attempt is made to understand how the annealing process affects the defects in graphene foam.

Chapter 5 investigates the synthesis of 3D graphene and 3D graphene/CNT hybrid materials, which are synthesised using the rapid annealing of nickel acetate. The synthesis of these materials is explored, including the role of temperature, time, annealing rate, hydration of the precursor, and annealing procedure. These allow an understanding of the formation mechanism of these materials. Following this, some of the materials were explored as catalyst supports for thermally produced Pt particles. The size and distribution of these Pt particles are studied using TEM, and explanations are given for the differences observed. Finally, these materials are tested in CV experiments and benchmarked against a commercial catalyst. Possible explanations for the differing performances of these materials are given.

Chapter 6 pertains to the CVD synthesis of graphene over Pt crystals in a commercial Pt/C catalyst. Covering Pt nanocrystals with a protective layer has been attributed with increasing the durability of Pt/C catalysts. The effect of growth temperature on the Pt/C catalysts was studied using TEM and CV experiments. It was found that graphene shells could be grown over the Pt particles with minimal change to the characteristics of the support as indicated by Raman spectroscopy and thermogravimetric analysis (TGA). It was found that the graphene shells decreased the active surface area, but did not lead to the increased durability that was seen in other studies. Explanations for this are discussed. Finally, a conclusion of the work carried out is presented along with potential future experiments.

Chapter 2

Literature Review

2.1 Introduction

Fuel cells, such as proton exchange membrane fuel cells (PEMFCs) which use hydrogen or small organic molecules as fuel, are promising clean and renewable sources of energy.[1] The core of the fuel cell is made up of a membrane electrode assembly (MEA) where hydrogen (or another fuel) is oxidised at the anode of the cell and oxygen is reduced at the cathode to produce water. For the commercial applications of fuel cells to be realised, the durability and performance must reach a certain standard whilst minimising production costs. The reactions which take place in the fuel cell require a catalyst, platinum (Pt) has the highest activity for most fuel cell reactions. The U.S. Department of Energy 2017 targets for fuel cells aim for a Pt group metal loading of 0.125 mg cm^{-2} to produce MEAs with power densities of 8.0 kW g^{-1} of Pt, furthermore the fuel cell must also reach a durability target of 5000 hours. Achieving these targets will require improvements to both the electrodes and the integration of catalysts into them.

A fuel cell electrode requires several characteristics such as high conductivity, chemical stability, good mass transport and high surface area.[2] Graphene, a two dimensional material consisting of carbon atoms sp^2 bonded in a hexagonal lattice equivalent to a single layer of graphite, has been identified as a promising material for use as an electrode and catalyst support in PEMFCs. Excitement in the scientific community has been generated since experiments involving the confirmed isolation of graphene and the exploration of its characteristics were carried out in 2004.[3] Among graphene's excellent properties include very

high thermal[4] and electrical[3] conductivity, high strength and Young's Modulus[5] and very high surface area.[6] In addition to this, graphene has a chemical stability which is vastly superior to commonly used fuel cell electrode materials.[7]

There are multiple ways to produce graphene which is suitable for use in fuel cells. Individual graphene sheets can be compacted[8] or three-dimensional graphene structures can be formed which results in superior conductivity and porosity.[9] Catalyst nanoparticles can then be integrated into graphene by growing them in-situ on the graphene surface and numerous procedures for this exist. This review will aim to cover several areas. Firstly, the operation of the PEMFCs and the reactions which take place at the electrodes will be covered. Popular catalyst supports used as electrodes will be introduced and the qualities of graphene will be compared to these materials. The interactions of Pt atoms, clusters and crystals with the graphene surface will be explored, which will draw upon both experimental and theoretical studies. Following on from this, synthetic methods for the formation of fuel cell electrodes will be described, beginning with the synthesis of graphene and three dimensional graphene materials and moving on to methods for the integration of noble metal catalysts into graphene. Finally some strategies to increase the durability of these catalysts will be discussed.

2.1.1. Polymer Electrolyte Membrane Fuel Cells

PEMFCs consist of stacks of repeating units consisting of a cathode, an anode, an electrolyte, gas diffusion layers, and bipolar plates. This is known as a membrane electrode assembly (MEA).[10] Different fuels can be utilised at the anode and oxygen is the fuel consumed at the cathode. The anode and cathode are separated by a solid polymer ion exchange membrane

(commonly Nafion) which allows protons to cross from the anode to the cathode, electrons cannot move across the membrane. Instead the electrons move through an external circuit. In the simplest anode reaction, hydrogen (H_2) is oxidised in the hydrogen oxidation reaction (HOR). A schematic of the MEA and the reactions can be seen in Figure 1.

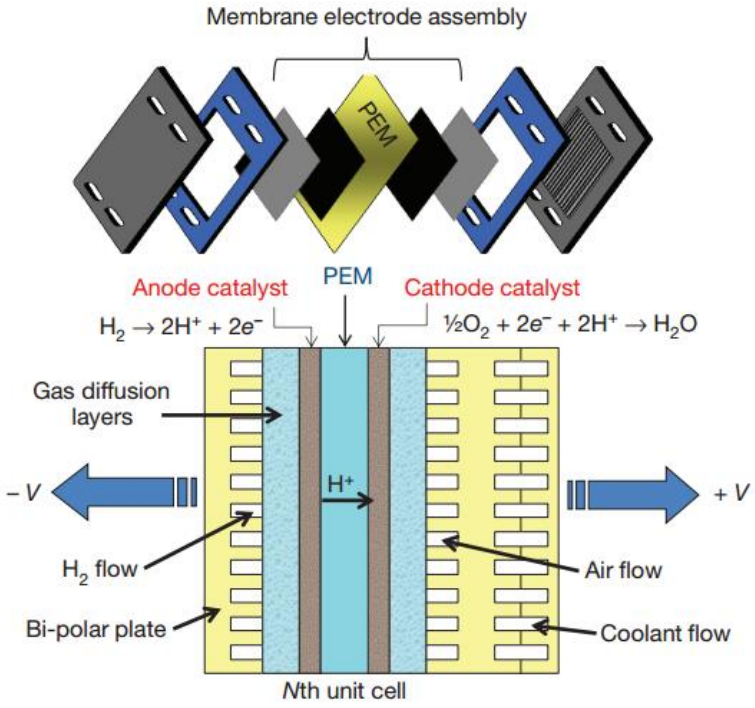

Figure 1. Diagram showing the components in a unit cell of a fuel cell stack where hydrogen (H_2) is the fuel. The reactions taking place at the anode and cathode are shown. Reprinted with permission from ref [1]. Copyright Nature Publishing Group 2012.

In this reaction water and heat are the only products; however hydrogen is not a primary fuel and must first be produced by another process. Other fuels can be used such as in direct alcohol fuel cells, where an ethanol or methanol solution is supplied to the anode. Formic acid can also be used, however in this reaction palladium (Pd) has been shown to be more suitable than Pt.[11] Using alcohol or formic acid as a fuel produces CO_2 as a by-product, which means that the fuel cell is only environmentally advantageous to other CO_2 producing

methods of energy production if the efficiency of the fuel cell is higher than other methods. Adsorbed CO is also an intermediate in these reactions which leads to poisoning of the catalyst and a reduction in the activity of the electrode. CO is also present in hydrogen fuel cells at concentrations of over 10ppm because of the H_2 production process.[12] CO will strongly adsorb on the Pt active sites responsible for dissociating H_2.

The cathode reaction is the same irrespective of the fuel used at the anode. This reaction is the oxygen reduction reaction (ORR). This reaction often limits the performance of the fuel cell due to the slow kinetics of the reaction. Furthermore the majority of durability issues arise from the cathode and consequently the development of new active and durable cathode catalysts is of great interest to the fuel cell community.[13] The ORR can take place either through a four electron pathway (Equation 1) or a less efficient two step pathway with two electrons supplied in each step (Equation 2).[14] Pt and Pt-alloy catalysts are the most active catalysts for this reaction.[15]

Eqn. 1 $$O_2 + 4H^+ + 4e^- \rightarrow 2H_2O$$

Eqn. 2 $$O_2 + 2H^+ + 2e^- \rightarrow H_2O_2$$

$$H_2O_2 + 2H^+ + 2e^- \rightarrow 2H_2O$$

2.2. Carbon Supports in Fuel Cells

In order to make fuel cells more cost-effective, an appropriate catalyst support must be chosen on which catalyst particles can be well dispersed to minimise the amount of Pt that

can be used. There are several requirements for a catalyst support; 1) The support must be highly electrically conductive so that electrons can travel through the electrodes and through the circuit, 2) The support must have a high surface area so that catalyst particles can be dispersed over a wide area, 3) Porosity is also important to aid gas flow so that the catalytic sites can be constantly supplied with fuel, 4) The durability of the support with regards to the acidic environment is also a key factor for the longevity of the fuel cell.[2] The support can become damaged by the operating conditions of the cell, which leads to detachment of catalyst particles from the support and loss of catalytic activity.

2.2.1. Carbon Blacks

A standard carbon support for low temperature fuel cells are carbon blacks (CBs) such as Vulcan XC-72. These materials are formed by pyrolysing hydrocarbons such as in the furnace black process where the hydrocarbon materials (natural gas or oil fractions) are burned with a limited air supply at 1400˚C.[2] This produces spherical particles of polycrystalline turbostratic graphite which aggregate to make particles of around 250 nm in diameter. For Vulcan XC-72, the surface area is ~250 $m^2 g^{-1}$ and the low cost of producing carbon blacks makes them a common choice of catalyst support.[16]

There are disadvantages to using carbon blacks however. The pyrolyzation process introduces sulfur-containing impurities. Another issue with carbon black materials is their stability. In PEMFCs the pH is low and the temperature is at a minimum of 80˚C.[17] Water and water vapour are also present in the cell. These issues damage the carbon support which result in Pt nanoparticles becoming detached from the support, decreasing the Pt surface area which is contributing to the electrochemical activity.

2.2.2. Mesoporous Carbon Materials

Mesoporous carbon materials (MPCs) have attracted attention in recent years as alternatives to carbon blacks. These materials are produced by the three-dimensional assembly of a template such as self-assembled silica spheres which is then infiltrated by carbon precursors prior to pyrolysation.[18] Following this the template is removed. This allows controllable pore size down to a few nanometres and smaller Pt crystals can be stabilised than with CBs.[19] Though these materials are superior to carbon blacks in terms of surface area, they suffer from poor conductivity.[20]

2.2.3. Carbon Nanotubes

Carbon nanotubes (CNTs) offered unique advantages when they were first utilised in fuel cells. They have a tubular structure analogous to one or several sheets of graphene rolled up into a cylinder. They can be single or multi-walled. They have an extremely high surface area, high conductivity and good stability with regards to acidic environments.[21] They are most commonly produced using the chemical vapour deposition (CVD) process.

Due to the high degree of graphitisation of carbon nanotubes compared to carbon blacks and MPCs, CNT-based fuel cell electrodes have proven to be much more durable than these materials. They retain their electrochemically active surface area (ECSA) and degrade at a slower rate.[22] This confirms that CNTs are much more resistant to oxidation compared to carbon black and MPC supports and the retention of active surface area indicates a stronger attachment of Pt particles compared to these supports. A difficulty of utilising these

materials in fuel cells is the lack of large scale production techniques and the costs involved in the synthesis and processing of CNTs.[16]

2.2.4. Graphene

In recent years, graphene has drawn attention as a catalyst support because of its high conductivity and surface area. The fast electron transfer rate achieved with graphene is advantageous for the oxygen reduction reaction which suffers from slow kinetics.[15] Graphene fulfils all the requirements for a good catalyst support in a fuel cell, it has high surface area and conductivity and it has good electrochemical stability. Graphene is a single-atom thick material where carbon atoms are sp^2 bonded in a hexagonal lattice (Figure 2).[23] Each carbon atom has a valence electron not involved in σ bonding and these electrons reside in p_z orbitals and overlap with neighbouring carbon atoms to form π orbitals.[24] The theoretical specific surface area of graphene is 2600 m^2g^{-1} which is extremely high and double that of single-walled carbon nanotubes as the inner surface of a CNT is not utilised. For monolayer graphene, both sides of the sheet are equally accessible and can be decorated with catalyst nanoparticles, though many catalysts utilising multilayer graphene as a support have been produced. Several methods of producing graphene for fuel cell applications exist and graphene derived from graphene oxide can be readily mass-produced, giving it an advantage over CNTs.[25] The properties of graphene as a support can be altered by using graphene with different degrees of oxidation or defects. This allows a great deal of control to be exerted over the properties of graphene in fuel cells and a way to control the interactions of catalyst nanoparticles with graphene.[26] Graphene can also be readily functionalised and has different reactivities at the edges and basal plane.[27] This makes graphene a very versatile catalyst support that is compatible with a wide variety of nanoparticle synthesis methods.

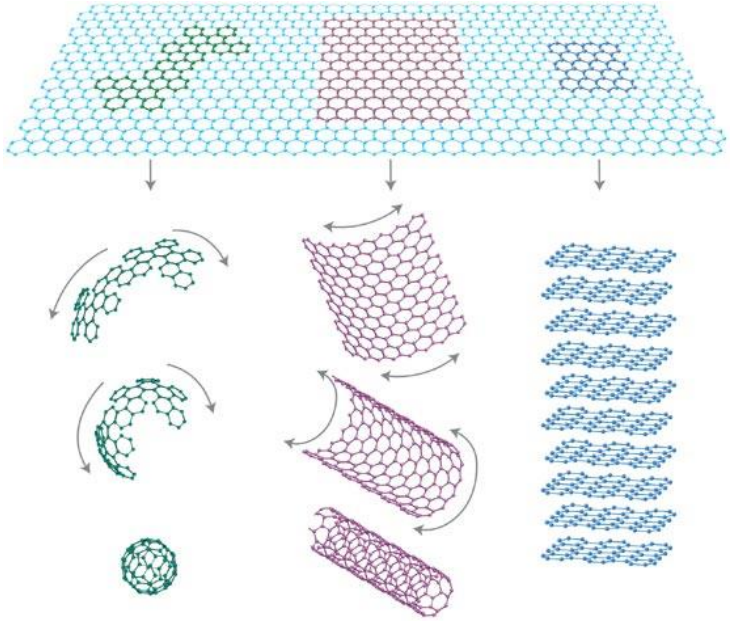

Figure 2. Diagram showing the structure of graphene (top) and how the structures of fullerenes, carbon nanotubes and graphite can be derived from that of graphene. Reprinted with permission from ref [23]. Copyright Nature Publishing Group 2007.

Although individual graphene sheets can be compacted onto conductive substrates to act as fuel cell electrodes,[8] recently three-dimensional structures produced from graphene have become popular. This field has recently expanded and a range of synthesis methods have been developed to produce three-dimensional graphene structures.[28] Some synthesis methods allow for controllable pore size and many of these structures are mechanically robust.[29] These structures can also be produced using CVD graphene which has superior conductivity to chemically derived graphene. A range of synthesis methods also exist for the doping of graphene using heteroatoms such as nitrogen and boron which provide further benefits in fuel cells.[30] These heteroatoms can allow the formation of smaller particles of Pt on the graphene surface.[31] Doped graphene also has intrinsic catalytic activity for fuel cell reactions and has been identified as a potential cathode catalyst for the ORR; [32] however this is beyond the scope of this thesis.

2.2.5. Degradation Mechanisms of Pt/C Catalysts in Fuel Cells

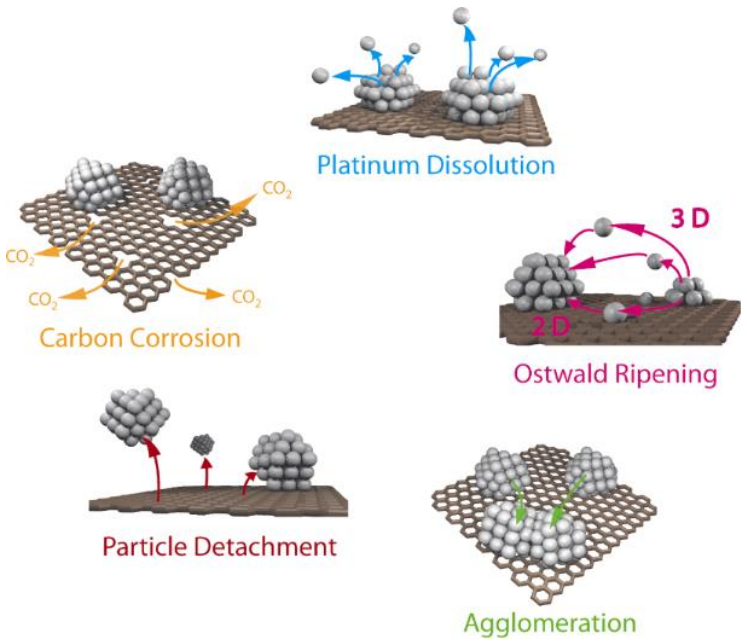

Figure 3. Schematic diagram showing different mechanisms of Pt/C catalyst degradation in fuel cells. Reprinted with permission from ref [33]. Copyright Beilstein Journal of Nanotechnology 2014.

As one of the primary aims of fuel cell catalyst research is to increase the durability of fuel cell electrodes in the fuel cell environment, it is important to understand the different mechanisms by which the degradation can occur. Figure 3 shows a schematic diagram illustrating different Pt/C catalyst degradation methods.[33] Pt atoms on nanocrystals can dissolve, where they can either leave the cell (platinum dissolution) or redeposit on other Pt crystals. This can either occur where Pt atoms move along the support surface (2D Ostwald ripening) or via the electrolyte (3D Ostwald ripening). The high surface area of smaller particles often means that they are more susceptible to disappearing via these mechanisms. The acidic environment can cause corrosion of the carbon support, especially during the start –up and shutdown processes.[34] Corrosion of the carbon support can lead to agglomeration, where particles move over the surface of the support, come into contact, and coalesce, leading to a loss of ECSA or to particle detachment where Pt particles leave the surface of the

support. Preventing one or more of these sintering mechanisms from occurring is necessary for improving the durability Pt/C catalysts.

2.3. Interactions of Platinum with Graphene

In order to produce Pt/graphene hybrids with improved properties, a good understanding of how Pt nanocrystals form and move on the surface of graphene is important. An understanding of the in-situ formation mechanism of Pt nanocrystals on graphene will allow for better control over particle morphology, distribution and size, enabling the Pt loading to be minimised whilst providing electrodes with high activity and stability. The study of how premade crystals transform and migrate on the surface of graphene as the surface is heated is also relevant for the stability of graphene-Pt electrodes. Decreasing the catalyst loading can be accomplished not only by varying the synthesis conditions of the hybrid materials but also by understanding how different sites on the graphene sheets such as dopants and vacancies interact with Pt atoms. Pt atoms have been shown to have a higher binding energy with these features. This can be taken advantage of to increase the interactions between Pt and graphene and to decrease the migration and sintering of Pt crystals on the graphene surface, thereby increasing the durability of this class of catalyst.[30, 35]

This section will discuss existing studies into the formation, transformation and migration of Pt nanocrystals on the graphene surface. Studies have been published over the past few years which show the formation of very small clusters of Pt on graphene and show them as being stable around edges, functional groups and defects.[36] In-situ transmission electron microscopy (TEM) is particularly useful in this regard as individual crystals can be directly

visualised whilst they are undergoing changes.[37] Density functional theory (DFT) can also be used to explore the nature of the interactions of Pt with graphene and explore their stability.

The decoration of graphene edges by Pt nanoparticles was first observed in 2008, where Yuge et al. found that Pt precursor molecules selectively decorated carboxyl groups on the edges of oxidised graphene.[36] The characteristics of these Pt clusters and their formation and stability on graphene have since been of great interest.

2.3.1. Experimental Studies

2.3.1.1. Interactions of Platinum with Few Layer Graphene

One of the earliest indicators of the utility of graphene as a catalyst support for Pt was published by Yoo et al.[38] They annealed a Pt precursor on the surface of 10-20 layer reduced graphene oxide (rGO). The formation of graphene oxide involves the exfoliation of graphite using acids at high temperature, leading to irreversible damage to the graphene lattice even upon reduction to graphene. This process also leaves the graphene with oxygen containing functional groups at both the edges and the basal plane. When compared with Pt on carbon black produced using the same procedure, the Pt/graphene showed a much higher activity for the methanol oxidation reaction. Using TEM, they observed little difference between these catalysts, however using high angle annular dark field scanning transmission electron microscopy (HAADF STEM) they were able to see very small clusters much smaller than 0.5 nm in size in addition to larger crystals seen in TEM. A comparison between the TEM and HAADF STEM images can be seen in Figure 4. These small clusters consist of only 10-15

atoms and the increased activity for the methanol oxidation reaction was attributed to these small clusters which have also been observed on pristine graphene.[39]

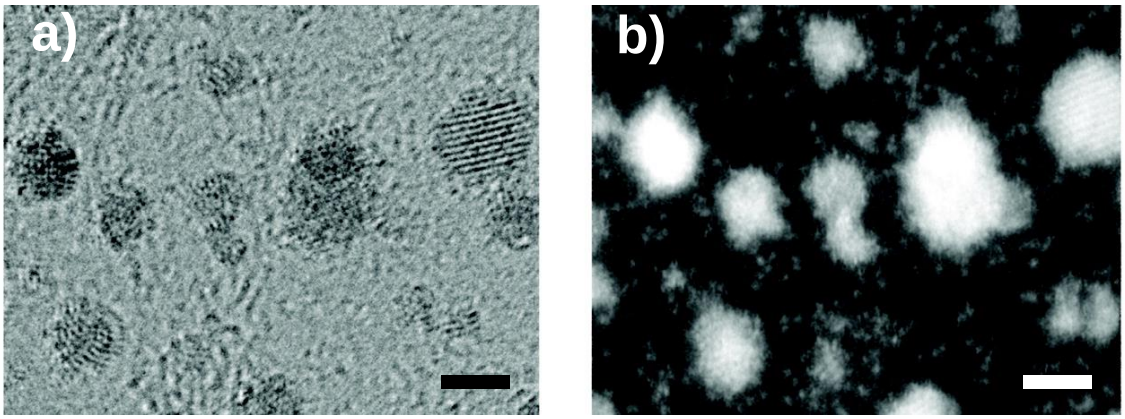

Figure 4. a) HRTEM and b) HAADF-STEM images of Pt clusters on the surface of graphene. Scale bars: 2nm. Reprinted (adapted) with permission from ref [38]. 2009 Copyright American Chemical Society.

To function as a durable catalyst for fuel cells and other applications, it is important that the functionality is retained even after being subjected to elevated temperatures. This catalyst was studied using an annealing temperature of 400˚C, which demonstrated that small Pt crystals can be stabilised on the surface of graphene and resist aggregation in H_2 atmospheres, at least for the duration of the annealing processes (2 hours).

Janowska et al. conducted an in-situ TEM study in which a Pt/graphene composite material was heated to a temperature of 700˚C.[37] The nanocrystals were grown in solution on the surface of the graphene using chloroplatinic acid and sodium borohydride as a reducing agent. The graphene was produced using expanded graphite which was sonicated in ethanol prior to microwave irradiation to produce few layer graphene. It was found that the concentration of Pt nanoparticles was considerably higher at the edges and this was attributed to the influence of oxygen containing functional groups. They found that heating sintered the Pt particles, generating a distribution of particle sizes with two maxima attributed to the original and coalesced particles. Despite the high temperature of 700˚C for periods of 2 hours, much

higher than the operating temperature of PEMFCs, the average particle size remained lower than 5 nm. Unlike with studies of gold particles on graphene that had been previously conducted,[40] the size and behaviour of the Pt particles was found to be similar independent of the layer number, 3-5 layered graphene was most commonly observed in this study.

The increased temperature was also found to change the particle shape. Spherical particles were observed to form (111) facets upon heating at 430˚C. This is attributed to the movement of the Pt atoms in the crystals allowing access to lower energy conformations. This faceting could possibly prevent further diffusion of the particles due to the increased contact of the nanocrystal with the graphene surface. Overall, diffusion of the Pt particles on the surface and edges of graphene was rarely observed.

A follow-up study examined in more detail the effect of high temperature on the morphology and size of the particles using a similar methodology with more extensive molecular dynamics simulations.[41] This experiment was performed using the same synthesis procedure for the Pt/graphene hybrid material.

Upon heating, they found a broadening of the nanoparticle size distribution and an average size increase from 1.8nm at room temperature to 2.2, 2.5, 2.8, 3.0 and 3.1 nm at 200, 300, 400, 500 and 600˚C respectively. The movement of small particles toward their larger nearest neighbours was observed upon heating, with nanoparticles at edges more readily coalescing. At 700˚C, the melting of the outer layer of the NPs was observed to cause the increase in nanoparticle size. The TEM images can be seen in Figure 5. `

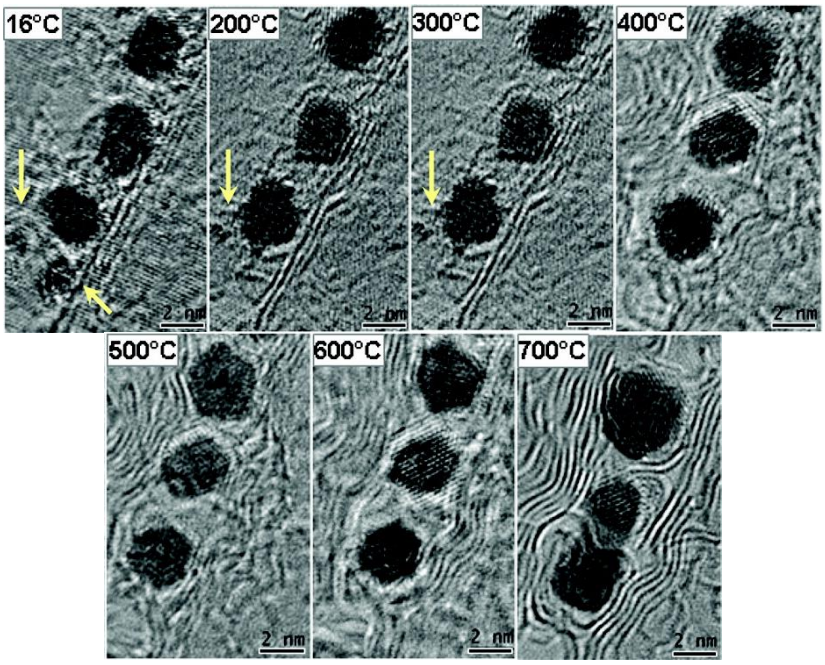

Figure 5. TEM images showing the effect of temperature upon the morphology of Pt nanocrystals on graphene. The arrows show small clusters. All scale bars 2 nm. Reprinted (adapted) with permission from ref [41]. 2012 Copyright American Chemical Society.

They explained their findings using three different mechanisms; at low temperatures below 400˚C, isolated atoms and small clusters move towards their closest neighbours. At higher temperatures, the nanoparticles themselves coalesce. Above 600˚C, the outside of the nanoparticles melt and the Pt wets the surface of graphene leading to further sintering of neighbouring particles.

Accompanying molecular dynamics (MD) simulations carried out on monolayer graphene show that the spherical particles transform into particles with (111) facets on the surface. In the simulations monolayer graphene was used and a much higher temperature was required for melting of the Pt nanoparticles. Unlike the previous study which indicated layer number was inconsequential, this indicates that layer number could play an important role with regards to the stability of particles on graphene.

2.3.1.2. Interactions of Platinum with Freestanding CVD-Grown Graphene

More recently, small Pt particles on free-standing graphene produced by a sputtering process were investigated using TEM, scanning tunnelling microscopy (STM) and MD simulations.[42] This was the first study on free-standing and pristine graphene and approximates to the ideal scenario in which graphene sheets in fuel cells are well separated from one another to ensure a maximum surface area and prevent restacking to form graphite. The graphene used was grown using a CVD technique and will therefore have a surface with a much lower concentration of defects and oxygen containing groups present. The sample consisted of 1-6 layers of graphene; the studies previously mentioned did not have any regions of monolayer graphene present. Experimental studies on the functionalisation of this free-standing, pristine graphene surface with Pt nanoparticles had not been carried out prior to this recent work. It was found that crystals produced using this method were well dispersed over the basal plane of graphene with an average nearest neighbour distance of 4 nm, with (200) and (111) planes visible. The particles were monodisperse with an average size of 1.4 nm. STM measurements showed that the Pt prefers to wet the surface of graphene, producing crystals which are much wider than they are tall, but their height is not uniform over a single crystal. Molecular dynamics simulations found that the Pt crystals were elevated above the surface of the graphene and in fact made the graphene underneath slightly convex due to the formation of sp^3 carbon bonds. Their simulations also indicate that several Pt atoms in each cluster covalently bond with the graphene sheet even without a defect present. The self-organisation of the particles could also be explained; upon sputtering from the target, atoms of Pt move around the graphene sheet until they encounter other atoms and nucleate into a cluster; upon growth, the local distortion of the graphene sheet increases and creates a local strain field, preventing more Pt atoms from joining the cluster as they move across the graphene. The

MD observations indicated a stability of the crystals up to 1000 K with the face centered cubic (FCC) structure intact.

These findings indicate an interesting contrast between the particles grown on defective, multi-layered graphene and the particles sputtered onto pristine graphene with monolayer regions in terms of their characteristics and reaction to temperature, though no experimental heating studies have been done on the particles on free-standing graphene to confirm the MD results. In the in-situ study, particles became progressively larger and coalescence occurred to join particles together, this is in contrast to the self-limited growth with sputtered particles. This gives some indication of how different types of graphene with different Pt crystal synthesis methods could have a profound implication for the stability and surface area, and therefore the durability and activity, of Pt/graphene fuel cell catalysts.

2.3.1.3. Effects of Functional Groups on the Growth of Nanocrystals

The different interactions and characteristics of the Pt nanocrystals reported in the literature indicate that the type of graphene used has a noticeable effect on the growth of Pt nanocrystals. These previous studies have shown the ability of Pt to interact in different ways with different features of the graphene sheet. Defects, edges, oxygen-containing functional groups, dopant atoms and pristine regions of the graphene lattice all have unique interactions with Pt allowing the structural and electronic properties of the crystals to be controlled.

The quality of graphene used therefore has a large impact upon the growth of nanocrystals on the surface of graphene. Wang et al. first reported on the effect of the degree of oxidation of rGO on the growth of $Ni(OH)_2$ and Fe_2O_3 particles in a hydrothermal process.[26] It was observed that graphene with a low concentration of oxygen-containing groups yielded

nanocrystals on the surface of graphene with well-defined shapes such as platelets or rods. Increasing the concentration of oxygen containing groups produces smaller crystals with irregular shapes. This was attributed to the pinning of crystals by oxygen containing groups, which hindered their migration on the graphene sheet and prevented their recrystallization. A similar effect was recently observed with Au, Pt and Pd[43] and is illustrated in Figure 6.

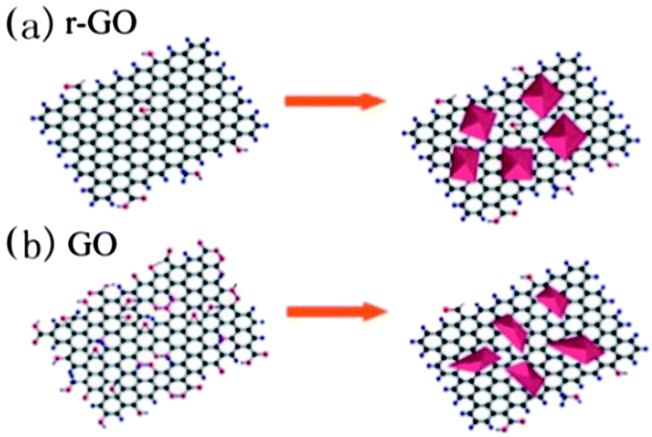

Figure 6. Schematic showing the hydrothermal growth of nanocrystals on a) reduced graphene oxide and b) graphene oxide. Reprinted with permission from ref [43]. Copyright Royal Society of Chemistry 2014.

More recently, the basal plane of rGO was functionalised with different groups in order to understand the attachment of Pt particles to the graphene surface.[44] rGO was functionalised with p-phenyl SO_3H and p-phenyl NH_2 groups. Pt particles were formed on the surface of the graphene materials in a solution based Pt synthesis using ethylene glycol as a reducing agent. It was found that the functional groups acted as nucleation sites, producing Pt crystals with smaller size and better distribution over the graphene surface.

2.3.2. Theoretical Studies

2.3.2.1. Pristine Graphene

Theoretical studies have also shed light on the interactions between Pt and graphene. A study on the interaction between Pt clusters of different sizes and graphene determined that the dispersion forces between the Pt and graphene interface remained constant per Pt atom in contact with the graphene sheet.[45] This explains the flattened crystals seen in some experimental studies as a way to maximise the interaction energy between Pt clusters and crystals with graphene. However, the overall interaction energy per atom in contact with graphene decreases. This is due to the fact that, only for small clusters, there is also a covalent contribution to the interaction energy which is larger per atom as the cluster size decreases. This means that covalent bonds are expected only for small clusters and can therefore be expected to bind more strongly to the surface of graphene.

This study also showed the geometry of the graphene local to the Pt cluster also contributes to the interaction energy. For larger clusters, decreasing the contact area between the cluster and graphene leads to a decrease in the interaction energy. For example, clusters adsorbed on convex portions of the graphene support will be weakly bound compared to those on the flatter or concave portions of the graphene surface. This indicates that clusters are more likely to reside in the folds or creases in the graphene surface than on flat areas. This has been recently observed for sputtered gold particles, which readily decorate wrinkles on the surface of graphene.[27]

It is thought that the π orbitals of the graphene interact with the d orbitals of the Pt atoms, referred to as π-d hybridisation. The π states of the support have been identified as a key factor for the strength of the interaction, with nonbonding π states induced by local doping or vacancies having a significant effect on the binding.[46] This hybridisation is stronger for smaller clusters, which have a higher proportion of under-coordinated Pt atoms. This results in an increased binding energy of the Pt 4f electrons which can be observed using X-ray photoelectron spectroscopy (XPS) as the proportion of sub-nanometre clusters increases.

2.3.2.2. Doped Graphene

Doping has also been extensively theoretically investigated as a method to modify the interaction between Pt clusters and graphene. Dopants can be introduced into graphene using a variety of experimental techniques.[47] Several dopants have been evaluated in theoretical studies including nitrogen, boron, beryllium, oxygen, silicon and sulfur.[45] These dopants have been studied as a means to increase the strength of the interaction between Pt and graphene.

These dopants are heteroatoms which substitute carbon atoms in the graphene lattice (Figure 7a). Several studies on this topic have been carried out which indicate an increased binding energy of Pt to graphene in the vicinity of a nitrogen, boron or silicon dopant.[30,48] The effects of boron and nitrogen will be discussed as these are the dopants which are commonly experimentally studied.

It has been calculated that on undoped graphene, Pt atoms bind to a bridge site with an energy of -1.43 eV and require only 0.18 eV to migrate to adjacent bridge sites.[49] Single Pt atoms can easily migrate in this way. It has been found that having a nitrogen atom within 14 Å of an adsorbed Pt atom increases the binding energy at some bridge sites to a value of -2.13 eV, although being directly atop the nitrogen or occupying the bridging site next to it is unfavourable. The increase in binding energy is due to the donation of electron density from nitrogen to the graphene π^* conduction band, which in turn donates electron density to the Pt. The removal of electron density through Pt allows local aromaticity to be regained and so is energetically favourable. Boron atoms have been shown to increase the binding of Pt atoms close to the boron with an adsorption energy of -2.16 eV on neighbouring bridge sites. Pt is able to form a covalent σ-bond with the B-C σ-bond. Trimers of pyridinic nitrogen dopants have been experimentally observed using XPS[50] and the structure of these can be seen in

Figure 7b. The centre of these trimers bind Pt atoms strongly (-2.86 eV and -5.3 eV for nitrogen and boron trimers respectively) and form strong bonds with Pt atoms (covalent for nitrogen and ionic in the case of boron trimers). This creates a site for cluster nucleation and it is suggested that creating these dopant structures in graphene would decrease the cluster size and increase the durability of Pt/graphene hybrids.

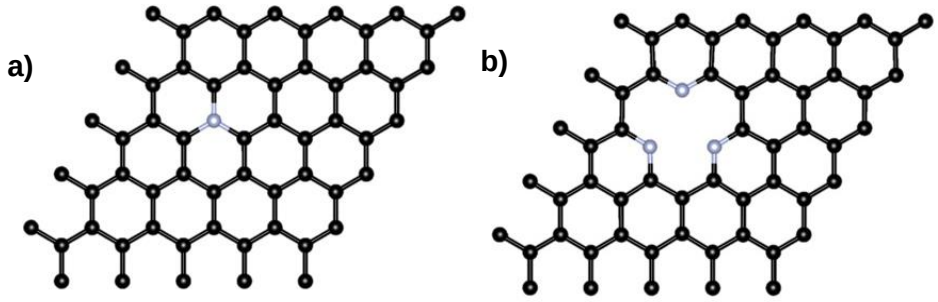

Figure 7. Atomic models showing a) a graphene sheet with a single N or B dopant and b) three N or B dopants in a trimer. Reprinted (adapted) with permission from ref [49]. 2013 Copyright American Chemical Society.

2.3.2.3. Defective Graphene

The naturally occurring defects in graphene have also been shown to increase the binding of Pt atoms. This can be used to prevent the migration of Pt atoms over the graphene surface. A consequence of this would be smaller, well dispersed and strongly bound clusters and crystals of Pt formed during the synthesis of Pt/graphene composites. Furthermore an increased binding strength would decrease the likelihood of detachment of the Pt from the graphene during the operation of the fuel cell, thereby increasing its durability. This ability for vacancies to trap atoms and dimers and prevent their migration has been experimentally observed with iron atoms using TEM.[51]

A theoretical study conducted by Fampiou and Ramasubramaniam investigated the binding of Pt atoms and small Pt clusters (2 -13 atoms) with graphene and graphene with defects.[35] They compared the pristine graphene surface, the monovacancy, the divacancy and the 5-8-5 and 555-777 reconstructed divacancies (Figure 8).

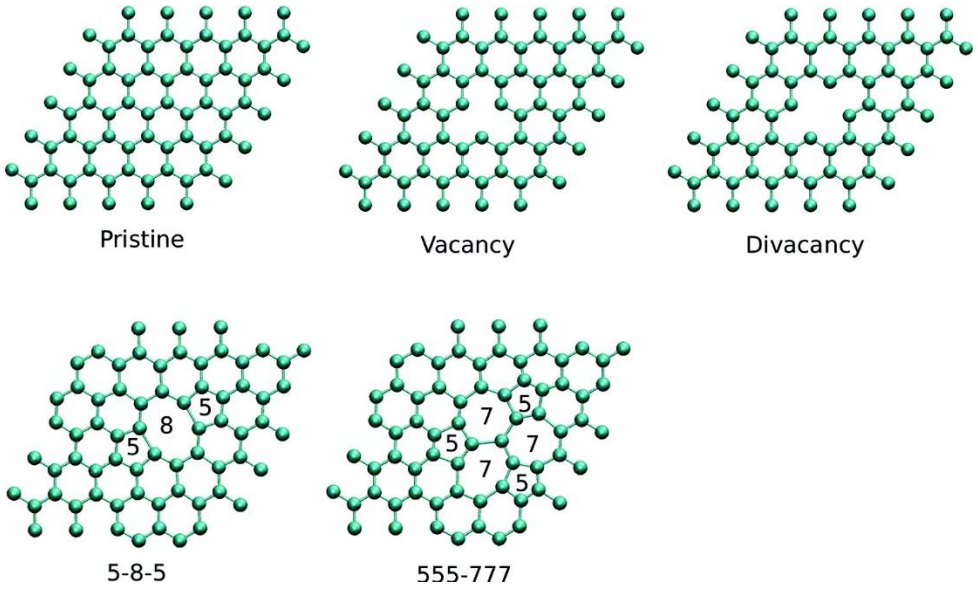

Figure 8. The structures of pristine and defective graphene surfaces investigated for the adsorption of Pt atoms and clusters. Reprinted (adapted) with permission from ref [35]. 2012 Copyright American Chemical Society.

All of the defects studied have a stronger binding energy than the pristine graphene surface over the range of clusters studied, with unreconstructed defects providing the strongest binding energy for Pt atoms. The study also showed that the average Pt bond length increases as the binding to the substrate increases which could have implications for catalytic activity. This bond lengthening between Pt atoms is caused by charge transfer from Pt clusters to the graphene surface, with more charge transferred corresponding to stronger binding.

As the binding energy between Pt clusters and graphene increases, the cluster d-band centre downshifts in energy (Figure 9). This also has interesting implications for durability of catalysts based on Pt and graphene. This lower d-band centre also means that the binding energy of CO molecules to the cluster is weakened relative to clusters which are not supported.[52] This means that Pt catalysts on graphene can be tailored to resist poisoning. This implies that other molecules will be affected by the d-band shift, which means that defects can be utilised to control the catalytic activities of Pt clusters on graphene.

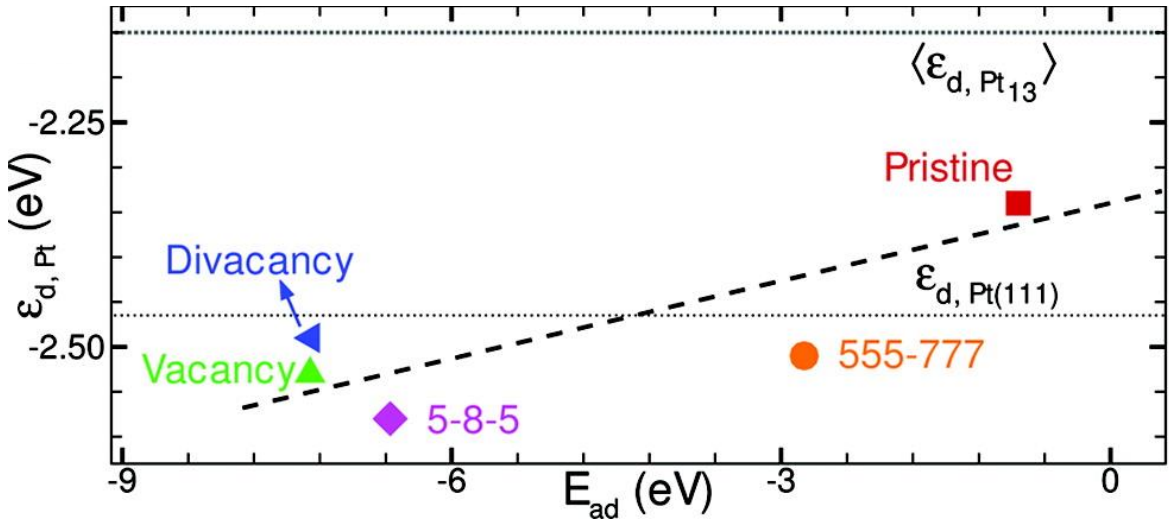

Figure 9. Energy of the d-band centre (ε_d) relative to the Fermi level for Pt_{13} clusters vs their energy of adsorption for different graphene surfaces (E_{ad}). $\varepsilon_{d,Pt_{13}}$ represents the energy for an unsupported Pt_{13} cluster and $\varepsilon_{d,Pt_{(111)}}$ represents the energy of the d-band centre for the Pt (111) surface. Reprinted (adapted) with permission from ref [35]. 2012 Copyright American Chemical Society.

The role of some oxygen containing functional groups on the surface of graphene on the binding of Pt atoms and clusters has also been investigated. This is relevant for Pt/C materials produced with rGO, as the improved dispersion and durability of these materials is attributed to residual oxygen-containing functional from the reduction process. In a DFT

study on the adsorption of single Pt atoms, chemisorption was found to be stronger on epoxy and hydroxyl functionalised graphene than on pristine graphene,[53] though binding was still weaker than the binding of Pt atoms to point defects seen in Figure 9. It was found that the Pt atoms do not bond to the oxygen containing functional groups themselves, but that functionalisation causes deformations in graphene, which lead to dangling bonds on carbon atoms which act as binding sites for Pt. Similar results were found for the binding of Pt_{38} clusters, where the cluster binding strength followed the trend monovacancy > hydroxyl – graphene > carboxyl – graphene > pristine graphene.[54] Again it was found that the oxygen functional groups influenced the surrounding carbon atoms to bind the cluster.

2.3.2.4. Others Factors Influencing Binding Energy

Other strategies have been explored theoretically to increase the binding energy of Pt clusters and atoms to the surface of graphene. It has been found that applying strain to graphene allows a further decrease in the d-band centre and increases binding of small Pt clusters.[55] The use of metal adatoms other than Pt to link Pt clusters to graphene has also been explored theoretically; using different metal atoms to link between the Pt and graphene would allow a control over the binding energy, with Ir, Os, Ru, Rh and Re being the most effective.[56] This has implication for the growth and deposition of bimetallic catalysts containing Pt on graphene such as PtRh catalysts. The synthesis of these catalysts is currently an active area of research.[57]

2.4. Synthesis of Graphene Supports

Several approaches have been used in order to produce graphene electrode materials which can act as supports for Pt nanocrystals. These different approaches produce graphene with different morphologies and concentrations of defects on the surface. These factors in turn can have an effect on their characteristics for binding Pt nanocrystals and in turn their durability in fuel cells. Therefore the method used to produce the graphene can have a significant effect on the electrode performance. Some relevant ways of producing graphene which have been used as supports for fuel cell electrocatalysts are presented in this section, along with a discussion of their relative merits.

2.4.1. Chemical Vapour Deposition (CVD) Grown Graphene and Graphene Foam

CVD is a popular process which can be used to produce graphene suitable for applications that require high conductivity and low defect concentration. This process involves passing a mixture of hydrogen (H_2) and a carbon precursor (commonly methane, CH_4) in argon (Ar) through a furnace at high temperature with a catalyst. The gases interact with the catalyst and graphene is formed on the surface.[58] The most popular catalysts are copper (Cu) and nickel (Ni), the latter being more regularly used for the production of three-dimensional graphene structures. In a typical nickel CVD process, the substrate is first annealed at high temperature, with 1000˚C in H_2/Ar being commonly used in order to increase the grain size of the polycrystalline substrate. After this, a carbon source such as CH_4 is added into the mixture of gases. The solubility of carbon in nickel is high at 1000˚C and the CH_4 will decompose, with carbon atoms dissolving in the nickel. Upon cooling the solubility decreases, leading to the precipitation of carbon on the surface of nickel as graphene which first nucleates in the metal grain boundaries. This produces continuous graphene films and by varying the synthesis

conditions it is possible to decrease the average layer number to between 3 and 4 layers using nickel as a catalyst, with some areas consisting of monolayer graphene.

For many applications of CVD graphene, such as in 2D heterostructure devices, a flat metal foil catalyst is used.[59] The nickel CVD procedure was then adapted by Chen et al. in order to produce a three-dimensional free standing graphene structure composed of high quality graphene.[60] To achieve this, they utilised a commercially available nickel foam substrate instead of nickel foil. Following the use of a CVD procedure identical to that for nickel foil, they had covered the template in multilayer graphene. The nickel could then be etched using hydrochloric acid or a mixture of hydrochloric acid and iron (III) chloride to obtain the free-standing graphene foam. The resultant structure can be seen in Figure 10.

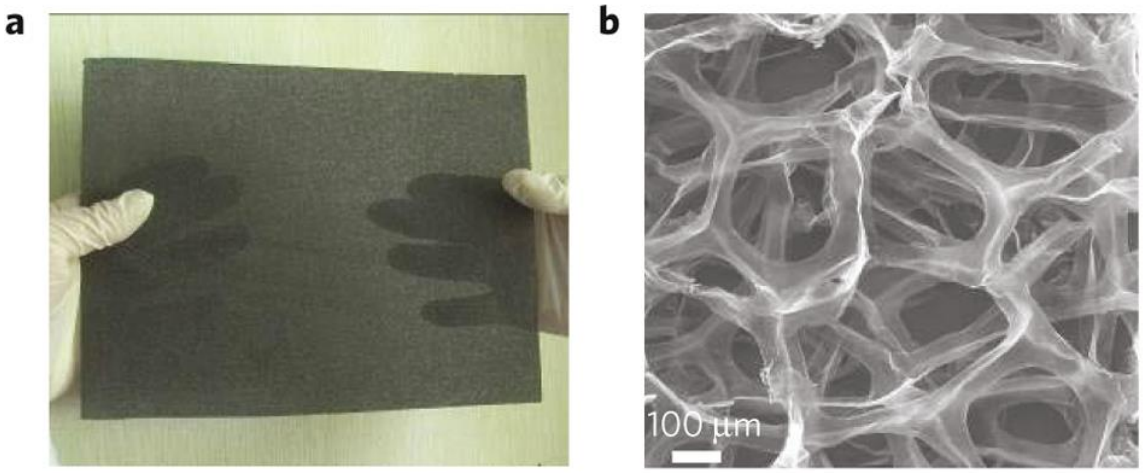

Figure 10. a) Photograph and **b)** SEM image of the CVD graphene foam. Reprinted with permission from ref [60]. Copyright Nature Publishing Group 2011.

The conductivity, specific surface area and density of the graphene foam can be controlled by varying the amount of methane in the CVD process to change the layer number. The template used had much larger pore sizes than those that can be achieved in other methods of 3D graphene production, however templates with smaller pore sizes have since been fabricated and used for the CVD synthesis of graphene.[61,62] The highest conductivity

achieved using this nickel foam was 1000 Sm^{-1} which is much higher than the majority of conductivities achieved using rGO, this is despite the low density and very large pore sizes of the CVD graphene foam which are hundreds of microns in diameter. The high conductivity is in part due to the defect-free nature of the CVD graphene, as indicated by the supressed D peak in the Raman spectra of the foams. The CVD technique produces a structure where individual graphene sheets are covalently bonded together at grain boundaries in contrast to structures produced using rGO which consist of overlapping graphene sheets which interact through π- π interactions.[63] This contributes to the lower conductivity of rGO structures by introducing junction contact resistance between individual graphene sheets.

This method of producing 3D graphene has become highly popular and has been widely used. The commercially available nickel templates used all have a similar morphology and pore size. This means that it can be easy to compare results produced in different papers that use this synthesis technique. To date, this structure has been applied to a wide variety of applications. In the original paper, the graphene foam was cast in polydimethylsiloxane (PDMS) and utilised as a stretchable and flexible conductive material, where it showed superior characteristics to rGO and CNT derived polymer composites.[60] These structures also have utility for several other applications. The inherent conductivity and sensitivity to changes in electron density of graphene mean that these structures can be utilised as chemiresistor gas sensors where the resistance of the graphene foam changes as molecule adsorb on the surface.[64] The structure of pristine graphene means that it is very hydrophobic, making 3D graphene structures useful for environmental remediation.[65] The graphene foam can also be integrated with nanomaterials such as zinc oxide and $LiFePO_4$ in order to produce chemical sensors[66] and battery electrodes.[67] These devices also have the advantage of being flexible.

These graphene structures have also been used as a platform for the synthesis of Pt particles for electrocatalysis, where they have performed favourably relative to commercially available catalysts.[68,69] The methods used to synthesise Pt crystals on graphene materials is discussed in a later section of this chapter. Despite the favourable performance of these materials in publications, these materials are not compatible with the currently used membrane electrode assembly fabrication process, where the electrode materials are sprayed onto a gas diffusion layer or onto the electrolyte membrane; this is followed by the application of heat and pressure to the membrane electrode assembly.[70] For this reason the catalysts traditionally used for fuel cell catalysis are in the form of powders which can be dispersed into a catalyst ink suitable for spraying, rather than electrodes comprising completely interconnected graphene.[71] This is in contrast to the three-electrode electrochemical experiments used for testing in some of the papers, where the graphene foam can be used as a free-standing electrode without the need for integration with other components. The fact that the nickel foam has to first be produced in a separate process makes it more expensive and less applicable to mass production than some other methods used to produce graphene for fuel cells. While the 3D graphene foam produced by this method can be used to create effective catalysts, the application of materials produced using this nickel foam template is limited in real fuel cells.

2.4.2. Reduced Graphene Oxide

Graphene oxide is most commonly obtained using modified versions of the Hummers method. In this method graphite is treated with sulfuric acid (H_2SO_4), sodium nitrate ($NaNO_3$) and potassium permanganate ($KMnO_4$).[72] This forms graphite oxide which contains epoxide, hydroxyl and carboxyl functional groups and increases the interlayer distance between

graphite sheets. Stirring or sonicating then exfoliates the graphite into graphene oxide sheets. Due to these functional groups, graphene oxide can be well dispersed in water and can form stable dispersions in many polar organic solvents. Graphene oxide is not conductive and is therefore not an appropriate catalyst support; it must first be reduced to graphene in some way to function as an appropriate support for fuel cell catalysis.

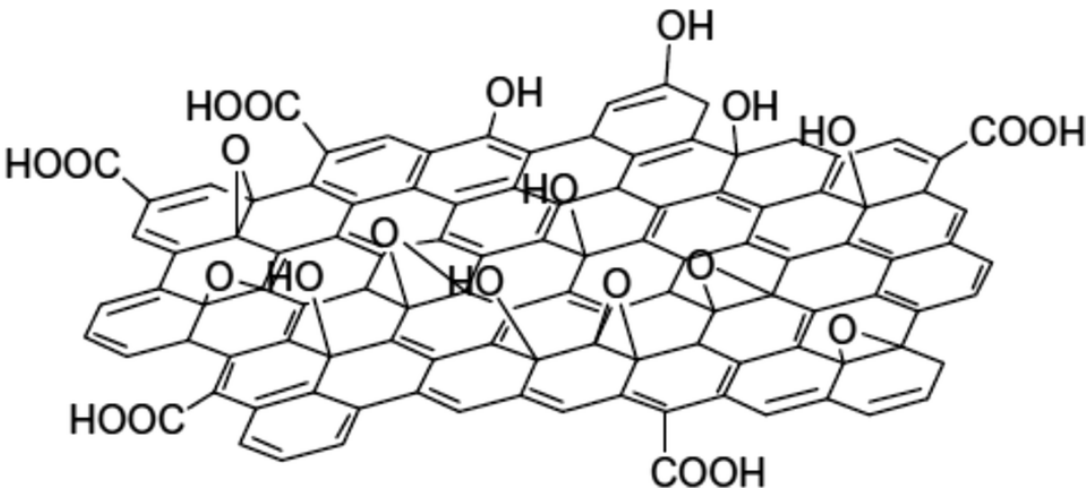

Figure 11. The structure of Graphene oxide. Reprinted with permission from ref [76]. Copyright Royal Society of Chemistry 2015.

There are numerous methods which facilitate the reduction of graphene oxide to graphene. These include thermal,[73] chemical[74] and electrochemical techniques,[75] though the first two are the most relevant to the production of 3D graphene structures. A schematic diagram showing the structure of graphene oxide is shown in Figure 11.[76]

The thermal reduction technique was first reported by McAllister et al.[77] Following the formation of graphite oxide using an established method, they were able to exfoliate this to single graphene sheets by heating the graphite oxide for 30 seconds at 1050˚C in an inert atmosphere. This exfoliation was due to the pressure caused by gases liberated from the basal plane from the decomposition of epoxy and hydroxyl sites. They calculated that at a temperature of 550˚C, the gas diffusion rate is lower than the gas production rate which is the

point at which exfoliation occurs. In this way, they were able to obtain a product where 80% of the sheets produced were monolayer.

The chemical reduction technique is also popular and can be combined with the reduction of precursor molecules to form Pt/graphene composites from GO, as will be seen later in this chapter. This involves treating graphene oxide dispersions with a reducing agent. Hydrazine was one of the first reagents used for this purpose, but metal hydrides such as sodium borohydride ($NaBH_4$) later became popular because they were more effective.[74] Following this, hydroiodic acid (HI) was then found to produce graphene from graphene oxide with superior conductivity, flexibility and strength when compared to hydrazine and sodium borohydride-reduced graphene.

Due to the nature of the synthesis method, the production of graphene via the reduction of graphene oxide has been identified as a potential method to mass produce graphene. However, due to the nature of the reduction process, some oxygen functional groups and holes remain following reduction,[78] which means that rGO is not as conductive as CVD graphene materials. Furthermore, oxygen functional groups have been identified as acting as centres for the corrosion of carbon materials under fuel cell conditions.[79] However, oxygen containing functional groups also have desirable effects for the distribution and binding of Pt atoms and clusters.

In electrochemical experiments and fuel cell tests, it has been found that rGO is susceptible to re-stacking to form multilayer graphene,[80] this could result in the blockage of Pt active sites, and to a decrease in mass transport. This is one drawback of the use of rGO/Pt composites. One approach which has been utilised in order to remedy this is the addition of spacers mixed with the rGO/Pt material, and which can act to keep rGO sheets separate and improve mass transfer through the electrode. Li et al. added carbon black particles to a Pt/Graphene

material to act as a spacer, and they found that the Pt/CB/Graphene composite exhibited enhanced ORR activity relative to the catalyst without carbon black; this was attributed to the superior oxygen transport to the Pt active sites.[81] Furthermore the CB particles also led to a higher percentage retention of ECSA after electrochemical cycling. While the ECSA was initially lower than the commercial Pt/C catalyst, ECSA retention was far superior, losing only 5% relative to the Pt/C loss of 50% ECSA after cycling. Carbon nanotubes have also been used as for this purpose, it was found that the Pt composite combining graphene and CNTs was superior in terms of ECSA to when only graphene or CNTs was used as a catalyst support, this translated to a higher power density.[82] For this reason, it has become desirable to be able to form 3D structured graphene materials which are resistant to re-stacking.

It is also possible to assemble rGO into 3D structures. Nickel foam has been used as a template for the assembly of rGO sheets, and Pt crystals have been combined with the hollow rGO foam post etching.[83] For the same reasons as for the CVD graphene foam, this material is probably not suitable for fuel cell applications. It is also possible to form rGO foams using a variety of methods including self-assembly via sonication,[84] centrifugation,[85] or hydrothermal treatments of solutions of GO.[63] Templating is also a popular method to produce these structures, where polymer[86] or silica[87] spheres can be used as removable templates to create pores of desired size in the rGO structures. Freezing mixtures of oil and water have also been used as a method to generate porous 3D rGO structures.[88]

2.4.3. Synthesis of 3D Graphene Powders

Pyrolysis has been used to produce 3D structured graphitic powders which can act as supports for Pt nanocrystals. These methods have the advantage of producing 3D graphene

which is therefore more resistant to stacking than rGO composites. Furthermore as these structures do not require pre-formed templates they are more suitable for mass production. In some cases the synthesis procedures can be modified in order to control the crystallinity of the graphene material, which could offer a means by which to control the Pt – support interactions.

A defective multilayered graphene structure was formed via the combustion of sodium ethoxide in air.[89] The material was sprayed onto a Nafion membrane and hot-pressed into an MEA, showing compatibility with traditional fuel cell production methods. The 3D graphene support exhibited a much higher initial ECSA than the commercial Pt/C catalyst, but retained a far lower percentage ECSA relative to the Pt/C catalyst, an improvement in ECSA retention was observed when the graphene foam was annealed, this was attributed to the removal of oxygen containing functional groups, however the durability of the industry Pt/C catalyst was not matched even after annealing.

Highly durable carbon nanocages comprising multilayer graphene were fabricated by Wang et al. The structures were formed using the spray pyrolysis of iron pentacarbonyl and pyridine, producing nitrogen doped carbon materials.[90] TEM images showing the graphene structures formed at different temperatures are shown in Figure 12. The synthesis temperature was controlled in order to form structures with different crystallinities. Pt crystals were formed on the surface of these novel supports using a solution based method. The initial ECSA was higher for the novel materials than for an industry Pt/C catalyst. The carbon nanocage material synthesised at 700 °C showed an ECSA percentage decrease comparable to the Pt/C (~80%), but the carbon nanocage synthesised at 1000 °C only showed a 50% decrease in ECSA. This enhanced durability was partially attributed to the increased crystallinity and the increased resistance of the support to electrochemical corrosion, in addition to synergising effects from the N doping.

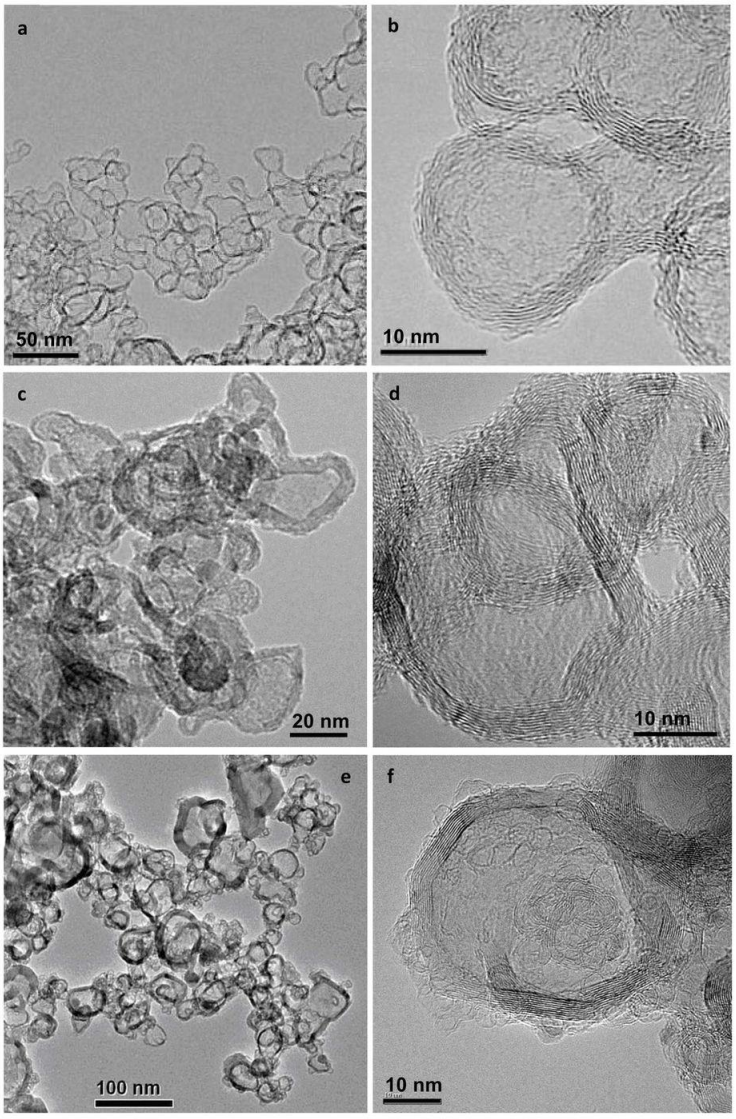

Figure 12. TEM images of carbon nanocages formed at a-b) 700 °C, c-d) 1000 °C, e-f) 1500 °C. Reprinted with permission from ref [90]. Copyright Nature Publishing Group 2014.

2.5. Synthesis of Platinum/Graphene Composites for Fuel Cells

This following section will outline the main synthesis techniques for producing Pt/graphene hybrid materials. The number of studies utilising compacted rGO sheets far outnumber those which use 3D graphene structures and so those papers most illustrative of the synthetic

methods are often those which utilise compacted rGO. Studies utilising 3D graphene have been included where possible however.

2.5.1. In-Situ Formation

For Pt nanocrystals to form on the surface of graphene in solution-based processes, a precursor molecule containing Pt must be reduced to produce Pt atoms with an oxidation state of zero. This can be accomplished by the same reducing agents as can be used to reduce graphene oxide (section 4.2.1.). It is intuitive therefore that the most frequently used methods for producing Pt/graphene hybrid materials are in-situ procedures where graphene oxide and a precursor molecule are mixed together and simultaneously reduced by the reducing agent. Alternatively already reduced graphene sheets can be produced and then mixed with the precursor and reducing agent.

An early example of the reduction process was that of Li et al.. They formed a Pt/graphene hybrid material containing spherical Pt crystals with an average size of 2.75 nm by mixing H_2PtCl_6 with GO in a mixture of ethylene glycol (EG) and water.[91] The EG acted as a reducing agent in this case. It was suggested that the functional groups on graphene act as anchoring sites for growing Pt nanocrystals. It was found that this method produced crystals smaller on average than those produced using an identical process on CNTs, leading to a higher electrocatalytic activity for the oxidation of methanol. The tolerance to CO was also found to be higher on the graphene material.

The reduction process can also be modified in order to control the shape of the Pt particles deposited. This is advantageous as certain crystal facets can have higher activities for certain reactions. Recently, Xia et al. were able to form Pt nanocubes with a high proportion of (100)

facets exposed by modifying the in-situ reduction technique with sodium hydroxide (Figure 13).[92] This simple way to alter the shape of the nanoparticles is far superior to the use of capping agents or surfactants, which have to be removed and can disrupt the shape of the crystal in the process. In an acidic electrolyte this was shown to have a higher activity for the ORR than Pt/CB catalysts.

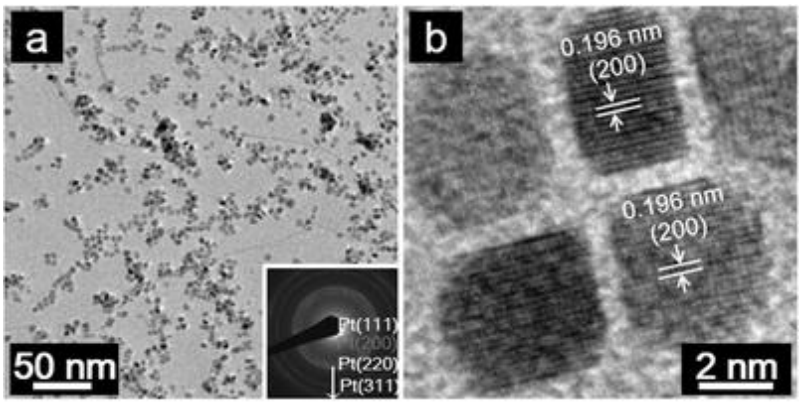

Figure 13. a) Low and b) high magnification TEM images of Pt nanocubes synthesised using the in-situ method on reduced graphene oxide (rGO). Reprinted with permission from ref [92]. Copyright Wiley 2014.

Wang et al. utilised a 3D graphene structure in the reduction process. This involved stirring nickel foams in a solution of GO and Pt precursor to infiltrate them into the pores of the foam.[83] The nickel foams were then placed in a vitamin C solution and heated to 60˚C to reduce both components. Following this, etching of the nickel foam using HCl produced the porous catalyst. This material was used as an electrode in an alkaline electrolyte for the electro-oxidation of methanol without needing additional current collectors or additives. This is in contrast to the other Pt/rGO catalyst made up of compacted sheets that was also tested; this had to be attached to a glassy carbon electrode with a Nafion binder in order to test its catalytic activity. The Pt/rGO foam exhibited an activity 2.6 times that of the Pt/rGO under the same conditions.

2.5.2. Electrodeposition

Electrodeposition is another technique which can be used to grow Pt nanocrystals on the surface of 3D graphene. Maiyalagan et al. used CVD grown graphene foam and grew Pt nanocrystals on the surface in a pulsed electrodeposition process.[69] This involved using the graphene foam as an electrode in an H_2PtCl_6 solution and using 200 ms pulses of 1000 mV with 500 ms between them. Controlling the pulse width and amplitude allowed control over the resulting nanoparticles. This method produces larger crystals than those produced in other methods, nanoparticles 10-30 nm in size were formed and well distributed over the surface of the graphene foam. This catalyst showed a higher current density than a Pt/carbon fibre catalyst for the oxidation of methanol.

2.5.3. Thermal Annealing

The subnano Pt clusters observed by Yoo et al. were formed using a thermal annealing process, in which the Pt precursor was first coated on the graphene using ethanol as a solvent.[38] Subsequently, the graphene was annealed in a reducing atmosphere of hydrogen and argon which caused the subnano clusters to form on the surface of graphene. As previously mentioned, this material gave a very high current density for the electro-oxidation of methanol. This catalyst was also shown to have far superior tolerance for CO poisoning and durability than Pt/CB.[93] It was found that increasing the amount of Pt precursor would also increase the size of the nanocrystals produced, which in turn lowered their activity for carbon monoxide oxidation.[46] When the loading was minimised at 10% by weight the

catalytic activity for this reaction was maximised. The mechanism for this process has also been suggested.[94] The precursor is deposited on the surface of graphene as large aggregates and is partially reduced by the ethanol used as a solvent. Upon heating in the reducing atmosphere the precursor is reduced and individual Pt atoms migrate over the surface of graphene and form small clusters.

2.5.4. Microwave Assisted

Microwaves have also been utilised in order to produce Pt nanocrystals on the surface of graphene. Kundu et al. created a solution of GO in EG and Pt precursor,[95] the solution was then subjected to microwave irradiation for 50 seconds at a time with 10 seconds in between irradiation for four cycles. This formed nanocrystals 2-3 nm in diameter on the rGO surface. The EG exfoliates the GO sheets and forms Pt^{4+} ions in the solution during sonication. The microwave radiation provides rapid heading, allowing Pt^{4+} to be reduced to Pt^{2+} at surface sites on GO. The Pt^{2+} then donates electrons to the GO surface, reducing it to rGO. In this way, a co-reduction takes place, where the microwave radio provides enough energy to facilitate the simultaneous reduction of GO and the Pt precursor, forming anchoring sites for Pt crystals on the graphene surface in the process.

2.5.5. Use of Other Molecules

One solution that has been explored for the purpose of producing well-dispersed Pt nanocrystals on the surface of graphene is the use of molecules which non-covalently bind to graphene. An example of this is the use of copper phthalocyanine (CuPc) to functionalise graphene. Phthalocyanine is a macrocyclic molecule with π bonds with can interact with the π system of graphene.[96] This was done by sonicating graphene with CuPc and then forming Pt crystals on graphene using the reduction process. The addition of the CuPc decreased the average Pt crystal size and improved the dispersion on the graphene surface, leading to a large increase in current density for the oxidation of methanol compared to the same catalyst prepared without CuPc.

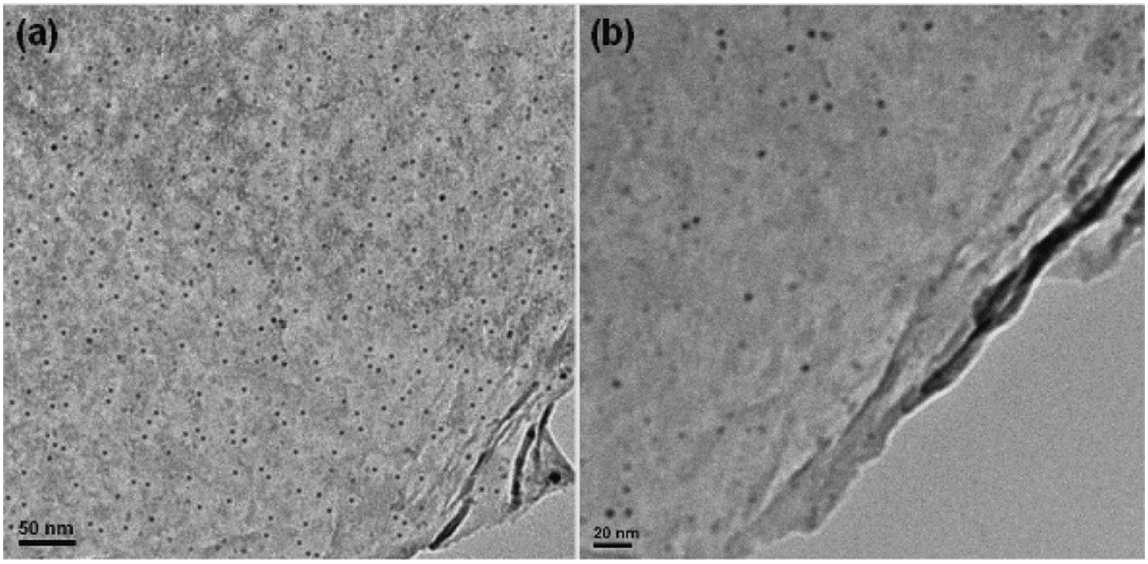

Figure 14. a) Low and b) high magnification TEM images of Pt nanocrystals synthesised using ferritin on the surface of CVD graphene foam. Reprinted (adapted) with permission from ref [68]. 2013 Copyright American Chemical Society.

Molecules such as proteins can also be used to disperse nanocrystals on the surface of graphene.[68] CVD produced graphene foams with monodisperse Pt particles 3 nm in diameter have been synthesised on graphene using ferritin. Adding a Pt precursor at a ratio of 20 Pt atoms per ferritin causes the ferritin to form aggregates of 24 units which encapsulate the Pt

atoms. Rinsing the graphene foam in this solution and then heating the product to remove the ferritin shell formed the final product (Figure 14). The fixation of the ferritin to the surface of graphene was attributed to the favourable hydrophobic interaction between the graphene surface and hydrophobic regions on the ferritin. This catalyst was shown to be superior to Pt produced on rGO, a commercial Pt-carbon catalyst and a Pt/graphene foam catalyst produced using electrodeposition in terms of current density and durability. Furthermore, the rGO and commercial catalyst had to be loaded on a glassy carbon electrode with some Nafion binder, whereas the graphene foam could be used as a free-standing electrode.

2.6 Preventing Pt Detachment and Sintering

A recent strategy which has been used in the literature in order to increase the durability of Pt catalysts is to cover the Pt crystals with a porous layer which aims to prevent the degradation caused by detachment and migration of the crystals. Galeano et al. formed hollow graphitic spheres templated by silica particles, these carbon spheres were made up of interlinked pores several nanometres in diameter.[97] Pt crystals were formed in the pores using a thermal annealing technique. The encapsulation of Pt particles in the small pores was attributed with preventing detachment and agglomeration, resulting in a much smaller degree of aggregation following electrochemical cycling compared to Pt/Vulcan. A smaller degree of ECSA loss was observed in the novel catalyst than in the commercial catalyst. Furthermore in-situ measurements were carried out using a real fuel cell, which indicated that the Pt particles in the pores could be fully accessed by the electrolyte under the operating conditions of the cell. This suggests that confining particles in pores might be a viable strategy for application in real fuel cell applications.

Recently, several studies have utilised a strategy where a porous layer is synthesised on the surface of ready formed carbon supports, such as Vulcan carbon, CNTs and graphene. Cheng et al. deposited a layer of zirconia on the surface of a Pt/CNT catalyst. [98] The zirconia catalyst retained a much higher percentage of its ECSA (92%) relative to commercial Pt/C (18%) and the same catalyst without zirconia (26%), however the initial ECSA was much lower with the addition of the zirconia covering, so that the absolute ECSAs of the commercial and novel catalyst were similar after electrochemical cycling.

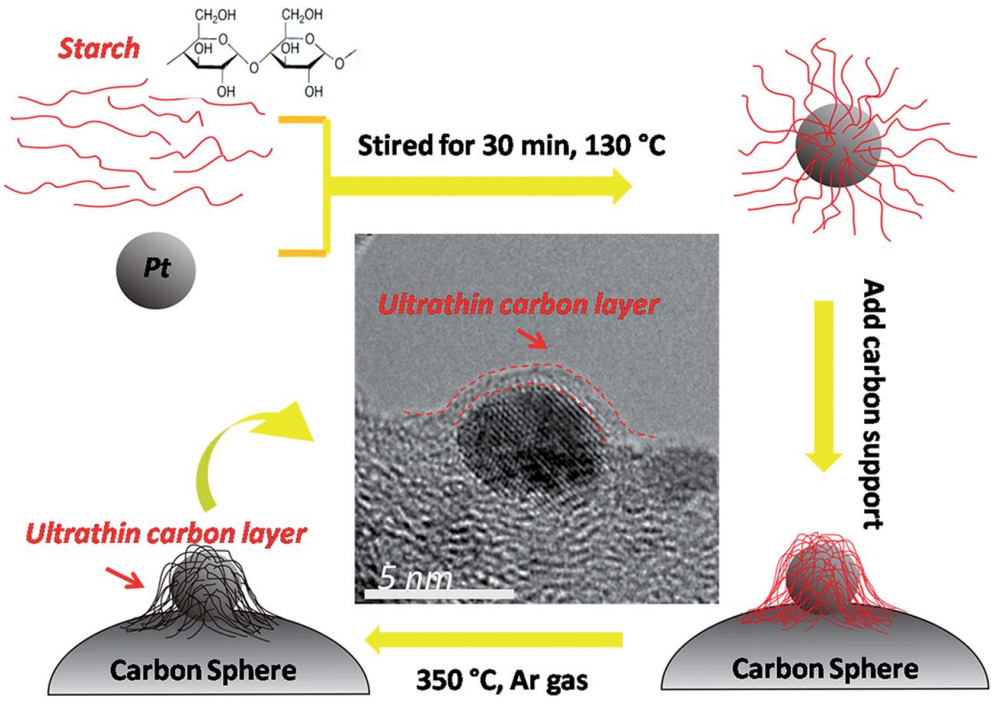

Figure 15. Schematic and TEM image showing the formation of a carbon layer over Pt nanocrystals on Vulcan carbon support. Reprinted with permission from ref [99]. Copyright Royal Society of Chemistry 2015.

The use of a porous carbon covering has also been used, and has produced catalysts that have initial ECSAs comparable to Pt/C catalysts which are retained following cycling. Cheng et al. mixed Pt particles with starch and Vulcan carbon, upon heating in argon at 350 °C, a porous carbon layer was formed over the surface.[99] A schematic diagram and TEM image of this structure is seen in Figure 15. This was accompanied only by a slight decrease in ECSA

relative to a Pt/C catalyst which had been heated at the same temperature without starch (75.8 vs 76.1 $m^2 g^{-1}$), in electrochemical cycling a much higher ECSA retention was seen for the carbon covered crystals (70% vs 50% ECSA retention).

Pt crystals in nitrogen-doped porous carbon layers have been formed on the surface of CNTs.[100] This was done by forming the Pt crystal and porous carbon layer simultaneously via annealing in argon. The covered catalyst had a slightly lower ECSA relative to commercial Pt/C (74 $m^2 g^{-1}$ vs 87 m^2 g^{-1}), but retained almost 100% of its maximum ECSA after electrochemical cycling, whereas Pt/C underwent a 65 % loss. The superior stability was attributed to the prevention of detachment or migration of the Pt particles, as shown by post-cycling TEM images. It was found that the average size of the Pt crystals on the novel catalyst was almost identical to the particle size pre-cycling, whereas Pt crystals on Pt/C had aggregated significantly. A very similar material to this one was fabricated and tested in an MEA assembly under real fuel cell conditions, and showed improvements relative to a commercial catalyst.[101]

2.7 Conclusions

Graphene's electrical conductivity, high surface area, mechanical strength and chemical stability make it an excellent candidate as a catalyst support in fuel cells. It is also an extremely versatile material with different synthesis methods allowing control over its properties as a support. Pt interacts favourably with the graphene substrate, having shown high CO tolerance, good catalytic activity and the stabilisation of small clusters and crystals. The interactions between graphene and Pt can be further enhanced in defective or doped regions, allowing extra control over electrode fabrication. Furthermore, there are many

techniques for growing Pt particles on the surface of graphene which allows further control over the properties. In three-electrode tests graphene has proven superior to other carbon supports, and can be utilised as a free-standing structure or as a catalyst ink. These three-dimensional structures are not suitable for utilisation in real fuel cells however, and Pt/graphene composites utilising rGO sheets can restack during the MEA fabrication process, leading to inferior performance. This leads to mass transfer issues in real cell tests. The combination of graphene with other carbon materials is a promising remedy to this problem. The use of three-dimensional graphene structures is also attractive, but more research is required in order to optimise the morphology of these materials, and to develop cheap and simple processes which would allow 3D graphene materials to be mass produced. Following this, appropriate Pt nanocrystal synthesis techniques compatible with the type of graphene support will need to be optimised to achieve the ideal metal loading, crystal size, and shape for particular reactions. Covering Pt crystals with porous layers which can protect them from detachment and aggregation has shown to be a potential strategy for increasing the durability of Pt/C catalysts. Furthermore, these benefits have been shown to translate to real fuel cell tests. The combination of graphene supports and this strategy could produce highly active and durable catalysts.

2.8 References

(1) Debe, M. K. Electrocatalyst approaches and challenges for automotive fuel cells. *Nature*, **2012**, *486*, 43-51.

(2) Antolini, E. Graphene as a new carbon support for low-temperature fuel cell catalysts. *Appl. Catal. B-Environ.*, **2012,** *123*, 52-68.

(3) Novoselov, K. S.; Geim, A. K.; Morozov, S. V.; Jiang, D.; Zhang, Y.; Dubonos, S. V.; Grigorieva, I. V.; Firsov, A. A. Electric field effect in atomically thin carbon films. *Science*, **2004,** *306*, 666-669.

(4) Balandin, A. A. Thermal properties of graphene and nanostructured carbon materials. *Nat. Mater.* **2011,** *10*, 569-581.

(5) Lee, C.; Wei, X. D.; Kysar, J. W.; Hone, J. Measurement of the elastic properties and intrinsic strength of monolayer graphene. *Science,* **2008,** *321*, 385-388.

(6) Stoller, M. D.; Park, S.; Zhu, Y.; An, J.; Ruoff, R. S. Graphene-Based Ultracapacitors. *Nano Lett.,* **2008,** *8*, 3498-3502.

(7) Hou, J.; Shao, Y.; Ellis, M. W.; Moore, R. B.; Yi, B. Graphene-based electrochemical energy conversion and storage: fuel cells, supercapacitors and lithium ion batteries. *Phys. Chem. Chem. Phys.*, **2011,** *13*, 15384-15402.

(8) Hsieh, S. H.; Hsu, M. C.; Liu, W. L.; Chen, W. J. Study of Pt catalyst on graphene and its application to fuel cell. *Appl. Surf. Sci.,* **2013,** *277*, 223-230.

(9) Kung, C.-C.; Lin, P.-Y.; Xue, Y.; Akolkar, R.; Dai, L.; Yu, X.; Liu, C.-C. Three dimensional graphene foam supported platinum–ruthenium bimetallic nanocatalysts for direct methanol and direct ethanol fuel cell applications. *J. Power Sources,* **2014,** *256*, 329-335.

(10) Pletcher, D. *A First Course in Electrode Processes*. 2nd ed.; Royal Society of Chemistry: London, 2009.pp 232-247.

(11) Ha, S.; Larsen, R.; Masel, R. I. Performance characterization of Pd/C nanocatalyst for direct formic acid fuel cells. *J. Power Sources,* **2005,** *144*, 28-34.

(12) Trens, P.; Durand, R.; Coq, B.; Coutanceau, C.; Rousseau, S.; Lamy, C., Poisoning of Pt/C catalysts by CO and its consequences over the kinetics of hydrogen chemisorption. *Appl. Catal. B-Environ.,* **2009,** *92*, 280-284.

(13) Higgins, D.; Zamani, P.; Yu, A.; Chen, Z. The application of graphene and its composites in oxygen reduction electrocatalysis: a perspective and review of recent progress. *Energy Environ. Sci*,. **2016,** *9*, 357-390.

(14) Yeager, E., Electrocatalysts for O2 reduction. *Electrochim. Acta*, **1984,** *29*, 1527-1537.

(15) Liu, M.; Zhang, R.; Chen, W., Graphene-Supported Nanoelectrocatalysts for Fuel Cells: Synthesis, Properties, and Applications. *Chem. Rev.*, **2014,** *114*, 5117-5160.

(16) Sharma, S.; Pollet, B. G. Support materials for PEMFC and DMFC electrocatalysts—A review. *J. Power Sources*, **2012,** *208*, 96-119.

(17) Shao, Y.; Yin, G.; Gao, Y. Understanding and approaches for the durability issues of Pt-based catalysts for PEM fuel cell. *J. Power Sources*, **2007,** *171*, 558-566.

(18) Stein, A. Advances in Microporous and Mesoporous Solids—Highlights of Recent Progress. *Adv. Mater.*, **2003,** *15*, 763-775.

(19) Ryoo, R.; Joo, S. H.; Kruk, M.; Jaroniec, M. Ordered Mesoporous Carbons. *Adv. Mater.*, **2001,** *13*, 677-681.

(20) Choi, J.-S.; Chung, W. S.; Ha, H. Y.; Lim, T.-H.; Oh, I.-H.; Hong, S.-A.; Lee, H.-I. Nano-structured Pt–Cr anode catalyst over carbon support, for direct methanol fuel cell. *J. Power Sources*, **2006,** *156*, 466-471.

(21) Wang, X.; Li, W. Z.; Chen, Z. W.; Waje, M.; Yan, Y. S. Durability investigation of carbon nanotube as catalyst support for proton exchange membrane fuel cell. *J. Power Sources*, **2006,** *158*, 154-159.

(22) Park, S.; Shao, Y. Y.; Kou, R.; Viswanathan, V. V.; Towne, S. A.; Rieke, P. C.; Liu, J.; Lin, Y. H.; Wang, Y. Polarization Losses under Accelerated Stress Test Using Multiwalled Carbon Nanotube Supported Pt Catalyst in PEM Fuel Cells. *J. Electrochem. Soc*. **2011,** *158*, B297-B302.

(23) Geim, A. K.; Novoselov, K. S. The rise of graphene. *Nat. Mater.*, **2007,** *6*, 183-191.

(24) Liu, H.; Liu, Y.; Zhu, D. Chemical doping of graphene. *J. Mater. Chem.* **2011,** *21*, 3335-3345.

(25) Huang, X.; Qi, X.; Boey, F.; Zhang, H., Graphene-based composites. *Chem. Soc. Rev.,* **2012,** *41*, 666-686.

(26) Wang, H. L.; Robinson, J. T.; Diankov, G.; Dai, H. J., Nanocrystal Growth on Graphene with Various Degrees of Oxidation. *J. Am. Chem. Soc.*, **2010,** *132*, 3270-3271.

(27) Yu, S. U.; Park, B.; Cho, Y.; Hyun, S.; Kim, J. K.; Kim, K. S. Simultaneous Visualization of Graphene Grain Boundaries and Wrinkles with Structural Information by Gold Deposition. *ACS Nano*, **2014,** *8*, 8662-8668.

(28) Cong, H.-P.; Chen, J.-F.; Yu, S.-H., Graphene-based macroscopic assemblies and architectures: an emerging material system. *Chem. Soc. Rev.*, **2014**, *43*, 7295-7325.

(29) Li, C.; Shi, G. Three-dimensional graphene architectures. *Nanoscale*, **2012,** *4* , 5549-5563.

(30) Groves, M. N.; Malardier-Jugroot, C.; Jugroot, M. Improving Platinum Catalyst Durability with a Doped Graphene Support. *J. Phys. Chem. C.* **2012,** *116*, 10548-10556.

(31) Stambula, S.; Gauquelin, N.; Bugnet, M.; Gorantla, S.; Turner, S.; Sun, S.; Liu, J.; Zhang, G.; Sun, X.; Botton, G. A. Chemical Structure of Nitrogen-Doped Graphene with Single Platinum Atoms and Atomic Clusters as a Platform for the PEMFC Electrode. *J. Phys. Chem. C.*, **2014,** *118*, 3890-3900.

(32) Liu, J. F.; Takeshi, D.; Orejon, D.; Sasaki, K.; Lyth, S. M., Defective Nitrogen-Doped Graphene Foam: A Metal-Free, Non-Precious Electrocatalyst for the Oxygen Reduction Reaction in Acid. *J. Electrochem. Soc.*, **2014,** *161*, F544-F550.

(33) Meier, J. C.; Galeano, C.; Katsounaros, I.; Witte, J.; Bongard, H. J.; Topalov, A. A.; Baldizzone, C.; Mezzavilla, S.; Schüth, F.; Mayrhofer, K. J. J. Design criteria for stable Pt/C fuel cell catalysts. *Beilstein J. Nanotechnol*, **2014,** *5*, 44-67.

(34) Castanheira, L.; Silva, W. O.; Lima, F. H. B.; Crisci, A.; Dubau, L.; Maillard, F. Carbon Corrosion in Proton-Exchange Membrane Fuel Cells: Effect of the Carbon Structure, the Degradation Protocol, and the Gas Atmosphere. *ACS Catal.*, **2015**, *5* 2184-2194.

(35) Fampiou, I.; Ramasubramaniam, A. Binding of Pt Nanoclusters to Point Defects in Graphene: Adsorption, Morphology, and Electronic Structure. *J. Phys. Chem. C*, **2012,** *116*, 6543-6555.

(36) Yuge, R.; Zhang, M. F.; Tomonari, M.; Yoshitake, T.; Iijima, S.; Yudasaka, M. Site identification of carboxyl groups on graphene edges with Pt derivatives. *ACS Nano*, **2008,** *2*, 1865-1870.

(37) Janowska, I.; Moldovan, M. S.; Ersen, O.; Bulou, H.; Chizari, K.; Ledoux, M. J.; Cuong, P. H. High Temperature Stability of Platinum Nanoparticles on Few-Layer Graphene Investigated by In Situ High Resolution Transmission Electron Microscopy. *Nano Res.*, **2011,** *4*, 511-521.

(38) Yoo, E.; Okata, T.; Akita, T.; Kohyama, M.; Nakamura, J.; Honma, I. Enhanced Electrocatalytic Activity of Pt Subnanoclusters on Graphene Nanosheet Surface. *Nano Lett.*, **2009,** *9*, 2255-2259.

(39) Shen, Y.; Zhang, Z.; Long, R.; Xiao, K.; Xi, J. Synthesis of ultrafine Pt nanoparticles stabilized by pristine graphene nanosheets for electro-oxidation of methanol. *ACS Appl. Mater. Interfaces* **2014,** *6*, 15162-15170.

(40) Luo, Z.; Somers, L. A.; Dan, Y.; Ly, T.; Kybert, N. J.; Mele, E. J.; Johnson, A. T. C. Size-Selective Nanoparticle Growth on Few-Layer Graphene Films. *Nano Lett.*, **2010,** *10*, 777-781.

(41) Moldovan, M. S.; Bulou, H.; Dappe, Y. J.; Janowska, I.; Begin, D.; Pham-Huu, C.; Ersen, O. On the Evolution of Pt Nanoparticles on Few-Layer Graphene Supports in the High-Temperature Range. *J. Phys. Chem. C*, **2012,** *116*, 9274-9282.

(42) Xu, P.; Dong, L.; Neek-Amal, M.; Ackerman, M. L.; Yu, J.; Barber, S. D.; Schoelz, J. K.; Qi, D.; Xu, F.; Thibado, P. M.; Peeters, F. M. Self-Organized Platinum Nanoparticles on Freestanding Graphene. *ACS Nano* ,**2014,** *8*, 2697-2703.

(43) Qin, Y.; Li, J.; Kong, Y.; Li, X.; Tao, Y.; Li, S.; Wang, Y. In situ growth of Au nanocrystals on graphene oxide sheets. *Nanoscale,* **2014,** *6* , 1281-1285.

(44) Xin, L.; Yang, F.; Rasouli, S.; Qiu, Y.; Li, Z.-F.; Uzunoglu, A.; Sun, C.-J.; Liu, Y.; Ferreira, P.; Li, W.; Ren, Y.; Stanciu, L. A.; Xie, J. Understanding Pt Nanoparticle Anchoring on Graphene Supports through Surface Functionalization. *ACS Catal.*, **2016**, *6*, 2642-2653.

(45) Schneider, W. B.; Benedikt, U.; Auer, A. A. Interaction of Platinum Nanoparticles with Graphitic Carbon Structures: A Computational Study. *ChemPhysChem,* **2013,** *14*, 2984-2989.

(46) Siburian, R.; Kondo, T.; Nakamura, J. Size Control to a Sub-Nanometer Scale in Platinum Catalysts on Graphene. *J. Phys. Chem. C,* **2013,** *117*, 3635-3645.

(47) Wang, H.; Maiyalagan, T.; Wang, X. Review on Recent Progress in Nitrogen-Doped Graphene: Synthesis, Characterization, and Its Potential Applications. *ACS Catal.,* **2012,** *2*, 781-794.

(48) Dai, X.-Q.; Tang, Y.-N.; Dai, Y.-W.; Li, Y.-H.; Zhao, J.-H.; Zhao, B.; Yang, Z.-X. Structures of Pt clusters on graphene doped with nitrogen, boron, and silicon: a theoretical study. *Chin. Phys. B,* **2011,** *20*, 056801.

(49) Muhich, C. L.; Westcott, J. Y.; Morris, T. C.; Weimer, A. W.; Musgrave, C. B. The Effect of N and B Doping on Graphene and the Adsorption and Migration Behavior of Pt Atoms. *J. Phys. Chem. C* **2013,** *117*, 10523-10535.

(50) Jeong, H. M.; Lee, J. W.; Shin, W. H.; Choi, Y. J.; Shin, H. J.; Kang, J. K.; Choi, J. W. Nitrogen-Doped Graphene for High-Performance Ultracapacitors and the Importance of Nitrogen-Doped Sites at Basal Planes. *Nano Lett.,* **2011,** *11*, 2472-2477.

(51) He, Z.; He, K.; Robertson, A. W.; Kirkland, A. I.; Kim, D.; Ihm, J.; Yoon, E.; Lee, G.-D.; Warner, J. H. Atomic Structure and Dynamics of Metal Dopant Pairs in Graphene. *Nano Lett.,* **2014,** *14*, 3766-3772.

(52) Fampiou, I.; Ramasubramaniam, A. CO Adsorption on Defective Graphene-Supported Pt13 Nanoclusters. *J. Phys. Chem. C.,* **2013,** *117*, 19927-19933.

(53) Dobrota, A. S.; Pasti, I. A.; Mentus, S. V.; Skorodumova, N. V. A general view on the reactivity of the oxygen-functionalized graphene basal plane. *Phys. Chem. Chem. Phys.,* **2016,** *18*, 6580-6586.

(54) Matsutsu, M.; Petersen, M. A.; van Steen, E. Pt38 cluster on OH- and COOH-functionalised graphene as a model for Pt/C-catalysts. *Phys. Chem. Chem. Phys.,* **2016,** *18*, 25693-25704.

(55) Kim, G.; Kawazoe, Y.; Lee, K. R. Controlled Catalytic Properties of Platinum Clusters on Strained Graphene. *J. Phys. Chem. Lett.* **2012,** *3*, 1989-1996.

(56) Sen, F. G.; Qi, Y.; Alpas, A. T., Anchoring platinum on graphene using metallic adatoms: a first principles investigation. *J. Phys.-Condes. Matter* **2012,** *24*, 225003

(57) Tian, N.; Xiao, J.; Zhou, Z.-Y.; Liu, H.-X.; Deng, Y.-J.; Huang, L.; Xu, B.-B.; Sun, S.-G. Pt-group bimetallic nanocrystals with high-index facets as high performance electrocatalysts. *Farad. Discuss.,* **2013,** *162*, 77-89.

(58) Zhang, Y.; Zhang, L.; Zhou, C. Review of Chemical Vapor Deposition of Graphene and Related Applications. *Accounts Chem. Res.,* **2013,** *46*, 2329-2339.

(59) Tan, H.; Fan, Y.; Zhou, Y.; Chen, Q.; Xu, W.; Warner, J. H. Ultrathin 2D Photodetectors Utilizing Chemical Vapor Deposition Grown WS2 With Graphene Electrodes. *ACS Nano.* **2016,** *10*, 7866-7873.

(60) Chen, Z. P.; Ren, W. C.; Gao, L. B.; Liu, B. L.; Pei, S. F.; Cheng, H. M. Three-dimensional flexible and conductive interconnected graphene networks grown by chemical vapour deposition. *Nat. Mater.,* **2011,** *10*, 424-428.

(61) Wilson, P. M.; Mbah, G. N.; Smith, T. G.; Schmidt, D.; Lai, R. Y.; Hofmann, T.; Sinitskii, A. Three-dimensional periodic graphene nanostructures. *J. Mater. Chem. C,* **2014,** *2*, 1879-1886.

(62) Sha, J.; Gao, C.; Lee, S.-K.; Li, Y.; Zhao, N.; Tour, J. M. Preparation of Three-Dimensional Graphene Foams Using Powder Metallurgy Templates. *ACS Nano,* **2016**, *10*, 1411-1416.

(63) Xu, Y.; Sheng, K.; Li, C.; Shi, G., Self-Assembled Graphene Hydrogel via a One-Step Hydrothermal Process. *ACS Nano,* **2010,** *4*, 4324-4330.

(64) Yavari, F.; Chen, Z.; Thomas, A. V.; Ren, W.; Cheng, H.-M.; Koratkar, N. High Sensitivity Gas Detection Using a Macroscopic Three-Dimensional Graphene Foam Network. *Sci Rep* **2011,** *1*,166

(65) Dong, X.; Chen, J.; Ma, Y.; Wang, J.; Chan-Park, M. B.; Liu, X.; Wang, L.; Huang, W.; Chen, P. Superhydrophobic and superoleophilic hybrid foam of graphene and carbon nanotube for selective removal of oils or organic solvents from the surface of water. *Chem. Commun.,* **2012,** *48*, 10660-10662.

(66) Yue, H. Y.; Huang, S.; Chang, J.; Heo, C.; Yao, F.; Adhikari, S.; Gunes, F.; Liu, L. C.; Lee, T. H.; Oh, E. S.; Li, B.; Zhang, J. J.; Huy, T. Q.; Luan, N. V.; Lee, Y. H. ZnO Nanowire Arrays on 3D Hierachical Graphene Foam: Biomarker Detection of Parkinson's Disease. *ACS Nano,* **2014,** *8*, 1639-1646.

(67) Li, N.; Chen, Z. P.; Ren, W. C.; Li, F.; Cheng, H. M. Flexible graphene-based lithium ion batteries with ultrafast charge and discharge rates. *Proc. Natl. Acad. Sci. U. S. A.* **2012,** *109*, 17360-17365.

(68) Qiu, H. J.; Dong, X. C.; Sana, B.; Peng, T.; Paramelle, D.; Chen, P.; Lim, S. Ferritin-Templated Synthesis and Self-Assembly of Pt Nanoparticles on a Monolithic Porous Graphene Network for Electrocatalysis in Fuel Cells. *ACS Appl. Mater. Interfaces,* **2013,** *5*, 782-787.

(69) Maiyalagan, T.; Dong, X. C.; Chen, P.; Wang, X. Electrodeposited Pt on three-dimensional interconnected graphene as a free-standing electrode for fuel cell application. *J. Mater. Chem.,* **2012,** *22*, 5286-5290.

(70) Tashima, D.; Sakaguchi, Y.; Hidaka, H.; Otsubo, M. Basic examination of membrane electrode assembly of proton exchange membrane fuel cell considering heat deterioration. *Chemical Engineering Research and Design* **2011,** *89*, 1088-1093.

(71) Shen, P. K. *PEM Fuel Cell Catalyst Layers and MEAs.* In *PEM fuel cell electrocatalysts and catalyst layers*; Zhang, J., Ed.; Springer: Berlin, 2008. pp 355-374.

(72) Marcano, D. C.; Kosynkin, D. V.; Berlin, J. M.; Sinitskii, A.; Sun, Z.; Slesarev, A.; Alemany, L. B.; Lu, W.; Tour, J. M. Improved Synthesis of Graphene Oxide. *ACS Nano,* **2010,** *4*, 4806-4814.

(73) Ganguly, A.; Sharma, S.; Papakonstantinou, P.; Hamilton, J. Probing the Thermal Deoxygenation of Graphene Oxide Using High-Resolution In Situ X-ray-Based Spectroscopies. *J. Phys. Chem. C.,* **2011,** *115*, 17009-17019.

(74) Pei, S.; Cheng, H.-M. The reduction of graphene oxide. *Carbon,* **2012,** *50*, 3210-3228.

(75) Chua, C. K.; Pumera, M. Chemical reduction of graphene oxide: a synthetic chemistry viewpoint. *Chem. Soc. Rev.,* **2014,** *43*, 291-312.

(76) Nasrollahzadeh, M.; Babaei, F.; Fakhri, P.; Jaleh, B. Synthesis, characterization, structural, optical properties and catalytic activity of reduced graphene oxide/copper nanocomposites. *RSC Adv.,* **2015,** *5*, 10782-10789.

(77) McAllister, M. J.; Li, J.-L.; Adamson, D. H.; Schniepp, H. C.; Abdala, A. A.; Liu, J.; Herrera-Alonso, M.; Milius, D. L.; Car, R.; Prud'homme, R. K.; Aksay, I. A. Single Sheet Functionalized Graphene by Oxidation and Thermal Expansion of Graphite. *Chem. Mater.* **2007,** *19*, 4396-4404.

(78) Bagri, A.; Mattevi, C.; Acik, M.; Chabal, Y. J.; Chhowalla, M.; Shenoy, V. B. Structural evolution during the reduction of chemically derived graphene oxide. *Nat. Chem.,* **2010,** *2*, 581-587.

(79) Young, A. P.; Colbow, V.; Harvey, D.; Rogers, E.; Wessel, S. A Semi-Empirical Two Step Carbon Corrosion Reaction Model in PEM Fuel Cells. *J. Electrochem. Soc.* **2013,** *160*, F381-F388.

(80) Si, Y. C.; Samulski, E. T. Exfoliated Graphene Separated by Platinum Nanoparticles. *Chem. Mater.* **2008,** *20*, 6792-6797.

(81) Li, Y.; Li, Y.; Zhu, E.; McLouth, T.; Chiu, C.-Y.; Huang, X.; Huang, Y. Stabilization of High-Performance Oxygen Reduction Reaction Pt Electrocatalyst Supported on Reduced Graphene Oxide/Carbon Black Composite. *J. Am. Chem. Soc.,* **2012,** *134*, 12326-12329.

(82) Jyothirmayee Aravind, S. S.; Imran Jafri, R.; Rajalakshmi, N.; Ramaprabhu, S. Solar exfoliated graphene-carbon nanotube hybrid nano composites as efficient catalyst supports for proton exchange membrane fuel cells. *J. Mater. Chem.,* **2011,** *21*, 18199-18204.

(83) Wang, X.; Li, C.; Shi, G. A high-performance platinum electrocatalyst loaded on a graphene hydrogel for high-rate methanol oxidation. *Phys. Chem. Chem. Phys.,* **2014,** *16* , 10142-10148.

(84) Compton, O. C.; An, Z.; Putz, K. W.; Hong, B. J.; Hauser, B. G.; Catherine Brinson, L.; Nguyen, S. T. Additive-free hydrogelation of graphene oxide by ultrasonication. *Carbon,* **2012,** *50*, 3399-3406.

(85) Liu, F.; Seo, T. S., A Controllable Self-Assembly Method for Large-Scale Synthesis of Graphene Sponges and Free-Standing Graphene Films. *Adv. Funct. Mater.*, **2010,** *20*, 1930-1936.

(86) Choi, B. G.; Yang, M.; Hong, W. H.; Choi, J. W.; Huh, Y. S. 3D Macroporous Graphene Frameworks for Supercapacitors with High Energy and Power Densities. *ACS Nano*, **2012,** *6*, 4020-4028.

(87) Huang, X. D.; Qian, K.; Yang, J.; Zhang, J.; Li, L.; Yu, C. Z.; Zhao, D. Y., Functional Nanoporous Graphene Foams with Controlled Pore Sizes. *Adv. Mater.*, **2012,** *24*, 4419-4423.

(88) Barg, S.; Perez, F. M.; Ni, N.; do Vale Pereira, P.; Maher, R. C.; Garcia-Tunon, E.; Eslava, S.; Agnoli, S.; Mattevi, C.; Saiz, E. Mesoscale assembly of chemically modified graphene into complex cellular networks. *Nat. Commun.* **2014,** *5*, 4328-4328.

(89) Liu, J.; Takeshi, D.; Sasaki, K.; Lyth, S. M. Defective Graphene Foam: A Platinum Catalyst Support for PEMFCs. *J. Electrochem. Soc.* **2014,** *161*, F838-F844.

(90) Wang, X. X.; Tan, Z. H.; Zeng, M.; Wang, J. N. Carbon nanocages: A new support material for Pt catalyst with remarkably high durability. *Sci. Rep.* **2014,** *4*,4437

(91) Li, Y. J.; Gao, W.; Ci, L. J.; Wang, C. M.; Ajayan, P. M. Catalytic performance of Pt nanoparticles on reduced graphene oxide for methanol electro-oxidation. *Carbon*, **2010,** *48*, 1124-1130.

(92) Xia, B. Y.; Bin Wu, H.; Yan, Y.; Wang, H. B.; Wang, X. One-Pot Synthesis of Platinum Nanocubes on Reduced Graphene Oxide with Enhanced Electrocatalytic Activity. *Small*, **2014,** *10*, 2336-2339.

(93) Yoo, E.; Okada, T.; Akita, T.; Kohyama, M.; Honma, I.; Nakamura, J. Sub-nano-Pt cluster supported on graphene nanosheets for CO tolerant catalysts in polymer electrolyte fuel cells. *J. Power Sources*, **2011,** *196*, 110-115.

(94) Siburian, R.; Nakamura, J., Formation Process of Pt Subnano-Clusters on Graphene Nanosheets. *J. Phys. Chem. C,* **2012,** *116*, 22947-22953.

(95) Kundu, P.; Nethravathi, C.; Deshpande, P. A.; Rajamathi, M.; Madras, G.; Ravishankar, N., Ultrafast Microwave-Assisted Route to Surfactant-Free Ultrafine Pt Nanoparticles on Graphene: Synergistic Co-reduction Mechanism and High Catalytic Activity. *Chem. Mater.,* **2011,** *23*, 2772-2780.

(96) Zhong, J. P.; Fan, Y. J.; Wang, H.; Wang, R. X.; Fan, L. L.; Shen, X. C.; Shi, Z. J. Copper phthalocyanine functionalization of graphene nanosheets as support for platinum nanoparticles and their enhanced performance toward methanol oxidation. *J. Power Sources,* **2013,** *242*, 208-215.

(97) Galeano, C.; Meier, J. C.; Peinecke, V.; Bongard, H.; Katsounaros, I.; Topalov, A. A.; Lu, A.; Mayrhofer, K. J. J.; Schüth, F. Toward Highly Stable Electrocatalysts via Nanoparticle Pore Confinement. *J. Am. Chem. Soc.,* **2012,** *134*, 20457-20465.

(98) Cheng, N.; Banis, M. N.; Liu, J.; Riese, A.; Li, X.; Li, R.; Ye, S.; Knights, S.; Sun, X. Extremely Stable Platinum Nanoparticles Encapsulated in a Zirconia Nanocage by Area-Selective Atomic Layer Deposition for the Oxygen Reduction Reaction. *Adv. Mater.,* **2015,** *27*, 277-281.

(99) Cheng, K.; Kou, Z.; Zhang, J.; Jiang, M.; Wu, H.; Hu, L.; Yang, X.; Pan, M.; Mu, S. Ultrathin carbon layer stabilized metal catalysts towards oxygen reduction. *J. Mater. Chem. A,* **2015,** *3*, 14007-14014.

(100) Guo, L.; Jiang, W.-J.; Zhang, Y.; Hu, J.-S.; Wei, Z.-D.; Wan, L.-J. Embedding Pt Nanocrystals in N-Doped Porous Carbon/Carbon Nanotubes toward Highly Stable Electrocatalysts for the Oxygen Reduction Reaction. *ACS Catal.,* **2015,** *5*, 2903-2909.

(101) Zhang, Q.; Yu, X.; Ling, Y.; Cai, W.; Yang, Z., Ultrathin nitrogen doped carbon layer stabilized Pt electrocatalyst supported on N-doped carbon nanotubes. *Int. J. Hydrog. Energy*., **2017**, *42*, 10354-10362.

Chapter 3

Methodology

3.1 Introduction

This section of the thesis is dedicated to describing the various techniques used to carry out the project. Experimental techniques used to produce the samples studied in this thesis are described in a general way, for example, the furnace equipment is described and the types of experiments performed using this equipment are explained. However, detailed experimental procedures to produce or modify different materials can be found in the relevant chapters to avoid confusion. Analytical techniques used to characterise the materials produced in this thesis are described, these include SEM, TEM, BET, TGA, Raman spectroscopy, and cyclic voltammetry. Very brief explanations of the scientific principles which underpin these techniques are given. Explanations regarding data analysis are given where appropriate.

3.2 Tube Furnace Experiments

A tube furnace was used for a variety of experiments in this thesis. The tube furnace allows samples to be heated in an atmosphere consisting of a desired mixture of gases (flow rates are expressed in standard cubic centimetres per minute – sccm) through the use of mass flow controllers, controlled using a laptop. The 1 inch diameter quartz tube runs through the middle of the furnace, and has gas inlets and outlets which are sealed with respect to the air, preventing oxidation of the sample. In addition, the furnace is fitted with rails, this allows rapid sliding of the furnace, in effect allowing the sample (loaded into an alumina crucible) to

be rapidly heated and cooled. Unless stated, these rails were used for in almost all furnace experiments in the thesis to achieve rapid heating and cooling. A schematic diagram of the furnace system is shown below in Figure 1. For clarity, the types of experiments performed using the furnace are described briefly below, but detailed procedures for these experiments are described in the relevant chapters, as a variety of protocols were used.

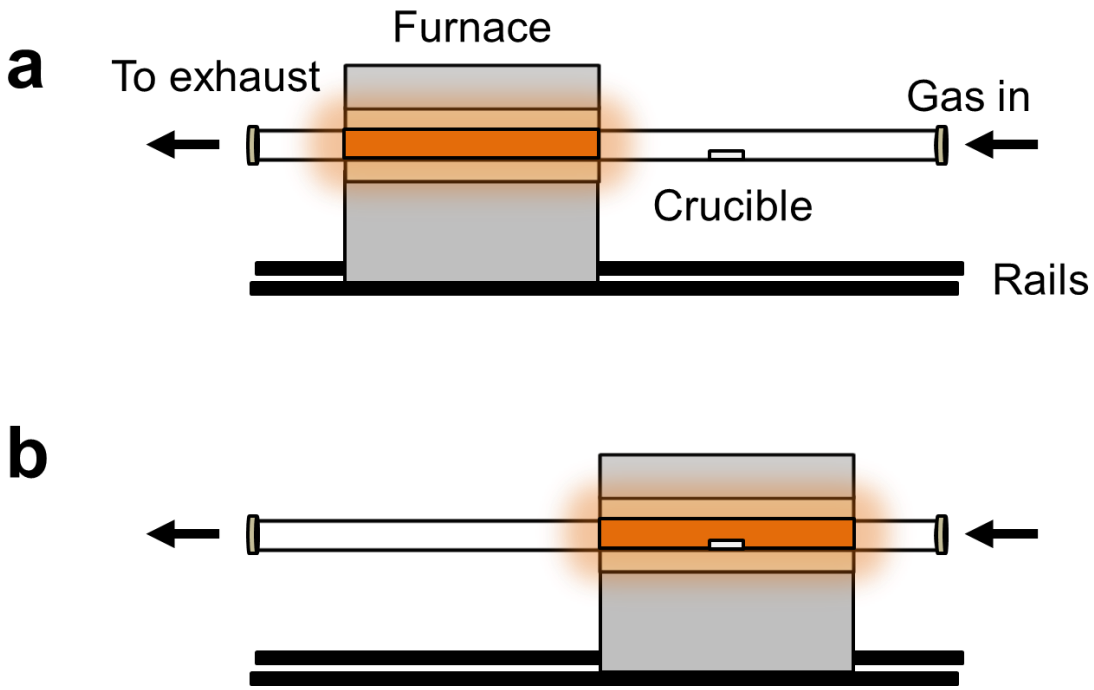

Figure 1. Schematic diagram of the furnace equipment used for annealing experiments. (a) The position of the furnace during the heating up and cooling stages of the experiments. The crucible containing the sample is at room temperature in this configuration. (b) The position of the furnace during the annealing of the sample. The rails allow the rapid movement of the furnace between these two positions.

The furnace was used for several types of experiment in this thesis. Chemical vapour deposition (CVD) is a popular method for the growth of graphene and was used in this thesis to grow graphene on the surfaces of nickel and platinum in Chapter 4 and Chapter 6 respectively. The CVD method was described briefly in Chapter 2. It involves the exposure

of a hot metal surface to a mixture of H_2 and CH_4 in argon. In this thesis, argon, 25% H_2 in argon, and 20% CH_4 in argon were used as the constituent gases.

Thermal annealing experiments were also regularly used in this thesis. In these experiments, only H_2 and Ar are introduced into the furnace system. This was used for a variety of purposes. In Chapter 4, thermal annealing is used to produce carbon materials from nickel acetate (only Ar is used in this case), in Chapter 6, it is used as a way to treat a commercially available Pt/C catalyst. In Chapters 4 and 5, it is used as a way to produce Pt nanocrystals on carbon materials, where the carbon material had been impregnated with H_2PtCl_6, which is reduced to Pt upon annealing. Detailed procedures are described in detail in their respective chapters.

3.3 Hydrochloric Acid (HCl) Etching

In experiments where carbon materials are produced via the CVD method on nickel substrates (Chapter 4) or the thermal annealing of nickel acetate (Chapter 5), the removal of nickel following the growth of carbon is desired. This is carried out using HCl, which etches Ni.[1] This produces $NiCl_2$ which is green in colour and therefore provides an indicator that etching is successfully taking place. For etching processes in this thesis, the nickel/carbon material was placed in 3M $HCl_{(aq)}$, and was heated to 80 °C using a water bath. It was held at this temperature for 5 hours, the acid was then exchanged. After a further three hours, the carbon material was retrieved and transferred to DI water several times for cleaning, and then to IPA. For graphene foams described in Chapter 3, this was done with the aid of glass slides to retrieve the foam from the surface of the liquid. For carbon powders in Chapter 5, this was

done by successive centrifugation. The foams/powders were then left to dry on a hotplate at 50 °C.

3.4 Oxygen Plasma Etching

Plasma etching is used in Chapter 4 in order to induce defects into CVD grown graphene foams. The sample is placed in the plasma chamber, which is then evacuated to a pressure of ~0.2 mbar, oxygen gas is then introduced so that the pressure in the chamber was 0.32 mbar. Following this the plasma was then generated with a power of 90W, the time was varied in order to vary the plasma treatment. Numerous ionised species are generated in the plasma, and etching is predominantly carried out by atomic oxygen.[2] After the treatment had finished the chamber was vented and the sample removed. The plasma cleaner used in this thesis is a Diener Zepto, which generates plasma using 40 kHz ratio radio frequencies.

3.5 Scanning Electron Microscopy (SEM)

Scanning electron microscopy (SEM) is a technique that scans electrons over the surface of the sample and uses the electrons collected from each point to build an image.[3] The contrast in the image relates to the topography of the sample or the constituent elements in the sample and SEM is therefore a useful technique for understanding the three-dimensional structure of materials which are too small to be resolved using the naked eye or light microscopy. In this case, a field-emission electron source was used, where an electric field close to a sharpened tip is used to produce electrons. This beam is then manipulated by electron lenses and scanning coils. Several interactions occur when the electron beam interacts with the sample,

for the formation of SEM images; the relevant processes are the generation of secondary electrons (SE) and backscattered electrons (BSE).

Secondary electrons are generated from the sample when the incident electron beam strikes the sample. These electrons have a much lower energy than electrons in the incident beam, and for this reasons SEs are more likely to reach the detector if emitted by parts of the sample that protrude from the surface. For this reason images generated using SEs give topographical information. BSEs are incident electrons which are deflected by the nuclei in the sample, for this reason heavier nuclei appear brighter in BSE images.

For this thesis, samples were imaged using a Hitachi S-4300 SEM with a field-emission electron source. Accelerating voltages of 3-10 kV were used. In this thesis, all SEM images displayed were formed through secondary electron detection.

3.6 Transmission Electron Microscopy (TEM)

Another type of electron microscopy used in this thesis is transmission electron microscopy (TEM). TEM utilises electrons which pass through the sample. Thick areas of the sample, or areas of the sample made of dense material, will decrease the number of electrons passing through the sample and will be seen as dark areas in a TEM image. Higher resolution TEM (HRTEM) makes use of phase-contrast imaging, where multiple electron beams interfere with each other, allowing atomic positions to be inferred.[3] This allows higher resolution images of the sample to be recorded. In addition, the use of aberration corrected (ACTEM) microscopes aides in the capture of higher resolution images.

TEM is an invaluable technique for the analysis of graphene materials and hybrid Pt/C materials and is heavily utilised in this thesis. The thickness contrast allows Pt nanocrystals

on carbon to be easily identified as areas of dark contrast, allowing the diameters of the particles to be easily measured. In some images the lattice spacing can be measured, which is possible for both Pt nanoparticles and for the interlayer spacing of graphene, the latter can be used as an indicator of graphene crystallinity.[4] Furthermore, the folds in graphene generate lines of contrast, which can be counted to ascertain the layer thickness of multi-layered graphene.[5]

In this thesis, TEM images were recorded using a JEOL JEM-2100, operated at accelerating voltages of 80 or 200 kV. ACTEM images were recorded by Dr Alex W. Robertson on a JEOL-2200 MCO operated at 80 kV.

3.7 TEM Sample Preparation

TEM requires very thin samples so that the density of electrons passing through is significant enough to form an image. For this purpose, the samples were placed on commercially available TEM grids, of which many types are available. For this thesis, most samples were spread on lacey carbon TEM grids, these have a copper grid structure with an amorphous carbon web spread over it to support the sample. When these grids were used, the sample of interest was placed in IPA and sonicated for ~15 minutes, before a few drops were placed on the lacey carbon TEM grid. For samples containing Pt, the sample was placed in a small volume of water before the IPA was added.

Some samples were prepared using folding TEM grids. These grids have a hinge which allows material to be placed on the grid and is then sandwiched by the grid to prevent sample movement. Due to the fact that most samples analysed in this thesis were in the form of powders, this type of grid is inappropriate in most cases. However these grids were used in

Chapter 4 to analyse graphene foams which had been treated with Pt precursor, both before and after they were annealing. These grids were used in Chapter 4 to produce Figures 10, 11, 12 and 13.

3.8 TEM Data Analysis

TEM data was analysed using the free computer program ImageJ. Lattice spacings in the image, such as the interlayer spacing of carbon materials and the spacing of Pt particles were measured using the "Plot Profile" functionality, the interlayer spacings were then averaged to calculate the values quoted in this thesis.

Nanocrystals were also measured using ImageJ. Most nanocrystals encountered in these experiments are of a spherical or oval shape, for this reason nanocrystals were measured by drawing an oval of approximately equal size to the crystal. The height and diameter of the oval was then averaged. Several hundred (usually >500) nanocrystals were measured per sample. This data was then used to produce nanoparticle size histograms.

3.9 Raman Spectroscopy

Raman spectroscopy is an invaluable technique for the characterisation of many different forms of carbon, and is applied in this thesis to the characterisation of graphene and graphene hybrid materials. Peaks in Raman spectroscopy occur due to the inelastic scattering of light, which is applied using a laser of specific wavelength. For graphene, Raman spectroscopy can provide several pieces of information from the relative peak heights.[6] Judgements about the defectiveness and layer number of graphene can be made from peak ratios observed.

Similarly, it is possible to study the crystallinity of carbon black materials in this manner. Peaks in the Raman spectra for these materials are discussed in more detail in subsequent chapters.

A Horiba Labram aramis Raman microscope equipped with a 532 nm laser was used to record spectra for this thesis. An 1800 mm^{-1} grating was used. At least 10 spectra were recorded for each sample. The OriginPro 2015 software was used for analysis of spectra. Baselines were subtracted and spectra were smoothed in the case of carbon black samples studied in Chapter 6 due to the poor signal-to-noise ratio obtained from these materials. Peaks of interest in the Raman spectra were fitted with Lorentzian functions.

3.10 Cyclic Voltammetry

Cyclic voltammetry (CV) is an electrochemical technique where the potential of a material of interest is cycled between two potentials (relative to a reference electrode) at a certain scan rate.[7] During the cycling, processes may occur on the electrode surface which result in the transfer of charge between the electrode and an appropriately chosen electrolyte, oxidation reactions occur in the positive scan and reduction occurs in the negative scan.

In this thesis, a three electrode system is used to carry out CV experiments. A glassy carbon electrode with a 3 mm diameter is used as the working electrode, on which an ink of the material of interest is deposited. An Ag/AgCl reference electrode is used which is filled with 3M NaCl electrolyte (separated from the acid electrolyte by a glass frit). The reference electrode has a fixed potential (~+0.227V) and is quoted with respect to a standard electrode, in this case relative to the reversible hydrogen electrode (RHE). The reference electrode allows the potentiostat to control the potential of the working electrode. To keep the potential

of the reference electrode stable, only a minute amount of current required for the measurement of potential difference must be passed. Therefore, to allow current to flow freely through the circuit, a counter electrode is required. For this thesis, a platinum wire counter electrode was used. 0.5M H_2SO_4 was used as the electrolyte and was prepared with DI water.

Cyclic voltammetry is often used to investigate Pt/C catalysts, because the peaks resulting from adsorption and desorption of H^+ are proportional to the platinum surface area. Knowing the platinum loading in the Pt/C catalyst and knowing the catalyst loading on the working electrode allows the electrochemically active surface area (ECSA) to be calculated. Cyclic voltammograms of Pt contain several features, as can be seen in Figure 2a, the relevant peaks which can be integrated to find the Pt area are seen in Figure 2b, where the blue boxes represent the integrated areas. In this thesis, only the hydrogen desorption region was used to determine ECSA.

In addition to allowing the ECSA to be obtained, the electrochemical cycling also degrades the Pt/C catalyst via the oxidation and reduction of platinum.[8] For this reason, repeated cycling is often carried out in order to evaluate the stability of the catalyst by comparing it to an industry catalyst. A certain number of cycles are run and the ECSA monitored with time, to track how the Pt surface area changes with cycle number and assess the durability.

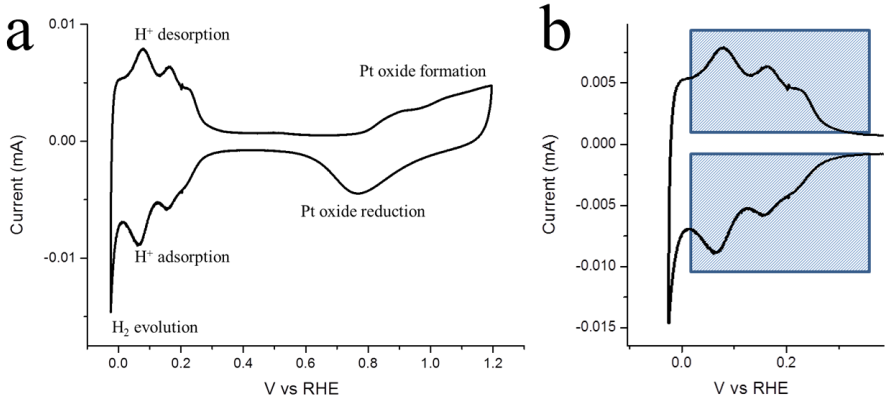

Figure 2. a) Cyclic voltammogram obtained from a Pt disc working electrode conducted in 0.5M H_2SO_4, the relevant peaks are labelled. b) Area of the cyclic voltammogram seen in a), the blue boxes show the relevant areas for the charge associated with hydrogen adsorption and desorption.

Preparing samples for cyclic voltammetry experiments is a multistep process. 7 mg of catalyst was mixed with 400 µL DI water, 1350 µL isopropyl alcohol and 250 µL of 5% Nafion in alcohol solution (Sigma-Aldrich). The mixture was then sonicated using a horn-tip sonicator for 30 minutes with 5 second pulses separated by rest periods of 5 seconds. For each CV measurement, 4 µL of the catalyst ink was pipetted onto a 3 mm glassy carbon electrode which had previously been polished. 0.5 M H_2SO_4 solution was used as the electrolyte in CV measurements, and was purged for 30 minutes with argon prior to measurements. CV measurements consisted of an activation step of 50 cycles between 0.05-1.2V vs RHE at 100 mV/s, before 1000 cycles at 40 mV/s between the same potentials. For this thesis, a Biologic VMP3 potentiostat and the EC-lab software were used to control the experiment and record the data.

In the analysis of CV data for Pt/C catalysts, the electrochemically active surface area (ECSA) was then calculated using the following formula.[3]

Eqn. 1
$$ECSA(m^2 g_{Pt}^{-1}) = \frac{Charge\ area\ (\mu C\ cm^{-2})}{[10 \times 210\ (\mu C\ cm^{-2}) \times Catalyst\ Loading\ (mg\ cm^{-2})]}$$

Where the ECSA is expressed in m^2g^{-1} Pt.

3.11 Brunauer-Emmett-Teller (BET) Surface Area Measurement

BET theory is a method for measuring the specific surface area of materials, where gas molecules adsorb on the surface of the material. Nitrogen is the most common adsorbent

used in BET experiments, and each nitrogen molecule covers an area of 16.2 Å^2.[3] An assumption in BET theory is that the molecules do not interact with each other and only one molecule can occupy a single site on the surface. The sample of interest is held at the boiling point of liquid nitrogen in a tube. Nitrogen gas is added and reaches equilibrium between adsorbed and free molecules. By measuring the equilibrium pressure, P, for different volumes of gas adsorbed, V, the surface area can be obtained through the following equation:

Eqn. 2

$$\frac{P}{V(P_0-P)} = \frac{1}{V_m C} + \frac{(C-1)}{V_m C}\frac{P}{P_0}$$

Where P_0 is the saturation pressure, V_m is the volume of gas molecules corresponding to a monolayer and C is a constant. The instrument plots $\frac{P}{V(P_0-P)}$ against $\frac{P}{P_0}$, which is a straight line for a range of P/P_0 values. V_m can be obtained from the slope and intercept of the graph. This calculation is performed automatically by the instrument, which gives a value of surface area in m^2g^{-1}.

To obtain accurate values of surface area for carbon materials, it is important to remove any unwanted contaminants from the surface of the sample, such as organic residue or adsorbed water. Contaminants can prevent N_2 from accessing the surface of the material and affect the result, and prevents the mass of the material from being determined accurately. For this reason, samples were placed in the BET tube (which had been weighed) and degassed in a nitrogen atmosphere at 230 °C overnight. The mass was then measured prior to the BET measurements. BET measurements were performed using a Micromeritics Gemini VI BET.

3.12 Thermogravimetric Analysis

Thermogravimetric analysis is a technique where the mass of a sample can be monitored as the sample is heated.[9] The technique can be controlled so that constant heating at a certain rate takes place, or so that a sample is held at a constant temperature. It is possible to use both these processes in a single experiment. The sample can be heated in different atmospheres, such as in air, oxygen, and nitrogen. In this case, the instrument consists of a balance with two arms, at the end of each arm sits a crucible, one crucible is empty and constitutes a blank sample, the other contains the sample.

It is possible to use TGA to determine study how the mass of a sample changes at different temperatures, which can be useful for understanding the thermal decomposition of materials. However, for this thesis, TGA was used in order to estimate the platinum content in Pt/C materials, and also residual nickel content, via heating in air. This simply requires the initial and final masses after heating, as the carbon is oxidised and removed in oxygen containing atmospheres. For nickel, the formation of NiO was taken into account when determining the percentage mass. TGA is regularly used for determining the metal content of carbon materials, and is frequently used for determining the Pt content in Pt/C catalysts.[10,11,12]

For the experiments conducted in this thesis, thermogravimetric analysis was carried out using a PerkinElmer Diamond TG/DTA, which has a 0.2 μg sensitivity. A small amount of sample (~10 mg) is loaded into an alumina crucible and placed into the furnace. A heating rate of 50 °C/minute was utilised with a maximum temperature of 850 °C, after this temperature had been reached it was held for 10 minutes. The furnace was then left to cool. The flow rate was 20 ml/min of air.

3.13 References

(1) Chen, Z. P.; Ren, W. C.; Gao, L. B.; Liu, B. L.; Pei, S. F.; Cheng, H. M. Three-dimensional flexible and conductive interconnected graphene networks grown by chemical vapour deposition. *Nat. Mater.*, **2011**, *10*, 424-428.

(2) You, H.-X.; Brown, N. M. D.; Al-Assadi, K. F. Radio-frequency (RF) plasma etching of graphite with oxygen: a scanning tunnelling microscope study. *Surf. Sci.*, **1993**, *284*, 263-272.

(3) Liao, S; Li, B; Li, Y. *Physical Characterisation of Electrocatalysts.* In *PEM fuel cell electrocatalysts and catalyst layers*; Zhang, J., Ed.; Springer: Berlin, 2008. pp 487-536.

(4) Samuels, T. O. M.; Robertson, A. W.; Kim, H.; Pasta, M.; Warner, J. H. Three dimensional hybrid multi-layered graphene-CNT catalyst supports via rapid thermal annealing of nickel acetate. *J. Mater. Chem. A*, **2017**, *5*, 10457-10469.

(5) Ferrari, A. C.; Meyer, J. C.; Scardaci, V.; Casiraghi, C.; Lazzeri, M.; Mauri, F.; Piscanec, S.; Jiang, D.; Novoselov, K. S.; Roth, S.; Geim, A. K., Raman spectrum of graphene and graphene layers. *Phys. Rev. Lett.*, **2006**, *97*, 187401.

(6) Ferrari, A. C.; Basko, D. M. Raman spectroscopy as a versatile tool for studying the properties of graphene. *Nat. Nanotechnol.*, **2013**, *8*, 235-246.

(7) Pletcher, D. *A First Course in Electrode Processes*. 2nd ed.; Royal Society of Chemistry: London, 2009.pp 187-189.

(8) Urchaga, P.; Kadyk, T.; Rinaldo, S. G.; Pistono, A. O.; Hu, J.; Lee, W.; Richards, C.; Eikerling, M. H.; Rice, C. A. Catalyst Degradation in Fuel Cell Electrodes: Accelerated Stress Tests and Model-based Analysis. *Electrochim. Acta*, **2015**, *176*, 1500-1510.

(9) Bottom, R. *Thermogravimetric Analysis*. In *Principles and Applications of Thermal Analysis*.; Blackwell Publishing: Oxford, 2008. pp 87-92.

(10) Wang, W.; Wang, Z.; Wang, J.; Zhong, C.-J.; Liu, C.-J. Highly Active and Stable Pt–Pd Alloy Catalysts Synthesized by Room-Temperature Electron Reduction for Oxygen Reduction Reaction. *Adv. Sci.*, **2017**, *4*, 1600486.

(11) Baturina, O. A.; Aubuchon, S. R.; Wynne, K. J. Thermal Stability in Air of Pt/C Catalysts and PEM Fuel Cell Catalyst Layers. *Chem. Mat.*, **2006**, *18*, 1498-1504.

(12) Chiang, Y.-C.; Liang, C.-C.; Chung, C.-P. Characterization of Platinum Nanoparticles Deposited on Functionalized Graphene Sheets. *Materials*, **2015**, *8*, 5318.

Chapter 4

Oxygen Plasma Treated CVD Graphene Foam as a Support for Pt Nanocrystals Produced by Thermal Annealing

4.1 Introduction

Hybrid materials combining a carbon support structure with an inorganic functional material are popular electrode materials for a several energy generation and storage applications. These include supercapacitors,[1] batteries,[2] and fuel cells.[3] In some cases high-quality and covalently bonded graphene electrode structures are desired for their high conductivity and surface area.[4] For this reason, the CVD synthesis of graphene foams using commercially available nickel foam as a template and catalyst is a popular starting point for the fabrication of these electrodes,[5] and has been applied as the carbon support in these applications.[6,7,8]

In considering the performance of these electrodes, the interaction between the active material and the carbon support is of great importance. In fuel cell electrodes for example, the interactions between Pt and the graphene support can determine the dispersion, size, and electrochemical and thermal durability of the Pt crystals, in turn influencing the active Pt surface area.[9] The interactions with the support, in addition to the nanocrystal size, can influence the electronic structure of the Pt nanocrystals.[10] This in turn can affect their activity for fuel cell relevant reactions.[11] For this reason it is desirable to be able to control the size and binding of Pt nanocrystals on carbon electrodes.

One way to do this is by modifying the surface with defects or functional groups to control dispersion and binding.[12] This has been explored for the solution based synthesis on reduced graphene oxide sheets, where graphene oxide was reduced to different degrees prior to Pt nanocrystal synthesis.[13,14] However, graphene oxide cannot be completely reduced to the quality of CVD graphene and many defects remain.[15]

We produced CVD graphene foam using a commercial nickel template, and characterised the foam using scanning electron microscopy (SEM), transmission electron microscopy (TEM) and Raman spectroscopy. The pristine surface was then modified with oxygen plasma in order to induce defects, and the effect of these treatments on the graphene foam structure was studied. We find that the plasma treatment creates holes in the graphene foam due to etching, and induces etch pits in the basal plane. We then explore the thermal annealing synthesis of Pt nanocrystals on the plasma treated graphene foams. We find that the large folds in graphene are detrimental to the even distribution of Pt over the surface. This persists even when oxygen plasma treatments are applied, though in certain well-distributed areas, the plasma treatments act to reduce the average Pt crystal size and eliminate the formation of undesirable large crystals, allowing a high proportion of sub-nanometre and nanometre sized Pt crystals to be formed. Lastly, the effect of the thermal annealing synthesis on the graphene support surface is explored using Raman spectroscopy.

4.2 CVD Synthesis of Graphene on Nickel Foam

A portion of nickel foam (MTI Corporation, 1.6 mm thickness) was rested on top of an alumina furnace crucible and inserted into a 1 inch diameter quartz tube in a horizontal tube furnace. A furnace system on rails was used so that the sample could be rapidly introduced

and removed from the hot zone. During the heat-up procedure, the system was flushed with argon, Ar (200 sccm), hydrogen, H_2 (25% in Ar, 100 sccm) and methane, CH_4 (20% in Ar, 20 sccm) whilst the furnace heated up at 50 °C/min to a temperature of 1000 °C. The CH_4 was turned off at around 600 °C. During this time, the nickel foam resided in the room temperature zone. Once the furnace had reached 1000 °C the nickel foam was introduced into the hot zone of the furnace, and was annealed for 30 minutes in Ar (200 sccm) and H_2 (25% in Ar, 100 sccm). CH_4 (20% in Ar, 7 sccm) was then introduced for a growth period of 15 minutes. Following this the CH_4 was turned off along with the furnace, and the sample was removed from the hot zone of the furnace. The sample was then removed once it had cooled to room temperature.

4.3 Formation of Pt Nanocrystals on Graphene Foams via Thermal Annealing

Unmodified and plasma treated graphene foams were dipped into 25 and 50 mM H_2PtCl_6 in EtOH solutions for 30 seconds each. Following this the foams were left on a PET slide and left to dry, they were then removed from the PET using another PET slide in a similar manner as in the retrieval of the foams following etching. The graphene foam with Pt precursor was then placed in the same furnace system used for the CVD synthesis of the graphene foam. The sample resided in the room temperature zone of the system during the furnace heating and cooling processes. The system was flushed with argon, Ar (200 sccm), hydrogen, H_2 (25% in Ar, 100 sccm) during heating. Once the desired temperature had been reached (400 or 800 °C) the foam was introduced into the hot zone of the furnace for the desired time (30 or 120 minutes). The sample was then removed from the hot zone of the furnace and was removed from the system upon reaching room temperature.

4.4 Results and Discussion

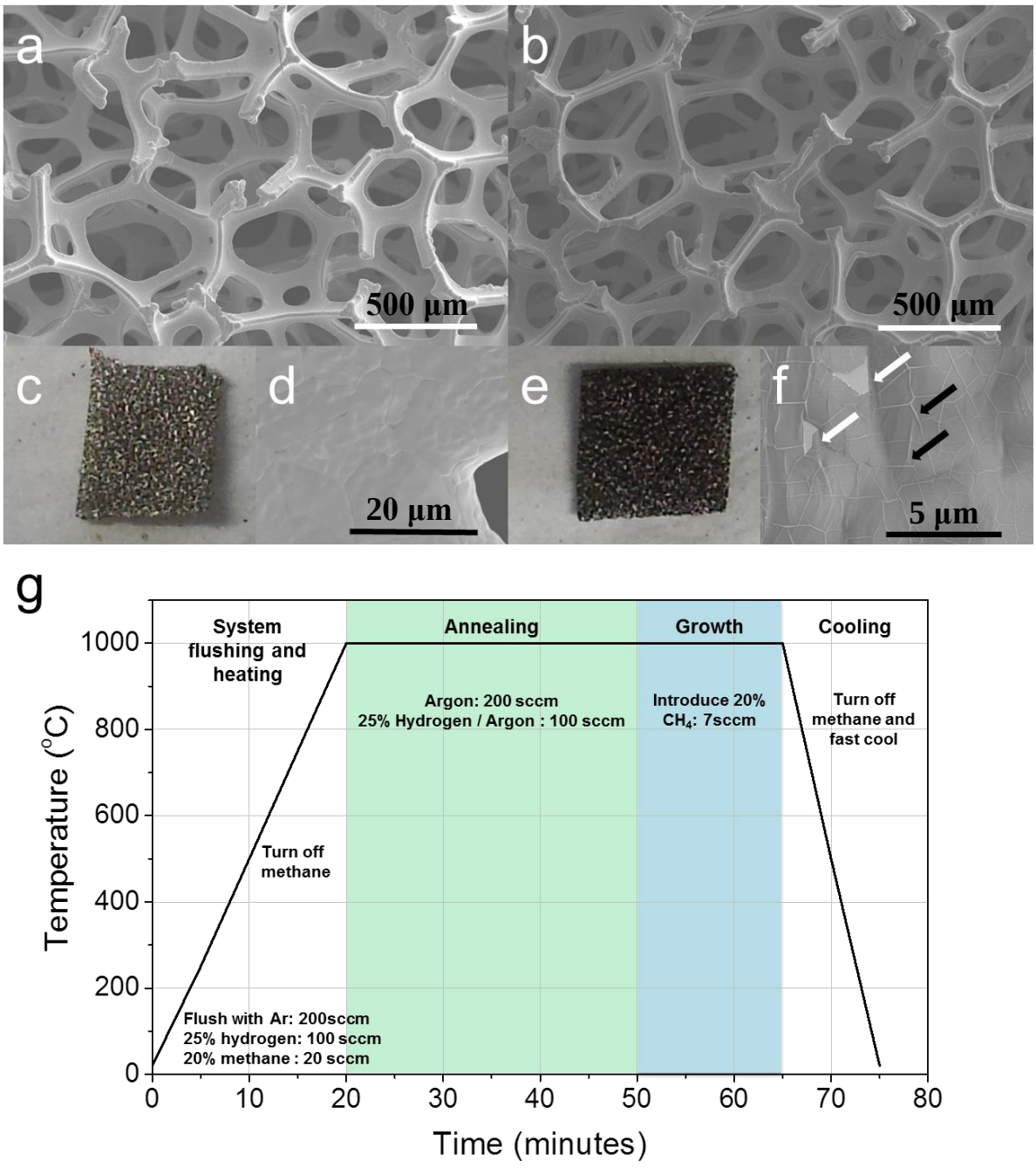

Figure 1. CVD synthesis of graphene on nickel foam. SEM images of nickel foam before (a) and after (b) graphene growth. c) Photograph of a 1 cm^2 piece of nickel foam and (d) SEM image of the nickel foam surface. (e) Photograph of a 1 cm^2 piece of nickel foam following graphene growth and (f) SEM image of the graphene on nickel foam, the white arrows indicate holes in the graphene with nickel underneath, and the black arrows indicate ripples in the graphene. g) Graph illustrating the CVD procedure. Scale bars: a,b) 500 µm d) 20 µm f) 5 µm

To produce the free-standing graphene foam, commercially available nickel foam was purchased, which acts simultaneously as the template and catalyst for the growth of graphene. This method was first used by Chen et al,[5] and is regularly used for the production of CVD quality, three-dimensional graphene foams.[7,16,17] A photograph of a1cm^2 piece of the nickel foam template can be seen in Figure 1c, and an SEM picture of the foam can be seen in Figure 1a. The CVD process was then used to grow graphene on the surface of the nickel foam, the procedure is shown graphically in Figure 1g and comprises a period of annealing, followed by graphene growth. In order to produce graphene foam with the thinnest walls possible (i.e. smallest number of layers), the amount of CH_4 introduced was increased in successive experiments until structurally stable graphene foam could be obtained following the acid etching process. A photograph of the nickel foam (Figure 1e) following the CVD process indicates an obvious change due to the graphene growth. Low magnification SEM images of the foam following CVD appear uniform, indicating coverage of the nickel by the graphene. Higher magnification SEM images of the surface (Figure 1f) show that the surface is covered with graphene, ripples in the graphene can be seen (indicated by black arrows) which are caused by the differences in the thermal expansion coefficients of graphene and nickel, small holes in the structure are also occasionally seen (white arrows).

As batches of graphene foam were desired for convenience, large pieces of nickel foam were used, which were then cut into pieces using scissors following growth. Raman characterisation of these long graphene foams pre-etching was carried out (Figure 2). In addition to gaining information about the thickness and defectiveness of the graphene produced by this method, the Raman characterisation also allows the uniformity of the graphene on the long nickel foams to be assessed. Figure 2a shows a photograph of one of the long foams following CVD graphene growth. The blue dots indicate areas which were sampled with Raman spectroscopy. These areas were chosen in order to study any variance

in the graphene due to position in the furnace, which is indicated by number; position 1 denotes the side of the foam closer to the inlet of the tube furnace, whilst position 4 indicates the centre of the furnace. The positions chosen for Raman measurements also allow any differences in the graphene at the centre and edge of the foam to be assessed, as well as any differences between the graphene growth on the top and bottom of the foam.

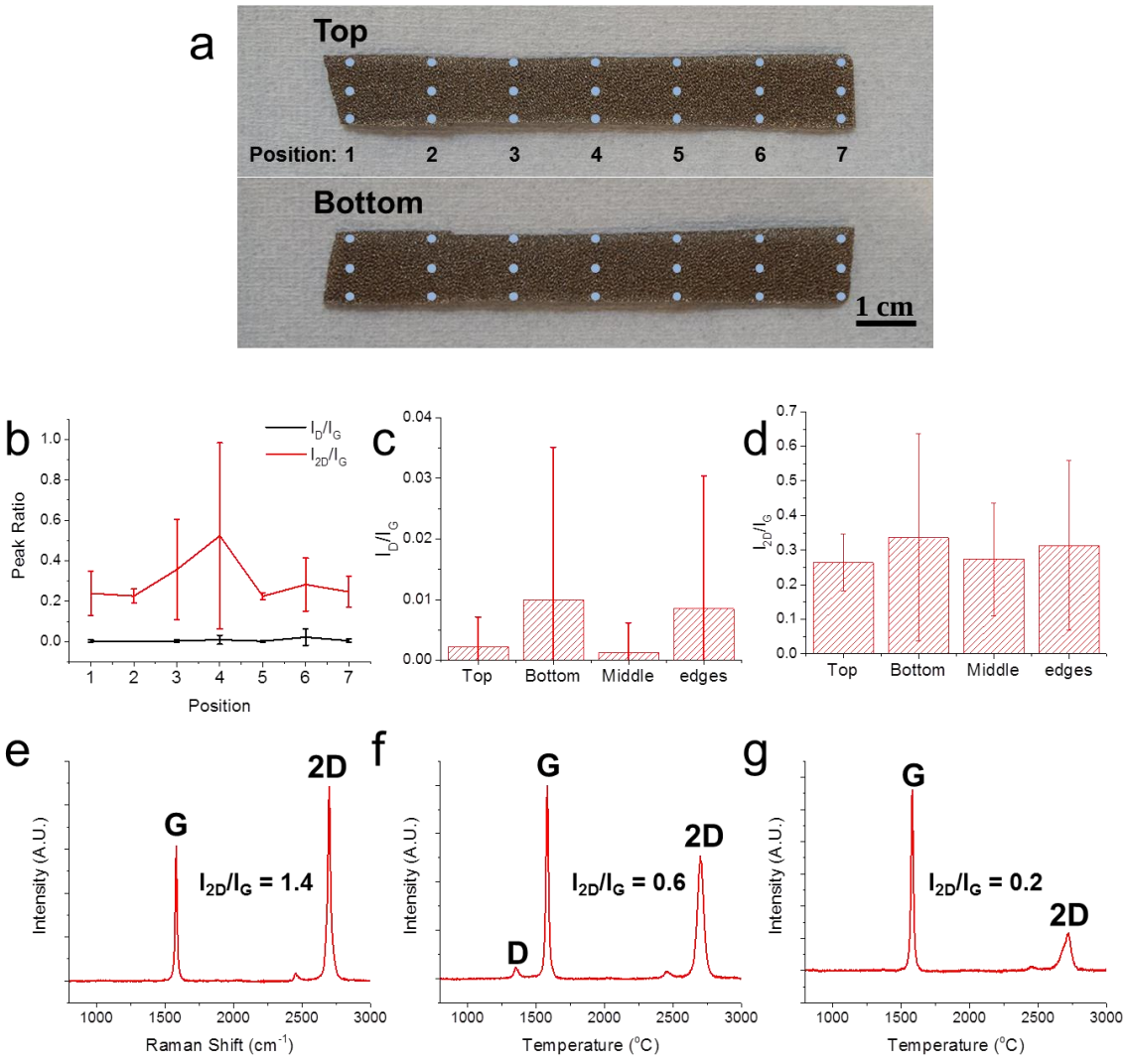

Figure 2. Production and Raman characterisation of large pieces of CVD graphene foam on nickel. a) Image of long graphene foam pre-etching, each blue spot corresponds to a location where Raman spectra were recorded. b) Raman D/G and 2D/G ratios as a function of the positions indicated in (a). Position dependant (c) D/G and (d) 2D/G Raman peak ratios. (e) Raman spectrum indicating the presence of bilayer graphene. (f) Raman spectrum

with D peak indicating the presence of defects. The 2D/G ratio indicates graphene with fewer than 5 layers (g) Raman spectrum indicating graphene with a thickness of >5 layers. Scale bar: (a) 1 cm

Figure 2b shows a graph of how the D/G and 2D/G peak ratios vary with position. It can be seen that the D/G peak ratios, indicated by the black line, are very low and fairly consistent, this is due to the fact that only a small proportion (9/42) of the acquired spectra contain a D peak. As the appearance of the D peak is caused by defects,[18] this indicates that the quality of the graphene grown by the CVD process is high. The red line represents the 2D/G peak ratio, which can be used to judge the thickness of the graphene produced. A high 2D/G ratio indicates thinner graphene, with a ratio >1 being indicative of monolayer or bilayer graphene.[19] Graphene produced on nickel is generally multi-layered due to the CVD growth mechanism, where carbon dissolves in the nickel and precipitates upon cooling.[20] The 2D peak ratio decreases with increasing layer number, and becomes indistinguishable from graphite for thicknesses 5 layers or above.[18] It can be seen from the 2D/G peak ratios that all values are within error of each other, indicating a fairly uniform thickness independent of position. Comparing the D/G peak ratio for the top/bottom and middle/edges of the sample indicates that a higher D peak is observed for spectra recorded from the bottom and edges of the graphene foam, though this is due to the appearance of the D peak in only a couple of spectra from these regions. Most of the spectra for these regions have no noticeable D peak. The average D/G peak ratio is 0.006 with a standard deviation of 0.018. This indicates the formation of high quality graphene. A higher 2D/G peak ratio is also seen for spectra taken from the edges and bottom of the foam.

Figures 2e-f show some example Raman spectra with different 2D/G ratios. Figure 2e shows a spectra where the 2D/G ratio is greater than 1, this spectra is probably indicative of bilayer graphene, as monolayer graphene spectra exhibit 2D/G peak ratios much greater than that shown here. This is far above the average 2D/G peak ratios obtained from the graphene foam

spectra, which is 0.3 with a standard deviation of 0.2. Figure 2f shows a spectrum with a lower 2D/G peak ratio, which is most likely from graphene with a thickness of 3-5 layers; this spectrum is also an example of one containing a D peak. Finally, figure 2g shows a spectrum with a low 2D/G peak ratio, one of the lowest values obtained. Spectra such as these have a similar appearance and 2D peak line shape to that of graphite, and typically correspond to areas graphene 5 layers or thicker.[18]

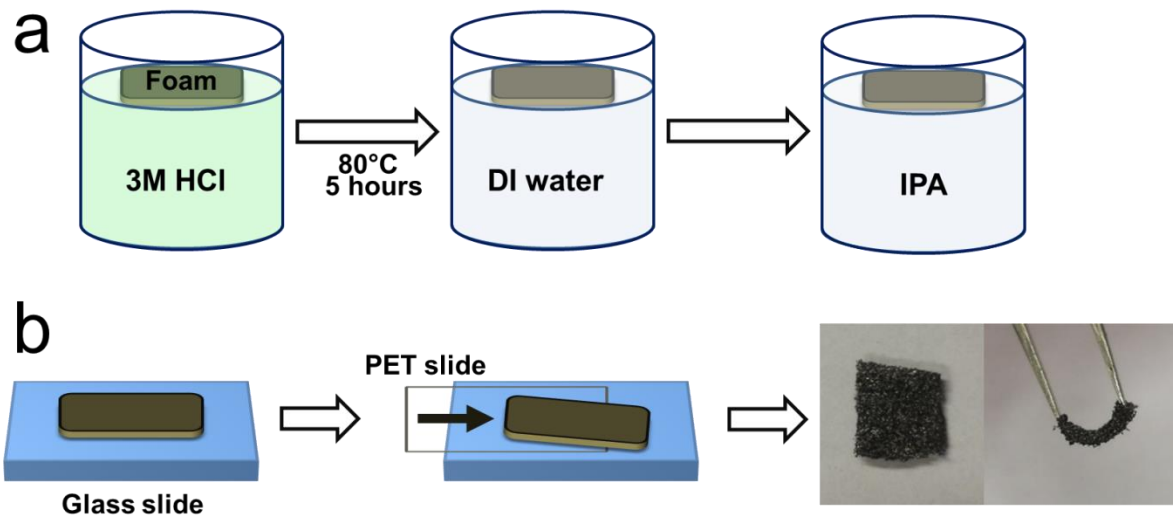

Figure 3. a) Schematic diagram showing the wet etching of the nickel foam to form graphene foam. The nickel is etched in HCl before repeated washing using DI water and finally IPA. (b) Schematic diagram showing the retrieval of the free-standing graphene foam. The graphene foam is collected from IPA on a glass slide, following drying, a PET slide is used to detach the graphene foam from the glass slide. Two photographs of a 1 cm^2 piece of free-standing graphene foam are shown.

Following the characterisation of the graphene grown on nickel foam, an etching method was used in order to remove nickel to produce free-standing graphene foam. A schematic diagram showing this process and the subsequent steps to obtain the free-standing product is shown in Figure 3. Acid etching was carried out for several hours at high temperature, and the acid was changed in order to ensure that nickel had been completely removed. The D/G

and 2D/G ratios for the foams produced before and after etching were similar, indicating that the HCl etching caused little damage to the graphene foam. Glass slides were used in order to transfer the fragile graphene foam between beakers. Following washing with DI and water, the graphene foam was left to dry on a glass slide. A method utilising a PET slide was then used to separate the graphene foam from the glass slide following drying overnight (Figure 3b). This step is not mentioned in the original publication for the synthesis of graphene foam , but was used in the original study and is necessary to obtain an intact, free-standing graphene foam.[21] In the original report, PMMA was coated on the graphene/nickel foam after CVD, which was then removed using acetone following acid etching of nickel.[5] This was not used in our study in order to minimise polymer residue on the graphene surface, though may have allowed graphene foams with lower average layer numbers to be obtained. Photographs of a 1 cm^2 piece of graphene foam are shown following retrieval of the foam from the PET slide, demonstrating that the foam is free-standing.

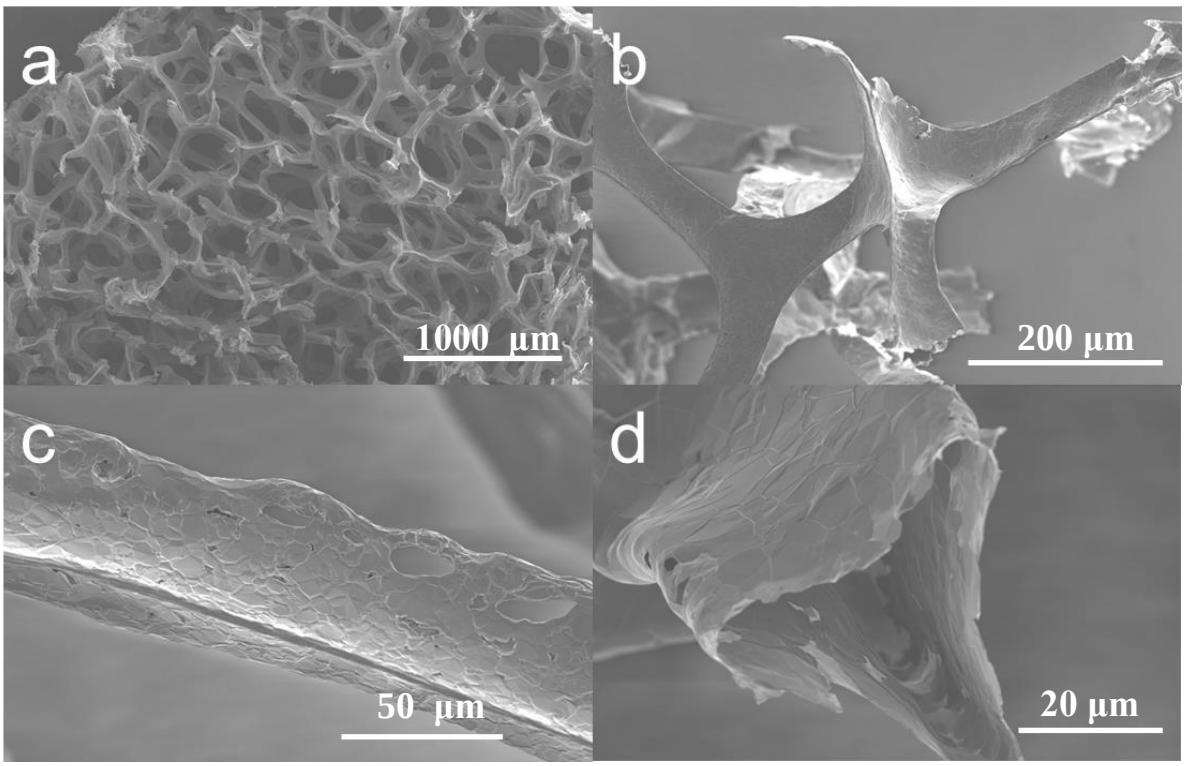

Figure 4. SEM characterisation of free-standing graphene foam. a) Low magnification image of the graphene foam. b) Edge of the graphene foam. c) Individual "arm" in the graphene foam showing holes. d) Image showing the hollow nature of the graphene foam. Scale bars: a) 1000 μm b) 200 μm c) 50 μm d) 20 μm

Figure 4 shows SEM images of the free-standing graphene foam, the low magnification image of the foam seen in Figure 4a shows that the foam has a similar morphology to the original nickel foam template seen in Figure 1, and a higher magnification image is seen in Figure 4b. Figure 4c shows an individual "arm" of the graphene foam, which has several holes in the surface, it can also be seen that the creases in the graphene remain. The hollow nature of the foam is seen at a higher magnification in Figure 4d.

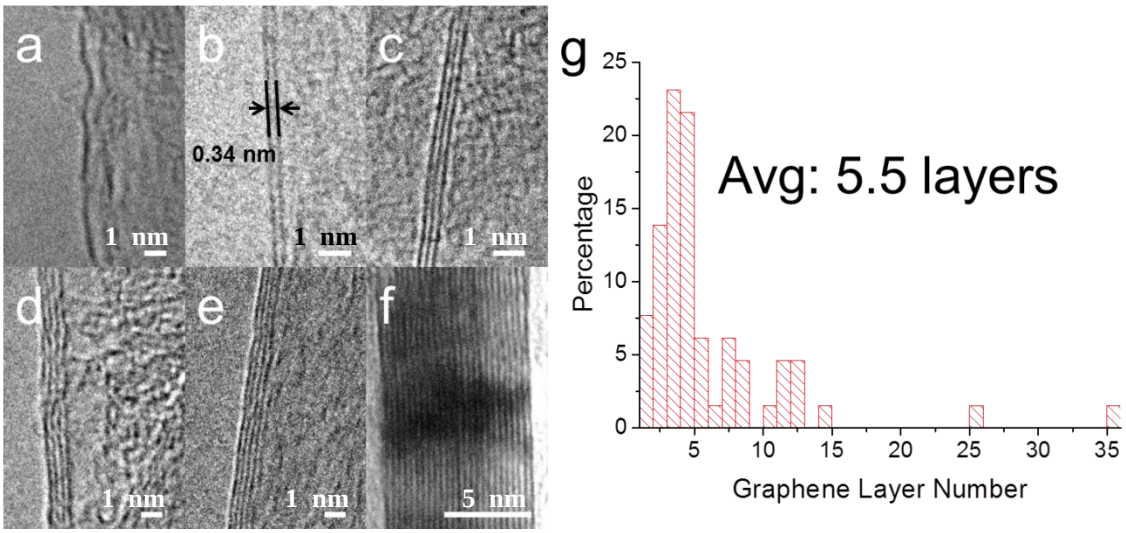

Figure 5. TEM characterisation of graphene foam. TEM images of folds in graphene foam showing regions of (a) monolayer (b) bilayer (c) trilayer (d) four layer. (5) five layer and (f) >10 layer graphene. The interlayer spacing of graphene is indicated in (b). (g) Histogram showing the distribution of layer number determined using folds seen in TEM images. Scale bars: a-e) 1 nm f) 5 nm

TEM was also used to characterise the etched graphene foam, which allows a better understanding of the layer thickness. Figure 5a-f show images of folds in the graphene foam, the lines of contrast observed can be used to obtain the layer number.[18] Images showing

graphene layers of increasing thickness can be seen. A layer number histogram is shown in Figure 5g. The majority of the graphene foam comprises multi-layered graphene less than 5 layers thick, though folds between 5-10 layers are regularly observed. Occasionally, very thick regions are observed, with the thickest region observed in this sample comprising 35 graphene layers. Graphene grown on nickel has been shown to be non-uniform with regards to layer number.[22] From the different methods used to characterise the graphene foam, it is clear that the CVD process produces a high quality, rippled 3D graphene structure with occasional holes, with morphology templated by the nickel template and an average thickness of 5-6 layers.

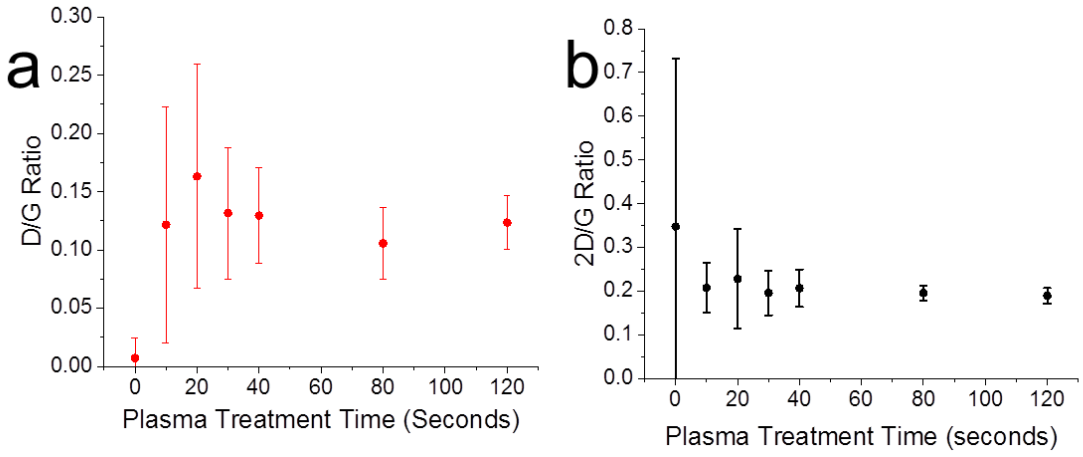

Figure 6. Raman characterisation of plasma treated graphene foam. (a) D/G and (b) 2D/G Raman peak ratios for different plasma treatment times.

In order to investigate the effect of plasma induced defects on the thermal synthesis of Pt nanocrystals, the graphene foams were subjected to oxygen plasma treatments for different periods of time, which is intended to introduce defects. Numerous studies have been carried out concerning the effect of oxygen plasma on monolayer,[23,24] bilayer,[25,26] and multilayer graphene,[27,28] as well as highly oriented pyrolytic graphite (HOPG).[29,30] The plasma treatments have been attributed with both the functionalisation and the etching of these

materials. Functionalisation of graphitic surfaces by oxygen plasma takes place in the form of epoxide groups, which decorate the basal plane.[31,32] Other oxygen-containing functional groups are also induced, which include carbonyl, hydroxyl, and occasionally carboxyl in varying proportions.[26] Some studies find that hydroxyl is the most frequent functional group after epoxide,[23,25,33] whilst others observe higher populations of carbonyl groups.[29,34] In either case, both these groups are observed both on the basal plane and the edges of graphene, but have higher proportions at the edges. There is some evidence to suggest that the carbonyl groups can only form on the basal plane after vacancy defects have already been induced. It was observed in one study that the XPS signal for the carbonyl group only appeared on the basal plane following oxygen plasma treatment if point defects had been already been induced via an argon plasma treatment.[35]

The etching of graphene is also observed in oxygen plasma treatments. This is due to the removal of carbon as CO or CO_2.[29] Short plasma treatment times have been utilised to selectively produce only monovacancy defects.[36] Further removal of carbon atoms results in 5-7 rings,[23] multivacancies, and pits.[37] This removal of carbon atoms results in etching of the graphene layers, which proceeds both at the basal plane and also from the edges at a faster rate. The inner graphene layers which do not have exposed surfaces remain unchanged by these treatments.[29]

It is observed from previous studies that the active species generated in the plasma affect only the outermost graphene layers with exposed surfaces.[29] This is supported by the observation of hillocks seen in microscopy images of the plasma treated foams (Figures 7 and 8). Hillock like structures would only be expected if holes in the topmost layer had to be created before the layer below could be etched. The TEM images shown in Figure 8 and discussed in more detail later show these hillock structures, indicating that in some instances the plasma affects the multilayer graphene to a depth of at least 16 layers due to holes formed in the upper layers

leading to exposed surfaces in the lower layers which are affected by the plasma. However, the number of layers which are completely etched away by the plasma treatment is unknown, and could not be revealed through layer number histograms recorded following plasma treatment (Figure 8i). The use of a system where better control over graphene layer number could be obtained where the layer thickness was homogenous over the whole structure would allow a much better understanding of the effect of the plasma on layer number.

Because of the variety of Raman active defects generated by oxygen plasma treatment, Raman spectroscopy was used to characterise the plasma treated graphene foams. Figure 6 shows the Raman characterisation of graphene foams subjected to oxygen plasma treatments of different durations (where plasma treatment time = 0 represents the untreated graphene foam). Figure 6a shows the D/G peak ratios, it can be seen that the ratio increases and reaches a maximum at 20 seconds of plasma treatment, before decreasing slightly and remaining constant even after 120 seconds. Longer treatment times were also used, though these resulted in the visual destruction of the graphene foam within the plasma chamber. Figure 6b shows how the 2D/G peak ratio changes with plasma treatment time. The 2D/G peak ratio decreases and stays constant even for very short treatment times. These observations are similar to Raman spectra seen for plasma treated HOPG, [29] and are consistent with the etching mechanisms described above. Initially, the plasma induces oxygen defects and creates vacancies and holes in the topmost layer of graphene, resulting in a growing D peak. In the case of monolayer graphene, this D peak continues to increase in size and becomes much larger than the G peak, meanwhile the 2D peak decreases causing a decrease of the 2D/G ratio.[26] However, Raman spectroscopy is not completely surface sensitive, and the Raman signal is influenced by the pristine subsurface layers.[38] The information depth for even the best confocal set ups is a minimum of 500 nm.[39] These results suggest that the D/G ratio reaches a stable value for sufficiently thick graphene, where

surface layers are slowly etched away and newly exposed surfaces begin to be modified by the plasma, but subsurface layers with a very small D peak significantly influence the spectra. The reason for the initial increase of D/G ratio could be due to increasing functionalisation and creation of defects in the top most graphene layer, as this functionalisation increases, the D/G peak ratio will increase. However, increased functionalisation will damage the graphene lattice to the point where the signals from the layer decrease in intensity relative to layers below.

The error bars associated with the D/G and 2D/G values are large for short plasma treatment times, but small for longer treatment times. The reason for this may be due to inhomogeneity of the plasma treatment over different parts of the surface. This inhomogeneity is suggested by TEM results in Figure 8 and is discussed later. During the initial period of the plasma treatment, where there is an increase then decrease in the D/G peak ratio, and a rapid decrease in 2D/G ratio it could be expected that any inhomogeneity in the treatment would lead to a large error bar. However at longer treatment times, when both D/G and 2D/G ratios have reached stable values, any inhomogeneity will result only in small differences in the ratios, hence smaller error bars relative to short treatment times.

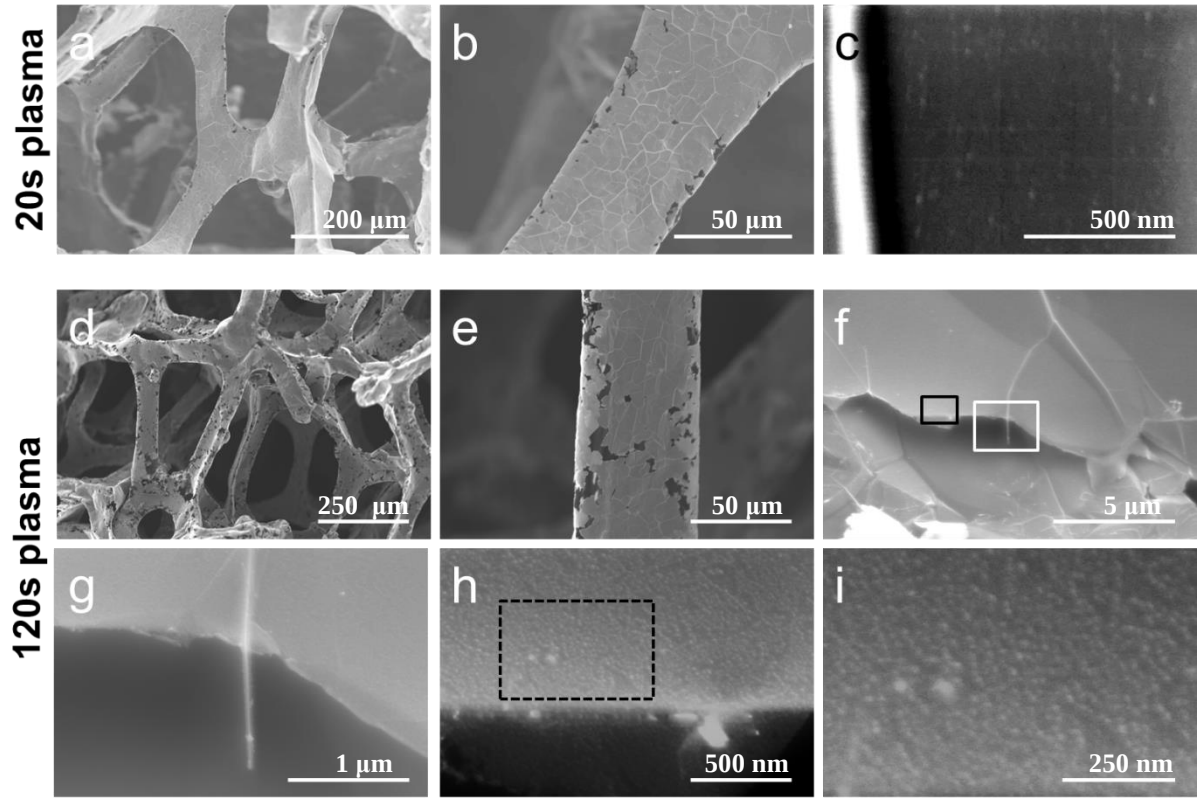

Figure 7. SEM characterisation of plasma treated graphene foams. (a-c) SEM images of 20s plasma treated graphene foam. (d-f) SEM images of 120s plasma treated graphene foam. (g) Region indicated by the white square in (f), showing the effects of plasma etching on the graphene foam edge. (h) Region indicated by the black square in (f), showing the surface of the plasma treated graphene foam. (i) Region indicated by the dotted square in (h), showing a close-up of the plasma treated foam surface. Scale bars: a) 200 µm b) 50 µm c) 500 nm d) 250 µm e) 50 µm f) 5 µm g) 1 µm h) 500 nm i) 250 nm

Electron microscopy was used to further characterise the plasma treated foams. Two plasma treatment times, 20 and 120 seconds, were chosen. SEM images of these foams can be seen in Figure 7. SEM images of 20s plasma treated foam (Figure 7a,b) appear similar to those of the unmodified graphene foam seen in Figure 4, some holes can be seen in Figure 7b, though these are no more frequent than the holes seen in the unmodified foam, such as those that can be seen in Figure 4c. A higher magnification image reveals bright dots which are fairly

uniform in size and are evenly distributed over the surface, though it is not clear as to the nature of these dots from this image. A longer plasma treatment of 120 seconds results in a more drastic change to the structure of the graphene foam. Low magnification SEM images (Figure 7d and e) show more holes compared to the unmodified and 20s plasma treatments. A region at the edge of a hole in the graphene foam is shown in Figure 7f; a fold in the graphene foam that runs to the edge of the hole can be seen. A magnified image of this area seen in Figure 7g reveals that the fold continues off the edge of the hole as a ribbon, this is indicative of the plasma etching of the graphene foam discussed earlier, the folds are twice as thick as the flat regions either side and therefore take longer to etch away. Etching at the basal plane has been shown to be much slower than etching at the edges,[29] but the presence of the graphene ribbons shows how the basal etching can play a role in determining the resultant morphology, despite the differences between these two rates. These ribbons were observed in several regions of the sample. We also turn our attention to the surface of the graphene foam, which can be seen in Figure 7h and I, a high density of what appear to be raised hillocks on the surface of the graphene foam can be seen. These hillocks are presumably the same type of feature seen in Figure 7c. The generation of features such as these has been observed on plasma-treated HOPG surfaces, and have been seen in studies which used higher powers or longer times and has been attributed to the combination of the previously described chemical etching (where oxygen reacts with the graphene surface) and physical etching, where high energy ions cause damage through collisions with the surface.[30]

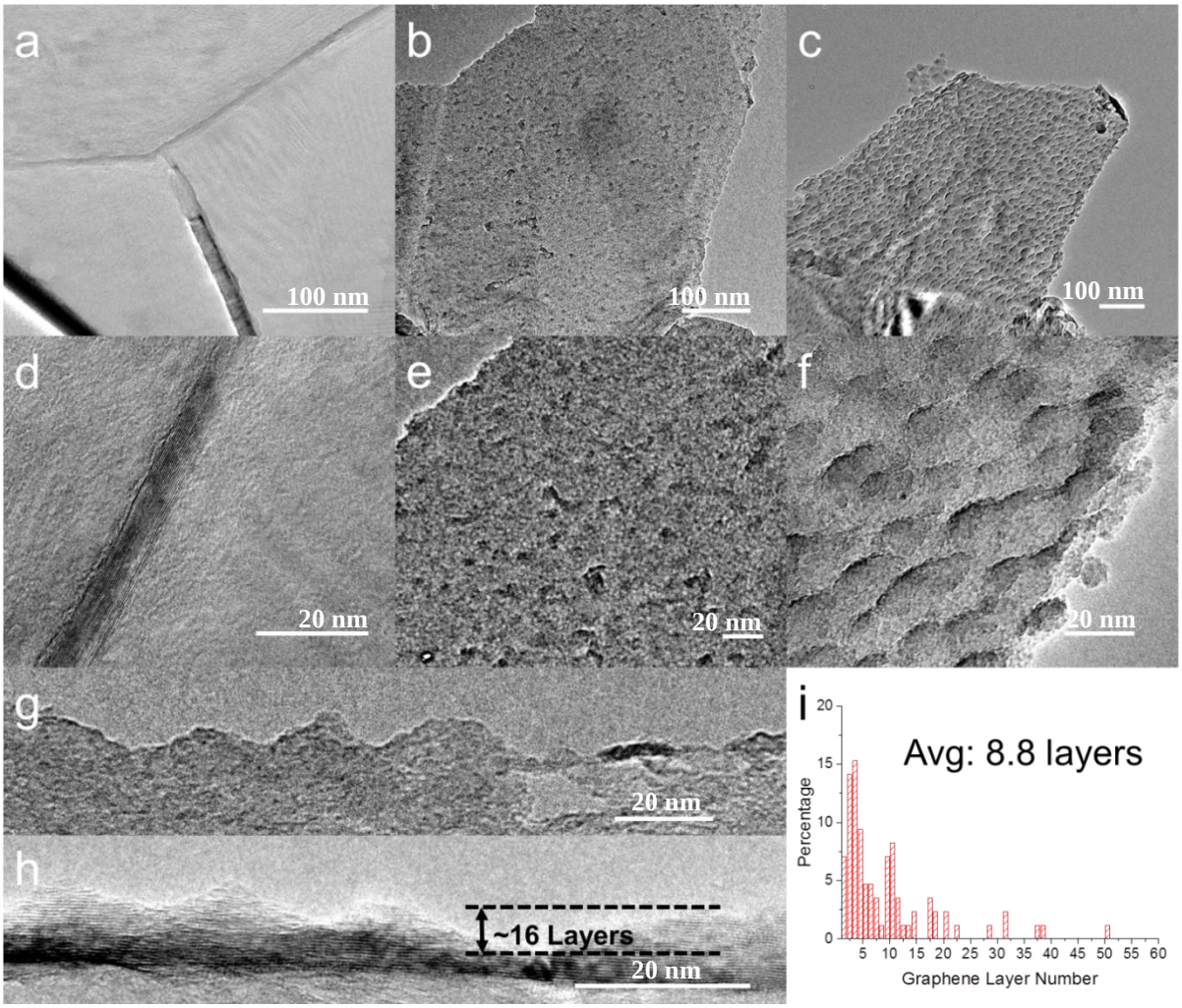

Figure 8. TEM characterisation of 120s plasma treated graphene foam. (a-c) Low magnification TEM images showing the surface regions of the plasma treated graphene foam with different degrees of modification. (d-f) Medium magnification images showing the same regions as seen in (a-c). (g) Image of the etched edge of the graphene foam. (h) A fold in the graphene foam showing the effects of plasma etching. (i) Histogram showing the distribution of graphene thicknesses determined from TEM images. Scale bars: a) 100 nm b) 100 nm c) 100 nm d) 20 nm e) 20 nm f) 20 nm g) 20 nm h) 20 nm

Finally we turn to TEM to characterise the graphene foams treated with 120s plasma. Figure 8a-c show low magnification images of the surface, and corresponding medium magnification images of the same areas are shown in Figure 8d-f. The areas seen in Figure 8a and d show no obvious sign of modification by the plasma treatment, whilst Figure 8b,c,e

and f appear significantly different from the surfaces seen in TEM images of the untreated plasma foam. The surface seen in Figure 8c and f appears to be the most heavily modified by the plasma treatment. The bump-like features seen in 8f have a similar size to those seen in the SEM image in Figure 7i. The fact that surfaces with different degrees of plasma modification are seen indicates an uneven etching of the graphene foam surface; this could possibly be due to poor mass transfer or a low mean free path of the plasma species throughout the porous graphene foam. An image of the jagged edge of an area of the plasma treated foam are seen in Figure 8g, and show further evidence for the etching of the graphene foam from the edges. A fold in the graphene foam was also observed (Figure 8h), which showed a similar etched appearance to the edge, this is most likely the same type of hillocks featured in Figure 8f, it can be seen that the height of these hillocks are over 10 layers thick or 3.4 nm, this is similar to heights of some of the hillocks previously produced on HOPG. It should be noted that not all of the folds seen had the same etched morphology as the one in figure 8h, a fold with a similar appearance to those seen in Figure 5 can be seen in Figure 8d, further evidence for the uneven plasma etching. In order to ascertain whether the plasma etching of the basal plane has an effect on the overall thickness of the graphene foam, folds in the graphene foam were observed in order to produce a layer number distribution graph, figure 8i. While the average layer number has increased from the value seen for the unmodified sample (Figure 5), the distribution of layers is similar in the two samples. Mono-, bi-, and tri-layered graphene are still seen in significant populations, it might be expected that these areas might have been etched away. This shows that while basal etching does occur as seen in Figure 7g, many thin regions still exist in the sample, most likely due to the uneven etching. Despite the fact that TEM results indicate that these thin regions of graphene foam are still present after 120s plasma treatment, Raman spectra with high 2D/G ratios are not encountered. This suggests that these thin regions have been modified by the treatment

(resulting in a decrease in the 2D/G ratio). Another possibility is that these thin regions have been reduced in lateral size via edge and basal etching, so that any Raman spectra recorded from these thin regions includes the contribution from adjacent, thicker portions of the graphene foam.

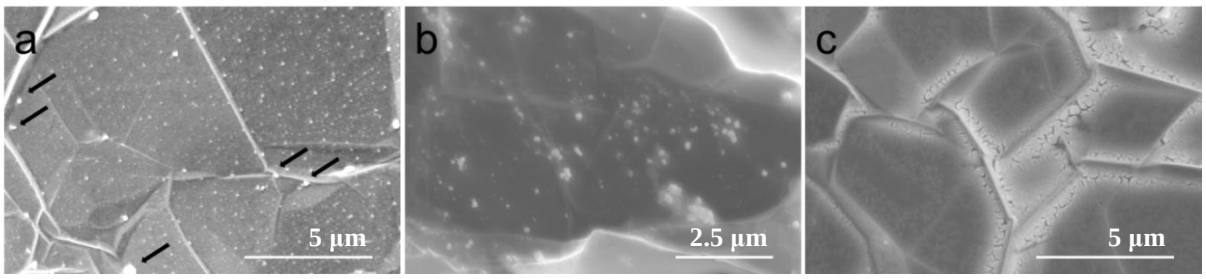

Figure 9. SEM images of Pt precursor on graphene foam. (a) SEM image showing an area of well distributed precursor, the black arrows indicate larger particles of precursor residing at the folds of the graphene foam, the folds themselves are indicated by the bright lines. (b) Region showing large aggregates of precursor particles. (c) Region showing the build-up of precursor at the folds in graphene foam when the precursor concentration was increased to 50 mM. Scale bars: a) 5 µm b) 2.5 µm c) 5 µm

In order to produce Pt nanocrystals on the graphene foams, the foams were dipped in a H_2PtCl_6 solution, which can be converted into Pt nanocrystals upon reduction in H_2 at high temperatures.[40] Figure 9 shows SEM images of the Pt precursor on the unmodified graphene foam surface, similar results were found for the 20s and 120s plasma treated samples. Figure 9a shows an area of graphene foam where the Pt precursor is well distributed, areas such as this are frequently seen in all samples. Small particles of precursor are observed over the surface, they are surrounded by areas of bright contrast, indicating that smaller particles of precursor which cannot be resolved using SEM are likely also present. Black arrows in the image indicate larger particles of Pt precursor, it should be noted that these particles all reside at a fold in the graphene foam. This shows how the ripples in the graphene may be detrimental for the even distribution of precursor on the graphene surface. Occasionally,

larger aggregates of particles are seen, such as in Figure 9b. Finally, Figure 9c shows the precursor distribution after the concentration was doubled from 25 to 50 mM, here the effect of the folds on the precursor distribution is clearer; much of the precursor has concentrated at the folds in the graphene foam. In the centre of the image, an area of bright contrast can be seen, where the close proximity of folds in the graphene foam has caused the precursor to become highly concentrated over a small portion of the surface. This uneven distribution of precursor on the surface due to folds may result in uneven distribution of Pt particles following annealing, and highlights a weakness of using these rippled foams as substrates for the thermal synthesis of nanoparticles.

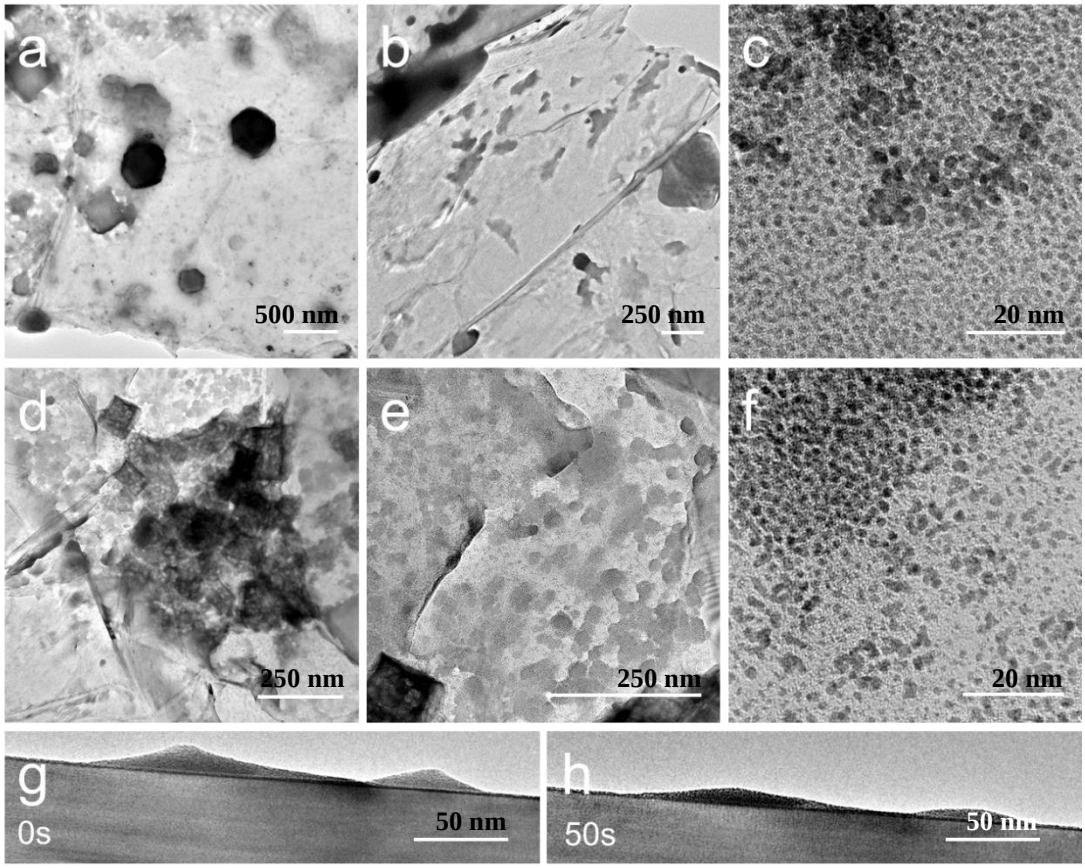

Figure 10. TEM images of precursor on plasma treated graphene foams. Images showing (a) aggregates of precursor, (b) well distributed precursor and (c) high magnification image of the region in (b) for 25 mM Pt precursor on unmodified graphene foam. Images showing (d) aggregates of precursor, (e) well distributed precursor and (f) high magnification image of the region in (e) for 25 mM Pt precursor on 120s plasma treated

foam. Images showing the effect of electron irradiation of the Pt precursor on unmodified graphene foam, (g) shows the precursor initially and (h) shows the same region after 50 seconds of electron irradiation. Scale bars: a) 500 nm b) 250 nm c) 20 nm d) 250 nm e) 250 nm f) 20 nm g) 50 nm h) 50 nm

The distribution of the precursor on unmodified and 120s plasma treated foams was also examined using TEM (Figure 10). Figure 10a and d show images of some of the large particles which are seen in the SEM images, for the unmodified and 120s plasma treated foams respectively. Figure 10b and e show the regions free of large particles, which have darker areas which are presumably also aggregates of precursor and represent some of the bright areas around the particles seen in Figure 9a. There is no noticeable difference in the appearance of either the large particles or the smaller precursor aggregates between the two foam samples. A closer look was taken at the boundaries between the dark aggregates and the lighter areas; these are shown in Figure 10c and f. Small particles can be seen in both images, the density of the particles is higher in the darker regions, but the whole surface of the graphene foam was observed to be covered with these particles. A factor to consider is that the precursor will rapidly be reduced by the electron beam to form Pt particles, so it is likely that these particles do not exist prior to examination of the surface using TEM. This effect has been previously used to rapidly synthesise cobalt nanocrystals of different sizes in-situ in the TEM.[41] It cannot be stated with certainty whether the entirety of the surface of the graphene foams is covered by the precursor, or if the electron beam reduction causes Pt species to spread across the surface as has been seen in the aforementioned Co nanocrystal study. To demonstrate that the Pt precursor is not already completely reduced prior to TEM imaging, some precursor was observed on the edge of a fold in the graphene foam (Figure 10g) and was continually imaged for 50 seconds. After this period of time, the size of the mound of precursor had noticeably decreased, and has become darker, consistent with the reduction of the precursor and the formation of a metallic Pt phase which is denser than the

amorphous precursor. These results show that the Pt precursor is not already reduced (at least not fully) upon drying on the graphene foam surface, and that the majority of the surface is covered by precursor for both samples.

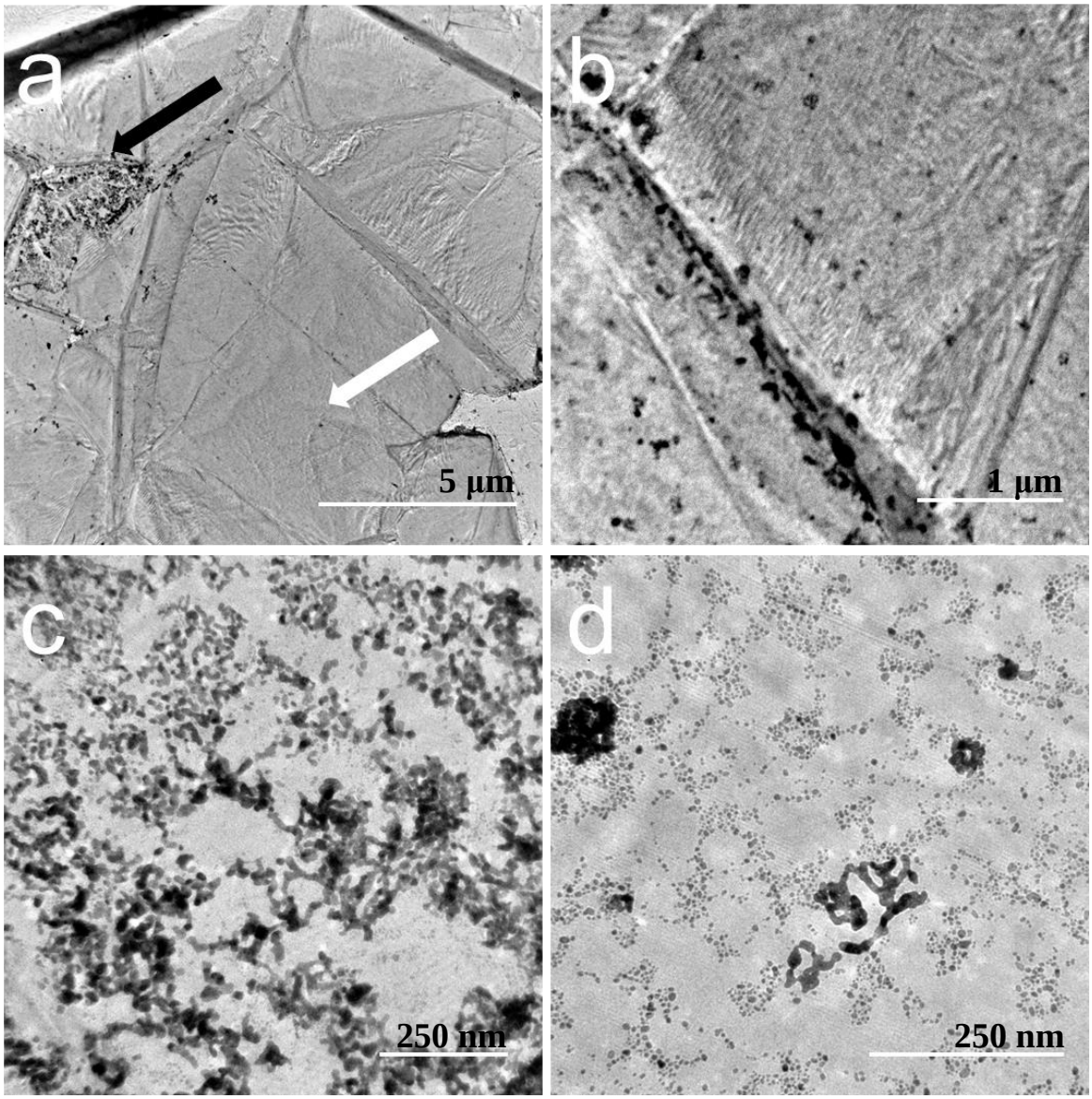

Figure 11. TEM images showing the distribution of Pt particles over the surface of unmodified graphene foam following heat treatment at 400 °C for 2 hours with 25 mM Pt precursor. (a) Low magnification TEM image showing uneven distribution of Pt over the graphene foam surface. The black arrow indicates a region containing large Pt aggregates. The white arrow indicates a region where the majority of Pt crystals are several nanometres in size (b) Image showing large particles at a fold in the graphene foam. (c) Medium magnification

TEM image of the area highlighted by the black arrow in (a). (d) Medium magnification TEM image of the area highlighted by the white arrow in (a). Scale bars: a) 5 μm b) 1 μm c) 250 nm d) 250 nm

The graphene foam samples dipped in Pt precursor were then annealed under different conditions in order to study the effect of the plasma treatments on the dispersion and size of the nanocrystals produced. HRTEM images of nanocrystals produced by this method can be seen in Chapter 5. Unmodified, 20s plasma treated, and 120s plasma treated samples were dipped in 25 mM Pt precursor were annealed at times of 30 and 120 minutes at 400 and 800 °C. From low magnification TEM images of the untreated foam treated with 25 mM Pt at 400 °C for 2 hours (Figure 11), it is obvious that the Pt crystal growth is not completely homogeneous, with the black area denoting an area containing undesirable large particles. The white arrow denotes an area which appears empty at this magnification. Figure 11b shows another low magnification image, where a fold in the graphene foam runs from the top left to the bottom middle of the image, it can be seen that the fold is decorated with large Pt particles. In addition to the folds acting to concentrate Pt precursor, the large folds may also act as good nucleation sites for large Pt particles. This is because the interaction between the particle and support is due to dispersive forces, which are maximised when as many atoms in the particle are in contact with the support as possible.[42] Figure 11c shows a higher magnification image of the area indicated with the black arrow in Figure 11a. It can be seen that heavy sintering of the crystals has taken place; most of the crystals have aggregated together. Figure 11d shows a higher magnification image of the area indicated by the white arrow in Figure 11a, which appeared empty at low magnification. While a couple of large aggregates can be seen, most of the surface is covered in much smaller crystals which are only a few nanometres in diameter, a much more desirable dispersion for maximising the Pt surface area. Similar uneven distribution of particles was observed for all samples. This demonstrates how large scale variations in the topography of the carbon support, such as in

the form of folds, can negatively impact the distribution of nanomaterials formed by thermal annealing.

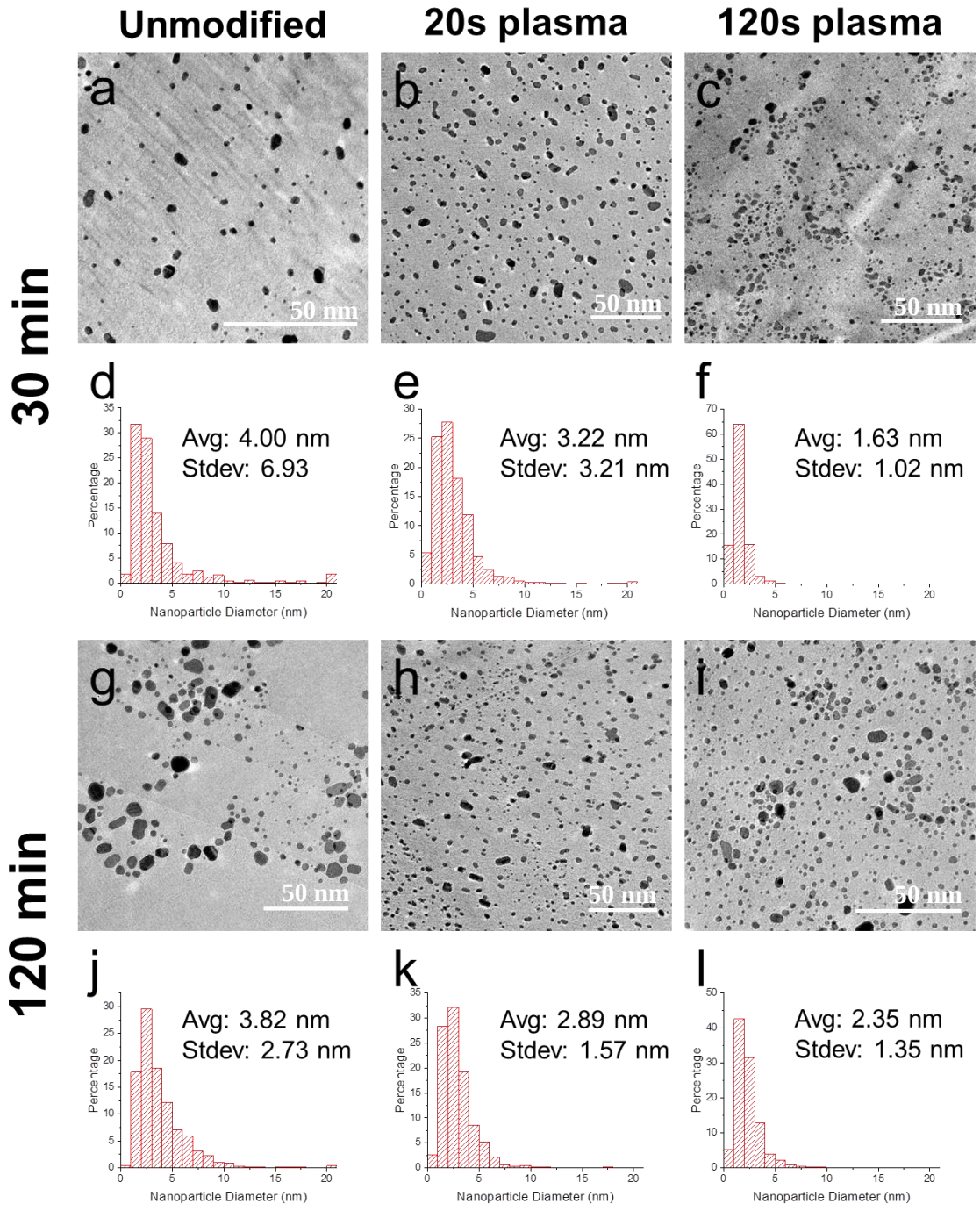

Figure 12. TEM images and particle size histograms for regions of well distributed particles on unmodified and plasma treated graphene foams. (a-c) TEM images and (d-f) particle size histograms for graphene foams treated with 25 mM Pt precursor solution annealed for 30 minutes at 400°C for unmodified, 20s plasma, and 120s

plasma treated graphene foams respectively. (g-i) TEM images and (j-l) particle size histograms for graphene foams treated with 25 mM Pt precursor solution annealed for 120 minutes at 400°C for unmodified, 20s plasma, and 120s plasma treated graphene foams respectively. Scale bars: a) 50 nm b) 50 nm c) 50 nm g) 50 nm h) 50 nm i) 50 nm

In order to ascertain the effect of the surface plasma treatment on the distribution of crystals, we turn our attention to the areas of well distributed crystals. Figure 12 shows medium magnification TEM images of areas of well distributed crystals for unmodified, 20s and 120s plasma treatments with 25mM of Pt precursor heated for 30 and 120 minutes at 400°C. As the Pt crystals grown on the graphene foam can be quite inhomogeneous, several areas of small, well distributed Pt crystals were measured for each sample. Images and distributions for nanocrystals produced after 30 minutes of heating can be seen in Figure 12a-f, the TEM images show areas of roughly equal size. In the unmodified foam case, it can be seen that a low proportion of the surface is covered by crystals, with large patches of graphene left bare. The plasma treatment was carried out following the etching of the nickel, so that both sides of the graphene foam surface are modified. For the samples treated with plasma, the density of nanocrystals increases, showing an improved dispersion of crystals in these areas (Figure 12b). This is because defects such as vacancies and oxygen-containing functional groups have been introduced into the unreactive graphene basal plane, which act as nucleation sites for Pt crystals with higher binding energies than the pristine surface.[43],[44] The particle size histograms for these samples reflect the increase in density. The increase in defects leads to more nucleation sites for the synthesis of Pt crystals, which in turn will result in a lower average crystal size. The average crystal size decreases as the plasma treatment is introduced and increased in duration (Figure 12d-f). In areas of well distributed crystals such as those examined in Figure 12a-c, some crystals larger than those observed in the TEM image shown

are also encountered (similar to the crystals seen in Figure 11d). These larger (>10 nm) crystals are more often seen in the untreated graphene foam sample, and will contribute to the larger average crystal size measured in this sample. It can be seen that the population of these >10 nm crystals disappears for the 120s plasma treated sample. Furthermore as the plasma treatment is introduced and the duration increases, the population of sub-nanometre sized crystals increases. This can be seen from Figure 12 d-f, where the leftmost column in each histogram represents nanocrystals <1 nm in diameter. Sub nanometre crystals have been observed on thermally produced Pt crystals on rGO, which contains residual defects following the reduction process.[40] It was found that STEM was required in order to properly observe all the sub-nanometre Pt species, it is possible that species too small to be seen using the TEM used for this study are also present in high proportions for the Pt treated 120s plasma foam sample, though we are unable to prove whether this is the case.

Longer treatment times of 120 minutes were also carried out (Figure 12g-l). It can be seen from TEM images in Figure 12g-l that the effect of the plasma treatment is similar as in the 30 minute annealing case. Plasma treatment induces nucleation sites over the surface which improves the Pt distribution. As before, the >10 nm crystal population decreases as the plasma treatment is introduced and the treatment time is increased. For the untreated and 20s plasma treated samples, the average nanocrystal size is similar to that seen for 30 minute treatment, with a slight decrease in average size in both cases. In the case of the 120 second plasma treated foam heat treated for 120 minutes (Figure 12l), the average Pt crystal diameter has increased and the size distribution has broadened relative to the 30 minute treatment (Figure 12f). This could be due to the fact that this sample has a much higher proportion of sub-nanometre and nanometre sized crystals, which are more prone to sintering under thermal and electrochemical stress.[45]

A higher temperature of 800 °C was also used for the synthesis of Pt nanocrystals. Areas of well distributed nanocrystals were produced on the graphene foams as with the 400 °C samples, but larger crystals were frequently seen at the edges of the graphene foams, which appear to have been damaged via etching at the higher temperature (Figure 13a). Observing some of the larger particles near the edge reveals etch paths behind them (Figure 13b), indicating that the Pt particles are responsible for the structural damage observed. Some metals, including Pt, can catalytically etch graphene with the aid of H_2 which is supplied in the heating process.[46] This process proceeds via catalytic hydrogenation, where carbon atoms in graphene which are in contact with the platinum particle dissociate onto the particle. H_2 then reacts with the carbon on the Pt surface to form methane. These particles are presumably large because they coalesce with other smaller Pt crystals as they etch paths across the graphene foam. It should be noted that the hillocks generated by the plasma treatments was not seen in the heated or Pt treated samples, possibly indicating their removal.

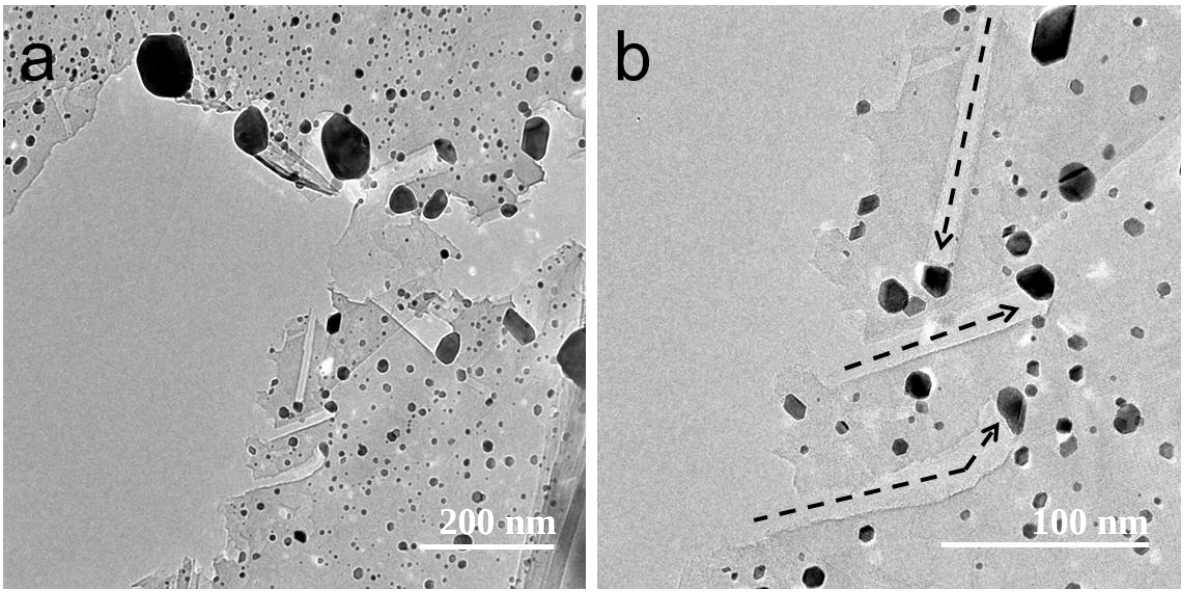

Figure 13. TEM images of particles produced on 20s plasma treated graphene foam treated with 25 mM Pt and heated at 800 °C for 30 minutes. a) TEM image showing large particles and the damaged graphene foam caused

by etching. b) Higher magnification image of (a) showing particles which have etched the graphene foam, the dotted arrows show the paths of the particles. Scale bars: a) 200 nm b) 100 nm

Raman characterisation of the Pt treated foams was carried out to try and understand what effects the Pt annealing had on the graphene support, in addition to the obvious etching observed at 800 °C. Figure 14 shows D/G peak ratios for different treatments carried out on unmodified, 20s plasma treated, and 120s plasma treated graphene foams. The D/G ratios for the foam prior to any heat treatments are also displayed and are denoted as "pristine". 2D/G peak ratios for all samples were found to be unaffected by the treatments. For all three samples, it can be seen that heat treatments without the addition of Pt resulted in a decrease in D/G ratio for all experiments, though this decrease is only observed after 120 minute treatments for the unmodified sample. For the unmodified graphene (Figure 14a), 30 minute heat treatments at both temperatures resulted in no change in the D/G peak ratio, however, after 120 minute treatments, no spectra with D peaks were encountered for either treatment temperature. Because the unmodified graphene foam has not been subjected to plasma treatments, the D peak in this sample is caused solely by defects induced during the CVD and transfer processes. For this reason, it is likely that the decrease in D peak is seen due to the thermal healing of these defects in graphene. The fact that this decrease is seen only after 120 minutes indicates that this healing does not occur rapidly. An example of the sort of defect which might heal over the course of the annealing are Stone-Wales defects and vacancies, the latter of which coalesce upon heating to form larger holes.[47] Due to the fact that the initial D/G ratio is very low (~0.006) for this sample, the effect of this defect healing may not be noticeable in the plasma modified samples.

For 20s and 120s plasma treated samples, the heat treatments without Pt also lead to a reduction in the D/G peak ratio, as seen in Figure 14b and c. Though the 20s plasma treated sample has a higher D peak than the 120s treated sample, all heat treatments for these

samples result in a reduction of the D peak to ~0.05 in the case of both plasma treatments. As previously mentioned, several types of oxygen containing functional groups are generated by the plasma, as well as etch pits and vacancies. Numerous studies have been carried out as to the effect of heating on the oxygen groups in the context of graphene oxide.[48,49,50] These studies describe various decomposition mechanisms and temperatures for the different groups, which can be catalysed by the presence of hydrogen,[51] but may also inhibit complete reduction.[48,52] Calculations show that the hydroxyl and epoxide groups react in close proximity and can generate thermodynamically stable carbonyl and ether groups, which are more stable.[53] Other experiments indicate that epoxide and hydroxyl groups migrate and form close packed groups, which makes further thermal decomposition more difficult.[15] The similarities in the D/G peak ratios in irrespective of the temperature or time suggests that these changes occur rapidly enough to have all been removed after 30 minutes of treatment at 400 °C. However, even after annealing at 2 hours at 800 °C, further reduction in the D peak to levels seen in the unmodified graphene foam after annealing is not observed. This indicates that there are Raman active defects which are not removed by the extended heat treatments, in agreement with several studies on the thermal reduction of graphene oxide in atmospheres both with and without hydrogen.[15, 48,53]

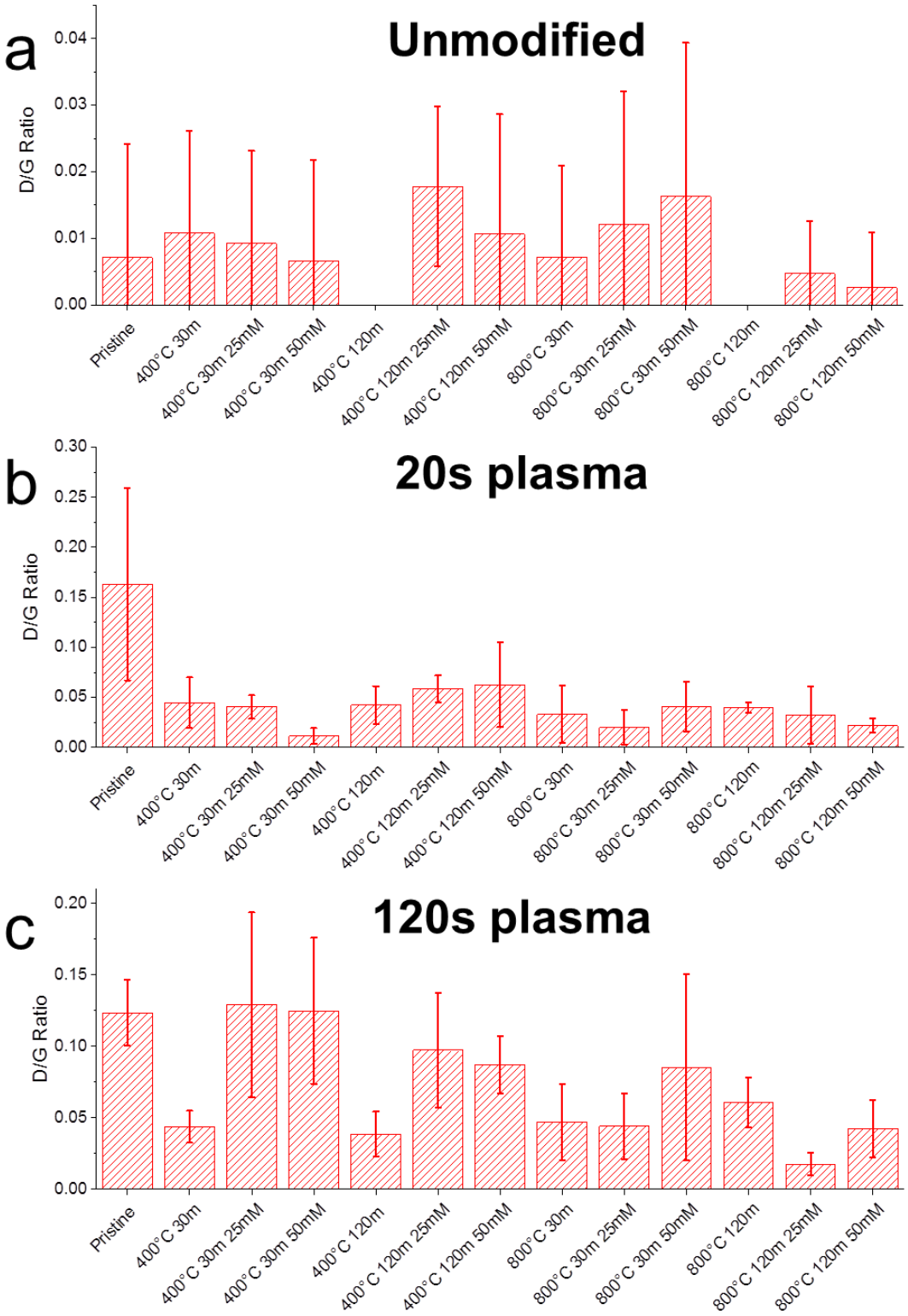

Figure 14. Raman D/G ratios for different treatments for a) unmodified b) 20s plasma treated and c) 120s plasma treated graphene foams.

The effect of the Pt treatments on the D/G ratios of the different graphene foams is more complicated than in the case of heat treatment alone. All three types of graphene foam used exhibit slightly different behaviour for Pt treatments. For the unmodified foam, all treatments with Pt resulted in no change of the D/G peak ratio when taking into account the standard deviation. It should be noted that doubling the concentration of the Pt precursor had no consistent effect on the D/G peak ratio. This suggests that the presence of Pt might protect existing defects from being healed by heat treatment. Monovacancies can be stabilised by Pt[54] and other transition metals such as nickel,[55] which might prevent their migration or healing.

For the 20s plasma modified graphene sample, all Pt treatments resulted in a similar decrease in D/G ratio, which was similar to that observed following heat treatments without Pt. No correlation between the precursor concentration, the annealing temperature, or the annealing time was observed. This suggests that the Pt is plays no role with regards to the oxygen containing defects on the graphene foam in this sample.

For 120s plasma, the change in the D/G ratio with Pt treatment is again different. It can be seen in Figure 14c that the D/G ratios for samples treated with Pt at 400 °C for 30 minutes are similar to those for the pristine 120s plasma modified foam, in contrast to the foam heated under the same conditions without Pt. This is similar to the behaviour seen in for the unmodified graphene foam. However the D/G peaks for the Pt treated samples seem affected by increases in annealing time and temperature, as the average D/G values for the 25 mM and 50 mM Pt treatments decrease with the trend 30 min 400 °C > 120 min 400 °C > 30 min 800 °C > 120 min 800 °C. This suggests a gradual healing of defects which is slower in the presence of Pt. One process which was observed for the 120s plasma modified sample, but

not in the unmodified and 20s plasma modified samples, was the noticeable sintering of particles between the 30 minute and 120 minute treatments at 400 °C. If the particles prevent the healing of defects by binding to their sites, then the sintering of particles would expose defects which can be healed. However, this explanation does not explain the immediate decrease across all samples of the D/G ratios for the 20s plasma modified sample. One reason could be the difference in the nature of the defects in the 20s and 120s samples, with the hillocks seen in the 120s plasma sample playing a role. The 120s plasma presumably contains many more multivacancies, holes, and edges than the 20s plasma, as evidenced by the etching observed for this sample. Whereas the defects in 20s plasma may predominantly be smaller vacancies and oxygen functional groups, as a much smaller degree of structural modification was seen for this sample than in the 120s foam sample (Figure 7). The different types of defects in the structure may be the cause of the different Raman observations following annealing, and if this is the case it suggests that the binding of Pt to these defects is different. Metal atoms are known to preferentially bind to edges[56] and vacancies[57] than to the pristine graphene lattice. For single Pt atoms, DFT calculations have shown that the adsorption for a Pt atom is stronger for vacancies in graphene than it is for epoxy and hydroxyl groups, which is in turn stronger than binding to the pristine graphene lattice.[43,44] This also applies to Pt_{38} clusters.[54] Pt atoms and clusters do not bind to the oxygen functional groups themselves unlike in the vacancy case; rather the influence of the functional groups causes the surrounding carbon atoms to act as binding sites.[54,44] This means that Pt clusters may not have a stabilising effect on these defects unlike in the case of vacancies, resulting in their removal upon heating even when Pt is present.

Using Raman spectroscopy alone makes it difficult to judge all of the changes occurring in these samples, a better understanding of the effects of both the plasma treatment and the Pt treatments on the nature of the defects in the various samples could be achieved in an X-ray

photoelectron spectroscopy (XPS) study. This would allow a quantitative analysis of the different oxygen containing functional groups to be carried out, resulting in a less ambiguous description of the plasma and Pt treatments. Furthermore, this technique would also allow the effect of the plasma and heat treatments on the electronic properties of the Pt crystals to be studied, which might affect their performance for catalytic reactions.

4.5 Conclusions

Free-standing graphene foams were successfully synthesised using a CVD approach. The graphene produced was found to be high quality. Defects were induced in these foams using oxygen plasma, which allowed the effect of oxygen plasma on multi-layered graphene materials to be studied, in addition to allowing the effect of defects on the thermal synthesis of Pt crystals to be ascertained. It was observed that the etching acts to both induce defects on the basal plane of graphene in addition to etching the graphene foam from the edges, which at longer times produces large holes which can be seen in low magnification SEM images. However, it was found that these treatments do not affect the whole surface of the foam to the same degree. It was found that by introducing defects into the graphene lattice in this way, the nucleation density for Pt crystals synthesised using a thermal annealing approach could be increased. For areas with good Pt distribution, the plasma treatments resulted in a narrower particle size distribution and lower average crystal size relative to the sample which was not plasma treated. This means that induced defects can be used to produce nanocrystal populations with a large proportion of nanometre sized crystals in certain areas of the substrate. However, the ripples in the graphene foam substrate can act as regions to concentrate the Pt precursor, which results in large aggregates of Pt following etching, which occurs independently of the plasma treatments. The variability in layer number,

plasma treatment and Pt particle size across the graphene foam mean that it is difficult to produce uniform particles using the thermal annealing method on these substrates. However in a structure with a more topographically uniform surface, inducing defects through plasma treatment could allow better distribution of thermally produced materials.

The role that the thermal synthesis of Pt crystals plays in the healing of the induced defects is unclear. It is believed that the healing of vacancies can be inhibited by the presence of Pt, but has little effect on oxygen functional groups. This is suggested by the fact that heating the pristine graphene foam in the absence of Pt results in a decrease in the D/G peak ratio, whereas no change is observed when Pt is present. In the case of the pristine foam, the defects present are expected to be mostly vacancy type defects. However, Pt does not have the same effect in plasma treated samples, where it can be expected that a many of the defects will take the form of oxygen-containing functional groups. Further investigation is required to confirm whether or not this is the case.

4.6 References

(1) Zhang, X.; Zhang, H.; Li, C.; Wang, K.; Sun, X.; Ma, Y. Recent advances in porous graphene materials for supercapacitor applications. *RSC Adv.* **2014,** *4*, 45862-45884.

(2) Kucinskis, G.; Bajars, G.; Kleperis, J., Graphene in lithium ion battery cathode materials: A review. *J. Power Sources* **2013,** 240, 66-79.

(3) Antolini, E. Carbon supports for low-temperature fuel cell catalysts. *Appl. Catal. B-Environ.* **2009,** *88*, 1-24.

(4) Antolini, E., Graphene as a new carbon support for low-temperature fuel cell catalysts. *Appl. Catal. B-Environ*. **2012,** *123*, 52-68.

(5) Chen, Z. P.; Ren, W. C.; Gao, L. B.; Liu, B. L.; Pei, S. F.; Cheng, H. M., Three-dimensional flexible and conductive interconnected graphene networks grown by chemical vapour deposition. *Nat. Mater.* **2011,** *10*, 424-428.

(6) He, Y.; Chen, W.; Li, X.; Zhang, Z.; Fu, J.; Zhao, C.; Xie, E. Freestanding Three-Dimensional Graphene/MnO2 Composite Networks As Ultralight and Flexible Supercapacitor Electrodes. *ACS Nano* **2013,** *7*, 174-182.

(7) Luo, J.; Liu, J.; Zeng, Z.; Ng, C. F.; Ma, L.; Zhang, H.; Lin, J.; Shen, Z.; Fan, H. J. Three-Dimensional Graphene Foam Supported Fe3O4 Lithium Battery Anodes with Long Cycle Life and High Rate Capability. *Nano Lett*. **2013,** *13*, 6136-6143.

(8) Maiyalagan, T.; Dong, X. C.; Chen, P.; Wang, X. Electrodeposited Pt on three-dimensional interconnected graphene as a free-standing electrode for fuel cell application. *J. Mater. Chem*. **2012,** *22*, 5286-5290.

(9) Meier, J. C.; Galeano, C.; Katsounaros, I.; Witte, J.; Bongard, H. J.; Topalov, A. A.; Baldizzone, C.; Mezzavilla, S.; Schüth, F.; Mayrhofer, K. J. J. Design criteria for stable Pt/C fuel cell catalysts. *Beilstein J. Nanotechnol.* **2014,** *5*, 44-67.

(10) Verga, L. G.; Aarons, J.; Sarwar, M.; Thompsett, D.; Russell, A. E.; Skylaris, C. K. Effect of graphene support on large Pt nanoparticles. *Phys. Chem. Chem. Phys*. **2016,** 18, 32713-32722.

(11) Shao, M.; Peles, A.; Shoemaker, K., Electrocatalysis on Platinum Nanoparticles: Particle Size Effect on Oxygen Reduction Reaction Activity. *Nano Lett.* **2011,** *11*, 3714-3719.

(12) Xin, L.; Yang, F.; Rasouli, S.; Qiu, Y.; Li, Z.-F.; Uzunoglu, A.; Sun, C.-J.; Liu, Y.; Ferreira, P.; Li, W.; Ren, Y.; Stanciu, L. A.; Xie, J., Understanding Pt Nanoparticle Anchoring on Graphene Supports through Surface Functionalization. *ACS Catal.* **2016**, *6* 2642-2653.

(13) Wang, H. L.; Robinson, J. T.; Diankov, G.; Dai, H. J. Nanocrystal Growth on Graphene with Various Degrees of Oxidation. *J. Am. Chem. Soc.* **2010,** *132*, 3270-3271.

(14) Qin, Y.; Li, J.; Kong, Y.; Li, X.; Tao, Y.; Li, S.; Wang, Y. In situ growth of Au nanocrystals on graphene oxide sheets. *Nanoscale* **2014,** *6*, 1281-1285.

(15) Zhou, S.; Bongiorno, A. Origin of the Chemical and Kinetic Stability of Graphene Oxide. *Sci. Rep.* **2013,** *3*. 2484

(16) Yue, H. Y.; Huang, S.; Chang, J.; Heo, C.; Yao, F.; Adhikari, S.; Gunes, F.; Liu, L. C.; Lee, T. H.; Oh, E. S.; Li, B.; Zhang, J. J.; Huy, T. Q.; Luan, N. V.; Lee, Y. H. ZnO Nanowire Arrays on 3D Hierachical Graphene Foam: Biomarker Detection of Parkinson's Disease. *ACS Nano* **2014,** *8*, 1639-1646.

(17) Beka, L. G.; Li, X.; Liu, W. Nickel Cobalt Sulfide core/shell structure on 3D Graphene for supercapacitor application. *Sci. Rep.* **2017,** *7*, 2105.

(18) Ferrari, A. C.; Meyer, J. C.; Scardaci, V.; Casiraghi, C.; Lazzeri, M.; Mauri, F.; Piscanec, S.; Jiang, D.; Novoselov, K. S.; Roth, S.; Geim, A. K. Raman spectrum of graphene and graphene layers. *Phys. Rev. Lett.* **2006,** *97*, 187401.

(19) Hao, Y.; Wang, Y.; Wang, L.; Ni, Z.; Wang, Z.; Wang, R.; Koo, C. K.; Shen, Z.; Thong, J. T. L. Probing Layer Number and Stacking Order of Few-Layer Graphene by Raman Spectroscopy. *Small*, **2010,** *6*, 195-200.

(20) Baraton, L.; He, Z. B.; Lee, C. S.; Cojocaru, C. S.; Châtelet, M.; Maurice, J. L.; Lee, Y. H.; Pribat, D. On the mechanisms of precipitation of graphene on nickel thin films. *EPL* , **2011,** *96*, 46003.

(21) Ren, W. Shenyang National Laboratory for Materials Science, Chinese Academy of Sciences, China. *Personal communication*, **February 2014**.

(22) Liu, X.; Fu, L.; Liu, N.; Gao, T.; Zhang, Y.; Liao, L.; Liu, Z. Segregation Growth of Graphene on Cu–Ni Alloy for Precise Layer Control. *J. Phys. Chem. C.* **2011,** *115*, 11976-11982.

(23) Gyeong Hee, R.; Jongyeong, L.; Dongwoo, K.; Hye Jin, J.; Hyeon Suk, S.; Zonghoon, L. Effects of dry oxidation treatments on monolayer graphene. *2D Mater*. **2017,** *4*, 024011.

(24) Gokus, T.; Nair, R. R.; Bonetti, A.; Böhmler, M.; Lombardo, A.; Novoselov, K. S.; Geim, A. K.; Ferrari, A. C.; Hartschuh, A. Making Graphene Luminescent by Oxygen Plasma Treatment. *ACS Nano*, **2009,** *3*, 3963-3968.

(25) Nourbakhsh, A.; Cantoro, M.; Klekachev, A. V.; Pourtois, G.; Vosch, T.; Hofkens, J.; van der Veen, M. H.; Heyns, M. M.; De Gendt, S.; Sels, B. F. Single Layer vs Bilayer Graphene: A Comparative Study of the Effects of Oxygen Plasma Treatment on Their Electronic and Optical Properties. *J. Phys. Chem. C.* **2011,** *115*, 16619-16624.

(26) Felten, A.; Eckmann, A.; Pireaux, J. J.; Krupke, R.; Casiraghi, C. Controlled modification of mono- and bilayer graphene in O-2, H-2 and CF4 plasmas. *Nanotechnology* **2013,** *24*, 355705.

(27) Xiao, N.; Dong, X.; Song, L.; Liu, D.; Tay, Y.; Wu, S.; Li, L.-J.; Zhao, Y.; Yu, T.; Zhang, H.; Huang, W.; Hng, H. H.; Ajayan, P. M.; Yan, Q. Enhanced Thermopower of Graphene Films with Oxygen Plasma Treatment. *ACS Nano*, **2011,** *5*, 2749-2755.

(28) Feng, T.; Xie, D.; Tian, H.; Peng, P.; Zhang, D.; Fu, D.; Ren, T.; Li, X.; Zhu, H.; Jing, Y. Multi-layer graphene treated by O2 plasma for transparent conductive electrode applications. *Materials Letters*, **2012,** *73*, 187-189.

(29) Nakahara, M.; Sanada, Y. Modification of pyrolytic graphite surface with plasma irradiation. *J. Mater. Sci.* **1993,** *28*, 1327-1333.

(30) You, H.-X.; Brown, N. M. D.; Al-Assadi, K. F. Radio-frequency (RF) plasma etching of graphite with oxygen: a scanning tunnelling microscope study. *Surf. Sci.,* **1993,** *284*, 263-272.

(31) Johns, J. E.; Alaboson, J. M. P.; Patwardhan, S.; Ryder, C. R.; Schatz, G. C.; Hersam, M. C. Metal Oxide Nanoparticle Growth on Graphene via Chemical Activation with Atomic Oxygen. *J. Am. Chem. Soc.* **2013**, *135*, 18121-18125.

(32) Amirhasan, N.; Mirco, C.; Tom, V.; Geoffrey, P.; Francesca, C.; Marleen, H. v. d. V.; Johan, H.; Marc, M. H.; Stefan De, G.; Bert, F. S. Bandgap opening in oxygen plasma-treated graphene. *Nanotechnology*, **2010,** *21*, 435203.

(33) Dey, A.; Chroneos, A.; Braithwaite, N. S. J.; Gandhiraman, R. P.; Krishnamurthy, S. Plasma engineering of graphene. *Appl. Phys. Rev.*, **2016,** *3*, 021301.

(34) Lee, G.; Kim, J.; Kim, K.; Han, J. W. Precise control of defects in graphene using oxygen plasma. *J. Vac. Sci. Technol. A*, **2015,** *33*, 060602.

(35) Vinogradov, N. A.; Schulte, K.; Ng, M. L.; Mikkelsen, A.; Lundgren, E.; Mårtensson, N.; Preobrajenski, A. B. Impact of Atomic Oxygen on the Structure of Graphene Formed on Ir(111) and Pt(111). *J. Phys. Chem.* C, **2011,** *115*, 9568-9577.

(36) Paredes, J. I.; Solís-Fernández, P.; Martínez-Alonso, A.; Tascón, J. M. D. Atomic Vacancy Engineering of Graphitic Surfaces: Controlling the Generation and Harnessing the Migration of the Single Vacancy. *J. Phys. Chem. C*, **2009,** *113*, 10249-10255.

(37) Paredes, J. I.; Martínez-Alonso, A.; Tascón, J. M. D. Early Stages of Plasma Oxidation of Graphite: Nanoscale Physicochemical Changes As Detected by Scanning Probe Microscopies. *Langmuir*, **2002,** *18*, 4314-4323.

(38) Ganesan, K.; Ghosh, S.; Gopala Krishna, N.; Ilango, S.; Kamruddin, M.; Tyagi, A. K. A comparative study on defect estimation using XPS and Raman spectroscopy in few layer nanographitic structures. *Phys. Chem. Chem. Phys.*, **2016,** *18*, 22160-22167.

(39) Hollricher, O. *Raman Instrumentation for Confocal Raman Microscopy.* In *Confocal Raman Microscopy* ; Dieing, T; Hollricher, O; Toporski, J., Ed.; Springer, Berlin Heidelberg, 2010, pp. 43-60.

(40) Yoo, E.; Okata, T.; Akita, T.; Kohyama, M.; Nakamura, J.; Honma, I. Enhanced Electrocatalytic Activity of Pt Subnanoclusters on Graphene Nanosheet Surface. *Nano Lett.*, **2009**, 9, 2255-2259.

(41) Gnanavel, T.; Mobus, G., In-situ cobalt nanocrystal synthesis by intense electron beams in TEM. In Electron Microscopy and Analysis Group Conference 2011, Moebus, G.; Walther, T.; Brydson, R.; Ozkaya, D.; MacLaren, I.; Donnelly, S.; Nellist, P.; Li, Z.; Baker, R.; Chiu, Y. L., Eds. Iop Publishing Ltd: Bristol, 2012; Vol. 371.

(42) Schneider, W. B.; Benedikt, U.; Auer, A. A. Interaction of platinum nanoparticles with graphitic carbon structures: a computational study. *ChemPhysChem* **2013,** *14*, 2984-9.

(43) Fampiou, I.; Ramasubramaniam, A. Binding of Pt Nanoclusters to Point Defects in Graphene: Adsorption, Morphology, and Electronic Structure. *J. Phys. Chem. C*, **2012,** *116*, 6543-6555.

(44) Dobrota, A. S.; Pasti, I. A.; Mentus, S. V.; Skorodumova, N. V. A general view on the reactivity of the oxygen-functionalized graphene basal plane. *Phys. Chem. Chem. Phys.* **2016,** 18 (9), 6580-6586.

(45) Shao-Horn, Y.; Sheng, W. C.; Chen, S.; Ferreira, P. J.; Holby, E. F.; Morgan, D. Instability of Supported Platinum Nanoparticles in Low-Temperature Fuel Cells. *Top. Catal.* **2007,** *46*, 285-305.

(46) Wang, M. X.; Liu, Q.; Li, Z. F.; Sun, H. F.; Stach, E. A.; Xie, J. Structural Modification of Graphene Sheets to Create a Dense Network of Defect Sites. *J. Phys. Chem. Lett.* **2013,** *4*, 1484-1488.

(47) Liu, L.; Gao, J.; Zhang, X.; Yan, T.; Ding, F. Vacancy inter-layer migration in multi-layered graphene. *Nanoscale*, **2014,** *6*, 5729-5734.

(48) Yang, D.; Velamakanni, A.; Bozoklu, G.; Park, S.; Stoller, M.; Piner, R. D.; Stankovich, S.; Jung, I.; Field, D. A.; Ventrice, C. A.; Ruoff, R. S. Chemical analysis of graphene oxide films after heat and chemical treatments by X-ray photoelectron and Micro-Raman spectroscopy. *Carbon*, **2009**, *47*, 145-152.

(49) Ganguly, A.; Sharma, S.; Papakonstantinou, P.; Hamilton, J. Probing the Thermal Deoxygenation of Graphene Oxide Using High-Resolution In Situ X-ray-Based Spectroscopies. *J. Phys. Chem. C*, **2011**, *115*, 17009-17019.

(50) Pei, S.; Cheng, H.-M. The reduction of graphene oxide. *Carbon*, **2012**, *50*, 3210-3228.

(51) Abolfath, R. M.; Cho, K. Computational Studies for Reduced Graphene Oxide in Hydrogen-Rich Environment. *J. Phys. Chem.* A, **2012**, *116*, 1820-1827.

(52) Cheng, M.; Yang, R.; Zhang, L.; Shi, Z.; Yang, W.; Wang, D.; Xie, G.; Shi, D.; Zhang, G. Restoration of graphene from graphene oxide by defect repair. *Carbon*, **2012**, *50*, 2581-2587.

(53) Bagri, A.; Mattevi, C.; Acik, M.; Chabal, Y. J.; Chhowalla, M.; Shenoy, V. B. Structural evolution during the reduction of chemically derived graphene oxide. *Nat. Chem.*, **2010**, 2, 581-587.

(54) Matsutsu, M.; Petersen, M. A.; van Steen, E. Pt38 cluster on OH- and COOH-functionalised graphene as a model for Pt/C-catalysts. *Phys. Chem. Chem. Phys.*, **2016**, *18*, 25693-25704.

(55) Jacobson, P.; Stöger, B.; Garhofer, A.; Parkinson, G. S.; Schmid, M.; Caudillo, R.; Mittendorfer, F.; Redinger, J.; Diebold, U. Disorder and Defect Healing in Graphene on Ni(111). *J. Phys. Chem. Lett.*, **2012**, *3*, 136-139.

(56) Gong, C.; Robertson, A. W.; He, K.; Ford, C.; Watt, A. A. R.; Warner, J. H. Interactions of Pb and Te atoms with graphene. *Dalton Trans.*, **2014,** *43*, 7442-7448.

(57) Robertson, A. W.; Montanari, B.; He, K.; Kim, J.; Allen, C. S.; Wu, Y. A.; Olivier, J.; Neethling, J.; Harrison, N.; Kirkland, A. I.; Warner, J. H. Dynamics of Single Fe Atoms in Graphene Vacancies. *Nano Lett.* **2013,** 13 (4), 1468-1475.

Chapter 5

Three Dimensional Multi-layered Graphene and Multi-layer Graphene-CNT Hybrid Materials via Rapid Thermal Annealing of Nickel Acetate as a Pt Nanoparticle Support

* TEM images in Figures 8 and 9 were recorded by Dr Alex W. Robertson.

5.1 Introduction

Graphene consists of a single layer of sp^2 bonded carbon atoms and is of interest as an electrode material for electrochemical energy generation and storage. This is because graphene has exceptional thermal and electrical conductivity, good chemical stability and a high surface area,[1] making it ideal for use in fuel cells,[2] batteries[3] and supercapacitors.[4] One issue surrounding the use of individual graphene sheets, such as those produced using chemical exfoliation and subsequent reduction from graphene oxide, is the tendency to re-stack over time, which lowers the surface area of the material and can make active sites of other materials supported on graphene inaccessible, leading to a loss of activity over time.[5] Recent research has focused on the production of three-dimensionally structured graphene materials which are more resistant to stacking.[6] Mass producing high quality three-dimensional graphene is still challenging however. In the chemical vapour deposition method, a gaseous source of carbon breaks down on the surface of the metal template.[7] Another option is the annealing method, where a mixture of a metal template (most often

nickel) and a carbon source is heated, the carbon source dissolves in the nickel and forms graphene upon cooling.[8] Both these methods require a pre-formed metal template, which increases the number of steps required to synthesise 3D graphene and increases cost.

Another strategy for enhancing the utility of graphene in electrochemical applications is the combination of CNTs, these act to enhance the conductivity of the graphene materials and prevent re-stacking.[9] This either requires the subsequent growth of CNTs on the graphene materials[10] or the mixing of CNTs and graphene grown separately, [11, 12] increasing the number of steps and processing required.

In this chapter we utilise nickel acetate, a readily available and cheap nickel compound, to form both the nickel template/catalyst and carbon source in-situ when rapidly heated in an inert atmosphere. By controlling the annealing temperature, we show that it is possible to form both high quality multi-layered graphene shells (GS) and a combination of graphene shells and cup-stacked carbon nanotubes (GS-CNT) using a single precursor.

One important application of 3D carbon materials is as a catalyst support for platinum (Pt) nanoparticles, which are important catalysts for the hydrogen oxidation (HOR) and oxygen reduction (ORR) reactions in PEMFC fuel cells, as well as the hydrogen evolution reaction (HER) for the production of hydrogen.[13, 14] To explore the novel materials produced, Pt nanoparticles are then grown on the different carbon supports using a thermal annealing method. Their electrochemically active surface areas and durabilities are then compared in cyclic voltammetry experiments.

5.2 Thermal Annealing Synthesis of Carbon Materials from Nickel Acetate

For each experiment, an alumina furnace crucible was half filled (~1.25 g) with nickel acetate tetrahydrate (98%, Sigma-Aldrich). The sample was placed in a 1 inch diameter quartz tube

in a horizontal tube furnace. A furnace on rails was used so that the sample could be rapidly introduced and removed from the hot zone of the furnace. Argon (200 sccm) was flowed through the system whilst the furnace reached the desired temperature, during this time the sample was in the room temperature zone of the system unless stated otherwise for certain experiments. For the experiment utilising dehydrated nickel acetate, the nickel acetate was heated for 30 minutes at 100 °C in the tube furnace, before being removed from the hot zone prior to the furnace being heated to the desired temperature. Once the furnace had reached the desired temperature the ceramic boat containing the nickel acetate tetrahydrate was rapidly introduced into the hot zone of the furnace. Following the desired annealing period the sample was removed from the hot zone of the furnace to allow rapid cooling to room temperature. The system was then cooled back to ambient temperature and the sample removed.

3D CNT-graphene hybrid (600, 700, 800, 900 and 1000GS-CNT): Argon was flowed through the system while the furnace reached 600-1000 °C depending on the desired product, the sample was moved into the hot zone of the furnace for a period of 2 hours unless otherwise stated, after this the sample was removed from the hot zone of the furnace and removed after it had cooled to ambient temperature.

3D graphene spheres (350GS): Argon was flowed through the system while the furnace reached 350 °C, the sample was moved into the hot zone of the furnace for a period of 2 hours unless otherwise stated, after this the sample was removed from the hot zone of the furnace and removed after it had cooled to ambient temperature.

Crystalline 3D graphene spheres (600GS and 1000GS): Argon was flowed through the system while the furnace reached a temperature of 350 °C. The sample was moved into the hot zone of the furnace and annealed for 1 hour, following this the furnace was set to 600 or

1000 °C with a ramp rate of 50 °C/min and the sample was annealed for another hour (including heating time). Following this the sample was removed from the hot zone of the furnace and allowed to cool to room temperature.

5.3 Synthesis of Pt nanocrystals on Carbon Supports using Thermal Annealing

20mg of 350GS, 600GS-CNT, 1000GS-CNT or carbon black (CB – Vulcan XC72R) was mixed with 0.6 mL of 50mM H_2PtCl_6 (Sigma-Aldrich) in ethanol. This mixture was evaporated at 50 °C overnight on a hot plate. The resultant powder was then introduced into the hot zone of a tube furnace with a 1 in. quartz tube at 400 °C for 30 minutes under a flow of H_2 (20% in argon, 100 sccm) and Argon (200 sccm). Following annealing the sample was removed from the hot zone and the system was cooled to room temperature.

5.4 Results and Discussion

Previous experiments have shown that above 350 °C nickel acetate decomposes into nickel (with residual carbon), some nickel oxide (which is reduced to nickel by other decomposition products at higher temperatures), and a mixture of gases which include H_2O, H_2, CO, CH_4 and other small organic molecules.[15] These are gases which are commonly utilised in chemical vapour deposition (CVD) processes for the growth of carbon materials on metal surfaces. CH_4 has been commonly utilised as a carbon source in CVD processes for the growth of both carbon nanotubes[16] and graphene.[17] CO is also used as a fuel for the growth of carbon nanotubes.[18] H_2 plays an important role in the synthesis of graphene, where it acts to aid CH_4 decomposition on the surface of nickel.[19] For the formation of CNTs, hydrogen can play an important role in determining the resulting morphology.[20] Nickel has been

extensively explored as a catalyst for the growth of carbon nanomaterials; carbon dissolves in nickel at elevated temperatures, which can then precipitate out as graphitic layers upon cooling.[21] Previous studies have taken advantage of this to synthesise both 2D and 3D graphene structures using solid precursors by mixing nickel particles[22] or foils[23] with polymer. The decomposition of nickel acetate is thought to take place via a metastable Ni_3C phase.[24, 25] A recent study indicates that this phase readily decomposes into amorphous carbon and a carbon-rich Ni phase.[26] This amorphous carbon can be graphitised at higher temperatures, with some additional carbon precipitating from the nickel particles upon cooling.

We decided to explore the growth of 3D graphitic materials using nickel acetate as the sole catalyst and carbon source, and attempt to utilise the gaseous decomposition products as a carbon source in addition to the carbon residue dissolved in the nickel during decomposition. Samples of nickel acetate were rapidly introduced to a range of temperatures (350-1000 °C) in an argon atmosphere using a furnace on rails, this allowed the sample to be moved in and out of the hot zone of the furnace quickly, allowing for rapid heating and cooling of the sample. Following the annealing process (2 hours), a wet chemical etching method was used to remove as much nickel as possible, to leave hollow carbon structures.

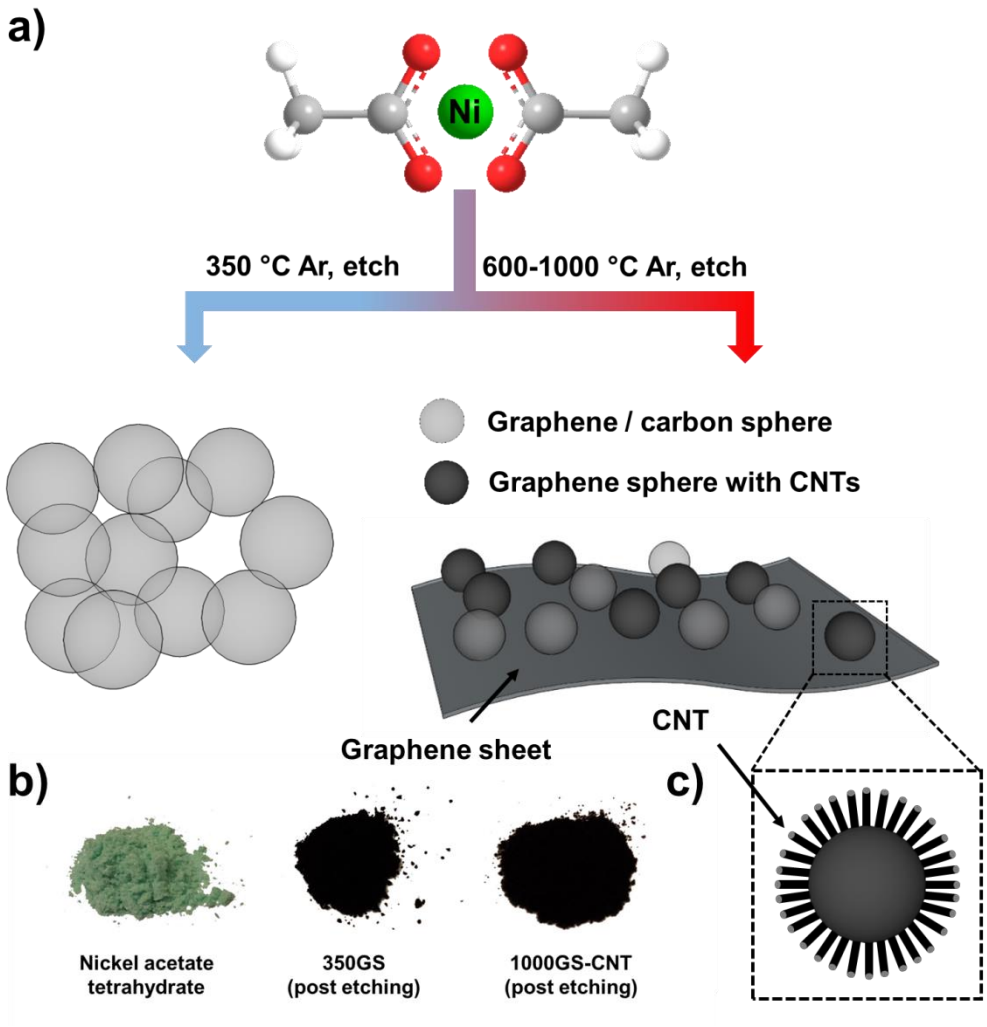

Figure 1. a) Schematic diagram showing the synthesis of GS and GS-CNT from nickel acetate. b) Photographs of the starting material and products following etching. c) Schematic of the CNT-graphene spheres which comprise parts of the GS-CNT samples.

Figure 1 shows a schematic diagram illustrating the synthesis of the material along with pictures of the reactant and products, and how the resultant morphology of the carbon material obtained following etching depends on the annealing temperature. It can be seen from Figure 1b that an obvious physical change has occurred following the annealing and etching procedures, going from green nickel acetate to a black powder. Figure 2 shows SEM and TEM images of the materials produced using the different heating procedures.

Annealing at 350 °C, the lowest temperature at which the acetate group decomposes into nickel (with dissolved carbon), nickel oxide, and gaseous products, yields aggregates of conjoined spherical particles, the SEM of which can be seen in Figure 3. Figure 2a, d and g show SEM and TEM images of the material which reveals that hollow, spherical particles (350GS) remain after etching, presumably carbon precipitated from spherical nickel particles which are removed during the etching process.

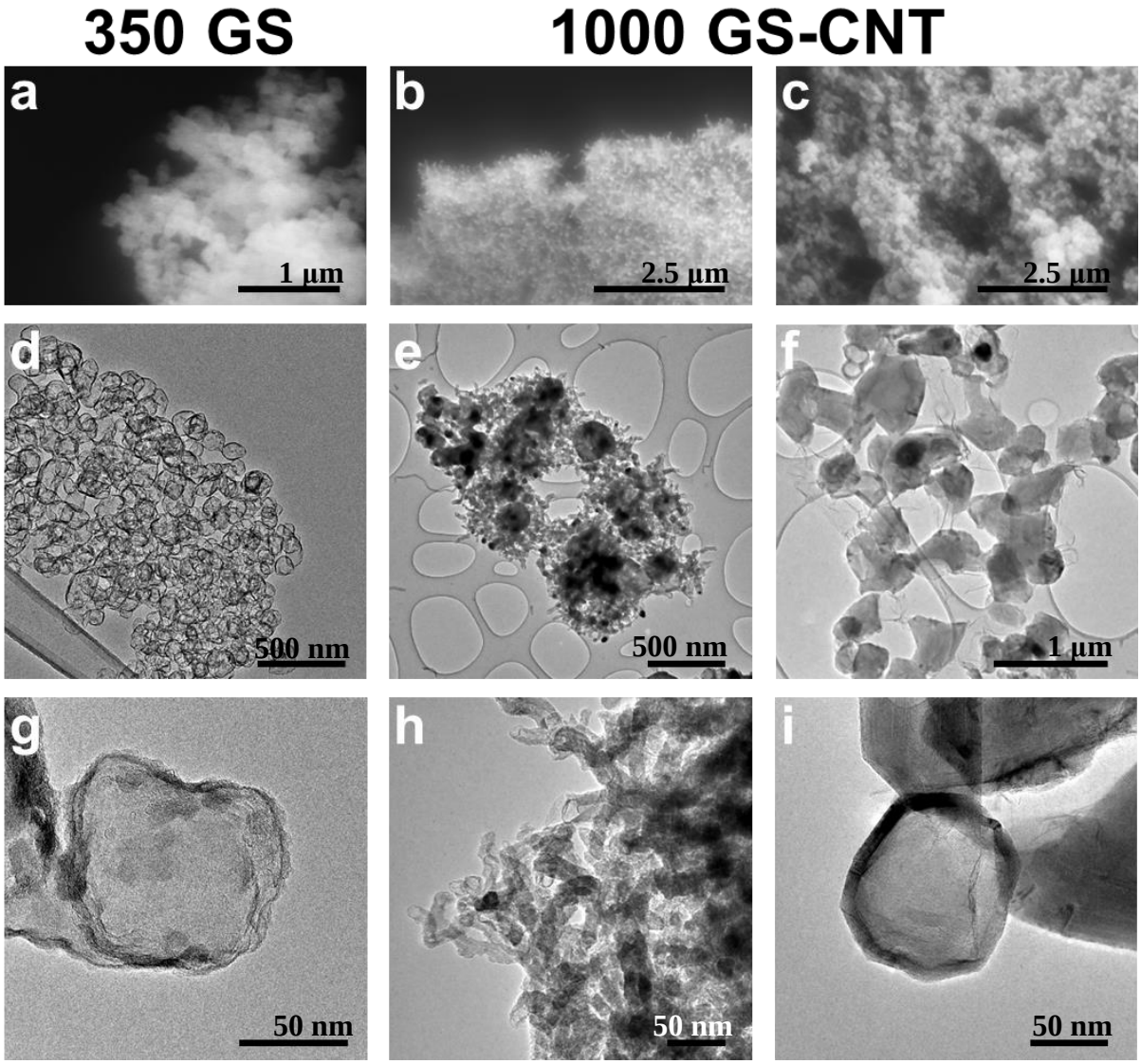

Figure 2. GS and GS-CNT materials following etching (a) SEM image of 350GS (b) SEM image of CNTs in 1000GS-CNT (c) SEM image of particles in 1000GS-CNT (d) low magnification TEM image of 350GS (e) low magnification TEM image of a CNT containing region of 1000GS-CNT (f)

low magnification TEM image of graphene spheres without CNTs in 1000GS-CNT (g) TEM image of a graphene sphere in 350GS (h) TEM image of CNTs in 1000GS-CNT (i) TEM image of a graphene sphere in 1000GS-CNT. Scale bars: (a) 1 µm (b) 2.5 µm (c) 2.5 µm (d) 500 nm (e) 500 nm (f) 1 µm (g) 50 nm (h) 50 nm (i) 50 nm.

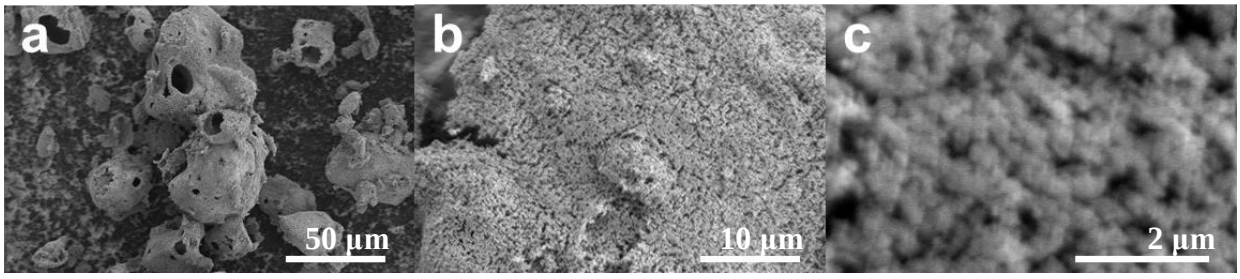

Figure 3. SEM images of 350GS. Scale bars: (a) 50 µm (b) 10 µm (c) 2 µm.

When the same procedure is carried out at higher temperatures (600-1000 °C), the structure of the material produced is more complex, and a mixture of different morphologies of carbon materials are produced. Figure 2b and c shows SEM images of different regions of the sample produced at 1000 °C, which indicates that some regions of the sample contain CNTs, whilst others contain spherical particles following etching (pre-etching images can be seen in Figure 4).

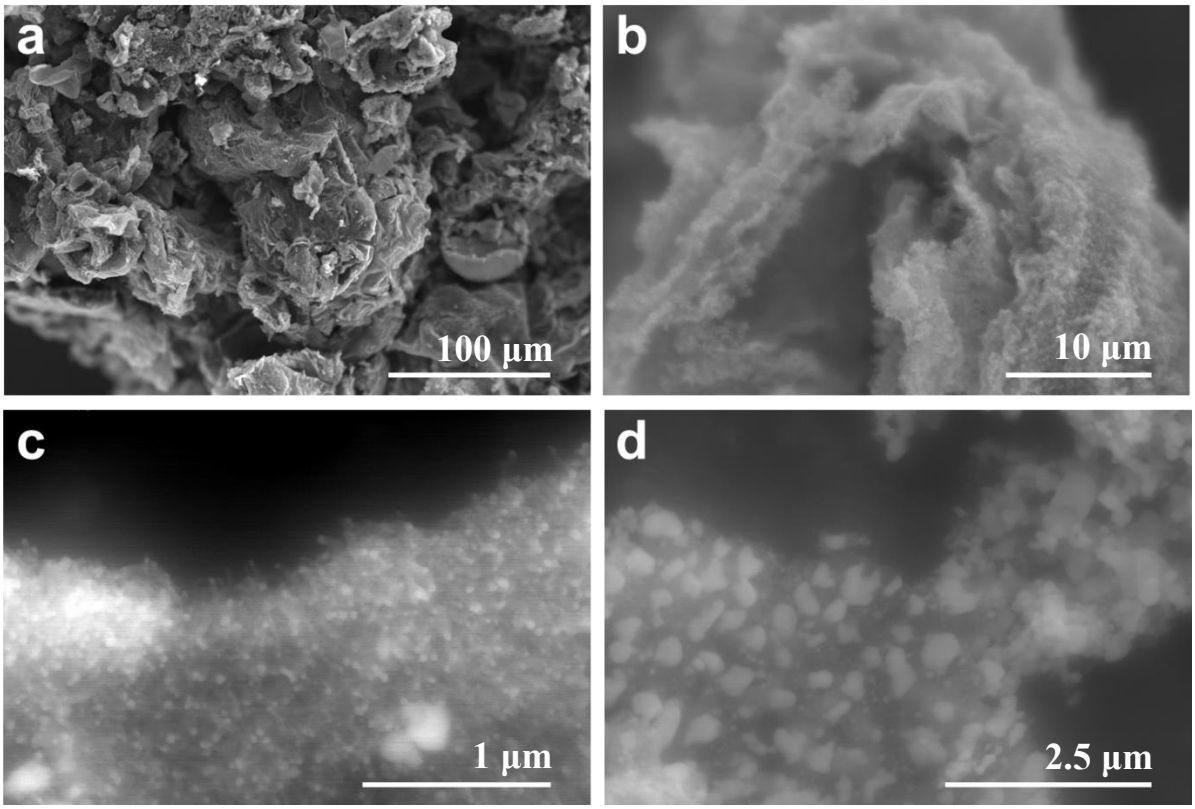

Figure 4. SEM images 1000GS-CNT before etching. (c) Region of the sample containing predominantly CNTs (d) Region of the sample containing predominantly spherical particles. Scale bars: (a) 100 µm (b) 10 µm (c) 1 µm (d) 2.5 µm.

TEM images of a region of the sample containing the CNTs are seen in Figure 2e and h; these reveal that the tubular structures have grown off spherical particles, similar to those seen in 350GS. TEM images of the regions of the sample without the CNTs (Figure 2f, i) show only spherical particles. Some of the regions comprising spherical particles indicate that they are linked together by larger graphene sheets, the wrinkles of which can be seen in Figure 1f. TEM images of other regions showing graphene sheets are shown in Figure 5.

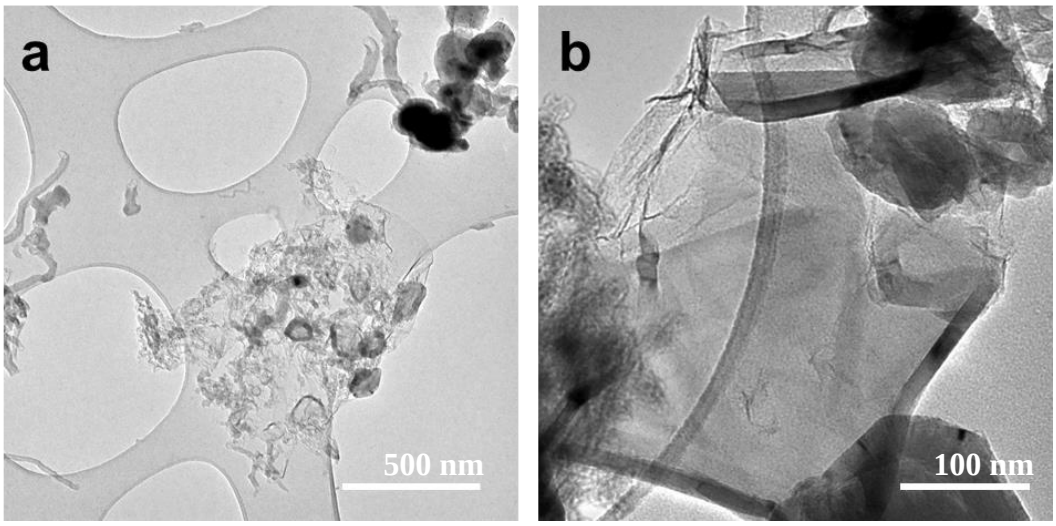

Figure 5. (a) Low and (b) high magnification images showing graphene spheres linked by larger graphene sheets. Scale bars: (a) 500 nm (b) 100 nm.

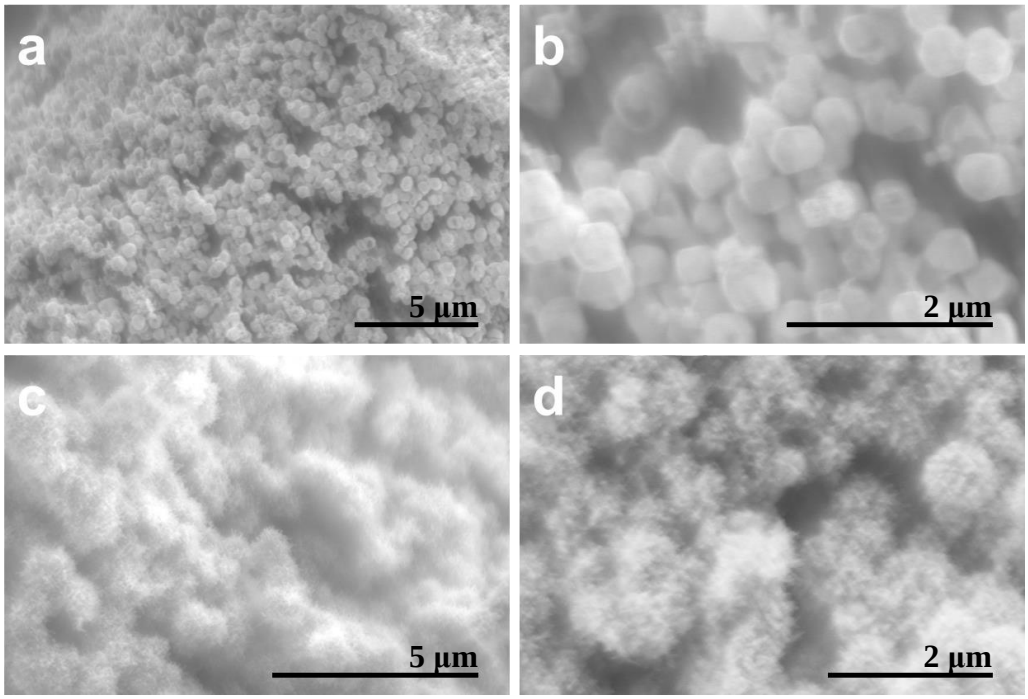

Figure 6. SEM images of 600GS-CNT prior to etching, showing different areas of the sample. (a) Shows a low magnification image of a region of the sample from bottom of the crucible, comprising only spherical particles (b) A higher magnification of the same area seen in (a). (c) A region of the sample from the top of the crucible comprising spherical particles covered in CNTs. (d) A higher magnification example of the same type of area as in (c). Scale bars: (a) 5 µm (b) 2 µm (c) 5 µm (d) 2 µm.

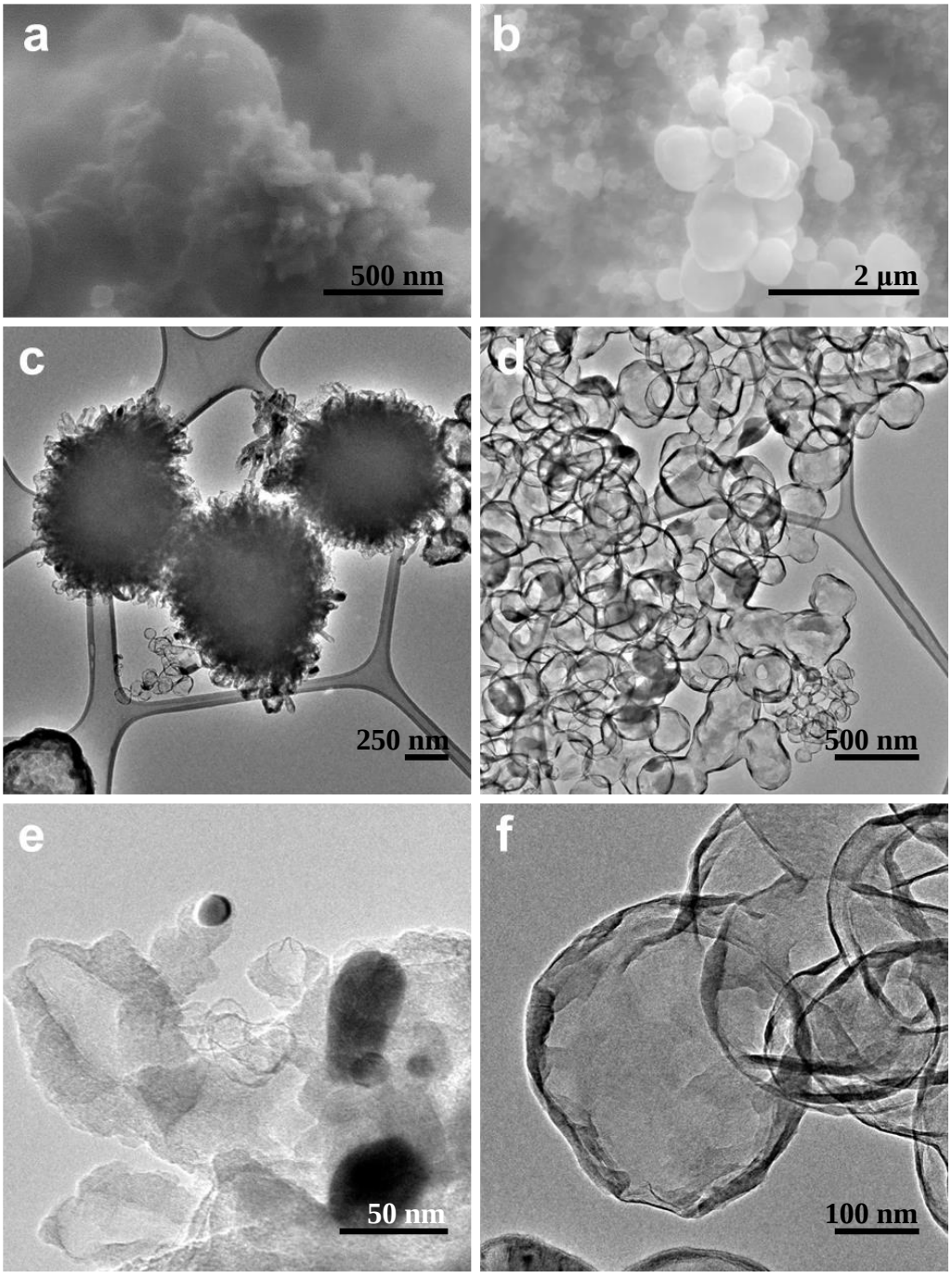

Figure 7. SEM and TEM images of different areas of 600GS-CNT following etching. (a) SEM image of a CNT containing region. (b) SEM image of a region comprising only graphene spheres. (c) Low magnification TEM image of a CNT containing region. (d) Low magnification TEM image showing an area comprising only graphene spheres. (e) High magnification TEM image of CNTs (f) high magnification TEM image of a graphene sphere. Scale bars: (a) 500 nm (b) 2 μm (c) 250 nm (d) 500 nm (e) 50 nm (f) 100 nm.

It was observed that the regions of the sample containing CNTs reside at the top of the product in the crucible following annealing, whilst at the bottom of the sample only particles were found. SEM images before etching showing areas of the sample produced at 600 °C (600GS-CNT) demonstrate this (Figure 6). SEM and TEM images of the etched samples produced at 600 °C are shown in Figure 7**,** it should be noted that the amount of tubular structures seen at 600 °C is lower than observed at 1000 °C, and there is a lack of graphene sheets that are seen in the 1000 °C sample.

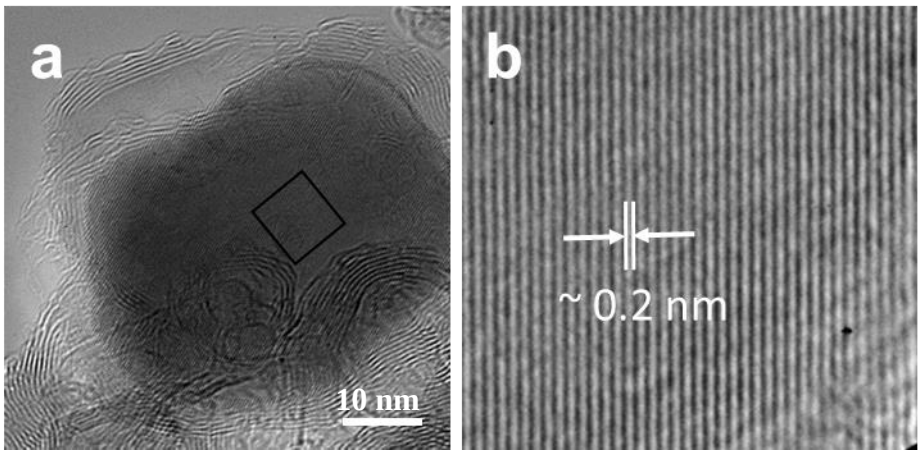

Figure 8. (a) TEM image showing a nickel nanocrystal which remained following the chemical etching process, a close-up of the black box is shown in (b) with the lattice parameter of 0.2 nm corresponding to the (111) lattice spacing of Ni. Scale bar: (a) 10 nm.

Despite an aggressive chemical etching process (see Experimental section), not all the nickel is removed by the hydrochloric acid (HCl). Thermogravimetric analysis (TGA) measurements indicate that most samples contain residual nickel; for 350GS, 600GS-CNT and 1000GS-CNT these values are 0.5, ~5 and ~10 % weight respectively. This increase in nickel content post-etching with annealing temperature is likely to be due to the multi-layered nature of the graphene shells and their crystallinity at higher temperatures. With higher annealing temperatures nickel particles with dissolved carbon will sinter into larger ones, producing thicker graphene shells upon cooling. Furthermore these layers are more crystalline and will act to protect nickel particles from the acidic environment of the etchant. Figure 8 shows a high resolution TEM (HRTEM) image of a crystal which was not removed during the etching process (1000GS-CNT). The lattice fringes measured in the crystal correspond to the (111) spacing of nickel, [27] indicating that the residual nickel has not been converted to nickel chloride ($NiCl_2$) by the HCl. These thicker, more crystalline layers and residual nickel particles also explain the surface areas of the materials as measured using the Brunauer-Emmett-Teller (BET) method. The measured surface areas of 350GS, 600GS-CNT and 1000GS-CNT were measured as 284, 188, and 110 m^2g^{-1} respectively. A summary of BET results for all samples can be found in Table 1. These surface areas are typically lower than 3D structured graphene powders, which typically have thinner walls than the structures produced using our method. This is most likely due to the high carbon solubility in nickel and the contribution from the metal which remains after etching. It is possible that materials with higher surface areas could be obtained from metal acetates where the metal has a lower carbon solubility, such as copper acetate. Another strategy could be to include other cheap metal precursors which do not contain carbon sources, such as nickel chloride ($NiCl_2$) in order to increase the metal/carbon ratio.

Material	Surface area (m^2 / g)
350GS	284.1
600GS	229.4
600GS-CNT	188.1
1000GS	71.2
1000GS-CNT	109.9
Vulcan XC-72	224.4

Table 1. Table of BET surface areas for samples prepared via the thermal annealing of nickel acetate at different temperatures and annealing procedures

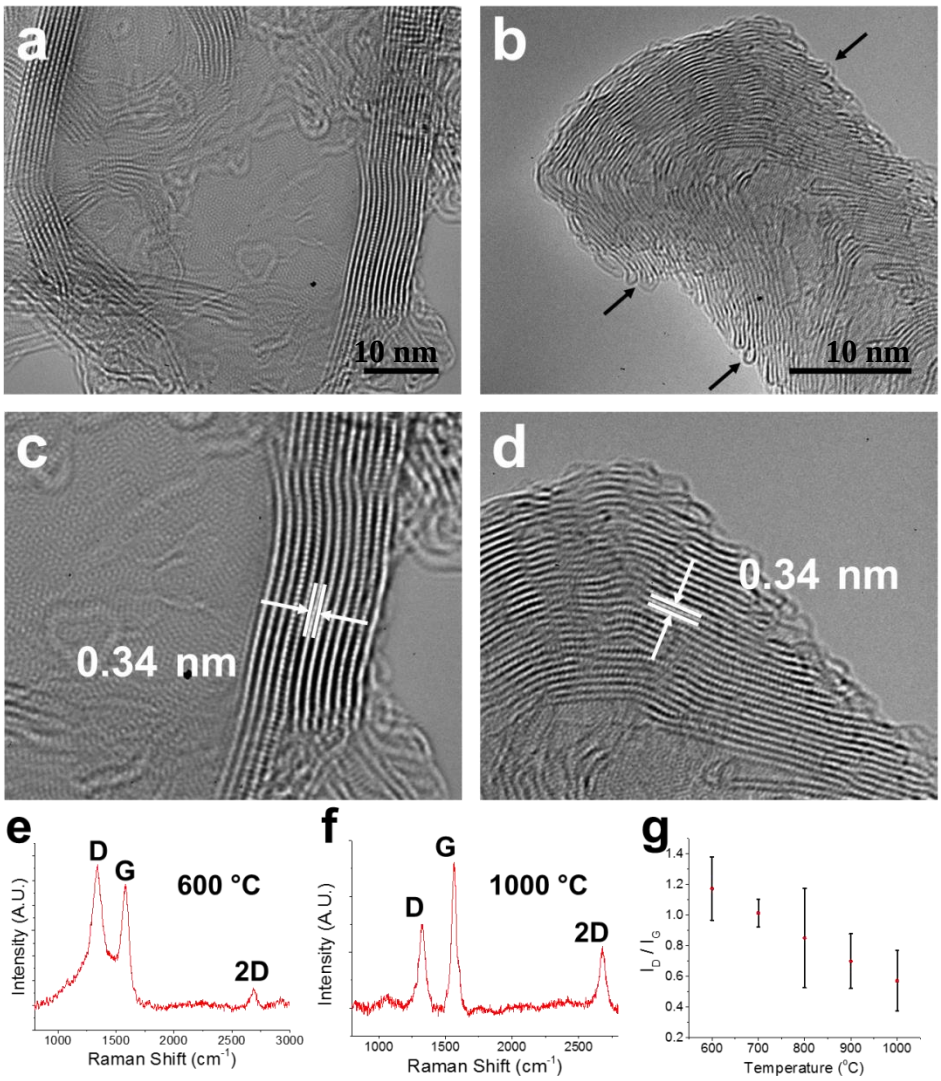

Figure 9. (a) HRTEM image showing a graphene shell from 1000GS-CNT. (b) HRTEM image showing the end of a CNT in 1000GS-CNT, the black arrows indicate the reconstructed loops of the stacked-cups comprising the nanotube (c) HRTEM showing the wall of the graphene shell shown in (a), the interlayer spacing is shown and the moiré pattern is visible. (d) HRTEM image of showing the wall of the CNT shown in (b), with the interlayer spacing shown. (e) Raman spectra of 600GS. (f) Raman spectra of 1000GS-CNT. (g) Graph of I_d/I_g versus the synthesis temperature for structures produced from nickel acetate with an annealing time of 2 hours. Scale bars: (a-b) 10 nm.

In order to evaluate the quality of graphene produced in the thermal annealing process, HRTEM and Raman spectroscopy measurements were recorded of the GS-CNT materials produced at different temperatures (600-1000 °C) (Figure 9). Closer examination of the CNTs reveals that they are carbon nanotubes with multilayer walls with the cup-stacked morphology. Black arrows in Figure 9b indicate where the edges of the stacked-cups have reconstructed to form loops, this reconstruction has been reported to produce nanotubes with a comparable electrical conductivity to multi-walled CNTs.[28] Measurements of the lattice spacings between the graphene layers for the graphene spheres (Figure 9c) and the CNTs (Figure 9d) gives a value of 0.34 nm, which is the value expected for pristine material.[29] Furthermore the moiré pattern can be seen from the graphene sphere in Figure 9c, which is also indicative of highly crystalline material.[30] HRTEM images were also recorded of 600GS-CNT (Figure 10), where the measured value of interlayer spacing was larger than 0.34 nm for both the graphene shells (0.36 nm) and CNTs (0.42 nm), indicating that lower quality material was formed when a lower annealing temperature was used.

The quality of the GS-CNT structures was also evaluated by Raman spectroscopy. The Raman spectra of the sample produced at 600 °C (Figure 9e) indicates carbon with poor crystallinity. The D peak is higher in intensity than the G peak, indicating a high concentration of defects. In contrast, the D peak is much lower in intensity relative to the G peak in samples produced at 1000 °C, indicating higher quality (Figure 9f). A noticeable D peak is still present, part of which is due to contributions from the carbon nanotubes, which have significant D peaks even for high quality samples.[31] Raman spectra of samples produced at intermediate temperatures were also recorded, and Figure 9g shows that the I(d)/ I(g) peak ratios strongly correlate to the synthesis temperature, indicating that the quality of the structure produced can be controlled using this thermal annealing method.

The ability to control the defect density in the carbon materials produced is advantageous for electrocatalysis. Edges and defects in CNTs and graphene have been shown to be active sites for the ORR.[32] It would be expected that the CNT-graphene hybrid materials formed in this study would have intrinsic ORR activity even without the addition of Pt nanoparticles due to the presence of edges and defects, the concentration of the latter can be controlled by synthesis temperature. Therefore it could be considered that the reconstruction observed for the cup-stacked nanotubes is a disadvantage as without the edge reconstruction to form loops, CNTs with a high density of edges active for the ORR would be formed. However, edges and defects in carbon materials also have disadvantages for fuel cell catalyst supports. Carbon corrosion at high cathodic potentials occurs firstly at defects and edges, and this can increase the rate of Pt particle detachment.[33]

Annealing time was also investigated as a method of controlling the quality of the carbon structure. SEM, TEM and Raman results for the product obtained after nickel acetate was annealed for just 10 minutes instead of 2 hours can be seen in Figure 11. These results indicate that the morphology of the product is determined very early in the annealing process, as SEM images indicate an indistinguishable morphology to that obtained with longer annealing times. However, the Raman spectrum indicates a much more defective structure, showing that annealing time can also be used to control the defectiveness of the multilayer graphene structures whilst keeping a similar morphology.

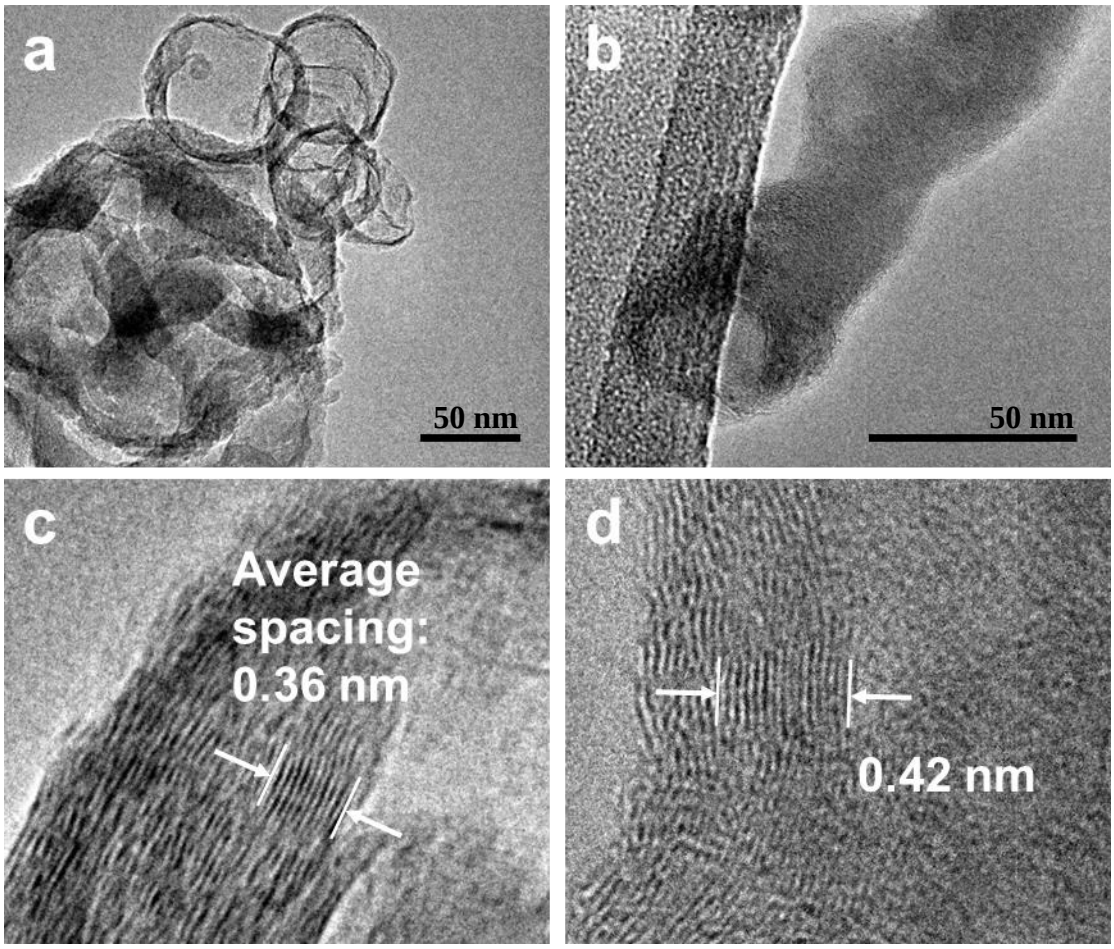

Figure 10. HRTEM images of 600GS-CNT. (a) Graphene spheres (b) CNT (c) TEM image of the edge of one of the graphene spheres shown in (a), showing the interlayer spacing (d) TEM image of the walls of the CNT shown in (b), showing the interlayer spacing. Scale bars: (a) 50 nm (b) 50 nm.

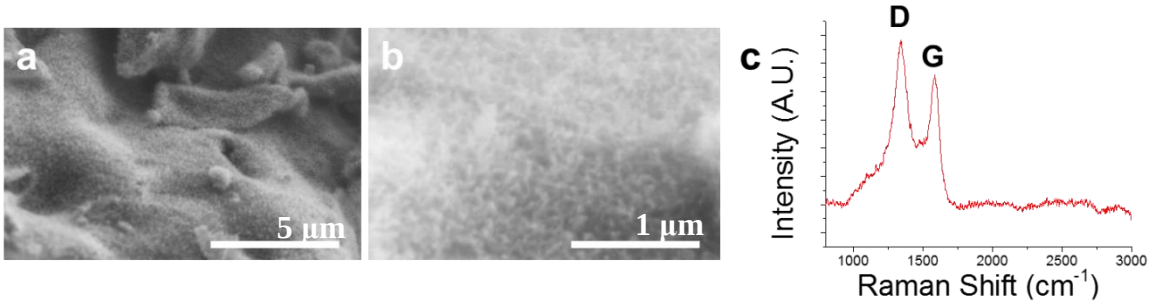

Figure 11. Sample produced after 10 minutes of annealing at 1000 °C. (a) Low magnification SEM image. (b) Higher magnification SEM image showing the presence of tubular structures. (c) Raman spectra. Scale bars: (a) 5 µm (b) 1 µm.

In order to attempt to exclusively produce graphene spheres with high crystallinity whilst avoiding the formation of CNTs, a two phase annealing method was adopted. The nickel acetate was introduced into the hot zone of the furnace at 350°C, following one hour of annealing the temperature was increased (50 °C/min) to 600 and 1000 °C, with a total annealing time of two hours (600GS and 1000GS). SEM, TEM and Raman results from the etched samples, along with the results from 350GS can be seen in Figure 12. Similarly sized structures are found in all three samples; the average diameter of the spherical graphene structures are 129, 111 and 134 nm for 350GS, 600GS and 1000GS respectively, though larger particles with diameters of several hundred nanometres, presumably formed through sintering, are seen when the annealing temperature is increased. The interlayer spacings reflect the increase in quality with increased temperature, as the spacing decreases from 0.36 to 0.34 nm when the synthesis temperature is increased from 350 to 1000 °C (Figure 12e-g). This is further corroborated by representative Raman spectra of the samples, showing a decreasing D peak and the emergence of the 2D peak with increasing temperature (Figure 12h-j). The BET surface area decreases as the crystallinity increases, the surface areas of the graphene sphere materials are 284, 229 and 71 m^2g^{-1} for 350GS, 600GS and 1000GS,

respectively. This shows that it is possible to selectively avoid the synthesis of the nanotubes whilst achieving high quality multi-layered graphene. Similar structures have been formed using preformed nickel nanoparticles and an external carbon sources in the form of polyols or poly (methyl methacrylate) and the resulting graphene shell structures were shown to be effective structures for lithium-ion storage.[22, 34]

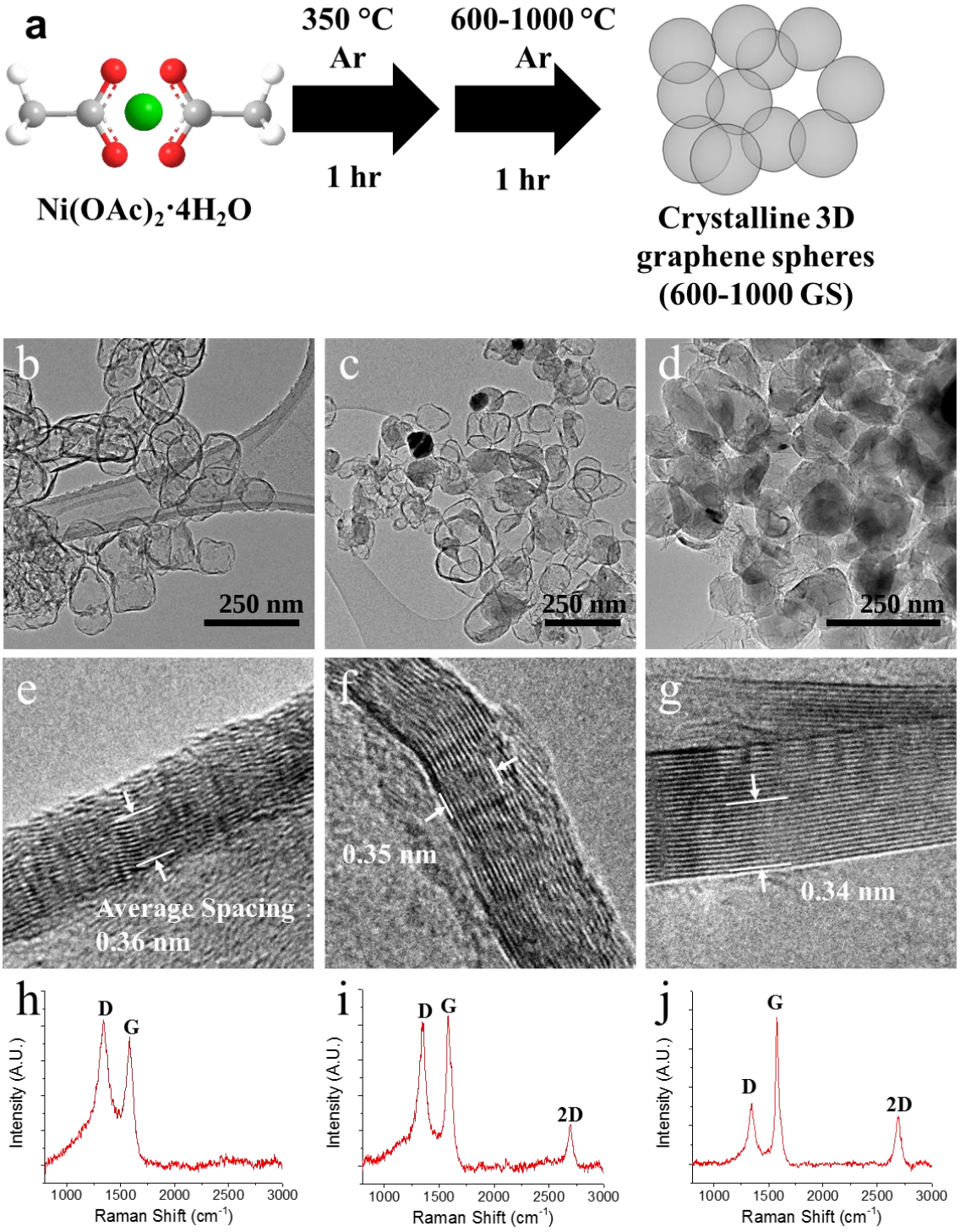

Figure 12. a) Schematic diagram showing the two-stage heating process to produce crystalline graphene spheres (b-d) Low magnification TEM images showing the graphene shells in a) 350GS b) 600GS and c) 1000GS. (e-g) High magnification TEM images showing the walls and average graphene interlayer spacing in d) 350GS e) 600GS and f) 1000GS. (h-j) Representative Raman spectra of h) 350GS i) 600GS and j) 1000GS. Scale bars: (b-d) 250 nm.

In order to understand the formation mechanisms of these materials, a slow heating procedure was used to try and form 1000GS-CNT instead of rapid heating. Figure 13 shows SEM images of the structures obtained when the nickel acetate is heated at 50 °C/min, rather than sudden introduction into the hot zone of the furnace. Significant portions of the structure have sintered together to form large chunks of nickel and no nanotubes can be seen in the sample. It is likely that, in the slow annealing procedure, all the carbon containing gases have been removed from the furnace long before the nickel reaches the temperature required to catalyse the formation of nanotubes. Any graphene formed during this process likely comes from the carbon dissolved in nickel during the gradual heating. The growth of CNTs using nickel as a catalyst relies on the precipitation of carbon from one side of a nickel particle as more carbon dissolves in the opposite side.[16] This requirement for a constant supply of carbon suggests that the carbon containing gases produced during the acetate decomposition step are utilised by the nickel particles to form the CNTs. To confirm the utilisation of the acetate decomposition products by the nickel particles, the weights of 350GS, 600GS-CNT and 1000GS-CNT were compared before and after chemical etching. It was found that 5.2 wt% of the nickel-carbon product after synthesis was retained following the chemical etching process for 350GS. For 600GS-CNT and 1000GS-CNT, the etched products were found to have retained 6.6 % and 14.3 % of the pre-etching weight respectively. This takes into account the differences in remaining nickel, as determined by

TGA. This suggests that more carbon from the acetate decomposition products is retained when the sample is introduced into the hot zone at a higher temperature. A calculation indicates that if the carbon dissolved in nickel was the sole carbon source, the yield post-etching would be ~6.4% compared to pre-etching, assuming a stoichiometry of Ni_3C, nickel carbide. This implies that at low annealing temperatures, all of the carbon in the product comes from the carbon retained by nickel during decomposition, whereas at an annealing temperature of 1000 °C most of the carbon is from gases generated during decomposition. The fact that the wt% carbon is lower for 350GS compared to the % carbon for the nickel carbide described in the literature may be due to removal of carbon from the nickel by hydrogen gas produced during decomposition, which may not occur when nickel acetate is heated up slowly.

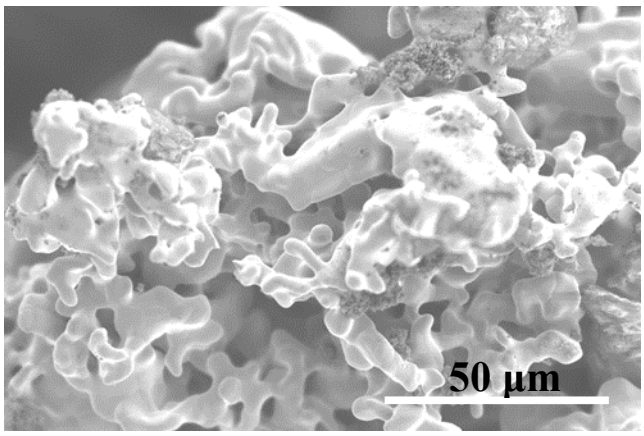

Figure 13. SEM image showing the result of gradual heating of nickel acetate at a rate of 50 °C/min to 1000 °C instead of rapid heating. Scale bar: 50 µm.

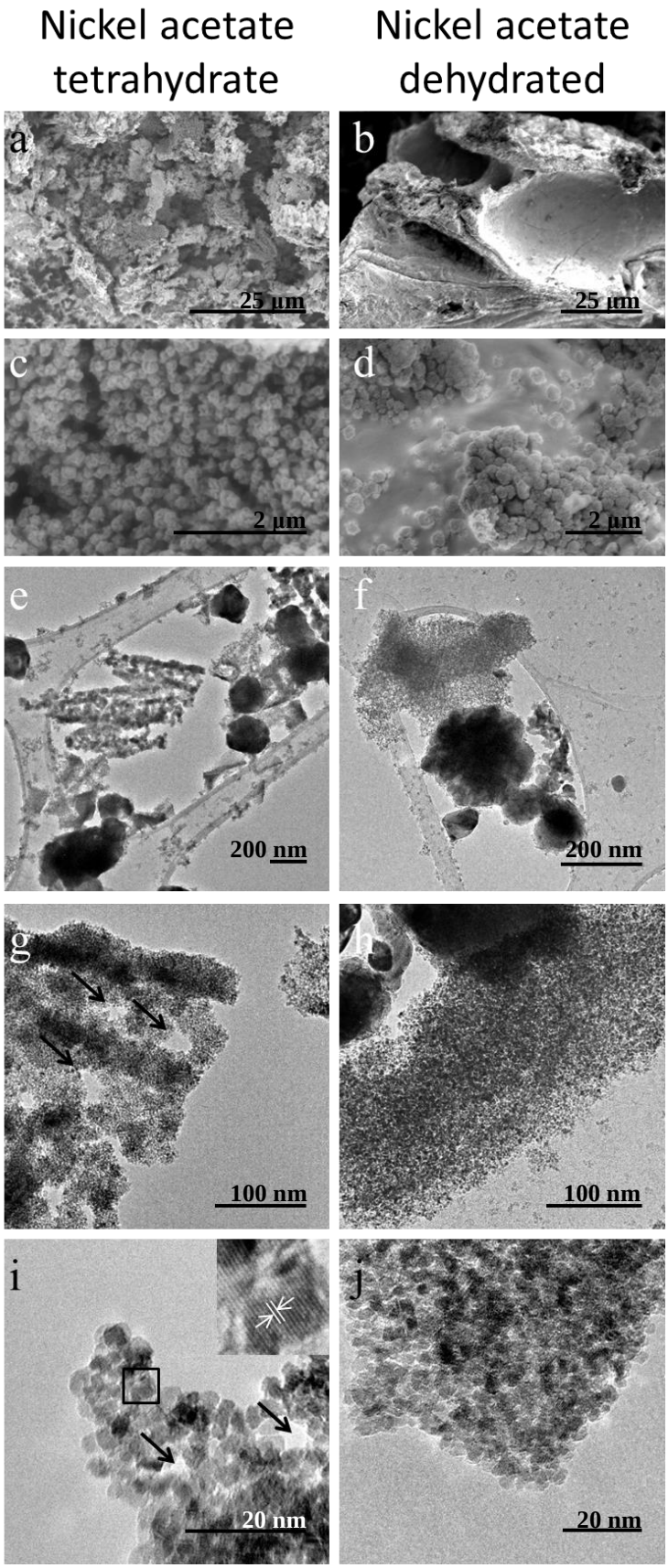
Nickel acetate tetrahydrate
Nickel acetate dehydrated
a
25 µm
b
25 µm
c
2 µm
d
2 µm
e
200 nm
f
200 nm
g
100 nm
h
100 nm
i
20 nm
j
20 nm

Figure 14. Comparison of products of hydrated and dehydrated nickel acetate after heating at 350 °C for 20 minutes. (a,c) SEM images of the hydrated sample. (b,d) SEM images of the sample that was dehydrated prior to heating. (e, g, i) TEM images of the hydrated sample, the arrows in (g) and (i) show pores in the material, the inset of (i) shows a nickel crystal, the lattice measurement is 0.2 nm. (f, h, j) TEM images of the dehydrated sample. Scale bars: (a) 25 μm (b) 25 μm (c) 2 μm (d) 2 μm (e) 200 nm (f) 200 nm (g) 100 nm (h) 100 nm (i) 20 nm (j) 20 nm.

The presence of CNTs and larger graphene sheets in 1000GS-CNT instead of just spheres in 350GS can be explained as follows; when the nickel acetate is introduced at a higher temperature into the hot zone of the furnace, increased sintering of the particles occurs, generating large particles of nickel which form the larger graphene spheres, some of which break into the sheets observed in 1000GS-CNT. However, the nickel on the top of the sample reaches the necessary temperature to catalyse the formation of graphitic structures in a shorter amount of time, which allows more carbon from the decomposition of acetate groups in the lower regions of the sample to be utilised relative to the annealing process at lower temperatures, which allows the formation of carbon nanotubes. This also explains the lower proportion of nanotubes seen in samples at lower temperatures, such as at 600 °C where fewer nanotubes are seen.

There is also some evidence that the rapid introduction into the furnace plays a role in determining the porosity of the structures. Figure 14 shows product obtained from samples of nickel acetate annealed at 350 °C for 20 minutes, which is the shortest amount of time needed for decomposition at this temperature judging by visual appearance. In one case the nickel acetate was dehydrated beforehand via heating in an inert atmosphere at 100 °C, prior to rapid introduction at 350 °C. This allowed water to be removed from the precursor

without any decomposition of the acetate group. SEM images in both samples show obvious differences, with the dehydrated sample having larger aggregates than the hydrated one and fewer obvious holes (Figure 14a-d). TEM images show that for both samples particles with large and small sizes have been formed (Figure 14e-f). Black arrows mark holes that are seen in the aggregates of small particles, which are regularly seen in the hydrated sample but not in the dehydrated sample (Figure 14g-j). It can be assumed that the departure of water during the earliest stages of the annealing procedure is responsible for creating space between the newly forming nickel particles.

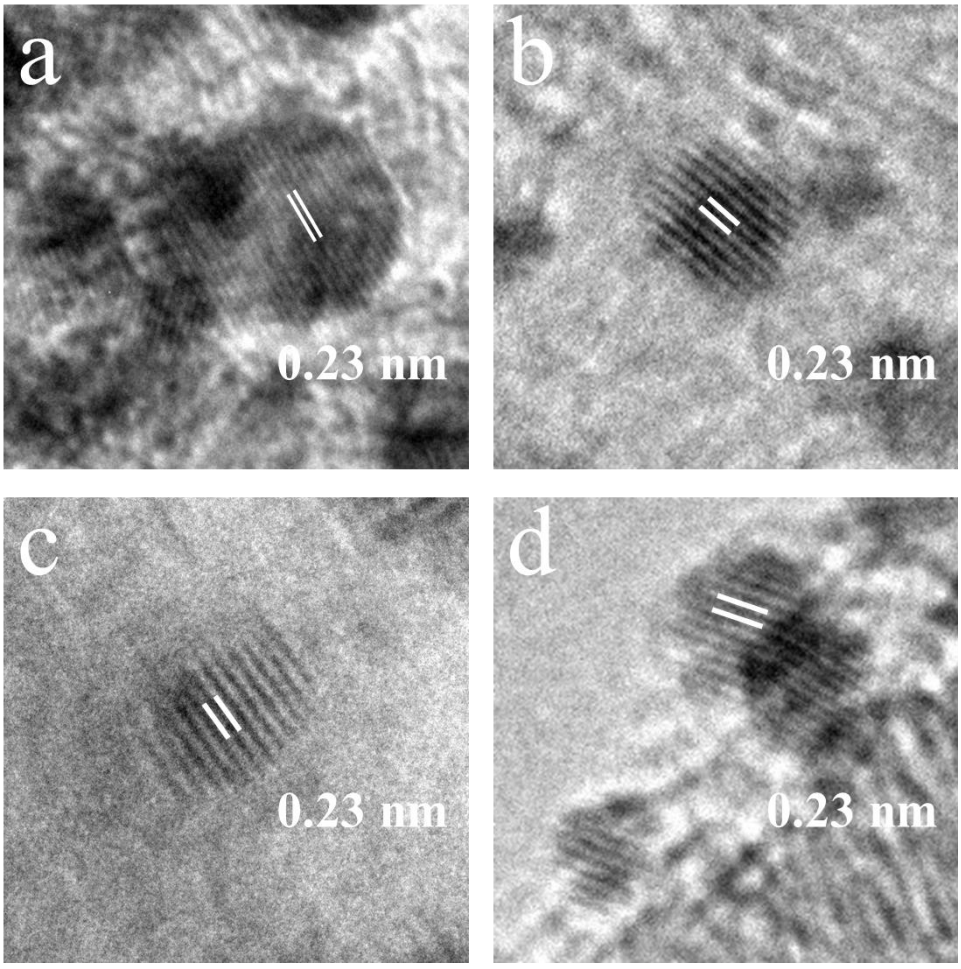

Figure 15. HRTEM images of Pt Nanocrystals synthesised on a) Vulcan XC-72R b) 350GS c) 600GS-CNT d) 1000GS-CNT. The white bars and measurement corresponds to the (111) lattice spacing of Pt.

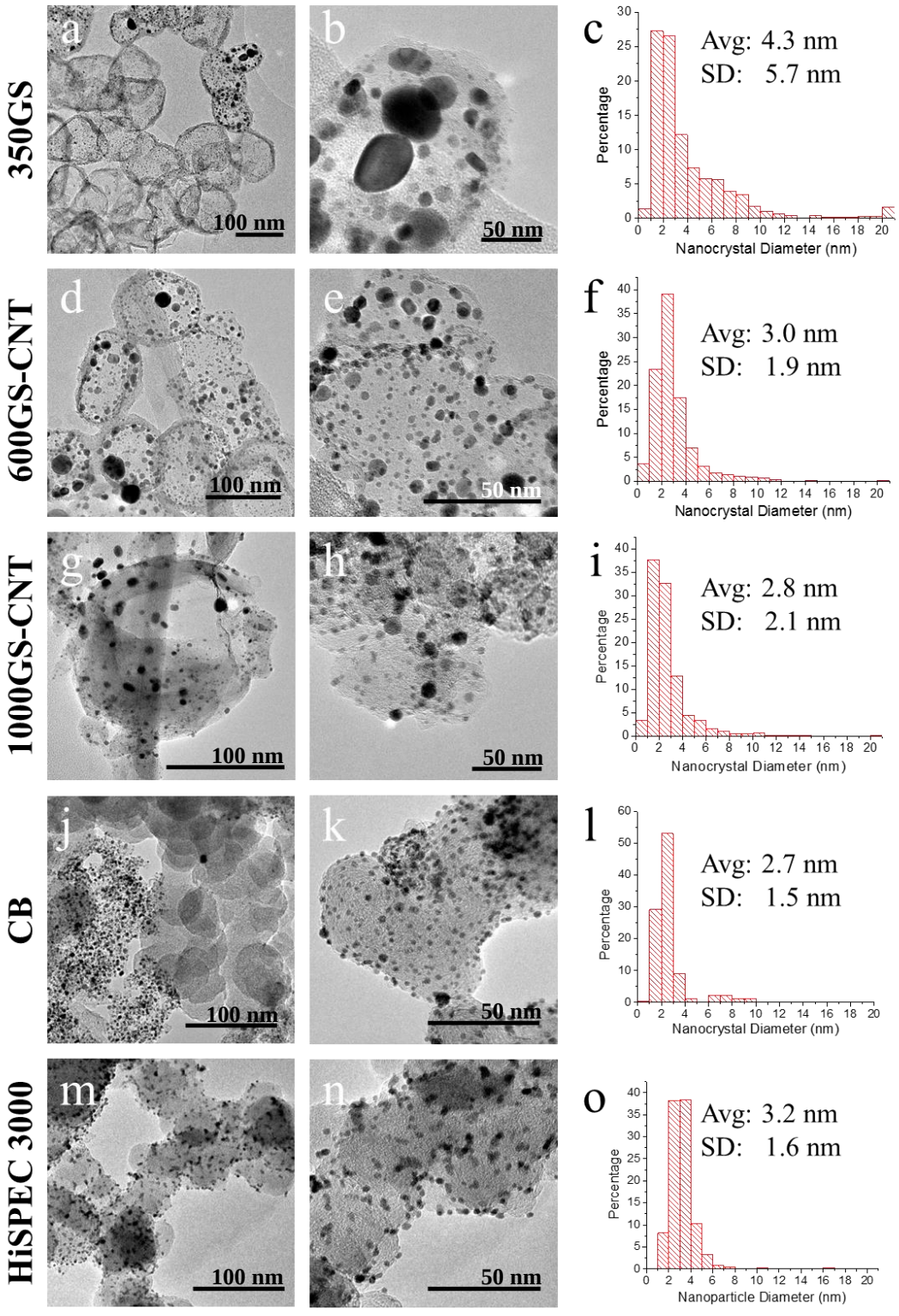

Figure 16. TEM of as-fabricated catalysts. Low magnification images, high magnification TEM images and particle size histograms with averages and standard deviations for 350GS (**a-c**), 600GS-CNT (**d-f**), 1000GS-CNT (**g-i**), CB (**j-l**) and HiSPEC 3000 (**m-o**). Nanoparticles with >20 nm

diameter are grouped for clarity. Scale bars: (a) 100 nm (b) 50 nm (d) 100 nm (e) 50 nm (g) 100 nm (h) 50 nm (j) 100 nm (k) 50 nm (m) 100 nm (n) 50 nm.

In order to demonstrate the use of the novel carbon materials, 350GS, 600GS-CNT and 1000GS-CNT along with commercial carbon black (CB, Vulcan XC-72R) were utilised as catalyst supports for Pt crystals synthesised using a thermal annealing (TA) approach. In the TA synthesis method, the carbon support is mixed with H_2PtCl_6 precursor solution and left to dry. The resultant powder is then annealed at 400 °C in a reducing atmosphere (H_2/Ar) to form Pt crystals over the surface of the support. Previous work indicates this takes place via a mechanism where individual atoms move over the carbon surface before colliding to form clusters.[35] High magnification TEM image of Pt nanocrystals produced by this method on different carbon supports can be seen in Figure 15. The measured lattice spacing of 0.23 nm corresponding to Pt (111) is slightly larger than that seen in some studies (0.224 nm[36, 37]) though it has been shown that strain can increase the lattice spacing for small Pt crystals on supports.[38] TGA results for the materials indicate that the Pt wt% for the catalysts was 16.53, 16.07, 15.74 and 15.34% for CB, 350GS, 600GS-CNT and 1000GS-CNT, respectively. HiSPEC 3000, a commercial catalyst, was determined to have a Pt wt% of 20.72%. Figure 16 shows TEM images of the resultant materials following annealing at different magnifications, along with nanocrystal size distributions. Also included is data from the commercial Pt catalyst, HiSPEC 3000. It can be seen from the low magnification TEM images that the distribution of crystals over the surface is not uniform for 350GS and CB, many regions of the carbon support remain uncovered by Pt crystals. The reason for this might be the formation mechanism and the graphitic quality of the carbon supports. Previous work also indicates that functional groups and defects on the support surface act as nucleation sites to strongly bind Pt crystals.[39, 40] If the formation mechanism indeed involves the

movement of atoms over the surface, it can be expected that the mean free path of these species is decreased on surfaces which are more defective, as is the case with 350GS and CB relative to 600GS-CNT and 1000GS-CNT. Whilst more defective graphitic surfaces are associated with smaller nanocrystals compared to pristine graphitic surfaces when solution based crystal synthesis methods are utilised,[39] we find that a wider size distribution with larger crystals are found on 350GS than on the more crystalline GS-CNT surfaces. This could also be attributed to the formation mechanism, once the precursor dries on the carbon surface, it can be expected to form aggregates instead of equally coating the whole of the carbon surface. A low mean free path for Pt atoms will result in large numbers of Pt crystals in close proximity, which could quickly sinter during the 30 minute growth period. Despite the dispersion issues with 350GS and CB, the average nanocrystal diameters for all samples was under 5 nm, though standard deviations in nanocrystals size for 350GS was much larger than for other supports.

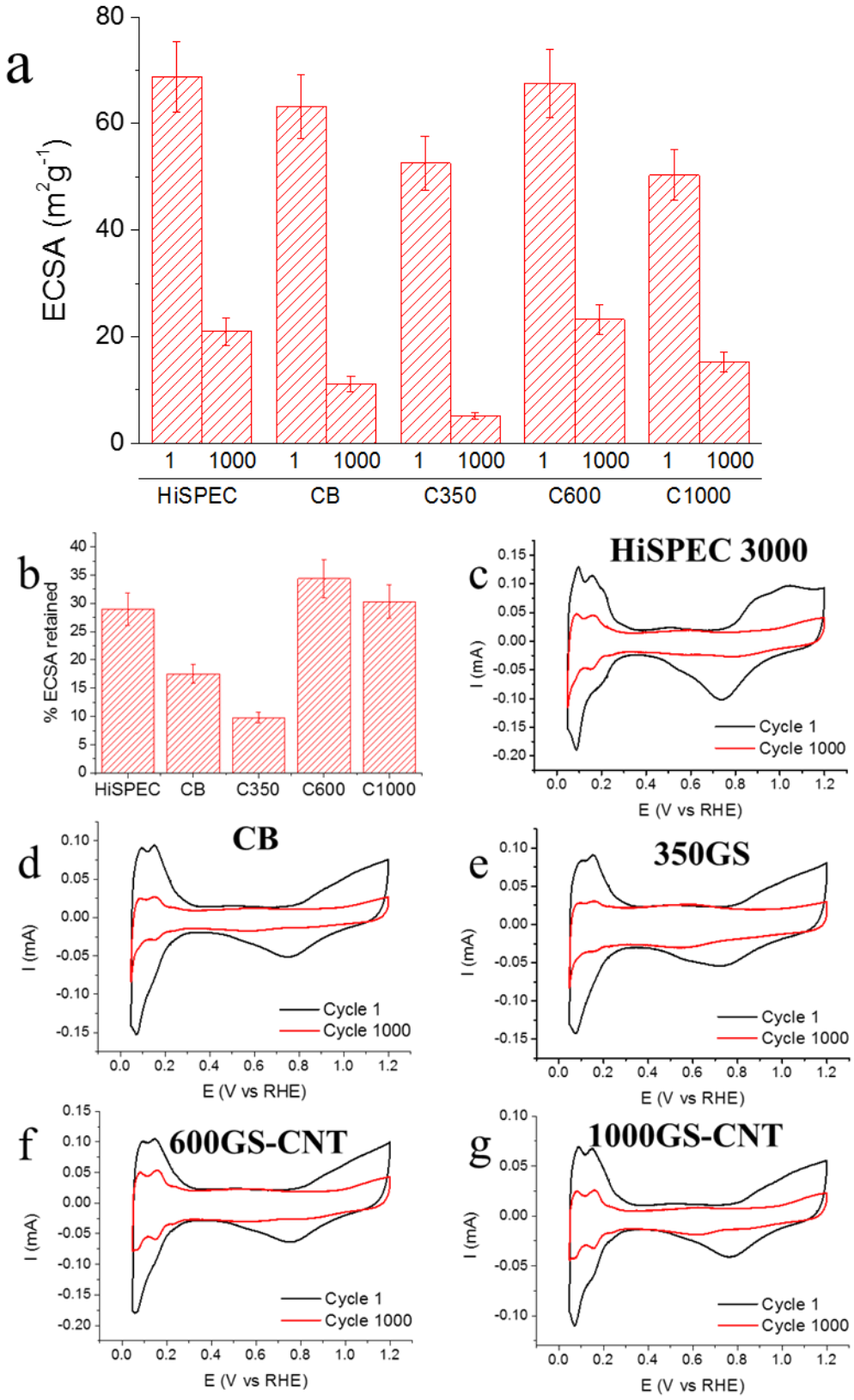

Figure 17. Electrochemical testing of Pt/C catalysts. a) Initial (1st cycle following activation) and final (1000th cycle) ECSAs for all tested catalysts. Error bars for HiSPEC 3000 represent the standard

deviations, while error bars for other samples are estimated based on the HiSPEC standard deviation. b) Graph showing the % ECSA retained by the catalysts after 1000 cycles, the error bar for HiSPEC is the standard deviation which was used to estimate the error in other samples. c-g) Cyclic voltammograms showing the initial and final voltammograms for HiSPEC 3000, CB (Vulcan XC-72R), 350GS, 600GS-CNT and 1000GS-CNT respectively.

Cyclic voltammetry (CV) measurements were recorded to evaluate the electrochemically active surface areas (ECSAs) and durabilities of the catalysts (see Experimental section). The initial and final ECSAs of the catalysts, along with their cyclic voltammograms and a graph of % ECSA retained following 1000 cycles are shown in Figure 17. The trend for initial ECSA follows the trend HiSPEC 3000 ≈ 600GS-CNT ≈ CB > 350GS ≈ 1000GS-CNT. The final ECSA follows the trend 600GS-CNT ≈ HiSPEC 3000 > 1000GS-CNT > CB > 350GS. In terms of the relative final ECSA as a percentage of original ECSA, the trend is 600GS-CNT ≈ 1000GS-CNT ≈ HiSPEC 3000 > CB > 350GS. Due to the many differences between the catalysts, for example their surface areas, catalyst size and distribution, support morphologies and the presence of CNTs in varying amounts, it is difficult to attribute the ECSAs and durability to any single factor. It should be noted that the supports with poor initial catalyst dispersion (CB and GS350) had the lowest ECSA both in absolute and relative terms after 1000 cycles, this could be due to poor dispersion resulting in closer crystals, which sinter more rapidly and result in higher ECSA loss.[41] The results show that 600GS-CNT had similar initial, final, and relative ECSAs compared to HiSPEC 3000. 1000GS-CNT had a similar final relative ECSA to HiSPEC 3000 and 600GS-CNT, though its low initial ECSA means that it shows inferior performance in absolute terms. Post-cycling TEM results were recorded for each sample (Figure 18). It should be noted that despite the higher average nanocrystal diameters post-cycling for 600GS-CNT and 1000GS-CNT, these catalysts had

higher final ECSAs than CB and 350GS. This indicates superior attachment of crystals in the case of the GS-CNT supports, it should be noted that the population of crystals with sizes >8 nm is very small for CB and 350GS post cycling, indicating that crystals on these supports are more likely to detach from the surface than migrate on the surface compared to GS-CNT supports. Previous work suggests that carbon supports with a higher degree of graphitisation, such as the GS-CNT supports, are more resistant to corrosion in acidic environments,[33] which is known to contribute to detachment of Pt nanocrystals from carbon surfaces.[42] It would be useful to compare these supports for the growth of Pt crystals via solution methods which can give more uniform Pt crystal size and which could provide better dispersion over 350GS, in order to give greater insight into the role of the support crystallinity in determining catalyst durability.

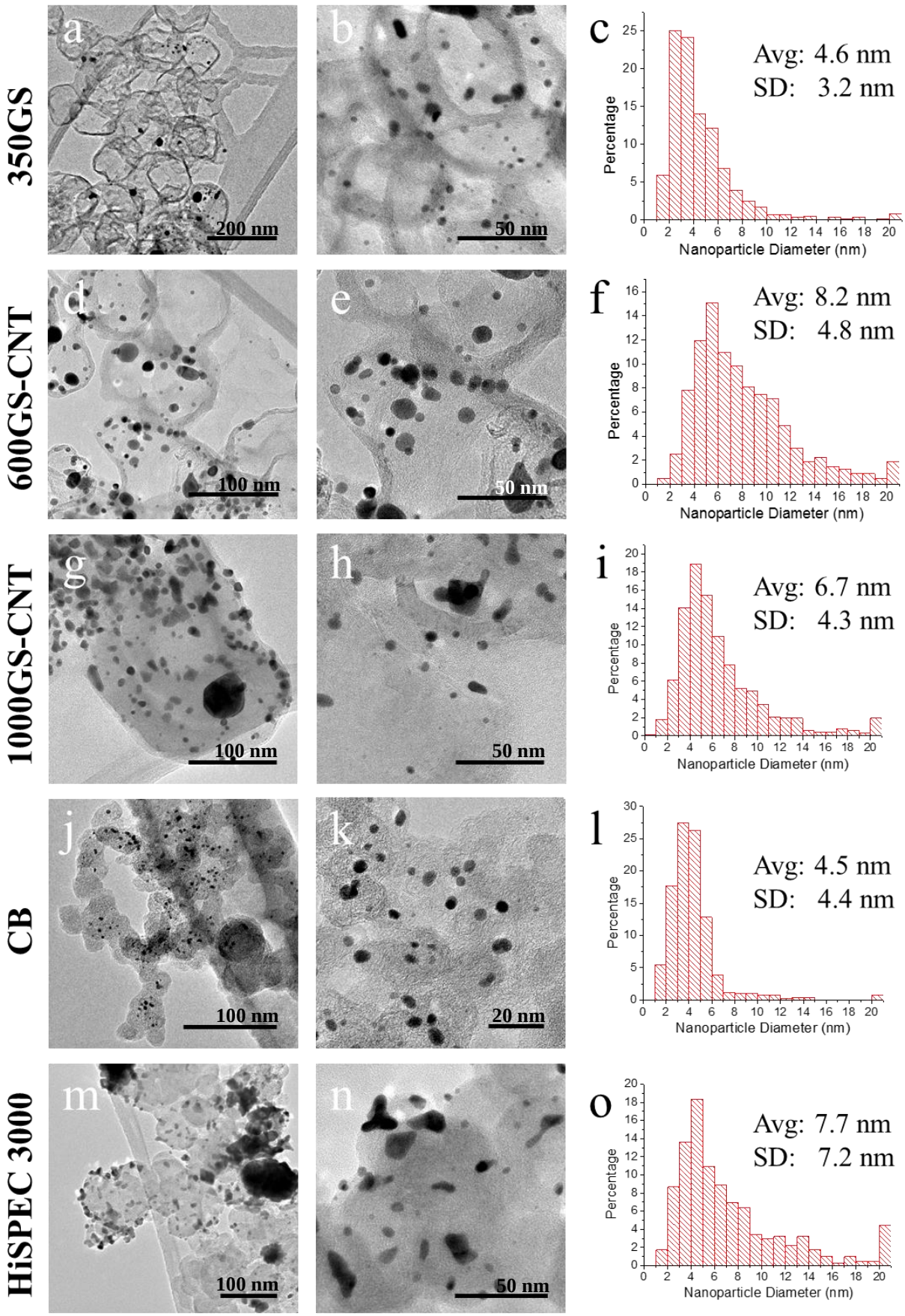
350GS
600GS-CNT
1000GS-CNT
CB
HiSPEC 3000
a
b
c
d
e
f
g
h
i
j
k
l
m
n
o
200 nm
50 nm
100 nm
50 nm
100 nm
50 nm
100 nm
20 nm
100 nm
50 nm
Avg: 4.6 nm
SD: 3.2 nm
Avg: 8.2 nm
SD: 4.8 nm
Avg: 6.7 nm
SD: 4.3 nm
Avg: 4.5 nm
SD: 4.4 nm
Avg: 7.7 nm
SD: 7.2 nm
Percentage
Nanoparticle Diameter (nm)

Figure 18. TEM of catalysts after electrochemical cycling. Low magnification images, high magnification TEM images and particle size histograms with averages and standard deviations for 350GS (a-c), 600GS-CNT (d-f), 1000GS-CNT (g-i), CB (j-l) and HiSPEC 3000 (m-o). Nanoparticles with >20 nm diameter are grouped for clarity. Scale bars: (a) 200 nm (b) 50 nm (d) 100 nm (e) 50 nm (g) 100 nm (h) 50 nm (j) 100 nm (k) 20 nm (m) 100 nm (n) 50 nm.

5.5 Conclusions

We have demonstrated the synthesis of multi-layered graphene spheres and graphene-CNT hybrid materials via annealing of nickel acetate, a cheap and readily available nickel compound. The nickel acetate decomposes to generate the catalyst/template and carbon feedstock in this process in-situ. In the presence of carbon, newly formed nickel particles catalysed the formation of graphene or carbon nanotubes, depending on the conditions. The sudden introduction of the acetate to the hot zone of the furnace was shown to be a key factor in the formation of these structures. This scalable method allows the crystalline quality of the material to be tuned by utilising different annealing times and temperatures, as indicated by TEM and Raman. Using high annealing temperatures, we have shown it is possible to produce materials which comprise high quality multi-layered graphene and CNTs. This method demonstrates a way to produce graphene spheres without requiring pre-formed nickel particles, and allows hybrid materials to be formed in a single step. The possibility of using other metal salts and varying the synthesis conditions may allow materials with other morphologies, decreased layer numbers and substitutional dopant atoms to be fabricated, for example, using copper salts in conjunction with nickel acetate may facilitate a reduction in layer number, and the addition of solid nitrogen containing nickel precursors such as nickel (II) dimethylglyoxime may allow the formation of crystalline nitrogen-doped graphitic

materials. The materials formed may be useful in electrochemical applications, where three-dimensional graphene and graphene-CNT hybrid materials have advantageous properties and where scalable processes are required. We utilised some of these materials as supports for the thermal annealing growth of Pt nanocrystals, where in some cases they exhibited superior performance to Vulcan XC-72 and showed comparable performance to HiSPEC 3000, a commercial catalyst, demonstrating the potential of this synthesis method.

5.6 References

(1) Antolini, E. Graphene as a new carbon support for low-temperature fuel cell catalysts. *Appl. Catal. B-Environ.* **2012**, *123*, 52-68.

(2) Antolini, E. Carbon supports for low-temperature fuel cell catalysts. *Appl. Catal. B-Environ.* **2009**, *88*, 1-24.

(3) Kucinskis, G.; Bajars, G.; Kleperis, J. Graphene in lithium ion battery cathode materials: A review. *J. Power Sources* **2013**, *240*, 66-79.

(4) Zhang, X.; Zhang, H.; Li, C.; Wang, K.; Sun, X.; Ma, Y. Recent advances in porous graphene materials for supercapacitor applications. *RSC Adv.* **2014**, *4*, 45862-45884.

(5) Lee, J. H.; Park, N.; Kim, B. G.; Jung, D. S.; Im, K.; Hur, J.; Choi, J. W. Restacking-Inhibited 3D Reduced Graphene Oxide for High Performance Supercapacitor Electrodes. *ACS Nano* **2013**, *7* (10), 9366-9374.

(6) Mao, S.; Lu, G.; Chen, J. Three-dimensional graphene-based composites for energy applications. *Nanoscale* **2015**, *7*, 6924-6943.

(7) Chen, Z. P.; Ren, W. C.; Gao, L. B.; Liu, B. L.; Pei, S. F.; Cheng, H. M. Three-dimensional flexible and conductive interconnected graphene networks grown by chemical vapour deposition. *Nat. Mater.* **2011**, *10*, 424-428.

(8) Sha, J.; Gao, C.; Lee, S.-K.; Li, Y.; Zhao, N.; Tour, J. M. Preparation of Three-Dimensional Graphene Foams Using Powder Metallurgy Templates. *ACS Nano* **2016**, 10 (1), 1411-1416.

(9) Chen, S.; Chen, P.; Wang, Y. Carbon nanotubes grown in situ on graphene nanosheets as superior anodes for Li-ion batteries. *Nanoscale* **2011**, *3*, 4323-4329.

(10) Liu, J.; Zhang, L.; Wu, H. B.; Lin, J.; Shen, Z.; Lou, X. W. High-performance flexible asymmetric supercapacitors based on a new graphene foam/carbon nanotube hybrid film. *Energy Environ. Sci.* **2014**, *7*, 3709-3719.

(11) Cheng, Q.; Tang, J.; Ma, J.; Zhang, H.; Shinya, N.; Qin, L.-C. Graphene and carbon nanotube composite electrodes for supercapacitors with ultra-high energy density. *Phys. Chem. Chem. Phys.* **2011**, *13*, 17615-17624.

(12) Yang, J.; Sun, H.; Liang, H.; Ji, H.; Song, L.; Gao, C.; Xu, H. A Highly Efficient Metal-Free Oxygen Reduction Electrocatalyst Assembled from Carbon Nanotubes and Graphene. *Adv. Mater.* **2016**, *28*, 4606-4613.

(13) Stephens, I. E. L.; Bondarenko, A. S.; Grønbjerg, U.; Rossmeisl, J.; Chorkendorff, I. Understanding the electrocatalysis of oxygen reduction on platinum and its alloys. *Energy Environ. Sci.*, **2012**, 5, 6744-6762.

(14) Sheng, W. C.; Gasteiger, H. A.; Shao-Horn, Y. J. Hydrogen Oxidation and Evolution Reaction Kinetics on Platinum: Acid vs Alkaline Electrolytes. *Electrochem. Soc.* **2010**, 157 (11), B1529–B1536.

(15) De Jesus, J. C.; González, I.; Quevedo, A.; Puerta, T. Thermal decomposition of nickel acetate tetrahydrate: an integrated study by TGA, QMS and XPS techniques. *Journal of Molecular Catalysis A: Chemical* **2005**, *228* , 283-291.

(16) Kumar, M.; Ando, Y. Chemical Vapor Deposition of Carbon Nanotubes: A Review on Growth Mechanism and Mass Production. *J. Nanosci. Nanotechnol.* **2010**, *10* (6), 3739-3758.

(17) Mattevi, C.; Kim, H.; Chhowalla, M. A review of chemical vapour deposition of graphene on copper. *J. Mater. Chem.* **2011**, *21*, 3324-3334.

(18) Nikolaev, P.; Bronikowski, M. J.; Bradley, R. K.; Rohmund, F.; Colbert, D. T.; Smith, K. A.; Smalley, R. E. Gas-phase catalytic growth of single-walled carbon nanotubes from carbon monoxide. *Chem. Phys. Lett.* **1999**, *313* (1–2), 91-97.

(19) Losurdo, M.; Giangregorio, M. M.; Capezzuto, P.; Bruno, G. Graphene CVD growth on copper and nickel: role of hydrogen in kinetics and structure. *Phys. Chem. Chem. Phys.* **2011**, *13*, 20836-20843.

(20) Behr, M. J.; Gaulding, E. A.; Mkhoyan, K. A.; Aydil, E. S. Effect of hydrogen on catalyst nanoparticles in carbon nanotube growth. *J. Appl. Phys.* **2010**, *108*, 053303.

(21) Baraton, L.; He, Z. B.; Lee, C. S.; Cojocaru, C. S.; Châtelet, M.; Maurice, J. L.; Lee, Y. H.; Pribat, D. On the mechanisms of precipitation of graphene on nickel thin films. *Europhys. Lett.* **2011**, *96*, 46003.

(22) Goh, B.-M.; Wang, Y.; Reddy, M. V.; Ding, Y. L.; Lu, L.; Bunker, C.; Loh, K. P. Filling the Voids of Graphene Foam with Graphene "Eggshell" for Improved Lithium-Ion Storage. *ACS Appl. Mater. Interfaces* **2014**, *6*, 9835-9841.

(23) Sun, Z. Z.; Yan, Z.; Yao, J.; Beitler, E.; Zhu, Y.; Tour, J. M. Growth of graphene from solid carbon sources. *Nature* **2010**, *468* , 549-552.

(24) Galwey, A. K.; McKee, S. G.; Mitchell, T. R. B.; Brown, M. E.; Bean, A. F. A kinetic and mechanistic study of the thermal decomposition of nickel acetate. *React. Solids* **1988**, 6, 173-186

(25) Mohamed, M. A.; Halawy, S. A.; Ebrahim, M. M. Non-isothermal decomposition of nickel acetate tetrahydrate. *J. Anal. Appl. Pyrolysis* **1993**, 27, 109-118.

(26) Bayer, B. C.; Bosworth, D. A.; Michaelis, F. B.; Blume, R.; Habler, G.; Abart, R.; Weatherup, R. S.; Kidambi, P. R.; Baumberg, J. J.; Knop-Gericke, A.; Schloegl, R.; Baehtz, C.; Barber, Z. H.; Meyer, J. C.; Hoffman, S. In Situ Observations of Phase Transitions in Metastable Nickel (Carbide)/ Carbon Nanocomposites. *J. Phys. Chem. C* **2016**, 120 (39), 22571-22584.

(27) Shibuta, Y.; Elliott, J. A. Interaction between graphene and nickel(111) surfaces with commensurate and incommensurate orientational relationships. *Chem. Phys. Lett.* **2012**, *538*, 112-117.

(28) Hayashi, T.; O'Connor, T. C.; Higashiyama, K.; Nishi, K.; Fujisawa, K.; Muramatsu, H.; Kim, Y. A.; Sumpter, B. G.; Meunier, V.; Terrones, M.; Endo, M. A reversible strain-induced electrical conductivity in cup-stacked carbon nanotubes. *Nanoscale* **2013**, *5*, 10212-10218.

(29) Spyrou, K.; Rudolf, P. An Introduction to Graphene. In *Functionalization of Graphene*, Wiley-VCH Verlag GmbH & Co. KGaA: Weinheim, 2014; pp 1-20.

(30) Worsley, M. A.; Pham, T. T.; Yan, A.; Shin, S. J.; Lee, J. R. I.; Bagge-Hansen, M.; Mickelson, W.; Zettl, A. Synthesis and Characterization of Highly Crystalline Graphene Aerogels. *ACS Nano* **2014**, 8 (10), 11013-11022.

(31) Li, Y.; Zhang, X. B.; Tao, X. Y.; Xu, J. M.; Huang, W. Z.; Luo, J. H.; Luo, Z. Q.; Li, T.; Liu, F.; Bao, Y.; Geise, H. J. Mass production of high-quality multi-walled carbon nanotube bundles on a Ni/Mo/MgO catalyst. *Carbon* **2005**, *43*, 295-301.

(32) Tang, C.; Zhang, Q. Nanocarbon for Oxygen Reduction Electrocatalysis: Dopants, Edges, and Defects. *Adv. Mater.* **2017**, *29*, 1604103

(33) Castanheira, L.; Silva, W. O.; Lima, F. H. B.; Crisci, A.; Dubau, L.; Maillard, F. Carbon Corrosion in Proton-Exchange Membrane Fuel Cells: Effect of the Carbon Structure, the Degradation Protocol, and the Gas Atmosphere. *ACS Catal.* **2015**, *5* (4), 2184-2194.

(34) Yoon, S.-M.; Choi, W. M.; Baik, H.; Shin, H.-J.; Song, I.; Kwon, M.-S.; Bae, J. J.; Kim, H.; Lee, Y. H.; Choi, J.-Y. Synthesis of Multilayer Graphene Balls by Carbon Segregation from Nickel Nanoparticles. *ACS Nano* **2012**, *6* (8), 6803-6811.

(35) Siburian, R.; Nakamura, J. Formation Process of Pt Subnano-Clusters on Graphene Nanosheets. *J. Phys. Chem. C* **2012**, *116* (43), 22947-22953.

(36) Ding, D.; Song, Z. L.; Cheng, Z. Q.; Liu, W. N.; Nie, X. K.; Bian, X.; Chen, Z.; Tan, W. H. Plasma-assisted nitrogen doping of graphene-encapsulated Pt nanocrystals as efficient fuel cell catalysts. *J. Mater. Chem. A* **2014,** *2* , 472-477.

(37) Zhang, B.; Wang, D.; Hou, Y.; Yang, S.; Yang, X. H.; Zhong, J. H.; Liu, J.; Wang, H. F.; Hu, P.; Zhao, H. J.; Yang, H. G. Facet-Dependent Catalytic Activity of Platinum Nanocrystals for Triiodide Reduction in Dye-Sensitized Solar Cells. *Sci. Rep.* **2013,** *3*, 1836

(38) Daio, T.; Staykov, A.; Guo, L.; Liu, J.; Tanaka, M.; Matthew Lyth, S.; Sasaki, K. Lattice Strain Mapping of Platinum Nanoparticles on Carbon and SnO2 Supports. *Sci Rep* **2015,** *5*, 13126

(39) Xin, L.; Yang, F.; Rasouli, S.; Qiu, Y.; Li, Z.-F.; Uzunoglu, A.; Sun, C.-J.; Liu, Y.; Ferreira, P.; Li, W.; Ren, Y.; Stanciu, L. A.; Xie, J. Understanding Pt Nanoparticle Anchoring on Graphene Supports through Surface Functionalization. *ACS Catal.* **2016**, *6* (4), 2642-2653.

(40) Fampiou, I.; Ramasubramaniam, A. Binding of Pt Nanoclusters to Point Defects in Graphene: Adsorption, Morphology, and Electronic Structure. *J. Phys. Chem. C* **2012**, *116* (11), 6543-6555.

(41) Meier, J. C.; Galeano, C.; Katsounaros, I.; Witte, J.; Bongard, H. J.; Topalov, A. A.; Baldizzone, C.; Mezzavilla, S.; Schüth, F.; Mayrhofer, K. J. J. Design criteria for stable Pt/C fuel cell catalysts. *Beilstein J. Nanotechnol.* **2014**, *5*, 44-67.

(42) Mayrhofer, K. J. J.; Ashton, S. J.; Meier, J. C.; Wiberg, G. K. H.; Hanzlik, M.; Arenz, M. Non-destructive transmission electron microscopy study of catalyst degradation under electrochemical treatment. *J. Power Sources* **2008**, *185* (2), 734-739.

Chapter 6

Influence of CVD Grown Graphene Shells on the Stability of Pt Catalysts on Carbon Supports

* TEM images seen in Figures 2, 4, 5 and 15 were recorded by Dr Alex W. Robertson.

6.1 Introduction

Platinum (Pt) is the most popular catalyst for the hydrogen oxidation reaction (HOR) and the oxygen reduction reaction (ORR) in polymer electrolyte membrane fuel cells (PEMFCs).[1] In addition to the high cost of Pt, the low durability of Pt catalysts under the operating conditions of the cell is also a barrier to the widespread use of PEMFCs. Pt is most frequently supported by carbon materials (with many commercially available catalysts utilising carbon black (CB) supports), where the catalyst degrades by several mechanisms, leading to a loss of activity. These include the dissolution of atoms from Pt crystals and redeposition on other crystals, the migration of crystals across the surface of the support where they coalesce with other crystals, and the detachment of crystals caused by electrochemical corrosion of the support.[2] Many studies have focused on different strategies in order to prevent these mechanisms from occurring.

One strategy with promising results is the physical encapsulation of the particles, thereby preventing them from migrating across or detaching from the support. This has been done using a variety of methods including the formation of particles in-situ inside the pores of hollow graphitic spheres,[3] electrodeposition of metal clusters around Pt crystals,[4] atomic layer deposition (ALD) of metal oxide cages around Pt crystals,[5] and the formation of porous

carbon layers around the Pt crystals.[6] These latter two approaches have also been combined to synergistically enhance durability.[7]

Several examples exist in the literature of porous carbon layers being grown around Pt crystals. This has been done both where the porous carbon encapsulating the crystals is itself the catalyst support,[8,9] and where existing carbon supports or Pt on carbon supports are modified with the carbon layer. The latter approach is most often accomplished by the pyrolysation of polymers over the surface of another catalyst support, which may already have Pt nanocrystals on its surface,[10] or may be added along with the polymer or formed in-situ during pyrolysation.[6,11] This has also been accomplished via the chemical vapour deposition (CVD) approach using acetylene as a precursor to a carbon layer.[12] In these cases, the entirety of the support is modified by a carbon layer which is a couple of nanometres thick and is poorly crystalline. These carbon layers have also been frequently doped with nitrogen which has been credited with enhanced activity for the ORR.[10]

Graphene is another material which has shown promise for increasing the durability of fuel cells. Often, graphene materials have shown superior performance as Pt supports when compared to carbon blacks.[13] Graphene encapsulation of crystals has been used recently in several papers for encapsulating other crystals such as cobalt, where the materials are formed in one step via the pyrolysation of metal organic frameworks (MOFs), the graphene shell has been attributed with forming materials with better durability.[14] Graphitic shells have also been explored for the purpose of Pt catalysts in fuel cells,[8] where the graphene shells simultaneously act as the catalyst support and to encapsulate Pt materials and so the effect of the graphene as the catalyst support cannot be separated from the contribution of the shell to durability.

We grew graphene shells over Pt crystals on a commercial Pt/C catalyst (HiSPEC 3000) using a CVD process. The original motivation for this was to see if existing catalysts could be made more durable by taking advantage of the effects of carbon/graphene layers reported in the literature. We found that we were able to grow the graphene shells on the Pt crystals with minimal sintering of the crystals, and minimal change to the catalyst support as indicated by Raman spectroscopy and thermogravimetric analysis (TGA). This allows the effect of graphene shells on the thermal and electrochemical behaviour of these materials to be studied without interference with other factors that are seen in previous studies. We found that the sintering resistance of the catalysts in reducing atmospheres at high temperature was greatly enhanced relative to that of the as-received catalyst. However, the electrochemical properties in terms of the electrochemically active surface area (ECSA) are only negatively affected by the encapsulation of the Pt crystals with the graphene shells, and the possible explanations for this are discussed.

6.2 Heat Treatment and Synthesis of Graphene Shells on Commercial Pt/C Catalysts

For each experiment, 15 mg of HiSPEC 3000 (Alfa Aesar) was placed into an alumina furnace crucible. The sample was placed in a 1 inch diameter quartz tube in a horizontal tube furnace. A furnace on rails was used so that the sample could be rapidly introduced and removed from the hot zone. During the heat-up procedure, the system was flushed with argon (200 sccm) and hydrogen, H_2 (25% in Ar, 100 sccm). If graphene growth over the Pt crystals was desired, methane was also introduced, CH_4 (20% in Ar, 20 sccm). The H_2 and CH_4 were switched off after 10 minutes whilst flushing with argon continued. During this time the sample remained in the room temperature zone of the furnace. Once the furnace reached the desired temperature, the H_2 (and CH_4 if graphene growth was desired) were

reintroduced and the sample moved to the hot zone of the furnace for 30 minutes. For some samples, a further 90 minute treatment with Ar and H_2 was used. Following the heating period, the H_2 and CH_4 was switched off and the sample was placed back into the room temperature zone of the furnace to allow fast cooling. The sample was removed once the system had cooled.

6.3 Results and Discussion

To explore the possibility of graphene growth on Pt nanocrystals on a Pt/CB catalyst, two initial experiments were performed at 1000 °C for 30 minutes (see above). A H_2/Ar atmosphere was used for both experiments and a small amount of CH_4 was introduced in one experiment as a carbon source for the CVD growth of graphene. Samples subjected to just H_2/Ar are denoted as "heat treated" samples whilst samples with CH_4 (in addition to H_2/Ar) are denoted as "graphene growth" samples, irrespective of whether graphene was found to have formed or not. It should be emphasised that for all furnace experiments carried out in this study, a furnace on rails was used so that samples could be rapidly introduced into and removed from the hot zone of the furnace. This acts to minimise sintering of the crystals that would otherwise occur during the heating and cooling processes by ensuring that the temperature for graphene growth is reached as quickly as possible, and also ensures that the differences in heating exposure times for samples produced at different temperatures are minimised. Figure 1 shows TEM images and nanoparticle size histograms for the as-received HiSPEC 3000, the heat treated sample (1000H) and the graphene growth sample (1000G). From the TEM images, the differences between the heat treated sample and the HiSPEC 3000 and graphene growth samples are obvious. Very large crystals can be seen even in low magnification TEM images (Figure 1d), whilst HiSPEC 3000 and graphene growth samples

appear similar (Figure 1a and g). The particle size histogram for 1000H (Figure 1f) shows that the particles have significantly sintered relative to the as-received HiSPEC 3000 (Figure 1c), having much higher average crystal size and greater standard deviation and with a much smaller relative population of the crystals having diameters less than 5 nm. The TEM images and histogram for 1000G sample (Figure 1g-i) are much more similar to HiSPEC 3000 than to the heat treated sample. Some sintering has occurred, as evidenced by the appearance of some larger crystals (Figure 1h) and by the increase in population of crystals with diameters greater than 4 nm which is accompanied by a slight increase in average size and standard deviation (Figure 1i), though this is much smaller than the increase seen for 1000H. Though there will be some difference in the relative amount of H_2 in the two mixtures of gases due to the addition of CH_4, this difference is probably too small to be responsible for the drastic differences between the samples with and without CH_4. Therefore, we conclude that the suppressed sintering seen in 1000G is due to the effect of Pt catalysed graphene shells, which act to prevent further migration of the crystals over the surface of the support upon formation.

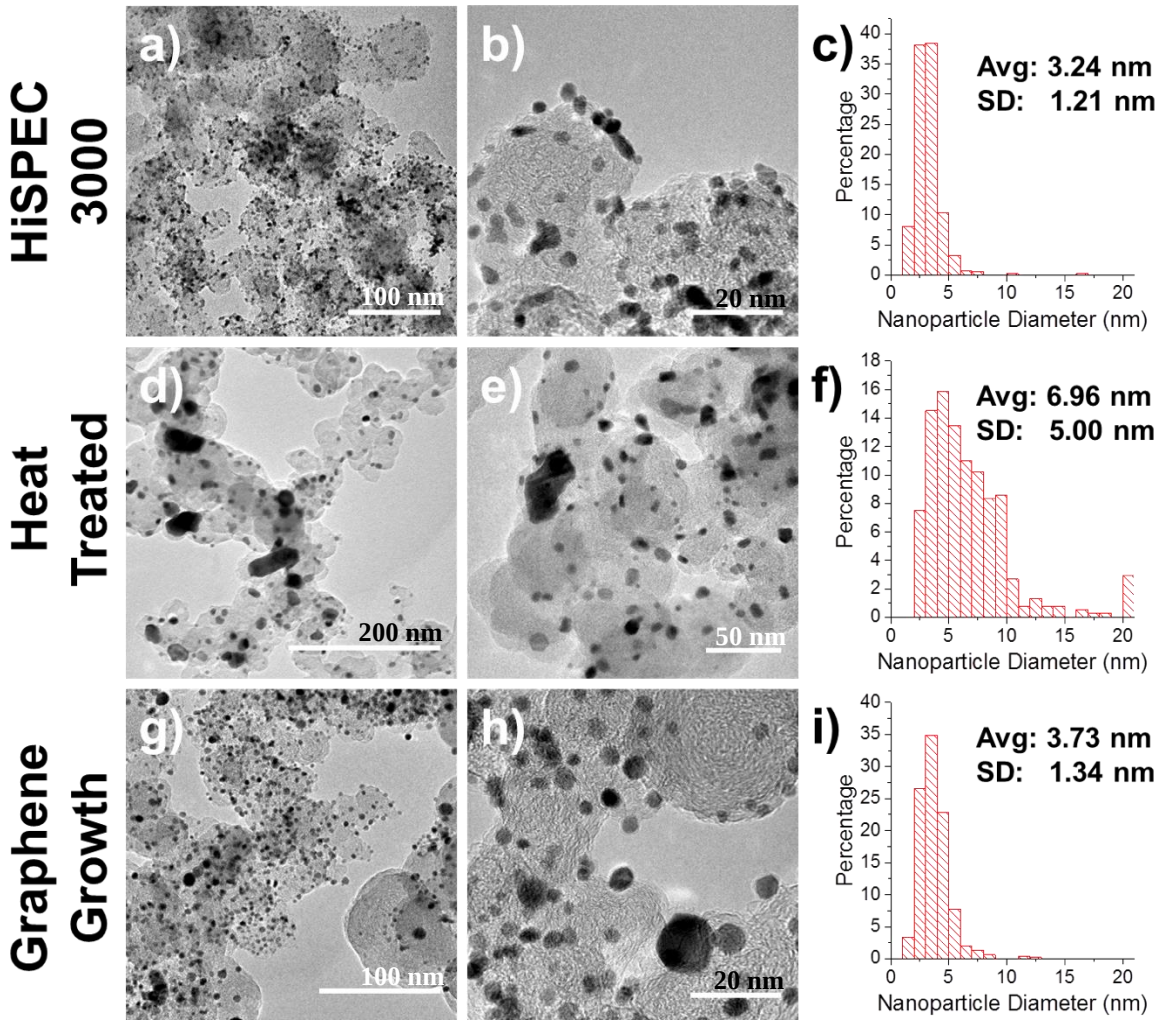

Figure 1. Low magnification TEM images and size-distribution histograms of as-received HiSPEC 3000 and modified catalysts. Both the heating treatment and graphene growth time was 30 minutes. Low magnification TEM images, medium magnification TEM image and particle size histograms of (a,b,c) as-received HiSPEC 3000 (d,e,f) 1000 °C heat treated HiSPEC 3000 and (g,h,i) 1000 °C graphene growth HiSPEC 3000 respectively. Crystals larger than 20 nm are grouped in the histograms for clarity. Scale bars: (a) 100 nm (b) 20 nm (d) 200 nm (e) 50 nm (g) 100 nm (h) 20 nm.

Aberration corrected transmission electron microscopy (ACTEM) was used to examine the differences between the surfaces of the Pt crystals in HiSPEC 3000, 1000H and 1000G, by imaging the edges of the crystals that lay over the vacuum region. Figure 2a shows a Pt crystal from HiSPEC 3000, the edge of the nanocrystal has no obvious covering or modification of the surface. A typical nanocrystal from the 1000H sample (Figure 2b) is similar, though there are some areas of weak contrast on the edge of the crystal; this could be carbon from the support which had dissolved into the Pt at high temperatures and subsequently precipitated. Because the carbon is only seen over some parts of the crystal and that contrast is only on certain crystals suggests that any carbon from the support has not formed complete graphene shells over Pt. All nanocrystals observed for the 1000G sample show obvious signs of graphene growth, as shown in Figure 2c-f. Figure 2c shows a nanocrystal with two lines of contrast around the edge, and a measurement of the distance between these lines of contrast corresponds to the interlayer spacing of graphite (0.34 nm), this deviates slightly in other parts of the shell. Nanocrystals with other layer numbers are seen in the sample, such as monolayer graphene coverage in Figure 2e. A larger nanocrystal in Figure 2f has parts of its edge covered in bilayer and trilayer graphene.

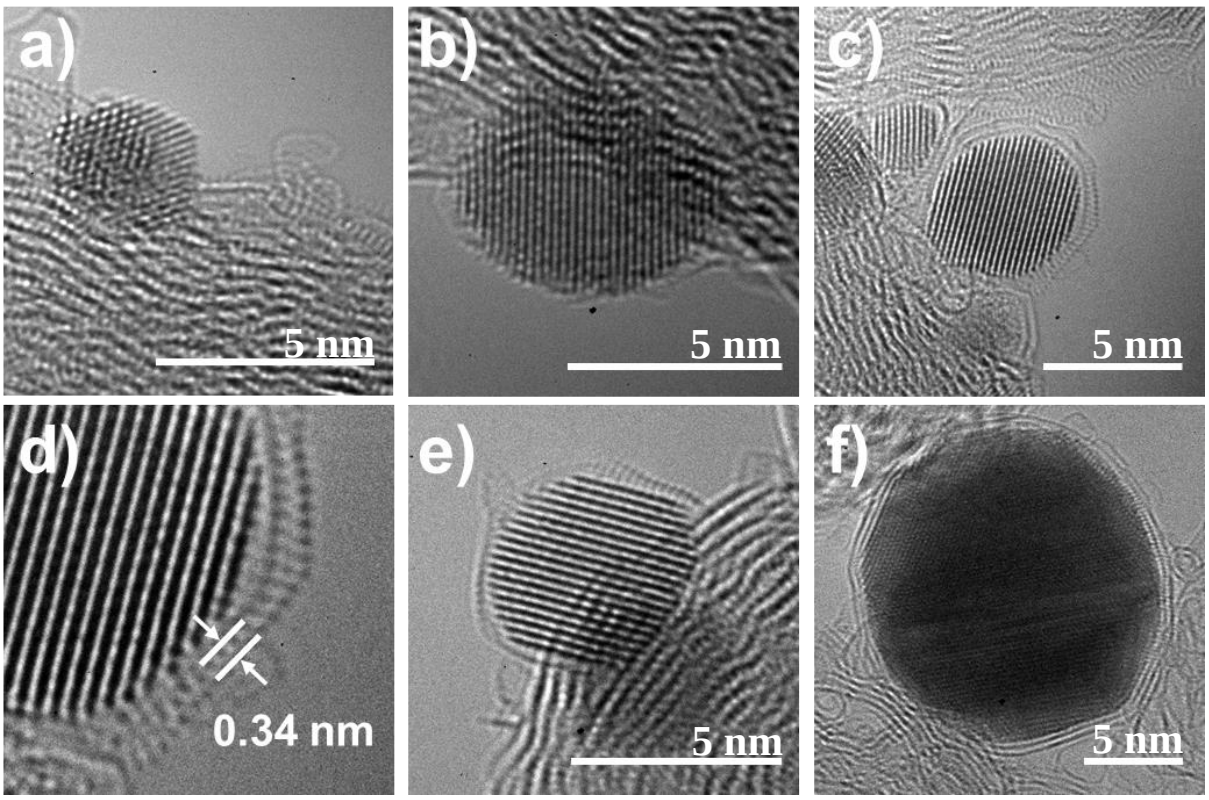

Figure 2. ACTEM images of Pt nanocrystals. a) Pt nanocrystal on unmodified HiSPEC 3000. b) Pt nanocrystal on 1000H. c) Pt nanocrystal on 1000G, the central crystal is covered in bilayer graphene. d) Higher magnification of the edge of the crystal shown in (c), showing the interlayer spacing between the graphene layers. (e) Pt crystal on 1000G showing monolayer graphene. (f) Larger Pt crystal on 1000G, mostly covered in trilayer graphene. Scale bars: 5 nm.

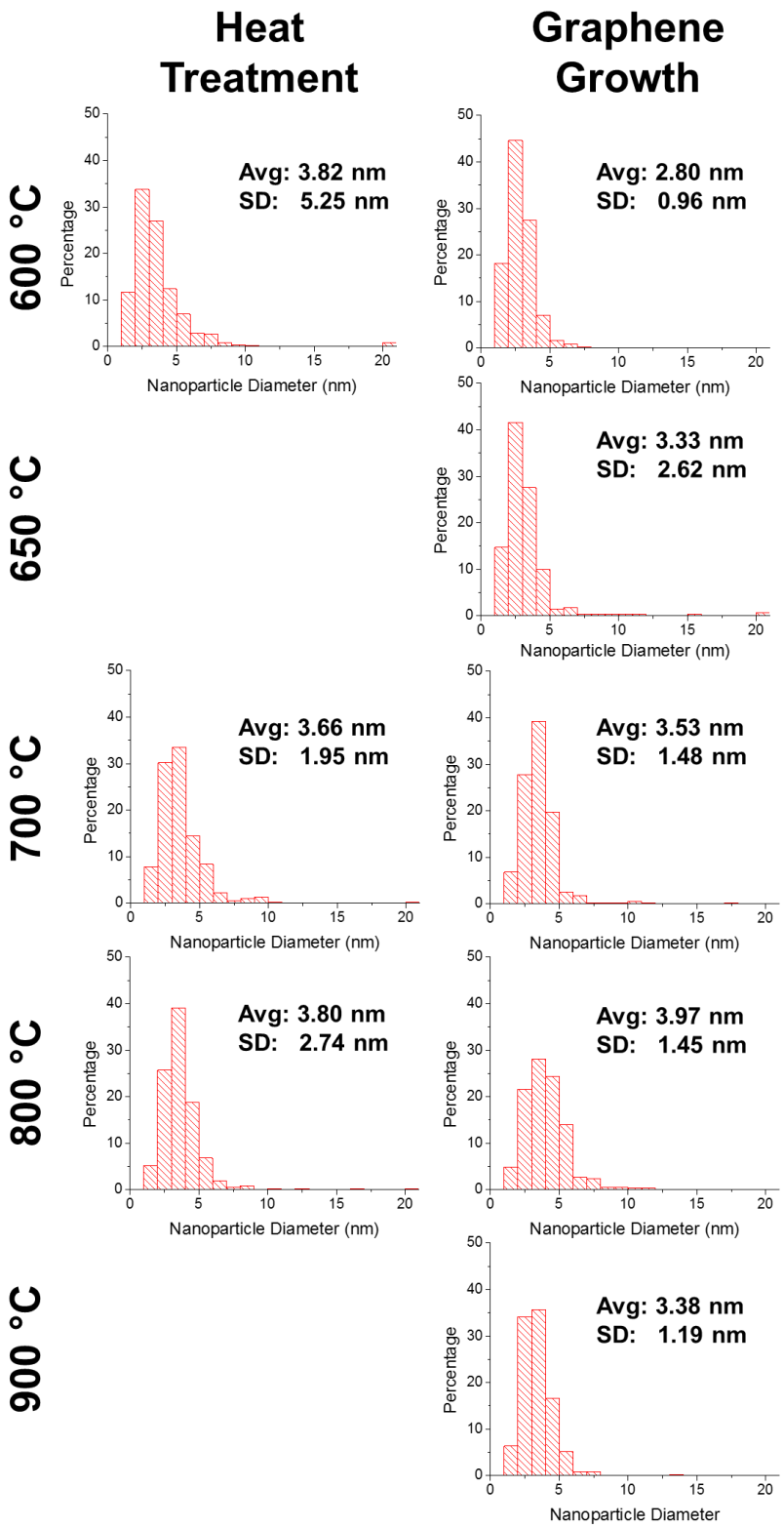

Figure 3. Size distribution histograms for heat treated and graphene growth Pt/C samples.

Having established the viability of growing graphene shells on Pt crystals whilst retaining a favourable crystal size, the effect of growth temperature on graphene shell formation was

then studied. Figure 3 shows histograms for samples produced both with and without CH_4 at temperatures ranging from 600-900 °C. For cases where heat treatment and graphene growth experiments were carried out at the same temperature, the average particle sizes were similar, though greater standard deviations were seen in the heat treated samples relative to the graphene growth ones. Therefore the difference between the graphene growth and heat treated samples is most noticeable at the highest temperature of 1000°C, where it can be expected that both the graphene growth rate and the sintering rate are at their highest. The samples produced at 600°C show anomalous behaviour. For the sample heat treated at 600°C (600H), the average and standard deviations are greater than 800H, and for the corresponding graphene growth sample (600G) the average crystal size is smaller than as-received HiSPEC 3000. Though taking into account the standard deviation both these average values are comparable to HiSPEC 3000. ACTEM examination of 600G indicates that the growth of graphene is unsuccessful at this temperature, as the crystals are similar in appearance to HiSPEC 3000 (Figure 4a). All Pt crystals observed at 700 and 800 °C have graphene shells (Figure 4b-c). Graphene growth was also attempted at 650 °C; electrochemical results presented later suggest that graphene shells did form at this temperature.

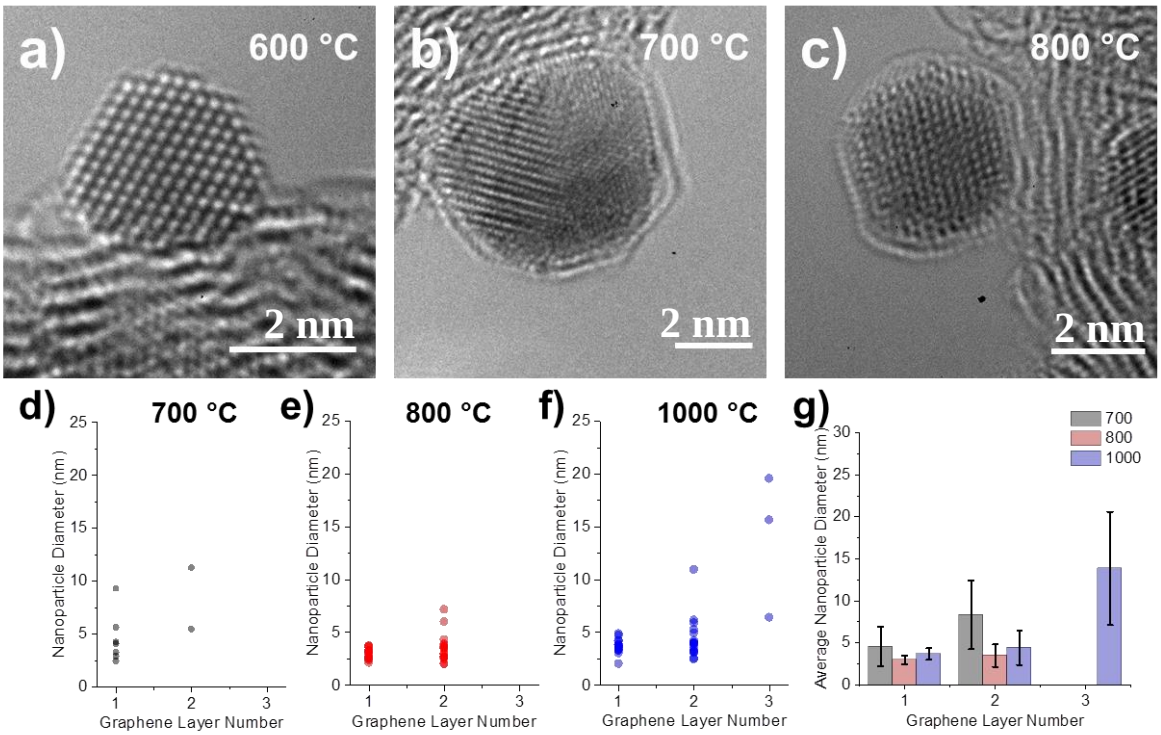

Figure 4. Attempts to grow graphene shells at different temperatures.a) A bare crystal following attempted graphene growth at 600 °C. b) A crystal covered in bilayer graphene following growth at 700 °C. c) A crystal covered in mono and bilayer graphene following growth at 800 °C. Graphs of graphene layer number vs nanoparticle diameter for (d) 700G (e) 800G (f) 1000G and (g) all three samples. Scale bars: 2 nm.

The CVD graphene growth mechanism on Pt has been studied previously, and is thought to occur firstly via the breakdown of hydrocarbons on the surface of Pt. Carbon on the Pt surface then dissolves into the bulk due to the solubility of carbon in Pt at elevated temperatures. A high enough carbon deposition rate results in the formation of a surface graphene layer which prevents further deposition. Lastly, some dissolved carbon precipitates from Pt as graphene during cooling.[15] The growth of graphene on Pt is therefore self-limiting, and the graphene layer number produced will depend on the carbon solubility in Pt and the surface to volume ratio of the Pt nanocrystal (i.e. the diameter). The rate of graphene formation is also a factor, though the fact that all nanocrystals appear completely covered at

the low temperature of 700 °C in 700G indicates this is probably less significant than the other factors. Carbon solubility will be higher at higher temperatures,[16] whilst the nanocrystal sizes are similar for all the graphene growth samples. The similarity in nanocrystal size for the graphene growth samples can be explained by the rapid graphene growth rate, graphene shells quickly impede the movement of nanocrystals over the support, meaning a similar degree of sintering occurs for all samples where graphene is successfully grown. Figure 4d-g presents graphs of nanocrystal diameter vs graphene layer number for three different temperatures (700, 800 and 1000 °C, samples 700G, 800G and 1000G respectively). The graph shows that most nanocrystals for all three samples are covered with one or two graphene layers, as most crystals have diameters less than 5 nm. There is also evidence that carbon solubility can have a significant effect on the number of layers, for example in 700G we observed a nanocrystal with ~10 nm diameter covered in monolayer graphene, whereas at higher temperatures monolayer coverage is limited to <5 nm nanocrystals. For 700G, only a couple of nanocrystals were observed with bilayer graphene compared to the other samples, and the average Pt nanocrystal size for bilayer graphene for 700G is higher than for 800G and 1000G. The average Pt size also increases from monolayer to bilayer graphene for all samples, which means that the contribution of carbon solubility to graphene layer number is noticeable. For 800G and 1000G the differences in size between monolayer and bilayer covered nanocrystals are very small however. Nanocrystals covered with trilayer graphene are only seen in 1000G sample, with the smallest trilayer Pt nanocrystal being greater than 7 nm in diameter, trilayers are not seen in the lower temperature samples, but this is likely due to the fact that nanocrystals with large diameters (>15 nm) were not observed or did not have edges lying over the vacuum. These measurements suggest that the carbon solubility does have an effect on the layer number, though nanocrystal size is a more dominant factor.

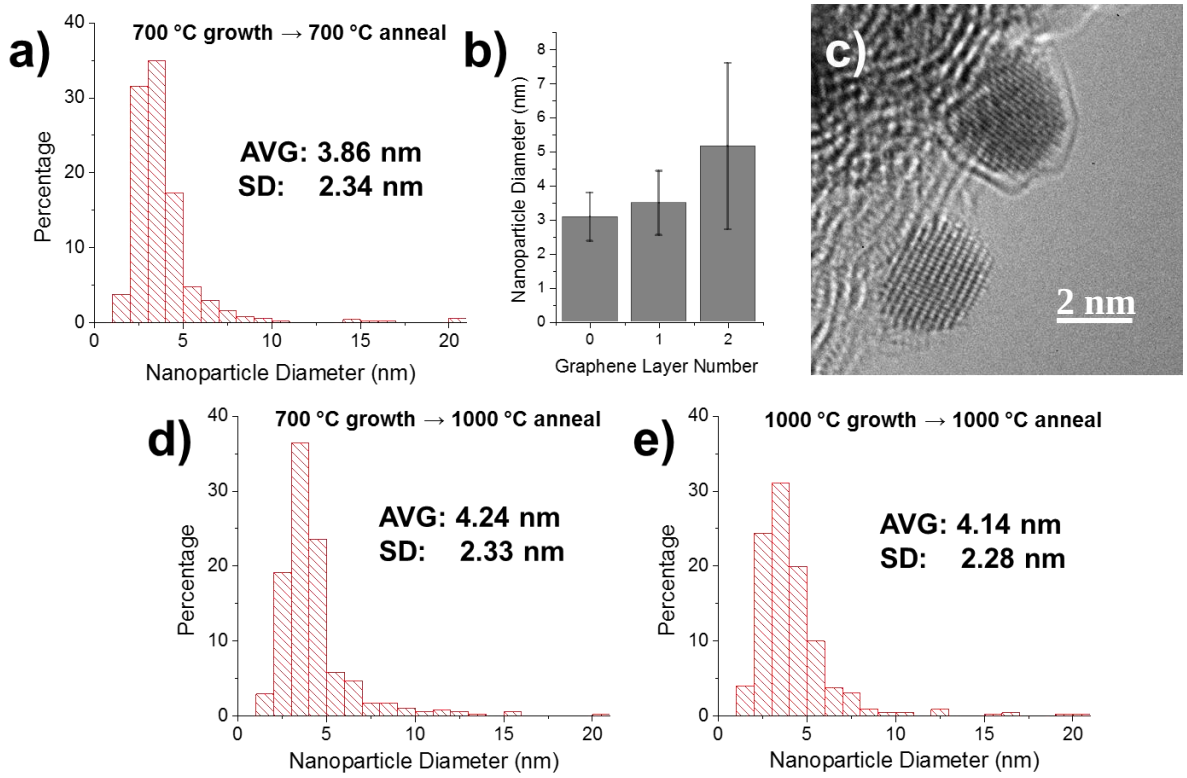

Figure 5. Resistance of graphene shells to heat-driven sintering in reducing atmospheres. a) Particle size histogram b) Pt nanocrystal diameter vs graphene layer number plot and c) ACTEM image of a bare Pt nanocrystal and a graphene covered Pt nanocrystals for samples CH_4 treated at 700 °C and subsequently heat treated at 700 °C (700G700H). Particle size histograms for d) 700G subjected to further heat treatment at 1000 °C (700G1000H) and e) 1000G subjected to further heat treatment at 1000 °C (1000G1000H). Scale bar: 2 nm.

Observations from the experiments where CH_4 was introduced imply that the graphene shells prevent sintering of the Pt nanocrystals at high temperature; however this is under conditions where CH_4 is being constantly supplied. We decided to further investigate the sintering resistance of the graphene shell covered Pt nanocrystals by subjecting them to further heat treatment in H_2/Ar following the initial graphene growth step. H_2 treatment at high temperatures has previously been used to reduce the layer number of graphene films grown on nickel substrates, where it acts to remove carbon dissolved in nickel.[17] Hydrogen

treatment can also etch graphene on the surface of metals such as copper.[18] As the CVD growth of graphene on Pt also proceeds via dissolved carbon, H_2 treatment could have a significant etching effect on the graphene shells, promoting the sintering of Pt nanocrystals. Figure 5a-c shows the histogram, graphene layer statistics and ACTEM image of a Pt/C sample that was treated with CH_4 for 30 minutes at 700 °C, followed by a further 90 minutes without CH_4 at the same temperature (700G700H). The histogram in Figure 5a indicates only a small degree of sintering has taken place, with a small increase in average nanocrystal size from 3.53 to 3.86 nm. The graphene layer statistics further demonstrate the effect of nanocrystal size on graphene layer number introduced in Figure 4; the nanocrystals which have had their shells etched to the point where their surface is uncovered have the smallest diameter (Figure 5b). Figure 5c shows two nanocrystals, one of which has been uncovered by the post-graphene growth annealing process. Similar experiments were also performed, with graphene shells produced at 700 °C and 1000 °C annealed at 1000°C for 90 minutes (700G1000H and 1000G1000H), the histograms of which are presented in figure 5d and 5e respectively. The average sizes and distributions of these two samples are similar. Though compared to their original sizes, a greater degree of sintering has occurred compared to the sample presented in Figure 5a. Both samples show particle sizes far below that of 1000H (Figure 1f). This shows that the graphene shells provide a good resistance to sintering at high temperatures in reducing atmospheres, even when the initial temperature used to synthesise the shells was comparatively low.

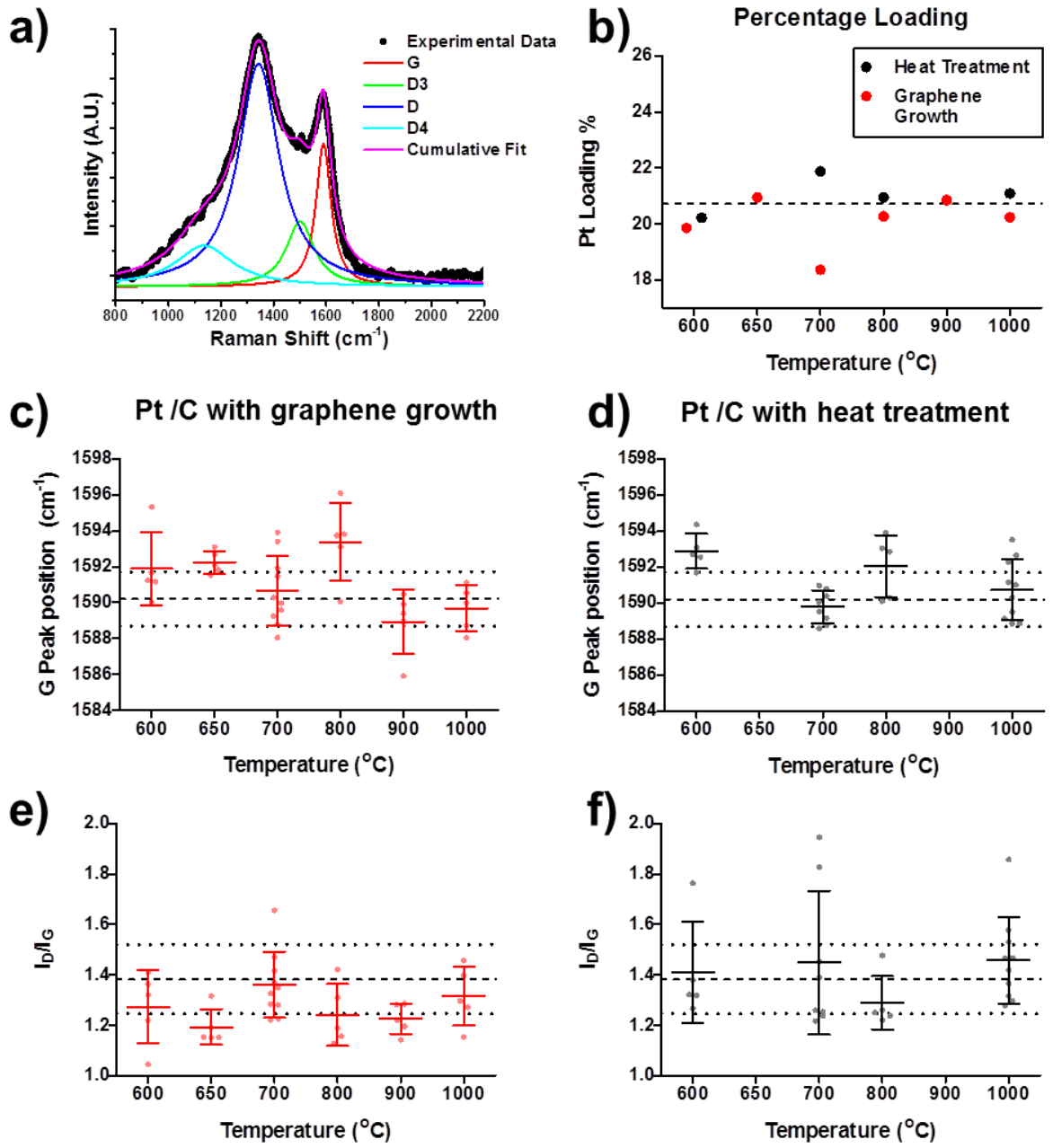

Figure 6. Raman and TGA evaluation of as-received and modified HiSPEC 3000. a) Representative Raman spectrum with Lorentzian fitting of HiSPEC 3000. b) TGA loading of samples treated for 30 minutes, where the dashed line represents the loading of HiSPEC 3000. Graphs of (c,d) G peak position and (e,f) I_d/I_g for graphene growth and heat treated samples respectively, the thick dashed lines represent the mean values for as-received HiSPEC 3000 and the dotted lines represent the ± standard deviation from the mean.

In the course of evaluating the catalysts in terms of both their resistance to sintering and their ECSA, it is important to elucidate whether any structural changes to the catalyst support have taken place during the course of the graphene growth and heat treatment experiments which could affect their performance under thermal or electrochemical stress. For example the graphitisation of the carbon support can have a significant effect on the electrochemical corrosion behaviour of these materials.[19] Furthermore, carbon supports with higher degrees of graphitisation have also been shown to improve sintering resistance under high temperature treatment with hydrogen.[20] For this purpose, Raman spectroscopy was employed to investigate the effect of different treatments on crystallinity, and TGA was used to ascertain whether any change in the Pt loading (wt%) had occurred due to any etching effects of the H_2 on the carbon support, or the deposition of carbon during the graphene growth processes.

Figure 6a shows a typical Raman spectrum from as-received HiSPEC 3000. The experimental data along with the Lorentzian fitted peaks are shown. Raman spectra of Vulcan XC-72R, the variety of carbon black used in HiSPEC 3000, are commonly fitted with three D peaks in addition to the G peak.[21-23] All spectra recorded across all samples were found to have these features. The three D peaks have previously been denoted as D, D3 and D4. A D2 peak is also commonly fitted in spectra from other varieties of carbon black, [24] though we were unable to fit this peak in our experimental data. Figure 6b shows TGA results for the catalysts subjected to 30 minute treatments, the dotted line represents the loading of the as-received catalyst. Repeated testing of the as-received catalyst deviates by >1% Pt loading. It can be seen that most samples lie very close to the as-received value, and that there are no trends with regard to temperature to be seen for either the graphene growth or heat treated samples. The results at 700 ° C for both treatments are anomalous and do not fit in with the other samples. The results could be explained as local changes to the Pt density

during the heating process, but uniform TEM results and a low degree of sintering make this very unlikely.

There are several metrics which can be obtained from the Raman spectra of carbon materials to assess changes in crystallinity. The G peak position (Figure 6c,d) and I_d/I_g ratio (Figure 6e,f) are values which will change with either decreasing or increasing carbon crystallite size.[25] In the case of carbon blacks, a decrease in the G peak position and the I_d/I_g ratio indicate an increase in crystallite size.[26] In Figure 6c-f, the mean values for the as-received catalyst values are represented by the thick dashed line, with the dotted lines representing the ± standard deviation from the mean. Again, no particular trends are seen with regards to either treatment with temperature, any deviations that are seen, for example the fact that all mean values of I_d/I_g for the graphene growth samples are lower than those for HiSPEC 3000, are not consistent with the results from the other metric, G peak position. In the case of most samples their means are within the ± standard deviation for HiSPEC 3000. The lack of any such changes suggests that the carbon support is unchanged in terms of crystallinity. The G peak full width at half maximum (FWHM), another indicator of crystallinity, was also found to show no trends (Figure 7). Raman and TGA measurements for the samples subjected to further annealing following the growth of graphene shells were also recorded and found to be similar to HiSPEC 3000 (Figure 8). Though no changes in crystallinity were found, it is possible that the treatments have an effect upon the surface chemistry of the carbon blacks, which usually contain numerous oxygen-containing functional groups.[27] Previous experiments have shown that heat treatment of these groups lead to their decomposition at temperatures lower than those used for some of the modification experiments.[28]

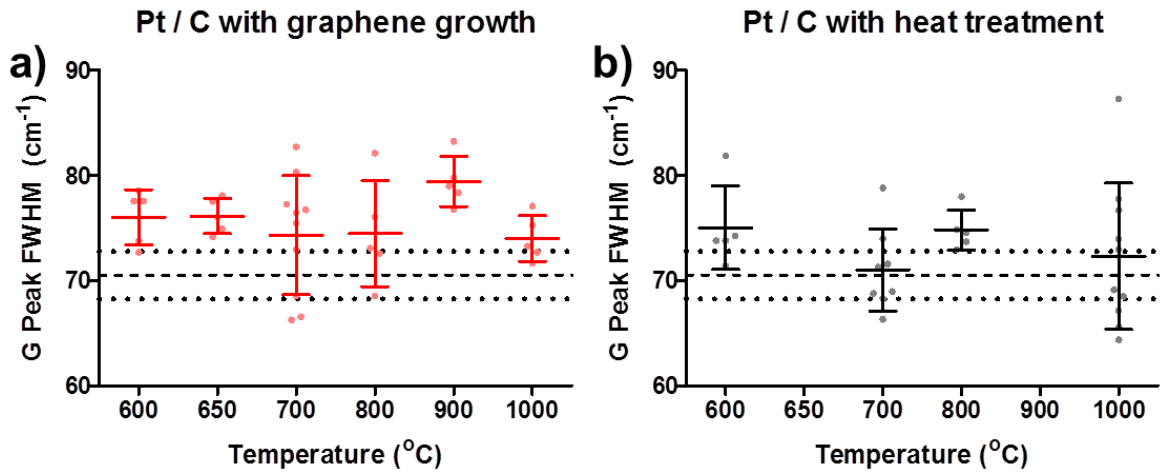

Figure 7. G peak FWHM for graphene growth and heat treated samples. The dashed lines represent the mean value for as-received HiSPEC 3000 and the dotted lines represent the standard deviation from the mean.

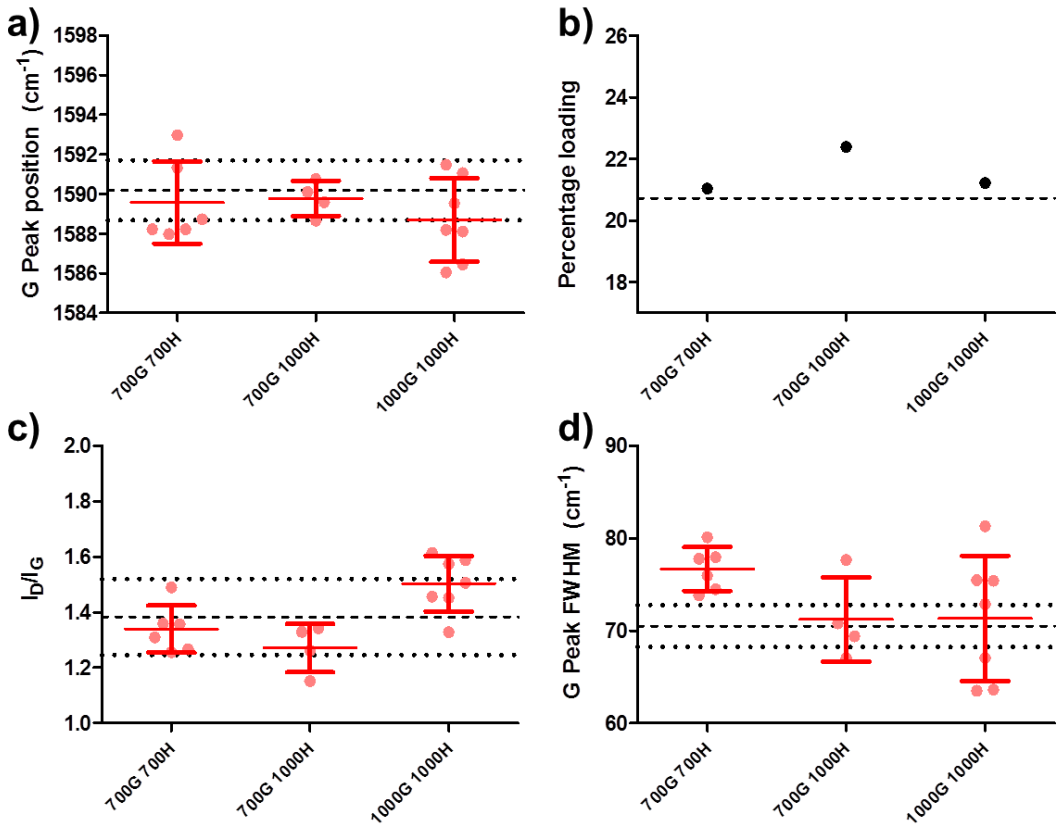

Figure 8. Raman and TGA data for samples annealed following graphene growth. (a) G peak position (b) TGA Pt % loading (c) I_d/I_g ratio (d) G peak FWHM.

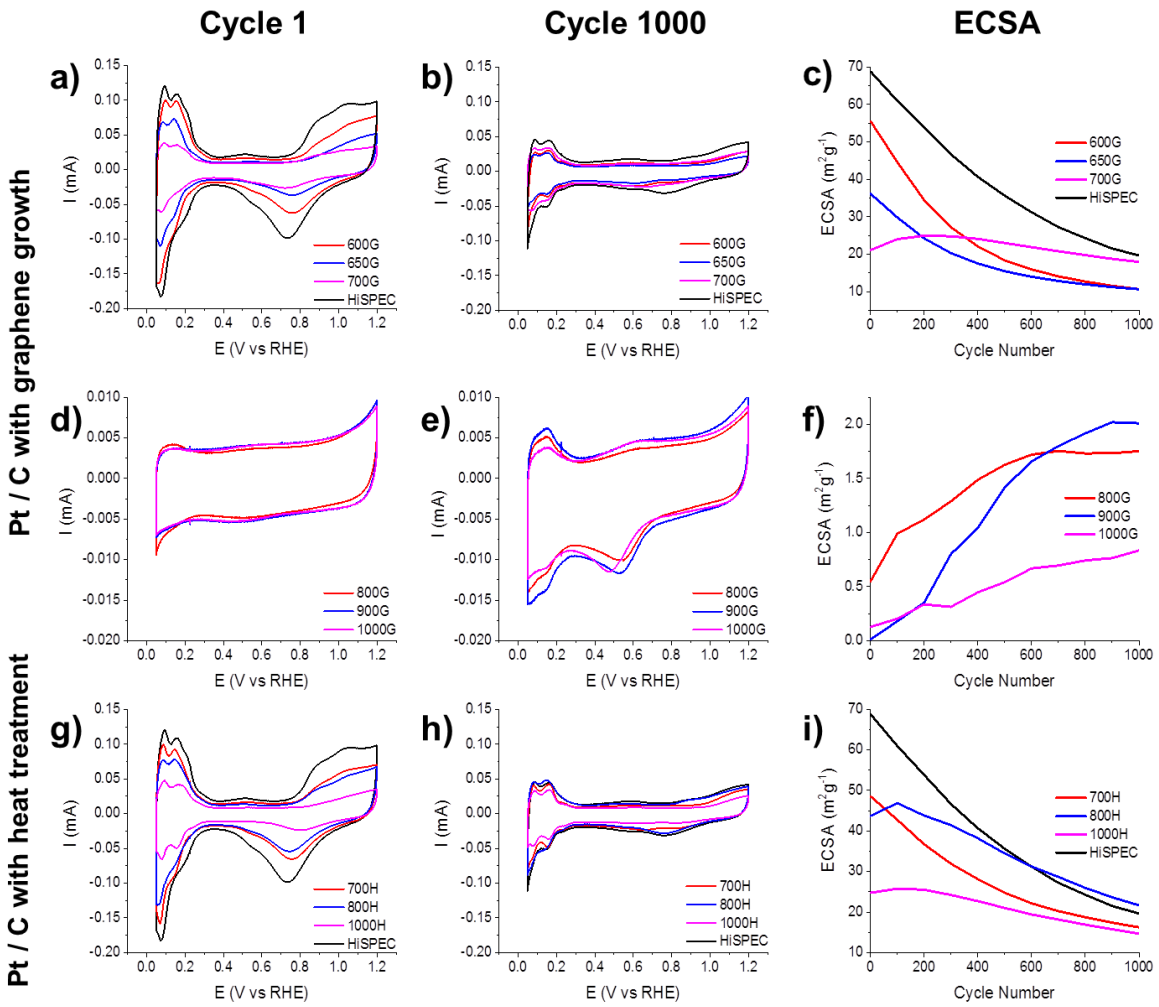

Figure 9. Cyclic voltammetry results for as-received and modified HiSPEC 3000. (a) Initial cycle (b) final cycle and (c) ECSA vs cycle number plot for HiSPEC, 600G, 650G and 700G. (d) Initial cycle, (e) final cycle and (f) ECSA plot for 800G, 900G and 1000G. (g) Initial cycle, (h) final cycle and ECSA plot for HiSPEC, 700H, 800H and 1000H.

Following the synthesis and characterisation of the modified catalysts using microscopy, spectroscopy, and thermal analysis, the electrochemical characteristics of the catalysts were evaluated using cyclic voltammetry experiments in acidic media (see Experimental section). Figure 9 shows the voltammograms from the initial and final cycles, as well as plots of ECSA with data points every 100 cycles. The graphs for graphene growth samples are split into two groups for clarity (Figure 9c,f). Figure 9a shows the initial voltammograms for HiSPEC 3000 and those for the three lowest graphene growth treatment temperatures (600G, 650G

and 700G); it is obvious that HiSPEC 3000 has the highest initial ECSA, and that the initial value decreases as the graphene growth temperature is increased. Whilst ACTEM to confirm the growth of graphene on Pt crystals at 650 °C was not acquired, the considerable decrease in initial ECSA when going from a 600 to 650 °C indicates that graphene growth has taken place. Taken together with the particle sizes of these samples being similar, it can be inferred that the resultant graphene has blocked the access of H^+ to the Pt nanocrystal surface. This is consistent with observations from previous experiments where crystalline graphene acted simultaneously as a Pt support and an encapsulating carbon layer, resulting in low ECSA values.[8] Figure 9c indicates that the effect of graphene growth on the initial ECSA is significant, resulting in an almost 50% reduction in ECSA for 650G. A 50 °C increase in growth temperature to 700°C results in a value less than a third of the initial HiSPEC ECSA, showing that the small increase in average layer number and crystallinity resulting from this small temperature change has a significant effect on the accessible Pt surface area.

When a temperatures 800°C and above are used for graphene growth, initial ECSA is reduced to practically zero, with only a very small peak seen in the adsorption and desorption regions for 800°C in the initial cycle (Figure 9d). The increased growth temperature and crystallinity has resulted in complete coverage of the Pt crystals, and an insignificant concentration of defects or holes exist to allow the electrolyte access to the Pt surface. The contribution of the graphene shells to this ECSA decrease is confirmed by the initial values for the heat treated samples, where no graphene was grown (Figure 9g). While 700H, 800H and 1000H show decreasing values of ECSA which can be attributed to sintering, it should be noted that the values of ECSA for the heat treated samples are higher than those subjected to graphene growth at the same temperature; this effect is more pronounced at temperatures of and above 800 °C.

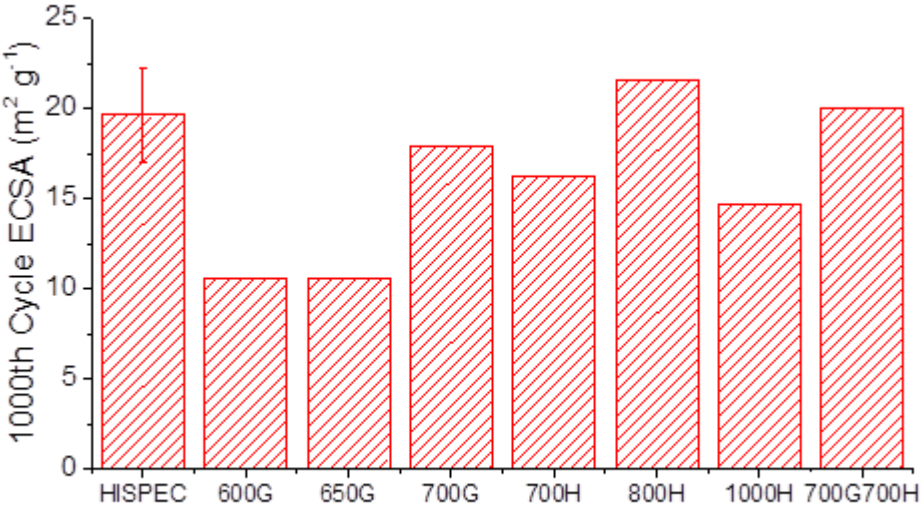

Figure 10. Final cycle ECSA for some of the samples, the error in the HiSPEC 3000 value is the standard deviation from the mean obtained from repeat experiments.

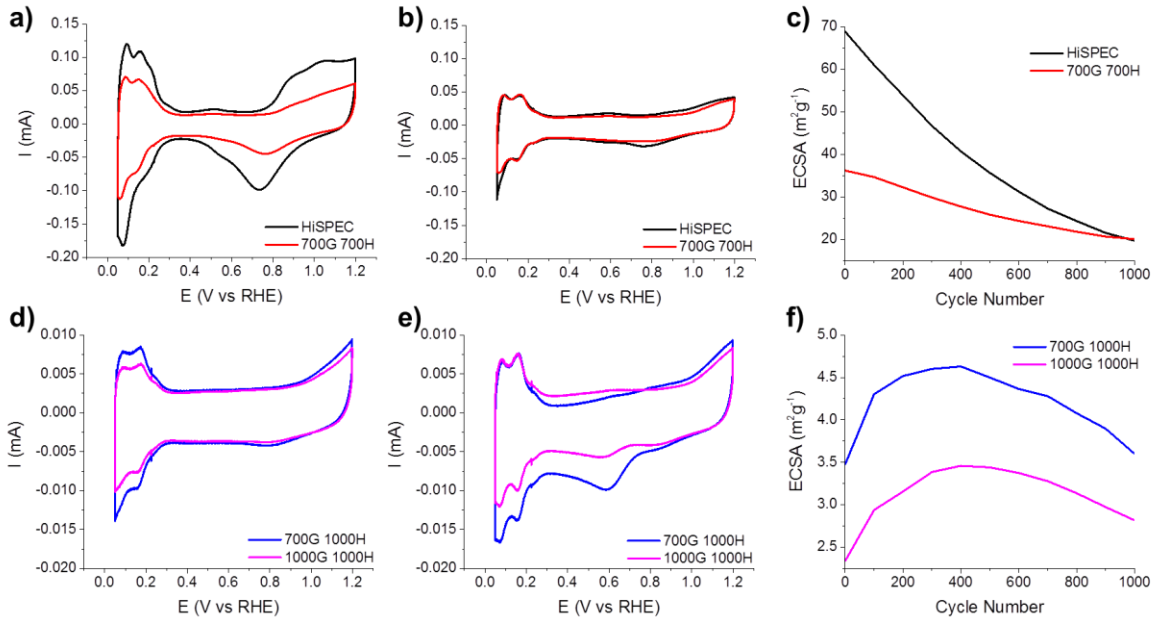

Figure 11. Electrochemical data from samples annealed following graphene growth. (a) Initial cycle (b) final cycle and (c) ECSA vs cycle number for as-received HiSPEC and 700G700H. (d) Initial cycle (b) final cycle and (c) ECSA vs cycle number for 700G1000H and 1000G1000H.

In addition to having the highest initial ECSA of all samples, HiSPEC 3000 also has the joint highest absolute ECSA following electrochemical cycling. 700H, 800H, 700G and 700G700H also had final ECSAs within the mean ± standard deviation of HiSPEC 3000(Figure 10). This indicates that the graphene growth has no beneficial effect upon the durability of the catalyst. In the case of graphene growth samples produced at 800-1000 °C, their ECSA never exceeds 2 m^2g^{-1}Pt. In terms of the final relative ECSA, a higher percentage retention of ECSA is seen as the graphene growth temperature is increased, the exception being that the percentage ECSA is higher for 900 °C than 1000 °C for graphene growth samples. A similar trend is seen for the heat treated samples, this effect has also been observed in previous studies of heat treated Pt/C catalysts,[29] and could be due to the decrease in relative population of smaller crystals due to sintering during heat treatment, which disappear faster than larger ones during electrochemical cycling.[30]

It should be noted that for the graphene growth samples, the catalyst takes an increasing number of cycles to activate as the synthesis temperature increases. This is not noticeable for 600 and 650 °C samples, but it can be seen that the 700 °C sample reaches an ECSA maximum at its 200th cycle. This maximum occurs at the 700th and 900th cycles for the 800 and 900 °C graphene samples respectively, whilst the 1000 °C does not reach a maximum value during the 1000 cycle period. These prolonged activation processes have been seen in other materials with porous carbon layers.[11] 800G, 900G and 1000G also show significant changes in the shapes of their voltammograms following 1000 cycles. In addition to the emergence of peaks due to the exposure of the Pt surface, a peak also appears from 0.4-0.6 V vs RHE in the reverse cycles, this is indicative of the presence of oxygen, which has dissolved into the electrolyte from the atmosphere over the course of the 1000 cycle experiment. This is only noticeable in these samples because of the similar magnitude of these oxygen peaks to the hydrogen adsorption/desorption peaks.

Recently, in the field of hydrogen evolution reaction (HER) catalysis, experimentalists have become aware of the disadvantages of using Pt as a counter electrode.[31] Pt has been shown to dissolve from the counter electrode and deposit on HER catalysts in electrochemical experiments, affecting the measured activity of the catalyst under study. It is possible that this deposition could also be occurring on the catalysts in this study, and would manifest itself as a gradual increase in ECSA, similar to the behavior seen for some of the graphene covered catalysts in this study. However, it is unlikely that deposited Pt causes the behavior observed for these catalysts, as the ECSA increase would be seen occurring at similar cycle numbers, rather than the increasingly long activation process seen here in the graphene covered catalysts as the graphene synthesis temperature increases. Furthermore, large particles visible using SEM were observed following Pt deposition from the counter electrode, which would cause an increase in Pt crystal average size post cycling which was not seen for 700G, 800G and 900G (Figure 12h). In addition, particles uncovered by graphene were not observed in post-cycling TEM images of 1000G (Figure 15) and the density of crystals on the surface of the 1000G catalyst decreased after 1000 cycles (Table 1), the opposite of what would be expected if Pt deposition from the counter electrode was occurring and if graphene covered Pt crystals were not gradually detaching from the support due to activation. Therefore it is believed that the observed ECSA behavior of the graphene covered catalysts is not due to the effect of the counter electrode.

The electrochemical data for 700G700H, 700G1000H and 1000G1000H is shown in Figure 11. Compared to 700G, 700G700H has a higher initial ECSA (Figure 11a) but as can be seen in the ECSA plot in Figure 11c, it also has a roughly equal final ECSA to that of 700G. This indicates that while annealing exposes more Pt surface, the electrochemical durability of the catalyst has not been significantly affected. 700G1000H and 1000G1000H have very low initial ECSA values as with 800G, 900G and 1000G. 1000G1000H has a higher initial ECSA than 1000G, consistent with the etching of the graphene shells. During the etching period, in addition to the removal of some of the graphene shell, it might also be expected that the crystallinity of the remaining graphene shells would increase. The ECSA profile of 700G1000H seems to suggest this, as the ECSA is much lower than that of 700G. This suggests that in determining ECSA, the crystallinity of the graphene shells is a more important factor than the layer number. The ECSA with cycle number for both 700G1000H and 1000G1000H are similar, with an initial activation step where the ECSA increases is followed by the levelling out and decrease in the ECSA. This decrease begins around the 400^{th} cycle for both samples, leading to final ECSA values similar to the initial values.

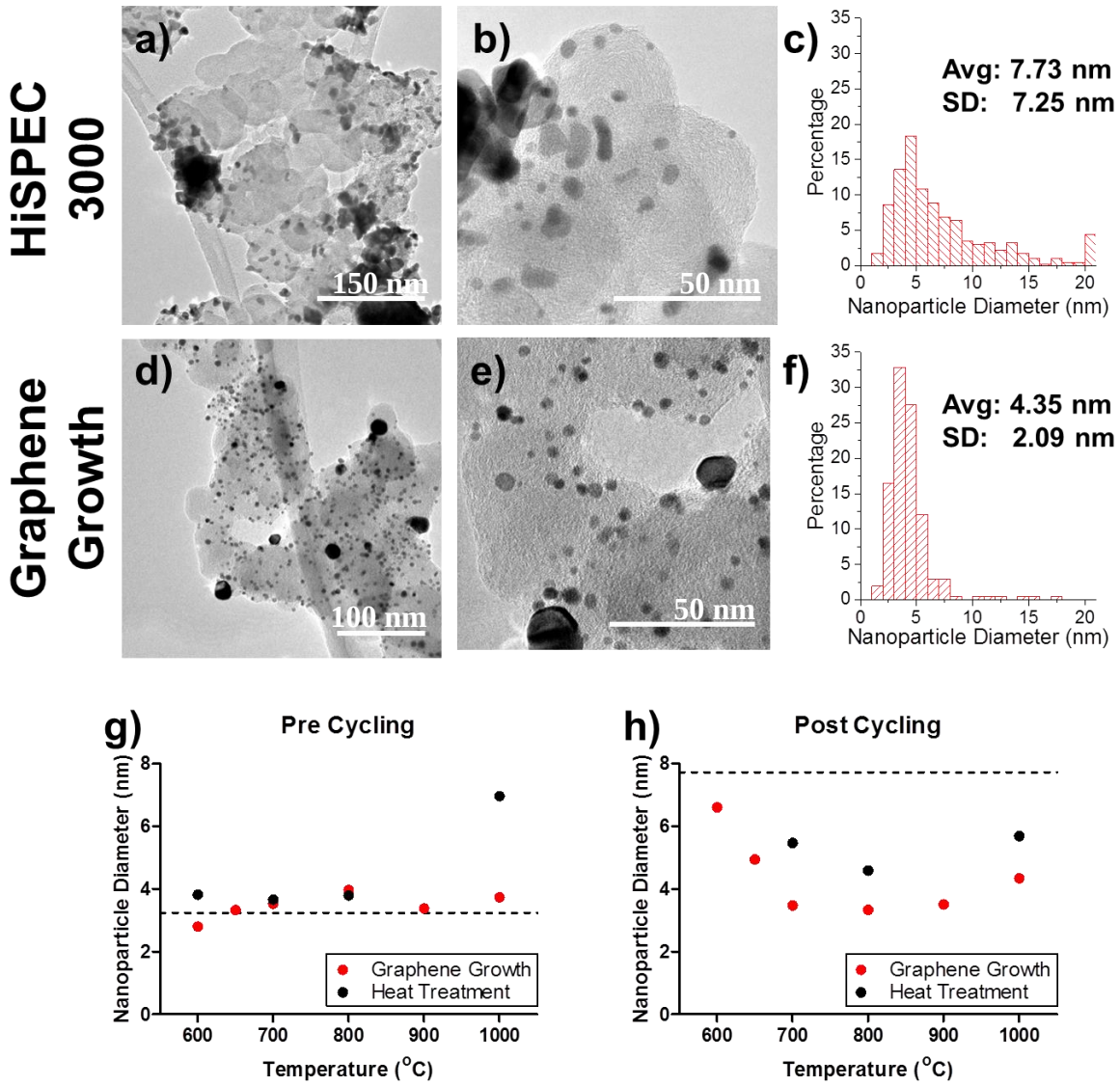

Figure 12. Post-cycling TEM analysis of as-received and modified HiSPEC 3000. a-b) Low magnification TEM images and c) particle size histogram for HiSPEC 3000 following electrochemical cycling. d-e) Low magnification TEM images and f) particle size histogram for 1000G following electrochemical cycling. Graphs of (g) pre cycling and (h) post-cycling average nanoparticle diameters for heat treated and graphene grown samples. The dashed lines represent the averages for HiSPEC 3000. Scale bars: (a) 150 nm (b) 50 nm (d) 100 nm (e) 50 nm.

These results seem to indicate that the graphene shells directly grown on Pt/C are largely detrimental with regards to electrochemical cycling, at best providing similar absolute values

of final ECSA to as-received HiSPEC 3000, and at higher temperatures leading to negligible ECSA values. In order to further understand the role the graphene shells have on the electrochemical behaviour of these catalysts, TEM images post-cycling were recorded. Figure 12 shows the post-cycling TEM results for HiSPEC 3000 (Figure 12a-c) and 1000G (Figure 12d-f). Graphs showing the average Pt crystal size pre cycling (Figure 12g) and post-cycling (Figure 12h) are also shown, where the dashed line represents the HiSPEC 3000 average size in both cases. The particle size histograms for the other samples post-cycling can be seen in Figure 13, and post-cycling TEM images and particle size histograms for samples that were annealed following graphene growth are shown in Figure 14.

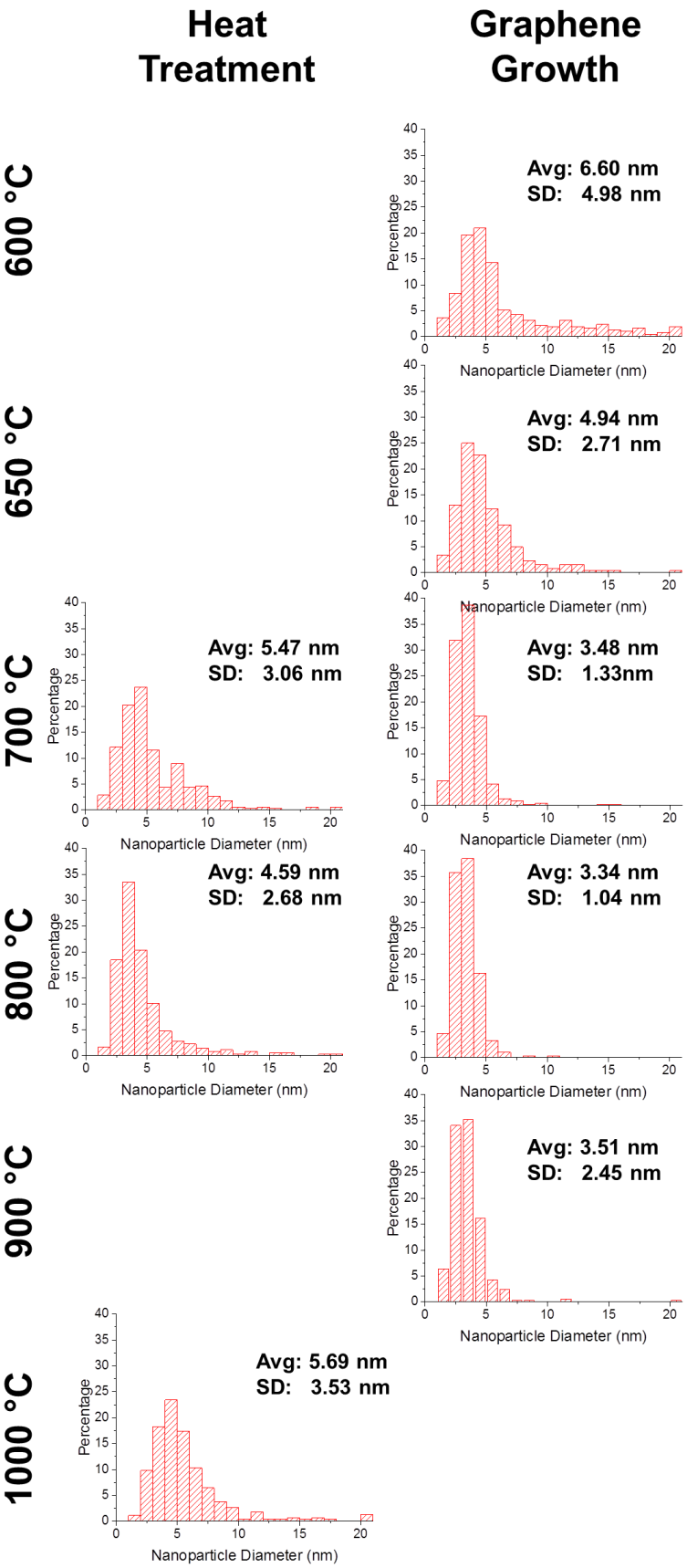

Figure 13. Particle size histograms of modified catalysts post cycling.

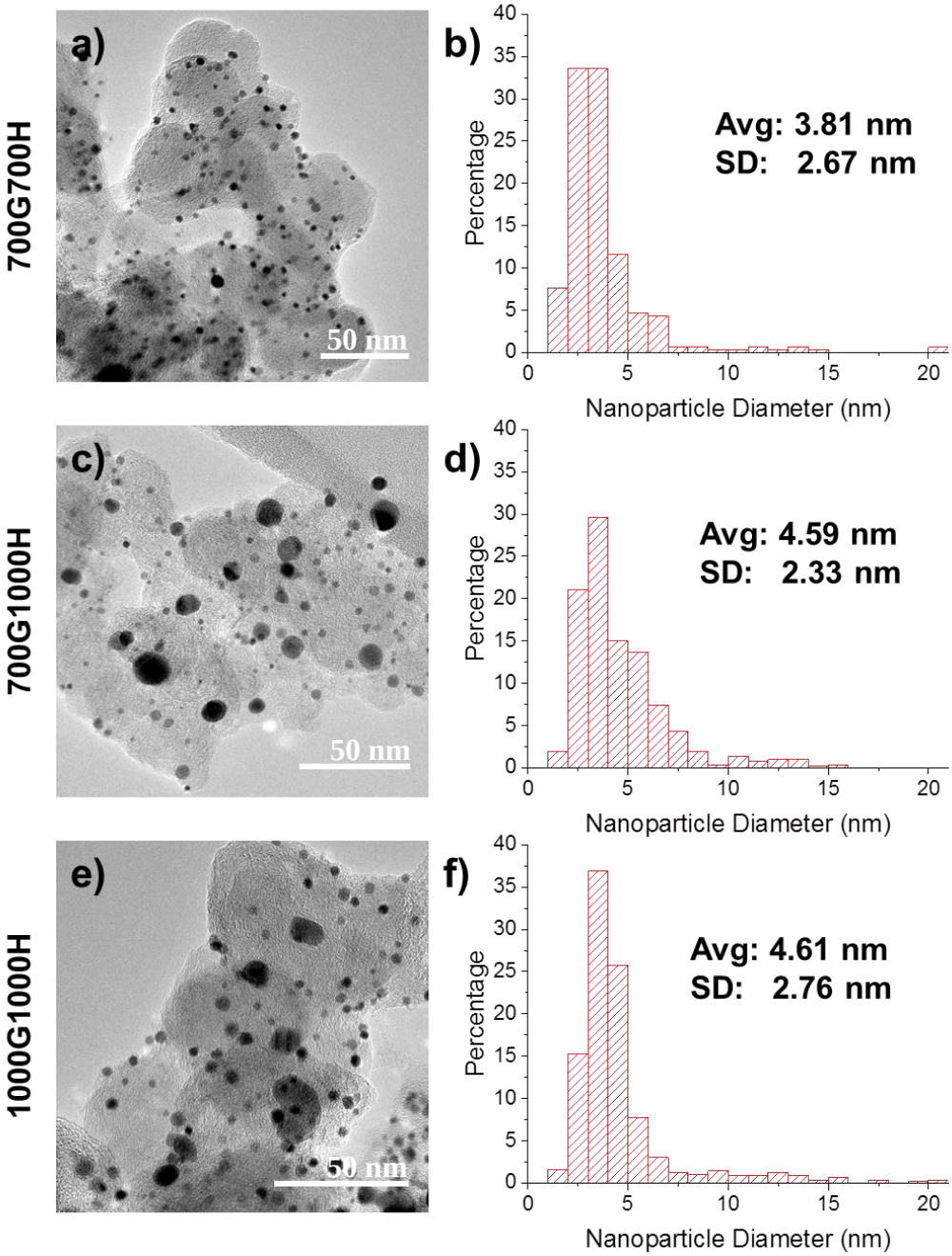

Figure 14. Post-cycling TEM images and particle size histograms for (a,b) 700G700H, (c,d) 700G1000H and (e,f) 1000G1000H respectively. Scale bars: 50 nm.

From the TEM images of HiSPEC 3000 following post-cycling (Figure 12a and b) large aggregates of Pt crystals can be observed and some areas of the carbon support no longer

contain Pt crystals, suggesting degradation of the catalyst has occurred. This is in contrast to the TEM images seen in Figure 1, which show well distributed crystals with a narrow size distribution. The particle size distribution, seen in Figure 12c, reflects this sintering, showing that the population has broadened, with a much higher average crystal size and standard deviation than that seen pre-cycling. This is consistent with the usual degradation mechanisms seen in Pt/C catalysts, where crystals and atoms migrate to form larger aggregates and crystals detach from the support entirely.[2] In the case of the 1000 °C graphene growth sample (Figure 12 d-f) the appearance is very similar to that seen pre-cycling, only a small degree of sintering has taken place, with a high population of crystals having diameters less than 5 nm. Furthermore the distribution of crystals over the surface is still uniform, indicating a far lower degree of Pt migration. By comparing the pre- and post-cycling Pt diameter averages for the other samples (Figure 12g and h) we find that samples with graphene grown at 700 °C and above have similar values, whereas samples treated with CH_4 below 700°C and the heat treated samples have higher average sizes. The exception to this is the sample heat treated at 1000 °C, which has a lower average Pt size. This could indicate that the heat treatment and possible modification of the surface groups has led to a weaker interaction between the Pt crystals and the carbon surface, as the lower average size indicates detachment of large crystals.

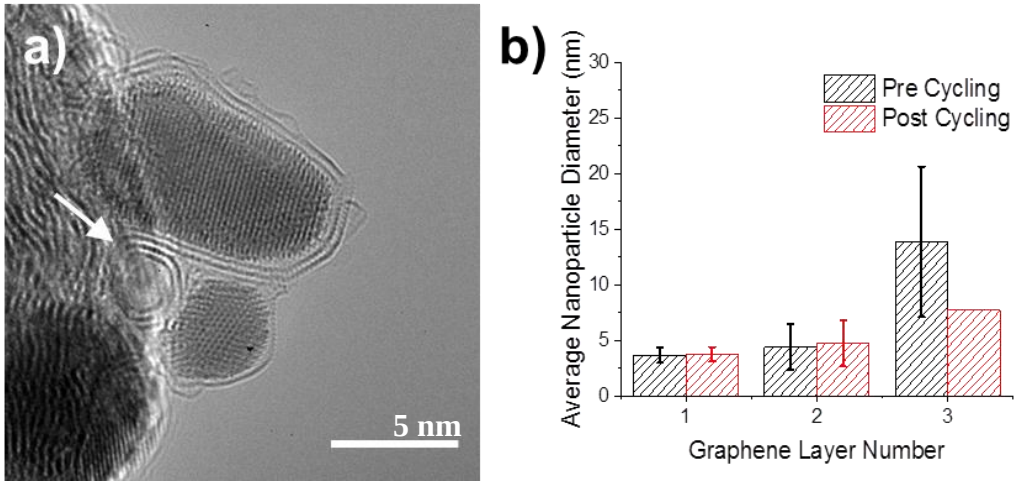

Figure 15. ACTEM data for 1000G post-cycling. a) ACTEM image of Pt crystals in 1000G, the white arrow indicates an empty graphene shell. b) Graph of Pt nanocrystal diameter vs graphene layer number, comparing 1000G pre and post-cycling. Scale bar: 5 nm.

Despite a low degree of sintering of the nanocrystals with graphene grown at 1000 °C, both initial and final ECSA are much lower than would be expected. These similar trends are seen for 700G, 800G and 900G. ACTEM images were acquired post-cycling for the 1000 °C graphene sample (Figure 15a). No obvious damage has occurred to the graphene shells following the electrochemical cycling, though the arrow indicates what appears to be an empty graphene shell, which could be caused by the corrosion of the Pt crystal inside. This was the only case in which an empty graphene shell was observed however. The nanocrystal diameter to graphene shell layer number ratio is also very similar to that seen in the pre cycling sample, as shown in Figure 15b. It could be expected that electrochemical cycling could gradually degrade the graphene shells, as observed for carbon layer wrapped Pt nanocrystals.[12] However, this effect is not observed in our ACTEM data, though data for other graphene growth samples post-cycling was not obtained. Because obvious sintering does not take place in our graphene covered samples over the course of electrochemical cycling, it is likely that detachment of Pt crystals from the support is the dominant

degradation mechanism seen in these materials. To confirm this, the crystal density was estimated from TEM images pre- and post- cycling for graphene grown samples produced at 700-1000 °C (Table 1). For these samples it is possible to use the crystal density to study detachment because of the minimised degree of sintering. Whilst the values of crystal density obtained are imprecise due to the inhomogeneity of the Pt crystal distribution both before and after electrochemical cycling, the results obtained for 700G and 1000G indicate that detachment of Pt crystals from the support is taking place. Despite detachment taking place, we do not see any evidence for "burst" graphene shells; this could be due to strong attachment between the Pt crystal and graphene shell, which is stronger than the interaction between the graphene shell and the carbon support itself, leading to simultaneous detachment of both graphene shell and Pt crystal from the support.

	Pre cycling		Post cycling	
Temperature (°C)	**Crystals per μm^2**	**St Dev (per μm^2)**	**Crystals per μm^2**	**St Dev (per μm^2)**
700	17000	8000	11000	8000
800	15000	4000	15000	6000
900	15000	11000	14000	8000
1000	17000	7000	8000	2000

Table 1. Nanocrystal density values for graphene growth samples pre- and post-electrochemical cycling. Values are rounded to the nearest thousand. The values were obtained by analysing different sample areas as seen in TEM images.

In summary, there are several factors which contribute to the observed electrochemical behaviour of the Pt catalysts with graphene shells. As the graphene synthesis temperature increases, the layer number and crystallinity of the graphene shells also increases, and post-growth annealing experiments indicate that the crystallinity plays a more significant role than layer number in determining the surface area accessible to the electrolyte. The thinnest and

most defective graphene shells produced in our experiments still lead to a significant ECSA decrease, even when the nanocrystal size remains similar to the untreated sample. When temperatures above 700 °C are used to grow graphene shells on Pt, increasingly longer activation processes take place as the temperature increases. This indicates that some damage to the graphene shells may occur, which exposes the surface of the nanocrystals, this process takes longer for the thicker and more crystalline graphene shells. In the case of 700G the ECSA levels out soon after the activation process and begins to decrease over the 1000 cycles. If longer cycling experiments were carried out, it is likely that this effect would be seen for the higher temperature samples also, as was observed for 700G700H and 1000G1000H. Though the ECSA decrease of the 700G sample has occurred, post-cycling TEM images indicates that little aggregation has occurred; suggesting detachment is the most dominant degradation mechanism for the graphene covered samples, though evidence for Ostwald ripening was observed for 1000G. The high coverage of graphene covered Pt nanocrystals post-cycling despite low ECSA values suggests that two competing processes take place, slow electrochemical degradation of the graphene shells which exposes the Pt surface, and detachment of the Pt crystals, the latter process of which becomes dominant increasingly later in the electrochemical cycling as the synthesis temperature increases.

It is clear that the stability afforded by graphene shells with respect to high temperature treatment in reducing atmospheres does not translate to increased stability with respect to electrochemical cycling treatments. One suggestion as to why electrochemical stability is not conferred to the Pt crystals by the graphene shells could be due to the processes taking place during electrochemical cycling. Electrochemical Pt oxidation occurs at the high potentials during each electrochemical cycle, [32] and is accompanied by a small volume change due to the formation of the surface oxide.[33] As the graphene shells in our method are templated by the Pt catalyst, rather than formed by pyrolysation of a polymer layer used in some other

experiments, the graphene shell is almost the same diameter as the Pt crystals. The graphene shell may not be able to accommodate the changes associated with the oxidation of Pt, and may result in detachment of the Pt nanocrystal and the graphene shells from the carbon support. The graphene-support attachment may not be strong enough to confer enhanced stability under electrochemical stress. We cannot conclusively prove that the poor electrochemical stability is related to the oxide formation however. A technique such as IL-TEM (identical location TEM), which allows the study of identical areas of samples pre- and post- cycling, would allow better insight into effects of electrochemical cycling on the graphene covered Pt materials.[34]

6.4 Conclusions

The spatial confinement of Pt nanocrystals within layers made of graphitised carbon or other materials has been identified as a way to increase the durability of PEMFC catalysts, by preventing sintering and detachment of nanocrystals from the support. However, in many cases the catalyst support and the Pt nanocrystal shell are formed simultaneously, and it is difficult to understand the effect of the shell on the ECSA and stability. Here, we demonstrate the growth of graphene shells over Pt nanocrystals in a commercial catalyst. The shells can be grown in a short time, and result in minimal modification of the loading and crystallinity of the carbon support. Furthermore it is possible to grow graphene shells whilst retaining narrow size distributions and similar average sizes to the unmodified catalyst. We find that the graphene shells allow the catalysts to be subjected to high temperature treatments in reducing atmospheres whilst preventing sintering. However, despite the strong anchoring of the crystals to the surface by the graphene shells with regards to thermal conditions, we find that the graphene shells provide no beneficial effect with regards to the

electrochemical stability of the catalysts, with no graphene modified catalysts exceeding the final ECSA of the as-received HiSPEC 3000. Furthermore, even the thinnest and least crystalline graphene shells produced in this chapter led to a substantial decrease in ECSA. Evidence suggests that the Pt crystals detach along with the graphene shells, suggesting the poor electrochemical stability of the graphene covered catalysts could be due to the poor interaction between the graphene shell and the carbon support. This emphasises the importance of a strong interaction between the Pt covering and the support, and may explain the high durability seen in materials which employ this strategy.[3,5,8,11] We hope this study will make it easier to make judgements regarding factors contributing to the stability of these materials, and therefore inform their design. Our CVD growth method involving rapid introduction to the furnace may be useful for carrying out the high temperature treatments of catalysts where sintering of supported nanoparticles is undesirable, and where graphene coverings can themselves be used as the catalyst, several examples exist in the literature where cobalt or cobalt-alloy nanocrystals covered in graphene (or doped graphene) formed by in-situ pyrolysis methods can induce graphene to act as a catalyst for the ORR[35] or HER[14,36,37] via charge-transfer of electrons from the metal core to the graphene shell.

6.5 References

(1) Debe, M. K. Electrocatalyst approaches and challenges for automotive fuel cells. *Nature* **2012,** *486,* 43-51.

(2) Meier, J. C.; Galeano, C.; Katsounaros, I.; Witte, J.; Bongard, H. J.; Topalov, A. A.; Baldizzone, C.; Mezzavilla, S.; Schüth, F.; Mayrhofer, K. J. J. Design criteria for stable Pt/C fuel cell catalysts. *Beilstein J. Nanotechnol.* **2014,** *5,* 44-67.

(3) Galeano, C.; Meier, J. C.; Peinecke, V.; Bongard, H.; Katsounaros, I.; Topalov, A. A.; Lu, A.; Mayrhofer, K. J. J.; Schüth, F. Toward Highly Stable Electrocatalysts via Nanoparticle Pore Confinement. *J. Am. Chem. Soc.* **2012,** *134*, 20457-20465.

(4) Huang, J.-F.; Hsiao, H.-Y. Electrochemically Identifying Degradation Pathways of Carbon-Supported Pt Catalysts Assists in Designing Highly Durable Catalysts. *ACS Appl. Mater. Interfaces* **2016,** *8*, 33749-33754.

(5) Cheng, N.; Banis, M. N.; Liu, J.; Riese, A.; Li, X.; Li, R.; Ye, S.; Knights, S.; Sun, X. Extremely Stable Platinum Nanoparticles Encapsulated in a Zirconia Nanocage by Area-Selective Atomic Layer Deposition for the Oxygen Reduction Reaction. *Adv. Mater.* **2015,** *27*, 277-281.

(6) Cheng, K.; Kou, Z.; Zhang, J.; Jiang, M.; Wu, H.; Hu, L.; Yang, X.; Pan, M.; Mu, S. Ultrathin carbon layer stabilized metal catalysts towards oxygen reduction. *J. Mater. Chem. A* **2015,** *3*, 14007-14014.

(7) Cheng, K.; Jiang, M.; Ye, B.; Amiinu, I. S.; Liu, X.; Kou, Z.; Li, W.; Mu, S. Three-Dimensionally Costabilized Metal Catalysts toward an Oxygen Reduction Reaction. *Langmuir* **2016,** *32*, 2236-2244.

(8) Kim, H.; Robertson, A. W.; Kim, S. O.; Kim, J. M.; Warner, J. H. Resilient High Catalytic Performance of Platinum Nanocatalysts with Porous Graphene Envelope. *ACS Nano* **2015,** *9*, 5947-5957.

(9) Shen, L.; Sun, T.; Zhuo, O.; Che, R.; Li, D.; Ji, Y.; Bu, Y.; Wu, Q.; Yang, L.; Chen, Q.; Wang, X.; Hu, Z. Alcohol-Tolerant Platinum Electrocatalyst for Oxygen Reduction by Encapsulating Platinum Nanoparticles inside Nitrogen-Doped Carbon Nanocages. *ACS Appl. Mater. Interfaces* **2016,** *8*, 16664-16669.

(10) Zhang, Q.; Yu, X.; Ling, Y.; Cai, W.; Yang, Z. Ultrathin nitrogen doped carbon layer stabilized Pt electrocatalyst supported on N-doped carbon nanotubes. *Int. J. Hydrog. Energy*., **2017,** http://doi.org/10.1016/j.ijhydene.2017.02.156

(11) Guo, L.; Jiang, W.-J.; Zhang, Y.; Hu, J.-S.; Wei, Z.-D.; Wan, L.-J. Embedding Pt Nanocrystals in N-Doped Porous Carbon/Carbon Nanotubes toward Highly Stable Electrocatalysts for the Oxygen Reduction Reaction. *ACS Catal.* **2015,** *5*, 2903-2909.

(12) Kou, Z.; Cheng, K.; Wu, H.; Sun, R.; Guo, B.; Mu, S. Observable Electrochemical Oxidation of Carbon Promoted by Platinum Nanoparticles. *ACS Appl. Mater. Interfaces* **2016,** *8*, 3940-3947.

(13) Antolini, E. Graphene as a new carbon support for low-temperature fuel cell catalysts. *Appl. Catal. B-Environ.* **2012,** *123*, 52-68.

(14) Zhang, H.; Ma, Z.; Duan, J.; Liu, H.; Liu, G.; Wang, T.; Chang, K.; Li, M.; Shi, L.; Meng, X.; Wu, K.; Ye, J. Active Sites Implanted Carbon Cages in Core–Shell Architecture: Highly Active and Durable Electrocatalyst for Hydrogen Evolution Reaction. *ACS Nano* **2016,** *10*, 684-694.

(15) Sun, J.; Nam, Y.; Lindvall, N.; Cole, M. T.; Teo, K. B. K.; Park, Y. W.; Yurgens, A. Growth mechanism of graphene on platinum: Surface catalysis and carbon segregation. *Appl. Phys. Lett.* **2014,** *104*, 152107.

(16) Siller, R. H.; Oates, W. A.; McLellan, R. B. The solubility of carbon in palladium and platinum. *Journal Less-Common MET* **1968,** *16*, 71-73.

(17) Gong, Y.; Zhang, X.; Liu, G.; Wu, L.; Geng, X.; Long, M.; Cao, X.; Guo, Y.; Li, W.; Xu, J.; Sun, M.; Lu, L.; Liu, L. Layer-Controlled and Wafer-Scale Synthesis of Uniform and High-Quality Graphene Films on a Polycrystalline Nickel Catalyst. *Adv. Funct.Mater.* **2012,** *22*, 3153-3159.

(18) Zhang, Y.; Li, Z.; Kim, P.; Zhang, L.; Zhou, C. Anisotropic Hydrogen Etching of Chemical Vapor Deposited Graphene. *ACS Nano* **2012,** *6*, 126-132.

(19) Forouzandeh, F.; Li, X.; Banham, D. W.; Feng, F.; Ye, S.; Birss, V., Evaluation of the Corrosion Resistance of Carbons for Use as PEM Fuel Cell Cathode Supports. *J. Electrochem. Soc.* **2015,** *162* (12), F1333-F1341.

(20) Coloma, F.; Sepulvedaescribano, A.; Rodriguezreinoso, F., Heat-Treated Carbon-Blacks as Supports for Platinum Catalysts. *J. Catal.* **1995,** *154*, 299-305.

(21) Ma, J.; Habrioux, A.; Guignard, N.; Alonso-Vante, N. Functionalizing Effect of Increasingly Graphitic Carbon Supports on Carbon-Supported and TiO2–Carbon Composite-Supported Pt Nanoparticles. *J. Phys Chem. C*, **2012,** *116*, 21788-21794.

(22) Chisaka, M.; Iijima, T.; Tomita, A.; Yaguchi, T.; Sakurai, Y. Oxygen Reduction Reaction Activity of Vulcan XC-72 Doped with Nitrogen Under NH_3 Gas in Acid Media. *J. Electrochem. Soc.* **2010,** *157*, B1701-B1706.

(23) Holade, Y.; Morais, C.; Servat, K.; Napporn, T. W.; Kokoh, K. B. Enhancing the Available Specific Surface Area of Carbon Supports to Boost the Electroactivity of Nanostructured Pt Catalysts. *Phys. Chem. Chem. Phys.* **2014,** *16*, 25609- 25620.

(24) Sadezky, A.; Muckenhuber, H.; Grothe, H.; Niessner, R.; Pöschl, U. Raman microspectroscopy of soot and related carbonaceous materials: Spectral analysis and structural information. *Carbon* **2005,** *43*, 1731-1742.

(25) Ferrari, A. C.; Robertson, J. Interpretation of Raman spectra of disordered and amorphous carbon. *Phys. Rev. B* **2000,** *61*, 14095-14107.

(26) Gruber, T.; Zerda, T. W.; Gerspacher, M. Raman studies of heat-treated carbon blacks. *Carbon* **1994,** *32*, 1377-1382.

(27) Boehm, H. P., Some aspects of the surface chemistry of carbon blacks and other carbons. *Carbon* **1994,** *32*, 759-769.

(28) Boehm, H. P. Surface oxides on carbon and their analysis: a critical assessment. *Carbon* **2002,** *40*, 145-149.

(29) Makharia, R.; Kocha, S.; Yu, P.; Sweikart, M. A.; Gu, W.; Wagner, F.; Gasteiger, H. A. Durable PEM Fuel Cell Electrode Materials: Requirements and Benchmarking Methodologies. *ECS Trans.* **2006,** *1*, 3-18.

(30) Shao-Horn, Y.; Sheng, W. C.; Chen, S.; Ferreira, P. J.; Holby, E. F.; Morgan, D. Instability of Supported Platinum Nanoparticles in Low-Temperature Fuel Cells. *Top. Catal.* **2007,** *46*, 285-305.

(31) Chen, R.; Yang, C.; Cai, W.; Wang, H.Y.; Miao, J.; Zhang, L.; Chen, S.; Liu, B. Use of Platinum as the Counter Electrode to Study the Activity of Nonprecious Metal Catalysts for the Hydrogen Evolution Reaction. *ACS Energy Lett.* **2017**, *2*, 1070.

(32) Hiraoka, F.; Matsuzawa, K.; Mitsushima, S. Degradation of Pt/C Under Various Potential Cycling Patterns. *Electrocatalysis* **2013,** *4*, 10-16.

(33) Jerkiewicz, G.; Vatankhah, G.; Lessard, J.; Soriaga, M. P.; Park, Y.-S. Surface-oxide growth at platinum electrodes in aqueous H2SO4: Reexamination of its mechanism through combined cyclic-voltammetry, electrochemical quartz-crystal nanobalance, and Auger electron spectroscopy measurements. *Electrochim. Acta* **2004,** *49*, 1451-1459.

(34) Mayrhofer, K. J. J.; Ashton, S. J.; Meier, J. C.; Wiberg, G. K. H.; Hanzlik, M; Arenz, M. Non-Destructive Transmission Electron Microscopy Study of Catalyst Degradation Under Electrochemical Treatment. *J. Power Sources*, **2008**, 185, 734-739

(35) Han, C.; Bo, X.; Zhang, Y.; Li, M.; Nsabimana, A.; Guo, L., N-doped graphitic layer encased cobalt nanoparticles as efficient oxygen reduction catalysts in alkaline media. *Nanoscale* **2015**, *7*, 5607-5611.

(36) Zhou, W.; Zhou, J.; Zhou, Y.; Lu, J.; Zhou, K.; Yang, L.; Tang, Z.; Li, L.; Chen, S. N-Doped Carbon-Wrapped Cobalt Nanoparticles on N-Doped Graphene Nanosheets for High-Efficiency Hydrogen Production. *Chem. Mat.* **2015**, *7*, 2026-2032.

(37) Yang, Y.; Lin, Z.; Gao, S.; Su, J.; Lun, Z.; Xia, G.; Chen, J.; Zhang, R.; Chen, Q. Tuning Electronic Structures of Nonprecious Ternary Alloys Encapsulated in Graphene Layers for Optimizing Overall Water Splitting Activity. *ACS Catal.* **2017,** *7*, 469-479.

Chapter 7

Conclusions and Future Work

7.1 Conclusions

In this thesis, several aspects of the usage of graphene in fuel cell applications were explored; the thermal synthesis of Pt crystals on plasma treated CVD graphene foam, the synthesis of novel 3D carbon structures via thermal annealing and the synthesis and testing of Pt particles on these materials, and the synthesis of graphene shells on a commercial Pt/C catalyst.

CVD graphene foams were successfully synthesised. Defects were induced via oxygen plasma, which were found to act as nucleation sites for Pt crystals. The results suggest that this method can be used to control the synthesis of thermally produced nanomaterials on the graphene foam surface. However it was also found that the characterisation techniques that were utilised, such as electron microscopy and Raman spectroscopy, cannot alone build a full picture of the structural changes induced by the plasma treatments, nor can they give a proper description of the effect of heat treatments on the plasma induced functional groups. It was found that while areas of well distributed crystals could be found on each sample, the folds in the graphene foam produced areas of highly aggregated platinum, highlighting a weakness of combining thermal annealing Pt synthesis with graphene foam substrates.

3D graphene and graphene/CNT hybrid powders were fabricated using the thermal annealing of nickel acetate as the sole precursor. This method proved to be versatile, with different annealing conditions allowing materials of different morphologies and crystallinities to be formed. When these materials were utilised as supports for the thermal annealing of Pt nanocrystals along with commercially available carbon black, it was found that the poorly

crystalline supports did not result in well distributed nanocrystals. This was theorised to be a consequence of the formation mechanism.

Finally, the growth of graphene layers on a commercial Pt/C with minimal sintering of the Pt crystals was demonstrated. It was shown that the layer number roughly depended on the synthesis temperature. The CVD processes used did not result in a change in the crystallinity of the carbon black support, nor the Pt weight percentage, as indicated by Raman spectroscopy and TGA respectively, indicating that this CVD method could be used to modify supported catalysts with graphene layers with minimal modification to the graphene support. It was found that the layers led to a decrease in the ECSA, with higher growth temperatures leading to more crystalline and thicker graphene layers, and in turn a Pt surface that was less accessible to the electrolyte. Furthermore, this led to no positive effects on the durability of the Pt crystals.

7.2 Future Work

There are several avenues which could be explored in order to expand on the work carried out in this thesis. With regards to the formation of Pt crystals on 3D graphene foams by thermal annealing, an XPS study would allow a more detailed and less ambiguous understanding of the processes occurring during Pt nanocrystal synthesis to be ascertained.

The synthesis of 3D hybrid graphene structures could be expanded upon by the exploration of different precursors, or the mixing of nickel acetate with other precursors. For example, in order to increase the specific surface area of these materials, nickel acetate could be mixed with a nickel or copper precursor that does not contain carbon, in order to lead to a reduced average layer number for the materials formed. In addition, heteroatom containing precursors

such as nickel (II) dimethylglyoxime could be explored to synthesise 3D graphitic materials. In addition to doped graphene providing better binding for Pt atoms, nitrogen doped graphene can also act as a metal-free catalyst for the oxygen reduction reaction. The Pt/C materials formed using the nickel acetate derived materials only performed comparatively at best to the commercially available Pt/C catalyst, this is partially due to the thermal Pt synthesis method, which only produces well distributed crystals on some of the novel catalyst supports, and always results in a broad nanoparticle size distribution relative to the solution based synthesis methods used for the commercial catalysts. Therefore it would be useful to be able to use a solution based Pt synthesis method for the novel supports, in order to properly compare them to the commercial catalyst.

The inability of the CVD synthesised graphene shells on the commercial catalyst to increase durability in electrochemical tests was theorised to be caused by the weak interaction between the graphene shells and the carbon black support, in combination with the processes occurring during electrochemical cycling. In order to further the understanding of the role of the graphene shells, polymer could be annealed on the surface of the commercial Pt/C catalyst, forming carbon over the whole surface of the catalyst, not just on the Pt crystals as in the CVD approach. This could confirm the explanations put forward in Chapter 6. In addition, XPS studies could be carried out in order to understand the electronic influence of the graphene shells on the Pt crystal.